IMFUFA tekst

- I, OM OG MED MATEMATIK OG FYSIK

# Dynamics of glass-forming liquids: Will theory and experiment ever meet?

Henriette Wase Hansen
Glass & Time, IMFUFA, Roskilde University
PhD thesis

**nr. 507 – 2018**

Roskilde University,
Department of Science and Environment, IMFUFA
P.O. Box 260, DK - 4000 Roskilde
E-mail: imfufa@ruc.dk

**Dynamics of glass-forming liquids:**
**Will theory and experiment ever meet?**

Henriette Wase Hansen
Glass & Time, IMFUFA, Roskilde University
PhD thesis

IMFUFA tekst nr. 507/2018 — 187 sider — ISSN: 0106-6242

The overall theme of this work has been to experimentally test the shoving model and isomorph theory related to the dynamics of glass-forming liquids, both of which, rather than being universal explanations, are expected to work in the simplest case.

We test the connection between fast and slow dynamics in light of the shoving model from the temperature dependence of the mean-squared displacement from neutron scattering at nanosecond timescale and the elastic modulus from shear mechanics. We find the fast dynamics to correlate with the alpha relaxation time and fragility in agreement with predictions from the shoving model. The shoving model is tested on three liquids with simple dynamic behaviour in two versions, one formulated in terms of the instantaneous elastic modulus and one expressed in terms of the mean-squared displacement. We also test the underlying assumption connecting the two versions, directly relating the temperature dependence of the mean-squared displacement and that of the shear modulus. In the viscous liquid, we find this to hold. We interpret the discrepancy at higher temperatures where the mean-squared displacement has a stronger temperature dependence than the shear modulus, as the alpha relaxation entering the neutron instrument window. In the view of the shoving model, the short-time properties govern the viscous slowing down.

We have developed a new sample cell for doing simultaneous dielectric and neutron spectroscopy at elevated pressure. This new high-pressure cell allows us to do experiments with high accuracy. From the dielectric signal, we can determine the alpha relaxation time fast and with high precision in a large area of the temperature-pressure phase diagram while studying nano- and picosecond dynamics from neutron spectroscopy.

We use the new sample cell to locate isochrones, i.e. lines of constant alpha relaxation time in temperature and pressure with the purpose of testing isomorph theory on three systems, two simple van der Waals and a hydrogen bonded liquid. We find density scaling and isochronal superpositioning to hold for all three systems on alpha relaxation dynamics, and for the two van der Waals liquids, also when we have separation of timescales, i.e. the alpha relaxation is not contributing to the picosecond dynamics. The concept of isomorphs is observed to break down in two cases for the hydrogen bonding system: in density scaling of intramolecular motion and in isochronal superposition of the picosecond dynamics when there is separation of timescales. We show for one of the van der Waals liquids how the picosecond dynamics can be expressed as a function of the alpha relaxation time in agreement with the prediction of the existence of a one-dimensional phase diagram from isomorph theory, where one parameter is believed to control all dynamics.

**PhD thesis**

by Henriette Wase Hansen

# Dynamics of glass-forming liquids: Will theory and experiment ever meet?

Glass & Time, Department of Science and Environment
Roskilde University

Supervisor: Kristine Niss
Co-supervisor: Bernhard Frick

PhD thesis
"Dynamics of glass-forming liquids: Will theory and experiment ever meet?"

by Henriette Wase Hansen

Submitted to
the Doctoral School of Science and Environment
Roskilde University
27 October 2017

Supervised by Kristine Niss
Glass & Time, IMFUFA, Roskilde University

and co-supervised by Bernhard Frick
Institut Laue-Langevin

# Abstract

The overall theme of this work has been to experimentally test the shoving model and isomorph theory related to the dynamics of glass-forming liquids, both of which, rather than being universal explanations, are expected to work in the simplest case.

We test the connection between fast and slow dynamics in light of the shoving model from the temperature dependence of the mean-squared displacement from neutron scattering at nanosecond timescale and the elastic modulus from shear mechanics. We find the fast dynamics to correlate with the alpha relaxation time and fragility in agreement with predictions from the shoving model. The shoving model is tested on three liquids with simple dynamic behaviour in two versions, one formulated in terms of the instantaneous elastic modulus and one expressed in terms of the mean-squared displacement. We also test the underlying assumption connecting the two versions, directly relating the temperature dependence of the mean-squared displacement and that of the shear modulus. In the viscous liquid, we find this to hold. We interpret the discrepancy at higher temperatures where the mean-squared displacement has a stronger temperature dependence than the shear modulus, as the alpha relaxation entering the neutron instrument window. In the view of the shoving model, the short-time properties govern the viscous slowing down.

We have developed a new sample cell for doing simultaneous dielectric and neutron spectroscopy at elevated pressure. This new high-pressure cell allows us to do experiments with high accuracy. From the dielectric signal, we can determine the alpha relaxation time fast and with high precision in a large area of the temperature-pressure phase diagram while studying nano- and picosecond dynamics from neutron spectroscopy.

We use the new sample cell to locate isochrones, i.e. lines of constant alpha relaxation time in temperature and pressure with the purpose of testing isomorph theory on three systems, two simple van der Waals and a hydrogen bonded liquid. We find density scaling and isochronal superpositioning to hold for all three systems on alpha relaxation dynamics, and for the two van der Waals liquids, also when we have separation of timescales, i.e. the alpha relaxation is not contributing to the picosecond dynamics. The concept of isomorphs is observed to break down in two cases for the hydrogen bonding system: in density scaling of intramolecular motion and in isochronal superposition of the picosecond dynamics when there is separation of timescales. We show for one of the van der Waals liquids how the picosecond dynamics can be expressed as a function of the alpha relaxation time in agreement with the prediction of the existence of a one-dimensional phase diagram from isomorph theory, where one parameter is believed to control all dynamics.

# Resumé

Det overordnede tema for denne afhandling har været eksperimentelt at teste shoving-modellen og isomorfteorien, begge relateret til dynamik i glas-dannende væsker, og som begge snarere end at være universelle, er forventet at virke i det simpleste tilfælde.

Vi tester forbindelsen mellem hurtig og langsom dynamik ud fra shoving-modellen ved hjælp af temperaturafhængigheden af middelvejsforskydningen målt med neutronspredning på nanosekond-tidskala og det elastiske modul målt med shear-mekanik. Vi tester shoving-modellen på tre væsker med simpel dynamik i to forskellige versioner, én udtrykt ved det instantane shear-bidrag og én udtrykt ved middelvejsforskydningen. Vi tester også den antagelse, der opstår fra de to versioner, nemlig den direkte sammenhæng mellem temperaturafhængigheden af middelvejsforskydningen og den for det elastiske modul. Antagelsen holder i den viskøse væske. Vi fortolker afvigelsen ved højere temperaturer, hvor middelvejsforskydningen vokser hurtigere med temperatur end shear-modulet, som alfa-relaksationen, der kommer ind i vinduet på neutronspredningsinstrumentet. Ud fra et shoving-model perspektiv er den langsomme dynamik styret af den hurtige dynamik.

Vi har udviklet en ny prøveholder til at lave samtidige målinger med dielektrisk og neutron-spektroskopi ved høje tryk. Med den nye prøveholder kan vi måle med stor nøjagtighed; fra det dielektriske signal kan vi hurtigt måle alfa-relaksationstiden i et stort område i temperatur og tryk, mens vi studerer dynamik på nano- og picosekund-tidsskalaer med neutronspredning.

Vi bruger den nye prøveholder til at identificere isochroner, som er linjer i et temperatur-tryk fasediagram med konstant alfa-relaksationstid, med det formål at teste isomorfteorien på tre systemer, to van der Waals-væsker og en med hydrogenbindinger. Vi finder, at isomorfteorien virker for de to van der Waals-væsker, men bryder ned for den hydrogen-bundne væske i to tilfælde: når vi kigger på intramolekulære bevægelser, og når vi har separation af tidsskalaer og kigger på dynamik på picosekund-tidsskala, som er helt separeret fra alfa-relaksationen. Vi viser for en af de van der Waals-bundne væsker, at den hurtige dynamik kan udtrykkes som funktion af alfa-relaksationstiden i overenstemmelse med forudsigelse fra isomorfteorien om, at én parameter styrer dynamik på alle tidsskalaer.

# Preface

I have had the pleasure of considering this PhD project my job for the past three years in the Glass & Time group at Roskilde University. The work has been carried out from November 2014 to October 2017 under the wings of Kristine Niss. The project was funded by the Danish Council for Independent Research (Sapere Aude: Starting Grant) and Roskilde University. A main part of this project has been the development of a new sample cell for neutron scattering experiments for combining dielectric and neutron spectroscopy under high-pressure, which has been carried out in collaboration between Roskilde University and Institut Laue-Langevin (ILL). This three-year Long-Term Proposal (LTP-6-7) that was accepted just after I started my PhD and which took off in January 2015, ended up being a very large part of my PhD project. I joined the project in autumn 2015 on the last beamtime of material testing after the main design ideas were made. I was so fortunate as to spend six months in beautiful Grenoble at the ILL from February to August 2016, working together with the SANE group, and in particular, with Bernhard Frick, who ended up co-supervising my PhD project. During these six months, the high-pressure cell and the dielectric setup were tested and implemented to prepare for the first real beamtime in July 2016. I am happy that this development project ended up taking a substantial amount of my time; I have had a lot of fun with the orange cryostats behind IN16B, and I have learned so much. During my PhD, besides the six-month stay at the ILL, which was mostly during shutdown, I have had a total of 50 days of beamtime also at ILL, mostly on IN16B and IN5, which left me sleepless in Grenoble many a night. All the work that has gone into this thesis could of course not have been carried out without help from the many great people that I have had the pleasure to work with.

## Acknowledgements

First, I want to thank my dear supervisors. Kristine Niss for being a caring mentor, teaching me about life, the universe and everything, and teaching me the true meaning of being a physicist, the beauty of simplicity and the joy of life on isochrones. I value our work-late evenings and weekends, and I feel very privileged that I ended up working with you. Bernhard Frick for sharing his vast knowledge on neutron scattering, especially in soft matter, and for always providing the best feedback. I thank you for your company and your warm humour, for all your beamtime and data-analysis related support and guidance, and for always finding time to read.

I am indebted to the whole Glass & Time group, where theoreticians and ex-

perimentalists talk, discuss and work together on daily basis. For our weekly group meetings that have been a great learning experience, with plenty of room for discussing new experimental as well as theoretical research, our own and from the rest of the world, and for always leaving all doors open. I thank Jeppe Dyre for putting together a fantastic group, and for the many great conversations on the importance of science that I treasure and will carry with me. I thank Alejandro Sanz for letting me in on the cell project and for keeping me company on beamtimes, it has been a pleasure working on this project with you. I thank Karolina Adrjanowicz for many great scientific discussions and for all your help on beamtimes. I thank Bo Jakobsen for all the help with the dielectrics, for accompanying me on beamtimes and in particular for the help on implementing the dielectric software into NOMAD. I thank Thomas Schrøder for the input on the interpretation of neutron data and comparison to simulations and for the more recent interest in cumene.

I thank all the people that have been involved in the development of the new sample cell. In particular, Ib Høst Pedersen and the workshop at IMFUFA at Roskilde University, Preben Olsen, Torben Steen Rasmussen, Ebbe Hyldahl Larsen, Per Nielsen and Torbjørn Attas, who compliment each other so well and have gathered an incredible amount of experience over the years that we all benefit from. They are a treasured asset to IMFUFA. The people in Services for Advanced Neutron Environment (SANE) at the ILL, Eddy Lelièvre-Berna and Julien Gonthier. Jean-Paul Gonzales and Yohan Memphis from cryogenics. Louise, James Maurice and Claude Payre from high-pressure, in particular, the first for making my life a lot easier and the latter for teaching me how to do everything in French. I also thank the technician at IN16B, Richard Ammer, who helped me modify bits and pieces time and time again. I thank Paolo Mutti and Yannick Le Goc from the Instrument Control Service on NOMAD related issues. I thank Simone Cappacioli for many great inputs and for taking part in beamtimes. I thank Marian Paluch for contributions on the cell design. I thank Judith Peters, Michael Marek Koza and Jacques Olivier, for assistance on IN13, IN6 and IN5, respectively, and of course, Bernhard Frick for assistance on my favourite instrument, IN16B. And heartfelt thanks to everyone I came to know in Grenoble, especially to College 10 for making me one of you. I am happy to consider you my friends.

I am grateful for having been introduced to the warm and welcoming environment at IMFUFA, I have really come to appreciate and value its culture. I thank Mette C. Nielsen for help on practical problems, and Heine Larsen for help on computer-related issues.

Last but not least, I thank my family and friends for moral support and for understanding how time-consuming a PhD can be. Especially my parents for their confidence in me and for all the times that I could go home to recharge, especially after beamtimes. My dear brother and my good friends for sharing what is my life with me. I thank Johanne for being the best office mate, and Daria, Kristijan and Ursula for moral support towards the end. I look forward to new adventures in 38.

Henriette, October 2017

*You're off to Great Places!*
*Today is your day!*
*Your mountain is waiting.*
*So ... get on your way!*

– Dr. Seuss, "Oh, the Places You'll Go"

# Contents

# Chapter 1

# Introduction

Materials science and in particular condensed matter physics are important branches of science that through their role in technological development shapes our society. Looking back, many historical eras have been named after the material that defined that exact period in time, for example, the stone age, the bronze age and the iron age up until the current period of time, sometimes referred to as the silicon age. Throughout the industrial revolution, two main breakthroughs were the engineering of metal alloys and chemical manufacturing, opening a new world of machinery and mass production. While research in general and materials science in particular is often done with the purpose of doing something better or more efficient, fundamental research plays an equally important role. The more we understand, the better questions we can ask. Breakthroughs have sometimes shown to take off when accompanied by blue skies research, be it the world-changing discovery of the transistor at Bell Labs or the serendipity that led Röntgen (and his wife) to discover X-rays. Fundamental research should be done for the sake of fundamental research: to educate, to push boundaries, to work across boundaries, to enlighten and to provoke and develop new ideas and ways of thinking. And in the end, most likely something useful will come out of it. This work is done with one such blue skies research problem in mind, namely, the understanding of the glass transition.

The title of this thesis was inspired by a conference held in Copenhagen in April 2017 organised by the author of this thesis and her supervisor, named exactly 'Dynamics of glass-forming liquids: Will theory and experiment ever meet?'. This was a meeting with the purpose of promoting the communication and not just coexistence between experimentalists and theoreticians in the glass science community. Reflecting the author's background and own experience as a young scientist in spe, the title could just as well have asked the question 'will physicists and chemists ever meet?'.

As a physicist, one is taught to simplify problems using, for example, Occam's razor or by turning everything into spherical cows, searching for solutions that are universal. And with large success in many aspects, although reality often turns out to be more complex. An example is how in quantum mechanics, as a physics student, you are not likely to make it much further than the hydrogen atom, while treatment of more complex systems is saved for chemistry courses attacked from a slightly different angle. A glass is a good example of a simple, yet complex system that physicists are trying to theorise with universal laws, and chemists are trying to

describe in great detail. The work in the present thesis will be this author's small and humble contribution to give an example of how theory and experiment can meet and develop together. This work is fostered by the scientific environment in the Glass & Time group at Roskilde University where the two communities, theoreticians and experimentalists, physicists and chemists, meet, talk and challenge each other every day.

A lot of the materials that surround us and constitute what we are made of are complicated systems that cannot be described by a single equation or law; we are past the hydrogen model, so to speak. A glass is a textbook example of a complex system which is simple in nature, and it is intriguing to think that solving this problem will make us capable of solving more complex problems.

Glass is a material that has been used as far back as the stone ages from natural occurring glasses from volcanoes. The first human-made use of glass dates back, according to archaeological findings, to ancient Egypt some 3000 BCE. Through the ages of the Roman Empire and the Middle Ages, glass developed from being a luxurious material used for beads, cups and cathedral windows to being something that has now effectively moved into every household in the western world with highly advanced triple-paned solutions for heat insulation. This is glass as we typically know it from household and history, but as a scientist, how do we define a glass?

A glass is per definition a liquid that upon cooling does not crystallise, but a frozen-in, non-ergodic, non-equilibrium system, in short, a disordered or an amorphous solid. The curious thing, however, as we will come back to in present work, is perhaps not the glass itself, but the glass transition, the nature of the glass transition and the dynamics related to the glass transition – the latter being the scope of this work. It is crucial to expand the phenomenology from normal glass to include all glass formers. With that, we want to include all kinds of glass formers and not just the transparent silica-based glass that we know from window panes, mirrors and drinking glass. A good glass-former is defined as a material which is readily supercooled below its melting point avoiding the crystalline state. Materials such as organic molecular liquids, metallic glasses, electrolytes or ionic liquids, and polymers are all examples of good glass formers. In fact, all materials can form a glass, and biological systems such as membranes, DNA and proteins have been shown to exhibit glassy behaviour. One of the reasons why the glass transition is such an interesting problem is that the ability to form a glass is universal, and it is therefore intriguing to think that a universal law can be formulated that can describe exactly the glass transition for all kinds of glass formers.

In 1995, Noble laureate Philip W. Anderson stated in a viewpoint on the future in Science [5]:

> "The deepest and most interesting unsolved problem in solid state theory is probably the theory of the nature of glass and the glass transition. This could be the next breakthrough in the coming decade. The solution of the problem of spin glass in the late 1970s had broad implications in unexpected fields like neural networks, computer algorithms, evolution, and computational complexity. The solution of the more important and puzzling glass problem may also have a substantial intellectual spin-off.

Whether it will help make better glass is questionable."

Although perhaps a bit optimistic regarding the timescale and possibly a bit pessimistic regarding the applicability, the nature of the glass transition is still very much a means of research in both theoretic and experimental work. To quote the professor of physics at Harvard, David A. Weitz, "There are more theories of the glass transition than there are theorists who propose them." [33]. This is quite telling of the complexity of the problem in hand. From an experimentalist's point of view, many theories are in principle a good thing and we could start from one end and test and challenge the theories, but to do so we have to speak the same language and it requires that theories are coupled to real systems. While theoreticians can lose their way in infinite dimensions, experimentalists can be caught up in the meaning of a methyl-group's rotation (as we shall see later). Although both scenarios are equally important and necessary, sometimes it may be useful to try and meet on common ground, to build bridges in order to develop experiment and theory together. A prerequisite for this to happen is to develop theories that have predictive power and to design experiments that can test theories.

## Reading guide

The work presented in this thesis concerns experimental tests on the dynamics of glass-forming liquids close to, at, and below the glass transition related to theories that have mainly been developed in the Glass & Time group. We will present experimental tests of the shoving model and the isomorph theory.

First will follow a general introduction to glass-forming liquids and the glass transition and in particular to the associated dynamics from a phenomenological and theoretical point of view, introducing aspects relevant for this work (Ch. 2), before moving on to present examples of insight and progress made by introducing pressure in experiments and an introduction to isomorph theory (Ch. 3).

Following the introduction to literature is an introduction to the most important aspects of the experimental techniques used in this work, namely on dielectric and neutron spectroscopy (Ch. 4). We will then move on to the actual experimental work done in relation to this thesis. In Ch. 5, we will present the shoving model that belongs to the class of models referred to as elastic models that relate fast and slow dynamics close to the glass transition and the work done in testing the model. The work is published in [71].

Hereafter, we present a new sample cell developed for doing simultaneous dielectric and neutron spectroscopy at high pressure (Ch. 6), which is published in [140].

We have used this new sample cell to test isomorph theory, which is presented in two parts. Part I in Ch. 7, will mainly deal with alpha relaxation dynamics in the liquid state, whereas Part II in Ch. 8, will focus on the dynamics at the glass transition and in the glass. The work presented in the first section of Ch. 8 is published in [72]. A summarising discussion and outlook are presented in Ch. 9.

There is a lot of experimental data presented in this thesis, and one could argue that some of it could have been put in an appendix, but to paint the full picture of what we have observed, all data is presented in the main part. The presentation of

the data has been tried kept in the same way throughout the two last chapters for ease of the reader, hopefully, with some success.

# Chapter 2

# Dynamics of glass-forming liquids

This chapter will serve as a general introduction to the glass transition and in particular to the dynamics of glass-forming liquids. The dynamics in glass-forming liquids that will be treated in this work spans many orders of magnitude and is different in nature on the different timescales. In this chapter, we will try to elucidate some of the differences and set the reference frame for this work, by presenting different models, theories and experimental observations relevant for this work. Several models and theories have been suggested in relation to the nature of the glass transition and the possible connections between fast and slow dynamics, in particular as the glass transition is approached. Some are phenomenologically based while others take a more theoretical approach, a few of them will be mentioned here. The shoving model that we test experimentally in this work will be presented in Ch. 5. The shoving model belongs to the class of elastic models presented at the end of this chapter.

The glass transition can be reached from the liquid either by cooling or compression, and while this chapter will solely deal with the more traditional approach, namely looking into temperature dependence, the next chapter will expand to include pressure dependence of the dynamics and try to sum up what insight has been gained by introducing pressure and introduce isomorph theory (Ch. 3).

## 2.1 Viscous liquids and the glass transition

The glass transition takes place when a liquid is supercooled below its melting point, i.e. by avoiding crystallisation (Fig. 2.1). Unlike an ordinary phase transition that occurs at a well-defined temperature, such as the melting temperature, the glass transition is defined as when within some experimental timescale, the liquid is no longer able to reach equilibrium. The glass transition and the glass itself therefore depend on the cooling rate, i.e. they depend on the timescale of the experiment. The ability to form a glass is universal, although some materials are better glass-formers than others. While some organic molecular liquids and polymers can be difficult or even impossible to crystallise, other systems require fast cooling rates in the order

of hundreds of Kelvin per second to supercool, for example some metal alloys [98].

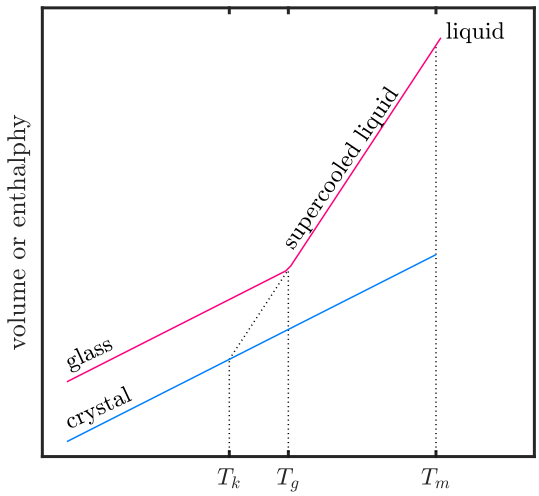


Figure 2.1: A sketch of volume or enthalpy change upon cooling from the liquid state into the supercooled liquid and the glass, or into the crystal state. An abrupt change in enthalpy as a function of temperature is observed at the transition from liquid to crystal state.

A liquid cooled below its melting point without crystallization, i.e. a supercooled liquid, is in a metastable thermodynamic equilibrium. Upon some external perturbation, the supercooled liquid will recover a state of equilibrium, but this will not happen instantaneously. An example is the change in volume given by the expansivity of a material caused by a change in temperature. The time it takes a system to reach its new position of equilibrium is given by the structural alpha relaxation time, $\tau_\alpha$. Usually and in this work, the glass transition temperature $T_g$ is defined as when the structural alpha relaxation $\tau_\alpha = 100\,\mathrm{s}$. We will in general refer to the alpha relaxation as the slow dynamics. In 1867, Maxwell [105] introduced a relation between the structural relaxation time and shear viscosity, $\eta$, via the infinite-frequency shear modulus, $G_\infty$: $\eta = G_\infty \tau_\alpha$. In terms of viscosity, the glass transition at $\tau_\alpha = 100\,\mathrm{s}$ corresponds to $\eta \sim 10^{12}\,\mathrm{Pa\,s}$. For comparison, the viscosity of bitumen in the pitch drop experiment from 1927 at the University of Queensland, Australia, which has so far shed nine drops, roughly one every ten years, is around $10^8\,\mathrm{Pa\,s}$ at room temperature, while the viscosity of water at room temperature is in the order of $10^{-3}\,\mathrm{Pa\,s}$.

Thus, a glass is in every way a solid. In the glass, the molecules are essentially frozen in and are no longer able to rearrange and relax into an equilibrium state within some experimental timescale. The volume in the glass will still decrease upon cooling, but the temperature-dependence will be much smaller than in the supercooled liquid and the volume changes are only due to the change in distance between the molecules as in the crystal. The lack of long-range order in the glass is illustrated in the static structure factor in Fig. 2.2, which can be probed for real

systems by different diffraction techniques or simulated in computer simulations from molecular dynamics models. The position of the atoms in the glass resembles that in the liquid; the atoms are frozen-in in an isotropic state and lack the long-range order seen as Bragg peaks for crystals, i.e. there is no structural change associated with the glass transition. The shift in peak position towards higher $Q$ in the glassy state compared with the liquid, is a signature of the closer packing of molecules.

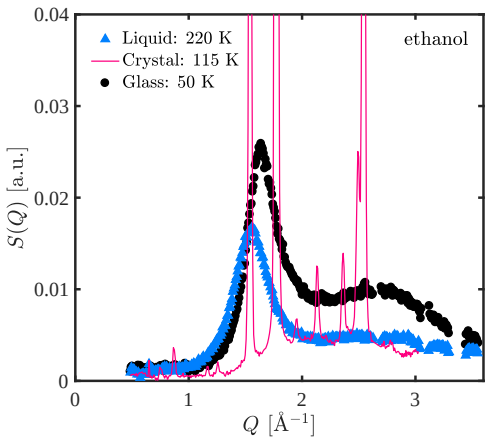


Figure 2.2: Static structure factor of ethanol in the liquid ($T_m = 159\,\mathrm{K}$), crystal and glassy state from neutron diffraction at D1B at ILL from A. Sanz [139]. Comparing the liquid and the glass, we observe only little difference in the static structure factor compared to the crystal with distinct Bragg peaks where only $\sim 10\%$ of the peak height is shown here. From the liquid to the glass, we observe a general increase in intensity, corresponding to less mobility, and a shift in the first peak position towards higher $Q$ from the decrease in volume upon cooling.

While there is practically no difference in structure between a glass and a liquid, a tremendous change in the dynamics is observed on cooling: As the glass transition is approached in the supercooled liquid, there is a dramatic slowing down of the alpha relaxation. Within a fraction of the glass transition temperature, the alpha relaxation time changes orders of magnitude. The fundamental question within our field is what causes and governs this tremendous slowing down of dynamics close to the glass transition.

A simple and compelling picture was introduced by Goldstein in 1969 [62] with the potential energy landscape. For a system of $N$ particles, the landscape is the potential energy as a function of the $3N$ particle coordinates plotted in a $3N + 1$ dimensional space. Dynamics of a system can then be thought of as movement around in the potential energy landscape. Goldstein proposed that the dynamics are controlled by the potential energy landscape, where slow dynamics corresponds to jumps between potential energy minima, while fast vibrations around the energy minima will take place on short timescales. As a liquid is cooled and the glass transition is approached, the potential energy barrier is overcome more and more rarely, resulting in slower relaxation time.

In this view, the relaxation process is governed by a potential energy barrier that

can be overcome by thermal activation, similar to an activation energy for chemical reactions, which would suggest that the relaxation time or viscosity slowing down is exponential with temperature. However, the behaviour of almost all glass-forming liquids deviates from such Arrhenius behaviour, and the degree of deviation is material dependent. The viscous slowing down shows super-Arrhenius behaviour with a temperature-dependent activation energy, which results in the following expressions:

$$\tau(T) = \tau_0 \exp\left(\frac{\Delta E(T)}{k_\mathrm{B}T}\right) \qquad \eta(T) = \eta_0 \exp\left(\frac{\Delta E(T)}{k_\mathrm{B}T}\right), \tag{2.1}$$

where $\tau_0$ and $\eta_0$ are high-temperature limits, typically a microscopic time $\tau_0 \sim 10^{-14}\,\mathrm{s}$ and viscosity of $\eta_0 \sim 10^{-5}\,\mathrm{Pa\,s}$.

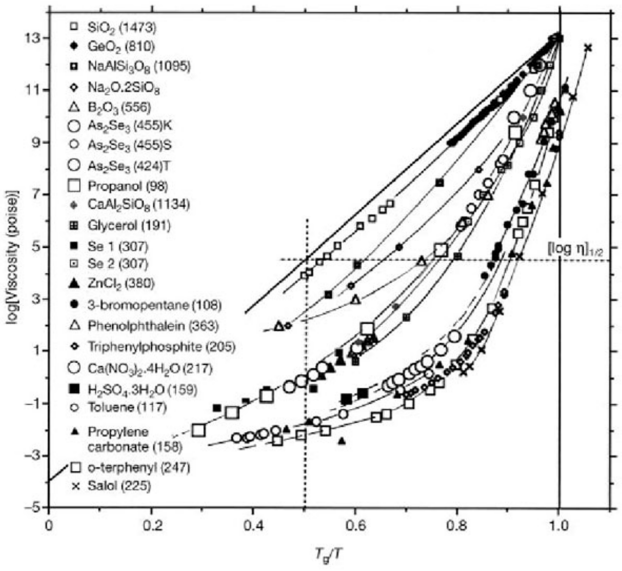


Figure 2.3: Angell fragility plot showing the non-Arrhenius behaviour of a range of glass-forming liquids. Reprinted from [103].

The deviation from Arrhenius behaviour is illustrated in the standard Angell plot (Fig. 2.3), where the logarithm of the viscosity or relaxation time is plotted against the inverse temperature normalised to $T_g$. Liquids with close-to-Arrhenius behaviour are referred to as strong liquids, closely following the straight exponential line in the Angell plot, while those with super-Arrhenius behaviour are referred to as fragile liquids. The fragility, $m$, is a measure of the deviation from Arrhenius behaviour [6]:

$$m = \left.\frac{\mathrm{d}\log_{10}\tau(T)}{\mathrm{d}(T_g/T)}\right|_{T_g}. \tag{2.2}$$

A fragility of $m = 16$ corresponds to Arrhenius behaviour with a constant activation energy. Typical values of fragility for a strong liquid like $Si_2O$ is $m \sim 20$ and for fragile molecular organic liquids is around $\sim 80$, while an extremely fragile liquid such as decahydroisoquinoline holds a value of $m \sim 160$ [131].

For an ordinary phase transition, one would expect a discontinuity in the viscosity and thermal properties at the phase transition. Instead, the change in viscosity happens gradually and will in principle continue to do so into the glassy state if one is patient enough for that kind of equilibration times. In the picture presented above, the curious thing may not be the glass transition as such, which in this view is understood as a simple falling out of equilibrium, but instead the major temperature-dependent increase in relaxation time or viscosity in liquids upon cooling as the glass transition is approached. And we then return to the fundamental question: what causes and governs the temperature dependence of the activation energy that seems to almost always increase upon cooling with only a few exceptions, causing the super-Arrhenius behaviour.

## 2.2 Timescales

The dynamics in glass-forming liquids and its various characteristics on different timescales is a key element in this work, and we will therefore in this section go through some definitions and key elements that will be used throughout this work.

When a liquid is cooled below its melting point and enters the supercooled regime, a separation of timescales is observed as the glass transition is approached. If we stay in the potential energy landscape view, the timescale of the slow structural dynamics on longer timescales, corresponding to jumps between potential energy minima, separates from that of fast vibrations, corresponding to vibrations around the energy minima on shorter timescales. This type of separation was shown in molecular dynamics simulations by Schrøder in 2000 [147]. In the potential energy landscape, the structural alpha relaxation is thus governed by the potential energy barrier heights between minima while the vibrations are governed by the shape of the minima; the softer the potential, the larger the vibrations.

Another view is the cage view [162], in which the dynamics of a particle is considered free at short times. The cage is formed by the nearest neighbours and jumps from one cage to another, corresponding to the alpha relaxation, are then caused by thermally activated collisions. On long timescales the jumps will cause a rearrangement of cages resulting in diffusion, supporting a notion of cooperative behaviour of the alpha relaxation. At low temperatures, the particles are blocked by neighbouring particles hindering long-time diffusion.

In Fig. 2.4, we have sketched different dynamic scenarios represented by their incoherent intermediate scattering functions, $I(Q,t)$. The space-Fourier transform of the incoherent intermediate scattering function is a self-correlation function that gives the probability of finding a particle with an initial position at time $t'$ at the same position after some time $t$. In the liquid, close to and above the melting point, the intermediate scattering function decays to zero almost instantaneously: The liquid comes into a new equilibrium really fast, i.e. the relaxation time is short. As the liquid is cooled into the supercooled regime, the different dynamic processes will begin to separate. From a state where fast relaxations and vibrations, taking place on short timescale, are merged with the alpha relaxation, to a state where the fast dynamics separates completely from the structural alpha relaxation as the glass

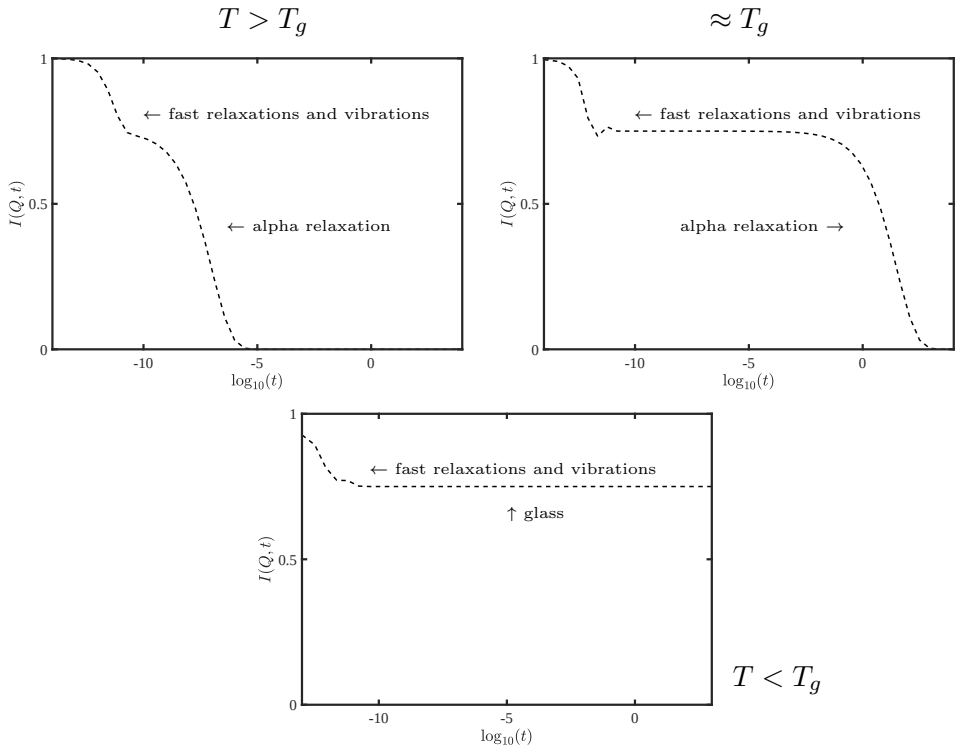


Figure 2.4: Top: Sketch of an incoherent intermediate scattering function above $T_g$ where relaxations and vibrations are merged (left) and at the glass transition where there is separation of timescales (right). Bottom: Intermediate scattering function in the glass where the liquid will not reach equilibrium within some experimental timescale.

transition is reached. A plateau in the intermediate scattering function can appear close to the glass transition, completely separating fast and slow dynamics. Finally, in the glass, one can still find vibrations and even fast relaxational processes taking place on very short timescales as illustrated in Fig. 2.4, but the alpha relaxation will be so slow that within an experimental timescale, it will no longer be able to reach equilibrium. As a consequence, a glass is a non-equilibrium system, and the dynamics will be history or path-dependent.

In general, fast dynamics refer to dynamics taking place on timescales shorter than the structural alpha relaxation. In this work, fast dynamics will typically refer to nano- and subnanosecond motion. The separation of timescales around the glass transition can cover more than ten orders of magnitude; all the way from picosecond timescales where fast relaxations and vibrations typically take place and all the way up to hundreds of seconds, the timescale of the alpha relaxation at the glass transition.

The dynamic scenarios sketched in Fig. 2.4 obviously represent very simple cases, in some views this would be over-simplified [108]. One can imagine all sorts of secondary relaxational processes taking place on timescales between picosecond and seconds in the proximity of the glass transition. Secondary relaxations are very system dependent, and typically much less temperature-dependent compared to the alpha relaxation, e.g. [104]. A lot of work has been put into understanding and modelling secondary relaxations that can appear in the relaxation map of liquids, e.g. [109, 66, 83, 110]. The work in relation to this thesis has been carried out on liquids with as simple dynamic behaviour as possible, trying to imitate the simple dynamic scenarios sketched in Fig. 2.4 without large secondary relaxation. While the term 'simple liquids' historically has also been used to identify liquids constituted of a single type of molecular species, 'simple' as opposed to 'complex' will throughout this work refer to the dynamic behaviour of a liquid, and not the composition or molecules themselves.

Another curious aspect of glass-forming liquids is also illustrated in Fig. 2.4, namely the fact that the alpha relaxation itself in the time or frequency domain is non-exponential. Typically, the relaxation is fitted with a stretched exponential to obtain the relaxation time. Thus, not only is the temperature-dependence of the relaxation time non-Arrhenius, but the relaxation is also non-exponential. The non-exponential behaviour adds to the curious behaviour of the dynamics related to the glass transition.

Numerous empirical and theoretical models have been developed in trying to encompass the nature of the glass transition and with that, a connection between the fast and slow dynamics. We will take a brief look at some theories and models below.

## 2.3 Theoretical approach

Many different models and theories have tried to explain the deviation from Arrhenius behaviour of the relaxation time towards the glass transition. This section contains a small introduction to a few of them, which will be useful for discussing

pressure-induced changes to dynamics and isomorph theory in the next chapter (Ch. 3) and the shoving model in Ch. 5.

The free volume model by Turnbull and Cohen from 1959 [39] explains the large increase in viscosity close to the glass transition by the mobility of molecules and is based on the Doolittles' equation on viscosity [43]:

$$\eta(T) = C \exp\left(\frac{B \cdot V_0}{V_f(T)}\right), \tag{2.3}$$

where $C$ and $B$ are constants. $V_0$ is the limiting specific volume of a liquid, which is defined as the volume to which a real non-associated liquid would contract to without any phase change all the way down to absolute zero and is not the same as the volume of the molecule itself. $V_f$ is then the free space or available volume, the free volume, defined as the difference between the specific volume of the liquid and $V_0$, i.e. the part of the volume associated with thermal expansion. Turnbull and Cohen suggested that when the free volume, $V_f$, is larger than some critical volume, $V_c$, there is an excess of free volume, and the molecule can move outside of its cage. Thus, diffusion can take place. This model and related modified versions [39, 38] imply that the viscosity or alpha relaxation time should only be governed by volume, or density, which we shall see in the next chapter is not the case.

A different approach was taken by Adam and Gibbs in their entropy model from 1965 [1] based on ideas developed from a lattice model for polymers by Gibbs and DiMarzio in 1958 [60]. In the Adam-Gibbs model, the increase in relaxation time close to the glass transition is understood as a large decrease of available configurations, which is reflected in the small equilibrium entropy close to the glass transition. The relaxation time is then given by

$$\tau(T) = \tau_0 \exp\left(\frac{C}{T \cdot S_c(T)}\right), \tag{2.4}$$

where $C$ is a constant, and $S_c(T)$ is the configurational entropy, i.e. entropy related to structure rather than dynamics. The dynamics is connected to the thermodynamics by assuming that there exists an underlying second-order phase transition to a state often referred to as an ideal glass, a state of zero configurational entropy. This is related to the 'apparent paradox' presented by Kauzmann in 1948 [85]. In the supercooled liquid, the difference in entropy between the liquid and the crystal decreases. By extrapolation of enthalpy below the glass transition, a temperature can be found where the entropy of the supercooled liquid is equal to that of the crystal, the Kauzmann temperature, $T_K$ (Fig. 2.1). Below the Kauzmann temperature, imagining that one could supercool at a rate so slow that $T_g$ would be lower than $T_K$, the entropy of the disordered system, the supercooled liquid, would be lower than that of the crystal, hence, the paradox.

If one allows the configurational entropy to be equal to the difference between the entropy in the liquid and that in the glass, arguing that the vibrational part of the entropy in the liquid is approximately equal to that of the crystal, then

$$S_c(T) \equiv S_{\text{liq}} - S_{\text{crystal}} = \int_{T_K}^{T} \frac{\Delta c_P}{T} \mathrm{d}T, \tag{2.5}$$

where the specific heat is defined as $\Delta c_P \equiv c_P^{\text{liq}} - c_P^{T_g}$. Under this assumption, the configurational entropy is zero at $T_K$ and a second-order phase transition is predicted to take place here into an ideal glassy state. Moreover, it is argued in the entropy models that the configurational entropy is expressed in terms of the size of regions of cooperative molecular rearrangements, suggesting that the temperature variation of the size of a cooperative rearranging region is related to the temperature dependence of the relaxation time. At low temperatures the regions of cooperative rearrangement are large, and assuming their volume is proportional to the activation energy, this results in slower relaxation. A growing length scale is thus associated with the liquid approaching the glass transition.

Substituting $T_0$ for $T_K$ in Eq. 2.5 and assuming $\Delta c_P \propto T^{-1}$, one finds the Vogel-Fulcher-Tammann (VFT) expression [164, 58, 155], which is often used to fit the super-Arrhenius behaviour of relaxation times or viscosity data. Questions have been raised about the assumptions going into the Adam-Gibbs model, e.g. [48], and it has been shown that $T_0$ is in fact not $T_K$ [156], and that there is not much evidence for any divergence in the relaxation time suggested by the VFT equation, suggesting a phase transition at the glass transition [75]. But the Adam-Gibbs model remains a celebrated model and the VFT equation is often used to fit experimental data and works well in the proximity of the glass transition.

A first-principles approach based on Newton's equation of motion was taken in the development of the mode-coupling theory (MCT) that took off in the 1980's, e.g. [18, 17, 63]. Mode-coupling theory is mathematically tedious, and we will therefore just state the main idea here. According to MCT, all dynamics in a system is determined from the fast modes of the system. The fast modes lead to a 'memory' term in the dynamical equations, thus, connecting fast and slow dynamics. The slow part of the dynamics is related to the autocorrelation of a fluctuation force, i.e. the fast modes or vibrations. Moving away from the ideal version of MCT by making some non-trivial assumptions, one ends with the prediction of a dynamic transition, a crossover temperature. At this bifurcation of the dynamics, the plateau sketched in Fig. 2.4 becomes infinite and results in a breaking of ergodicity, which means that even at long times, the system is no longer able to relax into an equilibrium state. Above the dynamic crossover temperature, the dynamics are often well described by MCT. In the idealised mode-coupling theory, the relaxational process above the dynamic crossover begins with a fast relaxation followed by the structural alpha relaxation whereas only the fast relaxation persists below the crossover. Over the past decades a lot of fast dynamics studies have been analysed with the MCT in mind.

Another set of models that also deal with a connection between fast and slow dynamics are the elastic models, [50, 49, 45], which are conceptually related to the free-volume models. In Ch. 5, we will take a closer look at a version of the elastic models called the shoving model and its predictions connecting fast and slow dynamics. In the elastic models we return to the energy landscape view, where a flow event, a molecular rearrangement, takes place on short timescales by energy barrier transition. The conjecture is that the transition itself is a fast process which, as the liquid is cooled down towards the glass transition, becomes rare, resulting in the viscous slowing down. In these models, fast and slow dynamics are thus inti-

mately connected; the transitions are considered to be governed by the properties of a liquid at short timescales, where the liquid appears solid-like, and the frequency of the transitions determines the relaxation time. In this way, the slow, long-time relaxation is linked to the vibrational, short-time elastic properties of a liquid. As a liquid is cooled, it becomes harder and the mechanical moduli will increase, while the vibrational amplitude decrease, leading to an increase in barrier height or activation energy. The increase in activation energy upon cooling will again lead to a slower relaxation, resulting in the super-Arrhenius behaviour of a liquid's alpha relaxation time. In this way, the elastic models can also be thought to be coupled to a liquid's fragility, the degree of deviation from Arrhenius behaviour. The details of the argument vary for different versions of the elastic models.

The above serves as a selected introduction to different ways of thinking about the glass transition. There exist numerous other models and theories trying to encompass the viscous slowing down close to the glass transition, see for example reviews [45, 154, 93, 171]. We will now proceed to present some experimental observations.

## 2.4 Phenomenological connections

A series of phenomenological results support the notion that there is a connection between fast and slow dynamics. One of the first observations was made in 1992 by Buchenau and Zorn [25], who found a relation between the temperature dependence of the slow structural relaxation in terms of viscosity and the fast picosecond mean-squared displacement studied with neutron time-of-flight.

Phenomenological observations that supports a connection between fast vibrational and slow structural dynamics can crudely be divided into two: one group that directly connects fast vibrational dynamics to the fragility, and one that connects the temperature-dependence of the fast dynamics to the alpha relaxation time, along the same lines as the original observation by Buchenau and Zorn [25] and the idea of the elastic models.

Starting with the direct connection, Sokolov et al. found in 1993 [152] from Raman spectroscopy a correlation between the fragility and the ratio between the vibrational and relaxation contribution to the dynamics; stronger glass formers showed a higher value of the ratio than more fragile systems. A similar correlation, although experimentally more challenging to obtain, was also found from Sokolov et al. in 1997 [151], between the intensity of the Boson peak relative to the Debye density of states and the fragility, showing that this ratio was large for strong liquids and small for fragile liquids. Scopigno et al. (2003) [148] found that the fragility of a liquid could be determined from the glassy state from the non-ergodicity factor. The non-ergodicity factor was determined from the ratio between elastic and inelastic scattering intensity in inelastic X-ray scattering. The non-ergodicity factor is a measure of the correlation of density-density fluctuations from vibrational dynamics and is well-described in mode-coupling theory. Novikov and Sokolov [116, 115] showed in 2004 for a number of systems how the Poisson's ratio is linked to the fragility of a system, which is the ratio between the transverse expansion and the longitudinal contraction when a solid is compressed in one direction, i.e. the rela-

tive strength between the shear and bulk moduli. The relation suggested that the better a system can resist shear deformation rather than dilatation, the stronger the behaviour in terms of fragility. However, this was shown not to hold in general [170].

Another group of observations regarding the connection between fast and slow dynamics is the connection between the temperature-dependence of short-time properties to the alpha relaxation time observed by Ngai [108] and Larini et al. [94, 19]. These observations are more in line with the observations from 1992 by Buchenau and Zorn [25]. Larini et al. argued from computer simulations that there is a universal correlation between the 'rattling amplitude' and the structural relaxation time and that a glass softens once the amplitude of the vibrations exceeds a critical value. Such value implies a glass criterion similar to the Lindemann criterion for melting of a crystalline solid, that melting of a crystal takes place when the vibrational mean-squared displacement exceeds a certain value, e.g. [45]. We will from neutron scattering and shear mechanics look into connections between fast and slow dynamics in Ch. 5.

## 2.5 Glassy dynamics

Until now, this chapter has been dealing with dynamics in the liquid state, in particular in the supercooled liquid in the proximity of the glass transition. This section will serve as a brief introduction to the dynamics observed at the glass transition and related to the glassy state.

As mentioned previously in this chapter, a glass is a frozen-in liquid. While the structure and density of a liquid are to a large degree frozen at $T_g$, the fast dynamics in the liquid can prevail into the glass. Short-time properties such as vibrations are often much less temperature dependent in the glass compared to in the liquid state. Close to the glass transition and in the glass, most glass-forming systems exhibit fast relaxational processes on picosecond timescales as illustrated in Fig. 2.4 that are visible in for example neutron scattering. Intramolecular dynamics, like methyl-group rotation, can also be observed contributing to the fast dynamics in the glassy state, visible with scattering techniques, see e.g. [56, 86].

As mentioned, another dynamic contribution that prevails into the glass is the vibrations. In particular, the excess vibrational density of states observed in all glassy systems referred to as the Boson peak. In crystalline materials, at low frequencies, the Debye vibrational density of states for acoustic modes, $g_{\mathrm{D}}(\omega)$, is known to be proportional to $\omega^2$. However, in all amorphous materials, a higher intensity than the Debye level show up over a range of frequencies or energy transfer. The Boson peak is the observation of an excess in the vibrational density of states compared to the Debye level found at low energy transfer, typically between 0.1 and 5 meV. The Debye value of a system can be estimated from the sound velocity. One way of probing the vibrational density of states is with neutron scattering, which can measure the vibrational density of states directly and the Boson peak as we shall see in Ch. 8.

The origin of the Boson peak is not well understood, even if it has kept experimentalists and theoreticians occupied for decades [123]. A basic question is whether

the excess modes arise from (i) collective motion associated with a modified version of the crystalline state with a heterogeneity in the elastic force constants [36, 65] or (ii) (quasi)local motion that is distinct from the phonons and can be ascribed to soft modes of the potential that arise from interatomic forces [161]. The Boson peak and glassy dynamics in general are closely related to the phenomenological observations presented above in Sec. 2.4.

The idea that there is a connection between fast vibrational dynamics and the slow alpha relaxation is intriguing in itself as the dynamics are separated by many orders of magnitude, exceeding ten close to the glass transition. Whether the connection falls out of a model or a theory or is based on experimental observations, a lot of work points in the direction that the fast and slow dynamics of glass-forming liquids are somehow related, and that an understanding of the viscous slowing down must encompass dynamics on an exceedingly large range of timescales.

# Chapter 3

# Introducing pressure and scaling behaviour

Pressure experiments on dynamics and transport properties of liquids have within the past couple of decades, opened up a new window into understanding the dynamics of glass-forming liquids. Pressure experiments on liquids began in the 1930's with Bridgman's pressure-temperature-volume measurements high above $T_g$, e.g. [23, 24], and extended by Barlow et al. in the 60's to include viscosity, e.g. [14]. Pressure has since then increasingly been introduced in experimental work in an attempt to disentangle thermal contributions to the dynamics from those arising from changes in volume or density. This is an approach similar to one often taken in computer simulations and theoretical work. But pressure experiments are, because of the requirements to experimental equipment that has to withstand elevated pressure, much more demanding than those done at ambient pressure.

A successful model or theory on the nature of the glass transition or the dynamics in glass-forming liquids should also encompass pressure and density effects. In that sense atmospheric pressure, as we know it, is somewhat arbitrary and there is no a priori reason to believe that the dynamics of liquids should be significantly different inside the core of the Earth or on top of the Himalayas.

This chapter will take the reader through some of the, for this work, key elements of what insight we have gained from introducing pressure into our experiments, challenging some of the models presented in the previous chapter. We will go through phenomenological findings from high-pressure studies related to the scaling behaviour, isochronal superposition and density scaling. Finally, in this chapter, we will present isomorph theory, which rationalises and explains exactly this kind of observed scaling behaviour. Isomorph theory is a key element in relation to the experimental work presented in Ch. 7 and 8. But first will follow a general introduction to how the dynamics is altered with increased pressure.

## 3.1 Pressure-induced changes in dynamics

In experimental work, pressure and temperature are the control variables. While theories and simulations are usually expressed in terms of temperature and density,

making the separation of dynamics into density and temperature induced contributions much simpler. In experiments, the study of the dynamics slowing down towards the glass transition is most often done along an isobar, as was introduced in the previous chapter for the atmospheric isobar. But as already mentioned, the alpha relaxation can be slowed down towards the glass transition in two ways, either by cooling or by compression. This gives rise to lines of constant alpha relaxation time in the temperature-pressure phase diagram, $\tau_\alpha(T, P)$. These lines are throughout this work referred to as isochrones, but have also sometimes been referred to as isoviscous or isokinetic curves, e.g. [160, 78]. Isochronal lines as a function of temperature and pressure are sketched in Fig. 3.1. Using the glass transition definition, $\tau_\alpha(T, P) = 100\,\mathrm{s}$, the glass transition line, $T_g(P)$, is one example of an isochrone in the temperature-pressure phase diagram. Moving across or perpendicular to the isochrones away from the glass transition isochrone towards higher temperature or lower pressure, the alpha relaxation time becomes faster. Moving the other way away from the glass transition towards lower temperature or higher pressure, into the glass, the system will no longer be able to reach thermodynamic equilibrium, causing hysteresis. The density in the glass is therefore history or path dependent. As is illustrated in Fig. 3.1, isochronal lines or isochrones are not the same as isochores, i.e. lines of constant volume or density. Therefore, density alone does not control the relaxation time, and the free volume models presented in the previous chapter can therefore not explain the viscous slowing down.

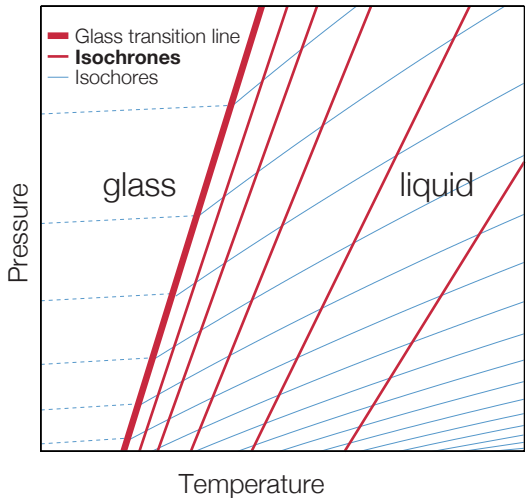


Figure 3.1: Temperature-pressure phase diagram illustrates line of constant relaxation time, isochrones, and constant density, isochores. The glass transition is defined as $\tau_\alpha = 100\,\mathrm{s}$. Moving towards higher temperature and lower pressure, away from the glass transition isochrone and perpendicular to the isochrones, the alpha relaxation time increases. The isochores in the glass are history dependent and are therfore illustrated with dashed lines.

Fragility as it was introduced in Eq. 2.2, was a measure of the deviation of the alpha relaxation time or viscosity from Arrhenius behaviour with changing tempera-

ture at atmospheric pressure where most experiments are done, i.e. the atmospheric pressure isobaric fragility. Fragility can also be measured along isobars at elevated pressure, where different systems show different trends, see e.g. the review by Roland [137]. When a liquid is cooled isobarically, both temperature and density will change and the isobaric fragility will therefore contain information on both the temperature and the density effect on the relaxation time. A way of isolating the effect from thermal energy is to examine the alpha relaxation time under constant density. Thus, in addition to the isobaric fragility, we define the isochoric fragility with constant density:

$$m_\rho = \left.\frac{\mathrm{d}\log_{10}\tau_\alpha(T,P)}{\mathrm{d}(T_g/T)}\right|_\rho (T=T_g). \tag{3.1}$$

Isochoric fragility assumes isochoric cooling and measures the deviation from Arrhenius behaviour with temperature along an isochore, i.e. constant volume. In computer simulations, density is an easyly accessible variable, whereas, experimentally, we can in practice only move along isobars and isotherms, i.e. with constant pressure and temperature, respectively. This means that for example state points along an isochrone of constant relaxation time, are in fact given by $(T_{\tau_\alpha}(P), \rho(T_{\tau_\alpha}(P), P))$. Isochoric fragility was used to check the robustness of phenomenological observations of the connection between fragility and for example the non-ergodicity factor (Ch. 2.4) evaluated at the glass transition, which was found not to hold for elevated pressure [114]. Through the short-time properties, fragility has also been suggested to be correlated with the intensity of the Boson peak and connected to fast relaxations as was discussed in the previous chapter.

Pressure has also been introduced in studying the glassy dynamics and the Boson peak. Hong et al. [79, 78] suggested a correlation between the pressure dependence of the Boson peak and the quasi-elastic fast relaxation intensity, while other studies have shown that the two intensities have different temperature and pressure dependencies, e.g. [118]. Niss et al. [112] showed that the shape of the Boson peak remains the same on compression, even if the position in energy and intensity is shifted towards higher energy and lower intensity, which they suggest cannot arise from soft intramolecular modes, but must instead be a result of a hardening of the system. The shift in Boson peak position on applied pressure has also been suggested to be due to a suppression of the fast relaxational contribution [53]. Chumakov et al. [35] found from pressure studies a correspondence between the Boson peak in the glass and the transverse acoustic phonon singularity observed in the crystal, suggesting that the excess modes arise from collective motion. Whether we can learn anything about the glass transition per se from the Boson peak is not certain, but it is another interesting pending question that we can add to the list of things we do not quite understand about glass formers. Regarding the dynamics of glass formers, adding another control variable in terms of pressure has definitely led to some new insight. One of those is related to the isochrones and was introduced in the beginning of this section, namely the experimental discovery of the scaling behaviour we will discuss in the next two sections.

## 3.2 Isochronal superposition

In the pioneering work of Tölle from 1998 [160, 158], high pressure was introduced to neutron scattering dynamic studies carried out at the Institut Laue-Langevin. They found that the spectral shape was invariant for the nanosecond and picosecond dynamics, studied with the backscattering instrument, IN16, and the time-of-flight instrument, IN6, respectively, for the van der Waals liquid *o*-terphenyl along state points with constant viscosity, i.e. an isochrone corresponding to $\tau_\alpha(T, P) \approx 1\,\mathrm{ns}$. The invariance of spectral shape for constant timescale is called isochronal superposition. This superposition of dynamic spectra was not found along isochores, lines of constant density [159]. This observation suggests that temperature influences the dynamics not only via free volume, but also from thermal contributions, an observation that had also been made from simulations using a Lennard-Jones potential in 1986 [17]. From light scattering data by Li et al. in 1995 [97], it was also suggested that density alone was not the only relevant parameter for controlling the dynamics, and they found the alpha relaxation dynamics measured on short timescales to correlate with the corresponding viscosity. Isochronal superposition, shown by Tölle for dynamics on nanosecond and picosecond timescales, was found to hold for different combinations of temperature and pressure corresponding to roughly constant $\Gamma \propto \rho T^{-1/4}$. This finding was motivated by results from soft spheres with an inverse power-law potential $\propto r^{-n}$, where the equilibrium thermodynamic properties can be characterised by a single variable $\Gamma \propto \rho T^{-n/3}$ [80, 73]. The exponential of the inverse power-law potential set to $n = 12$ gives the repulsive part of the Lennard-Jones pair potential. Tölle noted that "It was not expected that these results would apply literally in a complex molecular liquidlike OTP." [160] These first intriguing observations of isochronal superposition for *o*-terphenyl showed that the behaviour of *o*-terphenyl could be modelled as soft spheres with $n = 12$. The analysis of isochronal superposition of several van der Waals liquids by Tölle and Casalini et al. [160, 136, 32] was carried out in the light of mode-coupling theory, and they found that a dynamic crossover line would also coincide with an isochrone, implying that the alpha relaxation is driven by the same parameter as a fast beta relaxation.

Isochronal superposition implies that the average relaxation time determines the spectrum. In real systems, isochronal superposition has been shown to apply for numerous van der Waals liquids and polymers, in particular studied with dielectrics, while for hydrogen bonding systems this often breaks down [136, 137, 133]. In particular, for hydrogen bonded systems studied with dielectrics, isochronal superposition will apply for the alpha relaxation, but break down for faster secondary relaxational processes, e.g. [30, 66, 135, 2].

## 3.3 Density scaling

Where the implication of isochronal superposition is that the timescale of the relaxation determines the dynamics, density scaling is the observation that the timescale of the relaxation is determined by one governing parameter, $\Gamma = \rho^\gamma / T$.

Following up on Tölle's observations, Dreyfus et al. showed in 2003 [44] that relaxation times of *o*-terphenyl from light scattering data could be plotted as a

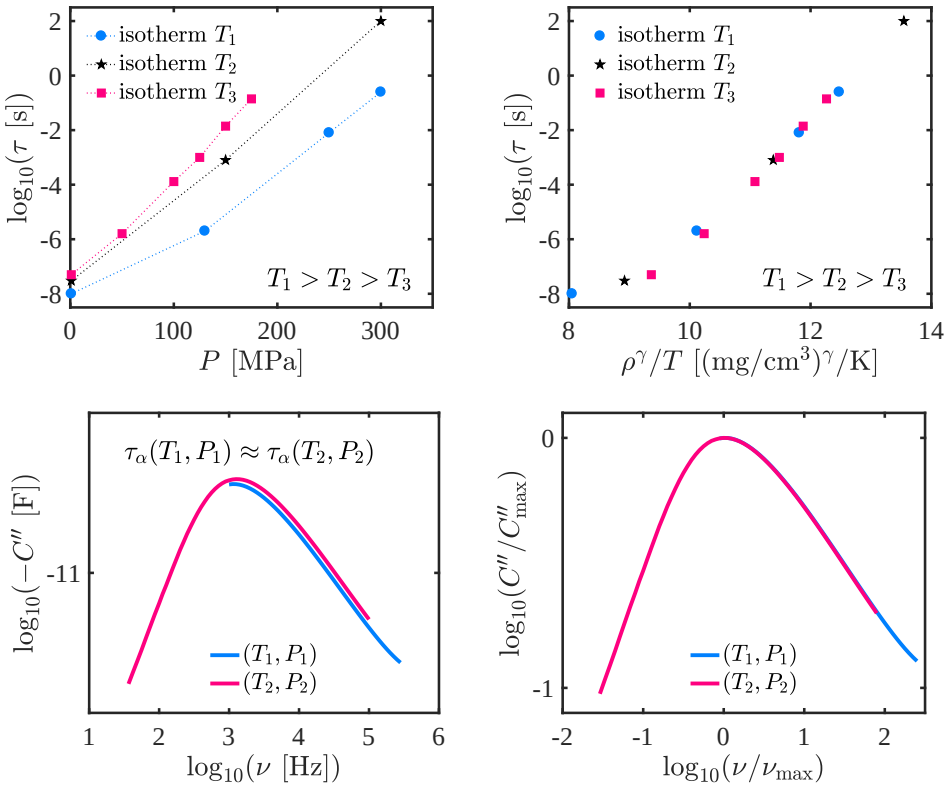


Figure 3.2: Top: Relaxation time along three isotherms as a function of pressure (left) and scaled with $\rho^\gamma/T$ (right) illustrating density scaling. Bottom: Illustration of isochronal superposition of two dielectric spectra. Two pairs of temperature and pressure with roughly the same alpha relaxation time have the same spectral shape.

function of $\Gamma = \rho^4/T$. The idea that the alpha relaxation time could be parametrised in one function was extended by Alba-Simionesco et al. [3] in 2004 who showed for several polymers that the alpha relaxation time found from dielectrics could be scaled with density and temperature. Only now, the exponent was not set to 4 as for the soft repulsive potential in the Lennard-Jones model that worked well for *o*-terphenyl, instead $\gamma$ was a free material-specific fitting parameter. The same year Casalini & Roland [31], referring to the scaling as thermodynamic scaling, found this to apply for a range of glass-formers with values of $\gamma$ ranging from 0.1 for D-sorbitol to 8.5 for BMMPC. The material-dependent exponent, $\gamma$, can for example be found from a power-law fit to density versus temperature. Density scaling suggests that in systems with high values of $\gamma$, density plays a larger role in the relaxation dynamics than in systems with low values of $\gamma$. A general trend seems to be that small values of $\gamma$ are found for density-scaling hydrogen-bonding systems. Density scaling has since been generalised to a large part of the temperature-pressure phase diagram, and the scaling behaviour has been shown to work for a very large number of different liquids in particular studied with dielectric spectroscopy [157, 137, 29].

Tarjus, Alba-Simionesco et al. [3, 157] examined the consequence of density scaling in terms of fragility. They suggested a way of disentangling density and thermal contributions to the dynamics under constant pressure using two coefficients for the expansivity. They found that the fragility is quantitatively independent of density and instead controlled by a single parameter, corresponding to $\Gamma = \rho^\gamma/T$. The two coefficients for expansivity are $\alpha_P$ and $\alpha_\tau$; one at constant pressure, $\alpha_P = -\rho^{-1}(\partial\rho/\partial T)_P$, i.e. along an isobar, and one for constant alpha relaxation time, $\alpha_\tau = -\rho^{-1}(\partial\rho/\partial T)_\tau$, i.e. along an isochrone. The ratio between the two parameters are used to determine the relative effect of temperature and density at constant pressure at a given relaxation time, typically at $\tau_\alpha = 100\,\mathrm{s}$. Using the fragilities introduced in Eq. 2.2 and 3.1, one can define the fragility,

$$m_{P,\tau}(P) = m_{\rho,T}(1 + \alpha_P/|\alpha_\tau|). \tag{3.2}$$

Density scaling has the consequence that the isochoric fragility is not dependent on the absolute value of the density when it is evaluated at a specific relaxation time, $T_\tau(P)$. This can be seen from the relative slopes of the isochrones and isochores in the temperature-pressure phase diagram in Fig. 3.1. The relaxation time will of course change with pressure, and so will the density, but as a function of temperature the deviation from Arrhenius behaviour will be the same along different isochores. In the case of density scaling, where $\Gamma$ controls the timescale of the relaxation, it can be shown that the isochoric fragility does not depend directly on density [3]. Thus, the variations in changing fragility with pressure that have been observed in experiments must come from relative changes in temperature and density contributions to the relaxation time.

## 3.4 Different classes of glass-formers

The idea of dividing and studying glass-forming liquids according to their type of interaction is not new and includes many studies on correlations of dynamics with

fragility. Its an attractive idea for both theoreticians and experimentalists; now that a universal description of the glass transition seems slightly distant, perhaps looking into different interaction mechanisms can help us move closer to a more general description. Systematic studies on density scaling have been done on different classes of systems, for example in [134] on three different classes of liquids, van der Waals, H-bonding and ionic liquids, i.e. non-associated systems, systems with directional bonding and systems with Coulomb interactions, respectively. In the latter two systems, there are competing interactions. The relative strength of the competing interactions varies for the specific system, in particular for ionic liquids.

Dielectric spectroscopy has especially been used for studies on density scaling because of the easy access to the alpha relaxation time from the loss peak (Sec. 4.3), but also viscosity measurements have been used, for example in the case of ionic liquids, where the conductivity completely overshadows any relaxational signature in the dielectric signal. For ionic liquids, density scaling has been shown for transport properties [100], and for viscosity in [134, 51]. While the van der Waals liquids seem to always obey density scaling, many hydrogen bonding liquids do not obey density scaling nor isochronal superposition under high pressure, e.g. [135, 128, 110].

The breakdown of density scaling for hydrogen bonding systems is often interpreted as the destruction of the hydrogen bonding network at high pressure, thus changing the physical structure of the system [66, 135, 2]. Although, it has been pointed out in some papers that density scaling and isochronal superposition work quite well also for hydrogen bonding systems, in particular for the alpha relaxation dynamics [128, 52, 2, 125, 138].

Based on the observations of isochronal superposition and density scaling, the invariance of spectral shape for constant timescale and the invariance of timescale of the alpha relaxation for constant $\Gamma = \rho^\gamma/T$, respectively, Ngai et al. [109] asked rhetorically in 2005 if celebrated classical models such as the free-volume model and the Adam-Gibbs model were in need of revision. They stressed the importance of the observation that for many materials, the dynamics is independent of the thermodynamic conditions, temperature and pressure, but instead controlled by the alpha relaxation time.

Extended versions of the free-volume model [166], where the viscous slowing down is identified as unoccupied volume, and the Adam-Gibbs model [28], where the alpha relaxation time is governed by configurational entropy, have been proposed to also implement the pressure behaviour, but neither of the models can explain or predict the existence of isochrones, the lines of constant $\tau_\alpha$ in temperature and pressure. Ngai et al. [109] argue that, of course, one can imagine a scenario where $\tau_\alpha$ is constant for different combinations of $T$ and $P$, even if for example specific volume and configurational entropy change, where the effects of changing temperature and pressure simply cancel out. But the spectral shape is not expected to be constant for the same combinations of temperature and pressure, and specific volume and configurational entropy may well have quite different $T$ and $P$-dependencies.

Thus, so far, based on the experimental observations presented above and in the previous chapter, a theory of the dynamics in glass-forming liquids should encompass i) a connection between fast and slow dynamics as discussed, ii) an invariance in dynamics for constant $\tau_\alpha(T, P)$, and iii) different behaviour that could be coupled

to the class of liquids, in this case characterised by the interaction mechanism.

## 3.5 Isomorph theory

The isomorph theory has been developed in the Glass & Time group at Roskilde University. The first version was published in a series of papers that came out in 2008-9 [11, 12, 145, 61], and was reformulated in a more generalised version in 2014 [146]. Isomorph theory is relatively simple in nature and rationalises exactly the experimental observations of density scaling and isochronal superposition, see e.g. [46]. A fundamental prediction from isomorph theory is the existence of isomorphs, which are curves in the phase diagram along which *all* dynamical processes and structure are invariant. The alpha relaxation, both its timescale and spectral shape, is one of the invariant properties along an isomorph. This section will take the reader through, for this work, relevant ideas and reasoning from isomorph theory [61].

From molecular dynamics simulations carried out at constant volume and temperature in a system of $N$ particles, in the $NVT$ ensemble, pressure $P$ is given by the sum of the ideal gas term, $Nk_{\mathrm{B}}T/V$, and a term from intermolecular interactions, the virial $W$,

$$PV = Nk_{\mathrm{B}}T + W. \tag{3.3}$$

This is the macroscopic virial, but we can also define the microscopic virial, where $W$ is a function of the particle positions with $\mathbf{R} \equiv (\mathbf{r}_1, \ldots, \mathbf{r}_N)$,

$$W(\mathbf{R}) \equiv \frac{1}{3}\sum_i \mathbf{r}_i \mathbf{F}_i = -\frac{1}{3}\mathbf{R} \cdot \nabla U(\mathbf{R}), \tag{3.4}$$

and $\mathbf{F}_i$ is the force on the $i$th particle. If we consider a soft-sphere model with an inverse power-law interaction potential $\propto r^{-n}$ [80], then as mentioned in Sec. 3.2, the excess thermodynamic properties can be determined from one parameter, and we have that

$$W(t) = \gamma U(t), \tag{3.5}$$

with the proportionality given by $\gamma = n/3$. The surprising observation was then that a Lennard-Jones potential approximated by what was referred to as an effective inverse-power law potential, consisting of an inverse-power law term plus a linear term, also showed a strong correlation between the potential energy and the virial [119]. By defining the instantaneous potential energy function minus its thermodynamic average, $\Delta U$, and $\Delta W$, the instantaneous virial minus its thermodynamic average, the degree of correlation for a given system can be found. The parameter $R$ will then at any given state point give the correlation between the potential energy and the virial:

$$R = \frac{\langle \Delta U \Delta W \rangle}{\sqrt{\langle (\Delta U)^2 \rangle \langle (\Delta W)^2 \rangle}}. \tag{3.6}$$

For the inverse-power law potential, we have perfect scaling with $R = 1$. From extensive computer simulations of various types of systems, systems with $R > 0.9$ fall into the category of "strongly correlating" or "$R$-simple" liquids. Systems that have proven to be strongly correlating include models of for example *o*-terphenyl

[82], polymers [11], bio-membranes [121], and iron under high pressure, similar to the core of the Earth [47].

Based on the observation that some liquids are $R$-simple, we make the assumption that there exist curves in the phase diagram along which, for any two state points there is a one-to-one correspondence between their respective microscopic configurations. These curves are what we will refer to as isomorphs.

Two state points $(\rho_1, T_1)$ and $(\rho_2, T_2)$ are then isomorphic whenever the following applies, represented in reduced units of $\rho_1^{1/3}\mathbf{R_1} = \rho_2^{1/3}\mathbf{R_2}$:

$$\exp\left(-\frac{U(\mathbf{R_1})}{k_\mathrm{B}T_1}\right) \cong C_{12}\exp\left(-\frac{U(\mathbf{R_2})}{k_\mathrm{B}T_2}\right), \tag{3.7}$$

where $U(\mathbf{R}_1)$ and $U(\mathbf{R}_2)$ are potential energy functions, and where $C_{12}$ depends on $\rho_1$ and $\rho_2$, but not on the microscopic configurations. Eq. 3.7 implies that the probability of two configurations with the same reduced coordinates are identical, i.e. for two isomorphic state points it is possible to map the potential energy landscape onto each other.

The only systems that obey Eq. 3.7 exactly, i.e. with an equality sign, are those with inverse power-law potentials, which is of course not descriptive for real glass-forming systems. Hence, as stated above, isomorph theory is approximate in its nature and is not expected to work for all systems. Isomorph theory is expected to work for $R$-simple systems. Directional bonding, as in for example water [11], or strong Coulomb interactions [129] have shown to significantly weaken the correlations. Thus, real systems with directional bonding and strong Coulomb forces are not expected to obey isomorph theory.

A system with isomorphs exhibits hidden scale invariance, i.e. an invariance in dynamics and structure, when its properties are presented in reduced units. The reduced units are per definition dimensionless and will throughout this work be presented with a tilde. Examples of length and time units, $l_0$ and $t_0$, respectively, which will be used in this work are given by:

$$\begin{aligned} l_0 &= \rho^{-1/3} \\ t_0 &= \rho^{-1/3}(m/k_\mathrm{B}T)^{1/2}, \end{aligned} \tag{3.8}$$

where $m$ is the average particle mass and $\rho$ is the number density. For length, wave vector and frequency, respectively, the reduced dimensionless units denoted with a tilde are then given by,

$$\begin{aligned} \tilde{\mathbf{r}} &= \mathbf{r}/l_0 = \mathbf{r}\rho^{1/3} \\ \tilde{Q} &= Q\ l_0 = Q\rho^{-1/3} \\ \tilde{\omega} &= \omega\ t_0 = \omega\ \rho^{-1/3}(m/k_\mathrm{B}T)^{1/2}. \end{aligned} \tag{3.9}$$

To test whether a system obeys isomorph theory, variables must be presented in reduced units.

In Eq. 3.7, two isomorphic state points were defined as when the probability of the two configurations is identical in reduced units. A consequence of the near

identical probabilities on the isomorphs is that the excess entropy, $S_{\text{ex}}$, for two isomorphic state points is also the same. The excess entropy in isomorph theory is the difference in entropy between the ideal gas and the liquid state, and is different from the configurational entropy in the Adam-Gibbs model (Eq. 2.5), which was the difference between the crystal and the liquid. The excess entropy, in the definition in the isomorph theory view, is per definition negative because the ideal gas state will always be more disordered than the liquid state. In computer simulations, an isomorph can be mapped out by following the curve of a configurational adiabat [61]

$$\mathrm{d}S_{\text{ex}} = \left(\frac{\partial S_{\text{ex}}}{\partial V}\right)_T \mathrm{d}V + \left(\frac{\partial S_{\text{ex}}}{\partial T}\right)_V \mathrm{d}T = 0. \tag{3.10}$$

This is (supposedly) a tedious method in computer simulations, not to think of impossible to do in experiments. Instead, in experiments, one way of identifying possible isomorphs is to use the alpha relaxation. Since the alpha relaxation is one of the properties that should be invariant along an isomorph, experimentally, possible isomorphs can to a good approximation be identified by the isochrones, i.e. mapping out lines of constant alpha relaxation time. As we shall see in Ch. 7, the relative difference between alpha relaxation times found from for example dielectric spectroscopy on a frequency scale presented in Hertz and that represented in reduced units is almost negligible.

The system or material dependent value of $\gamma$, used in density scaling, can be found directly from simulations using

$$\gamma = \left(\frac{\partial \ln T}{\partial \ln \rho}\right)_{S_{\text{ex}}} = \frac{\langle \Delta U \Delta W \rangle}{\langle (\Delta U)^2 \rangle}. \tag{3.11}$$

Gundermann et al. [70] showed in 2011 how $\gamma$ can be found independently from single state-point thermo-mechanical measurements for a real van der Waals liquid. The relation between Eq. 3.11 and density scaling in real glass formers has been shown in, e.g. [70, 21, 29]. Assuming that an isochrone to a good approximation is an isomorph, we see that the exponent can be found from a power-law fit to temperature and density.

Isomorph theory implies that the experimentalist's temperature-pressure phase diagram essentially can be turned into one of one dimension, where the only variable controlling the dynamics is $\Gamma = \rho^\gamma/T$. Remembering how density scaling was the observation of invariance of the timescale of the experiment, this implies the existence of lines of constant $\tau_\alpha(T, P)$, the isochrones. Thus, both density scaling and isochronal superposition are in agreement with isomorph theory. But the one-dimensional phase diagram extends beyond isochronal lines; the implication is that dynamics on all timescales are invariant along these lines, i.e. from fast picosecond vibrations to the much slower alpha relaxation in the viscous liquid. There is no prediction from isomorph theory about how the dynamics behaves on different timescales, but if a liquid has isomorphs, and the dynamics is invariant on one timescale, it will also be invariant on all other timescales. In this way, there is an indirect link between fast and slow dynamics for $R$-simple systems in isomorph theory.

Isomorph theory, however, does not reveal anything about causality between fast and slow dynamics, unlike e.g. the elastic models or mode-coupling theory discussed in Ch. 2, which suggest that fast dynamics is a precursor for the slow alpha relaxation. Nor does it reveal anything about the nature of the viscous slowing down towards the glass transition. Instead, isomorph theory deals with the consequence of the correlations observed in some systems. In isomorph theory, for a glass-former with isomorphs, this means that whatever underlying mechanism that drives the slow dynamics, the viscous slowing down, it must also drive the fast dynamics, and it must be controlled by the same governing parameter, $\Gamma = \rho^{\gamma}/T$.

Based on extensive computer simulations, the conjecture is that isomorph theory works for van der Waals liquids, metals and weakly bonded ionic liquids. Isomorph theory has proven extremely efficient in describing Lennard-Jones types of systems, even extending into higher dimensions [42], and including recently successful predictions of the freezing and melting line [120].

The computer simulations that have been carried out for testing isomorph theory have mainly been done on atomic models or flexible chains with rigid bonds. In an attempt to imitate more realistic systems, spring-like bonds have replaced the rigid bonds in some models. For such a system, the intra-molecular vibrations from the spring-like bond were shown to cause a breakdown of the invariance along an isomorph [163], using the configurational adiabat definition of an isomorph. However, it was shown that if the dynamics was separated into a contribution from intramolecular vibrations and a contribution from intermolecular interactions, the isomorphs could be recovered. It was then shown that the vibrations and the intermolecular interactions were invariant on the same lines in the phase diagram [117]. Such lines are referred to as pseudo-isomorphs.

The purpose of isomorph theory has not been to find a universal theory that applies to all systems. But, with Occam's razor in mind, to find a model that works for the simplest case. This is an approach that is characteristic for a lot of the work that has been done in the Glass & Time group, and we will see that a similar approach is taken in the shoving model that we will present and test in Ch. 5.

Direct experimental tests of the isomorph theory so far, focus primarily on the alpha relaxation dynamics [133, 168] and requires high precision measurements. In Ch. 6, we will present a cell developed for doing simultaneous dielectric and neutron spectroscopy under high pressure that secures neutron data collection done with high precision. A large part of the experimental work in this thesis has been carried out with the aim to test isomorph theory by studying dynamics on a range of different timescales separated by more than 13 orders of magnitude mainly with neutron scattering as we will see in Ch. 7 and 8. But first we will move the next chapter where we will present what we can actually probe in experiments from dielectric spectroscopy and in particular from neutron scattering.

# Chapter 4

# Experiments and observables

Experiments play various roles in science, both of course, in terms of testing the robustness of already put-forward theories, but also regarding observation of new phenomena, new correlations and trends that can help guide theorists in new directions. An example of the latter from studies of glass-forming liquids was given in the previous chapter with density scaling and isochronal superposition (Ch. 3). Before we move on to discuss actual experimental work, we will in this chapter deal with how to present physical measurements, what we can observe, how and why. This is discussed in relation to the two main experimental techniques used in this work, namely neutron scattering and dielectric spectroscopy. But first, follows a brief general introduction to linear response theory and correlation functions.

## 4.1 Linear response theory

Linear response theory is used to describe a system perturbed out of equilibrium and its response thereto coming back into equilibrium. In linear response theory, the external perturbation of a system is assumed to be so weak that the response to adjust into a new equilibrium depends linearly on the input. The external perturbation is the input variable, and the time-dependent readjustment is the output response. An example of a linear response function is the relative change in volume of a liquid with temperature change as the input function. The measured quantity, in this case, would then be the linear expansion coefficient, but one can think of all sorts of linear responses to measure.

In the linear response regime, it can be described by

$$O(t) = \int_{-\infty}^{t} \mu(t - t')h(t')\mathrm{d}t', \tag{4.1}$$

where $O(t)$ is the time-dependent output, $h(t)$ is the applied input and $\mu(t - t')$ is called a memory function.

We assume that the response function $\mu(t-t')$ depends only on the time difference $t-t'$, and is not affected by future perturbations, i.e. causality applies, and therefore $\mu(t - t') = 0$ for $t' > t$. We can rewrite Eq. 4.1 as

$$O(t) = \int_{0}^{\infty} \mu(t)h(t - t')\mathrm{d}t'. \tag{4.2}$$

In the simple case, where the perturbation is the Heaviside step function with an amplitude $A$,

$$h(t) = AH(t) = A \begin{cases} 0 & \text{for } t \leq 0 \\ 1 & \text{for } t > 0 \end{cases}, \tag{4.3}$$

the response function in the time-domain, $R(t)$, is:

$$O(t) = \int_{-\infty}^{t} \mu(t-t')AH(t')\mathrm{d}t' = A\int_{0}^{t} \mu(t)\mathrm{d}t' = A\ R(t), \tag{4.4}$$

and, thus,

$$\frac{\mathrm{d}R(t)}{\mathrm{d}t} = \mu(t). \tag{4.5}$$

Any time-dependent input can be Fourier transformed into the frequency domain, and vice versa. If we introduce a harmonically oscillating as input, $h(t) = h_0 e^{i\omega t}$, the output will oscillate with the same frequency. The output can be described by the relative amplitude and phase with respect to the input from the frequency-dependent response function, $R(\omega)$,

$$O_0 e^{i\omega t + \Phi} = R(\omega) h_0 e^{i\omega t}. \tag{4.6}$$

The relation between the response function in the frequency domain and time domain follows from Eq. 4.2 and 4.4:

$$R(\omega) = \int_0^\infty \mu(t')e^{-i\omega t}\mathrm{d}t' = \int_0^\infty \frac{\mathrm{d}R(t)}{\mathrm{d}t} e^{-i\omega t}\mathrm{d}t'. \tag{4.7}$$

The response function in the frequency domain, $R(\omega)$, is a complex function, where the relation between the real and imaginary part is given by the Kramer-Kronig relation.

## 4.2 Correlation functions

A linear response function of a system is directly related to thermally driven fluctuations that take place in a system in thermodynamic equilibrium via the fluctuation-dissipation theorem. The fluctuations can be described by correlation functions that we will introduce here, using the same notation as will be used in the section on neutron scattering (Sec. 4.4) adapted from [16].

First, we will consider the pair correlation function, $g(\mathbf{r}_1, \mathbf{r}_2)$, that gives the probability of finding a particle at $\mathbf{r}_2$ given that there is a particle at $\mathbf{r}_1$. On a perfect single crystal, the probability would be zero everywhere, but where $\mathbf{r} = \mathbf{r}_2 - \mathbf{r}_1$ would correspond to one of the lattice parameters or any combination thereof. For amorphous systems, however, it is meaningful to think in actual probabilities. Because amorphous systems per definition are isotropic, the only relevant distance is the magnitude of $\mathbf{r}$, $r = |\mathbf{r}_2 - \mathbf{r}_1|$, and we thus define the radial distribution function $g(r)$ for amorphous systems that gives the probability of finding another particle a distance $r$ away from the first particle (Fig. 4.1). The probability is proportional to the number of particles found in a shell of radius $r$ and thickness $\mathrm{d}r$, a local density. At shorter distances, this will give rise to peaks that correspond to coordination

shells of large probability. At larger distances, this will go to unity where there is no correlation between the position of the first and second particle. That is, in general, there is only short-range order.

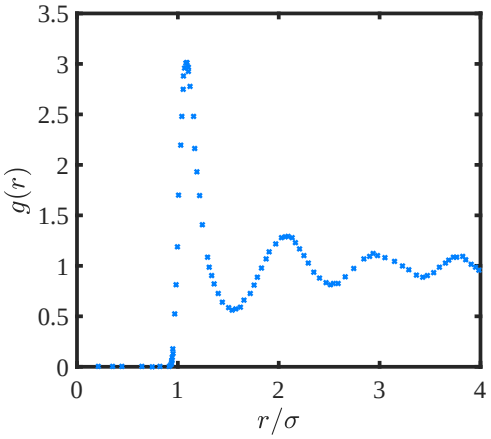


Figure 4.1: Sketch of the radial distribution function, $g(\mathbf{r})$, of an amorphous system. Peaks are seen for values of $\mathbf{r}/\sigma$ corresponding to first, second, etc. coordination shell in a liquid with molecules of size $\sigma$.

To follow correlations in both space and time of a system, we introduce the time-dependent pair correlation function $G(\mathbf{r}, t)$, the van Hove correlation function, defined from local atomic densities:

$$G(\mathbf{r}, t) = \frac{1}{N}\langle\sum_{i=1}^{N}\sum_{j=1}^{N}\delta(\mathbf{r} - \mathbf{r}_i(t) + \mathbf{r}_j(0))\rangle, \tag{4.8}$$

where the angled brackets refer to ensemble averages. The van Hove correlation function gives the probability of finding a particle $i$ at a distance $r$ from the origin at time $t$, knowing that a particle $j$ was at $r = 0$ at time 0. At $t = 0$, we therefore have

$$G(\mathbf{r}, 0) = \frac{1}{N}\langle\sum_{i=1}^{N}\sum_{j=1}^{N}\delta(\mathbf{r} - \mathbf{r}_i(0) + \mathbf{r}_j(0))\rangle = \delta(\mathrm{r}) + \rho g(\mathbf{r}), \tag{4.9}$$

which except for a singularity at the origin, is proportional to $g(\mathbf{r})$, the pair correlation function, and the density. The van Hove correlation function can be split into a self-part and a collective part:

$$\begin{aligned} G_s(\mathbf{r}, t) &= \frac{1}{N}\langle\sum_{i=1}^{N}\delta(\mathbf{r} - \mathbf{r}_i(0) + \mathbf{r}_i(t))\rangle \\ G_c(\mathbf{r}, t) &= \frac{1}{N}\langle\sum_{i\neq j}^{N}\delta(\mathbf{r} - \mathbf{r}_j(0) + \mathbf{r}_j(t))\rangle \end{aligned} \tag{4.10}$$

and is defined for non-zero times. The self part gives the probability that a particle has moved a distance $r$ after some time $t$, whereas the collective part provides

information on density fluctuations. It gives the probability of finding a particle at a distance $r$ after some time $t$, knowing that there was another particle at $r = 0$ at $t = 0$.

We will use correlation functions in the section on neutron scattering (Sec. 4.4). We will use that a measured response of a system to an external perturbation is directly coupled to the system's equilibrium thermal fluctuations, where the fluctuations can be described by correlation functions. If we consider some time correlation function,

$$F_{BB}(t) = \langle A(t)B(0))\rangle, \tag{4.11}$$

where the angled brackets refer to ensemble averages. $A(t)$ is then the measured physical quantity, the output, while $B(0)$ is coupled to the input. If $A = B$, this is an auto-correlation function. From the fluctuation-dissipation function, the relation between a linear response and the self-correlation function is given by

$$\frac{\mathrm{d}R(t)}{\mathrm{d}t} = -\frac{1}{k_B T}\frac{\mathrm{d}}{\mathrm{d}t}F_{BB}(t). \tag{4.12}$$

In the frequency domain, by Fourier transform, this is

$$F_{BB}(\omega) = \frac{1}{2\pi}\int_{-\infty}^{\infty} F_{BB}(t)e^{-i\omega t}\mathrm{d}t, \tag{4.13}$$

and contains the same information as Eq. 4.7. For a simple exponential decay, the complex linear response function, $R(\omega)$, will give a peak in the imaginary part for a relaxation process with a characteristic time $\tau \approx 1/\omega_{\max}$. In the self-correlation function, $F_{BB}(\omega)$, a relaxation process will give a peak with centre in $\omega = 0$, where the characteristic time is given by the width of the peak $\Delta\omega \approx 1/\tau$. These two connections to a relaxation time are exactly what is utilized in dielectric and neutron spectroscopy and will be discussed in the rest of the chapter.

## 4.3 Dielectric spectroscopy

Dielectric spectroscopy is an example of how linear response function can be used to probe dynamic properties of a system. Dielectric spectroscopy has been used extensively in the community of glass-forming liquids. It is a fast probe of dynamics that covers many orders of magnitude in the frequency domain, allowing one to study for example relaxational processes close to the glass transition. Dielectric spectroscopy is based on the interaction of an external electric field with the electric dipole moment or charges of a system.

In a molecular liquid with molecules with a permanent dipole moment, the frequency-dependent dielectric constant, which is measured by dielectric spectroscopy, provides information on the polarisation of the molecules. In the absence of an electric field, the dipole moments are distributed randomly in all directions. When the system is perturbed by an external electric field, the molecules tend to rearrange so the dipoles are aligned parallel to the electric field, resulting in a net dipole moment. The dielectric displacement field is defined through the electric field:

$$\mathbf{D} = \varepsilon^* \varepsilon_0 \mathbf{E}, \tag{4.14}$$

where $\varepsilon_0$ is the vacuum permittivity. The dielectric permittivity, $\varepsilon^*$, is a complex function, which is time or frequency dependent if time-dependent processes take place in a system, such as relaxational processes related to molecular fluctuations of dipoles in glass-formers. The displacement field can be expressed in terms of the polarisation, $\mathbf{P}$, a measure of the dielectric displacement as a response to an external field,

$$\mathbf{D} = \varepsilon_0 \mathbf{E} + \mathbf{P}. \tag{4.15}$$

The polarisation per volume is a macroscopic property that in general can be related to a molecule's microscopic dipole moment, $\mathbf{p}_i$, where the macroscopic polarisation of a given volume is simply a sum of the microscopic dipoles $\mathbf{P} = V^{-1} \sum \mathbf{p}_i$. The macroscopic polarisation is related to the measured complex permittivity, $\varepsilon^*$, through

$$\mathbf{P} = (\varepsilon^* - 1)\varepsilon_0 \mathbf{E}. \tag{4.16}$$

The microscopic dipole moment can be of permanent or induced character. The induced dipole moment stems from a change in the electron clouds which to a good approximation is instantaneous and therefore does not contribute to the frequency dependence of the signal that we are mainly interested in. All data reported in this work was done in low-field and can thus be assumed linear. Non-linear effects in dielectrics is an entire area of exciting research in itself, e.g. [132, 4], that will not be treated in this work.

In Fig. 4.2, we sketch a permittivity signal as a function of frequency, which is measured in dielectric spectroscopy under the application of an alternating electric field. Under the application of an electric field, the molecules in a system tend to rearrange so the dipoles are aligned parallel to the electric field, causing an increase in the permittivity. Under a steady field at a fixed temperature, this is the permittivity, $\varepsilon_{\text{eq}}$. If an oscillating electric field is applied with a sufficiently low frequency, which allows the rearrangement of the dipoles to follow the field orientation, then the permittivity will stay constant at $\varepsilon_{\text{eq}}$, illustrated as the low-frequency plateau in the real part in Fig. 4.2. As the frequency of the oscillating field is increased, the dipoles will at some point no longer be able to reach their equilibrium position, and the permittivity falls to its high-frequency limiting value $\varepsilon_\infty$. The difference between the two plateau values $\varepsilon_{\text{eq}}$ and $\varepsilon_\infty$ is the dielectric relaxation strength of a sample and is a measure of reorientation of the molecules in a sample.

In practice, the permittivity is measured through the capacitance of a sample as a function of a harmonically oscillating electric field through the sample between two electrodes. The capacitance is given by the relation between the area of the sample between the electrodes, $A$, the distance between the two electrodes, the sample thickness, $d$, and the frequency-dependent dielectric constant of the sample, $\varepsilon^*(\omega)$:

$$C^*(\omega) = \varepsilon^*(\omega)\varepsilon_0 \frac{A}{d}, \tag{4.17}$$

where $\varepsilon_0$ is the vacuum permittivity. The capacitance of the empty capacitor is given by

$$C_0 = \varepsilon_0 \frac{A}{d}, \tag{4.18}$$

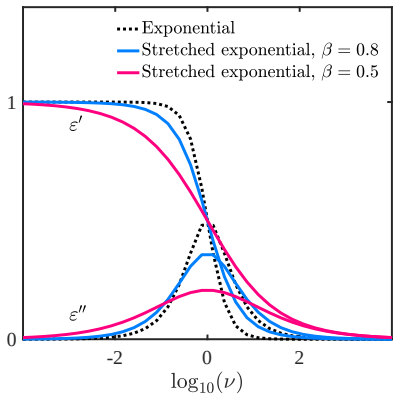


Figure 4.2: Sketch of real and imaginary part of dielectric spectrum, $\varepsilon'$ and $\varepsilon''$, respectively, for an exponential and strectched exponential decay with two different stretching exponents. A relaxation time can be determined from the maximum in the imaginary part.

and the permittivity is found from the ratio between the capacitance of the sample and that of the empty capacitor. Most standard dielectric setups can typically cover the frequency range from $10^{-2}$ to $10^{6}$ Hz, i.e. eight orders of magnitude in frequency or time. In far from trivial setups by the Lunkenheimer group, the range has been extended to cover as much as 17 orders of magnitude, e.g. [144]. Detailed information on dielectrics in general, the data and interpretation thereof can be found in the textbook by Kremer and Schönhals [92].

The alpha relaxation process is one of the relaxation phenomena that in many glass-forming liquids will give a pronounced and distinct peak in the imaginary part of the permittivity, and one of the reasons for the wide application within the experimental field. The measured alpha relaxation process in glass-forming systems is non-exponential, i.e. the measured dielectric response is broader than the expected exponential or Debye behaviour. The dielectric response of the alpha relaxation has empirically been described in the time-domain by the Kohlrausch-Williams-Watts function or the stretched exponential, $\Phi(t) = \exp(-(t/\tau)^{\beta})$. This is illustrated in the frequency domain in Fig. 4.2 for two different stretching exponents, $\beta$.

As for many experimental techniques, a disadvantage of the dielectrics is the exact interpretation of the measurements. For dielectrics this, in particular, concerns the translation from macroscopic to microscopic level and vice versa. Dielectric spectroscopy is widely used in dynamic studies in glass-formers, but also for kinetic studies of for example crystallisation and charge carrier properties. For example is DC conductivity observed in some glass-forming systems as a power-law decrease with frequency in the imaginary part of the capacitance, slower than the alpha relaxation. In systems such as ionic liquids, the conductivity will be so strong that it completely overshadows any signal from the alpha relaxation. In systems such as mono-alcohols, a large Debye-like relaxation is observed to practically hide the alpha relaxation.

For this work, dielectrics have primarily been used as a tool for finding the alpha

relaxation time of different simple organic glass formers, where the alpha relaxation is observed as a distinct peak. The particular setup used in this work and the cell that was developed to combine dielectric and neutron spectroscopy under high pressure is described in Ch. 6. We will now move on to introduce neutron spectroscopy.

## 4.4 Neutron scattering

Neutron scattering or neutron spectroscopy is used in many different sciencific disciplines such as solid state physics, molecular biology and polymer chemistry because it is an effective means for studying nuclear and magnetic structure and dynamics on atomic or molecular scale. In this section, we will focus on basic aspects of neutron scattering relevant for the dynamics in glass-formers presented in this work. This is in no way extensive and the reader is referred to one of many standard textbooks there exist on this topic for more details, e.g. [16, 153, 101].

From neutron scattering, we can obtain information about atomic and molecular position and movement because their length- and timescales overlap with that of neutrons. The length- and timescales in neutron spectroscopy also overlap with what can be reached in molecular dynamics computer simulations, which means that computer simulations can be used to interpret data, e.g. [8], or that it is possible to test more theoretical predictions based on computer simulations as we will do in Ch. 7 and 8.

### Basic principles

First things first, to do neutron scattering experiments, neutrons have to be removed from the atomic nuclei. For neutron scattering experiments today, this is done either in a nuclear reactor by spontaneous fission of $^{235}$U, which is the case at the Institut Laue-Langevin (ILL) and therefore the scenario we will assume, or in a spallation source by bombarding heavy elements with high-energy protons. Most experiments in soft condensed matter are conducted with cold or thermal neutrons roughly in the energy range $0.1 - 100\,\mathrm{m\,eV}$ or approximately $\lambda = 30 - 1\,\text{Å}$. Neutrons leave the nuclei with energies in the MeV-regime and are moderated to the meV-regime through for example $H_2O$ or liquid $H_2$.

As a consequence of quantum mechanics and wave-particle duality, neutrons can be described as particles, as is the case in the process of neutron creation and neutron detection for instance, and as interfering waves in the scattering processes themselves. The de-Broglie wavelength is the wavelength associated with a particle of mass, $m$, moving at velocity, $\mathbf{v}$:

$$\lambda = \frac{h}{m\mathbf{v}} = \frac{2\pi}{|\mathbf{k}|},\ E = \frac{\hbar^2 k^2}{2m}, \tag{4.19}$$

where $h$ is the Planck constant, and $\mathbf{k}$ is the wavevector, related to the momentum of a neutron via $\mathbf{p} = \hbar\mathbf{k}$. The velocity spectrum of neutrons leaving a moderator at a temperature, $T$, will be close to a Maxwell distribution around some average value

$\bar{v}$, with a maximum at

$$\bar{v} = \left(\frac{3k_{\mathrm{B}}T}{m}\right)^{1/2}, \tag{4.20}$$

which corresponds to a kinetic energy, $\bar{E} = \frac{1}{2}m\bar{v}^2 = \frac{3}{2}k_{\mathrm{B}}T$, where $k_B$ is the Boltzmann constant. Because of the relatively low velocity, we can disregard any relativistic effects. Standard velocity of thermal neutrons is around $\bar{v} = 2200\,\mathrm{m\,s^{-1}}$, which corresponds to a temperature of room temperature, an energy $\bar{E} \approx 25$ meV and a wavelength $\lambda \approx 1.8$ Å. The wavelength of thermal neutrons coincides with atomic and molecular distances. The neutrons' wavelength and energy along with their penetrating abilities make them excellent for probing intermolecular distances and energies, which is why neutron scattering is such an effective means for studying excitations, dynamics and structure in condensed matter.

The basic principle is to let an incoming neutron beam with a well-defined velocity hit a sample and measure the energy and wavevector of the outgoing, scattered beam. The difference in energy and momentum between the ingoing and outgoing beam gives information on the exchange of energy between neutron and sample. As a neutron passes close to a nucleus, there are in fact two possible interactions which it can undergo: it can either be absorbed or scattered by the nucleus. When a neutron is absorbed, the nucleus will be in an excited state from which it can decay by for example gamma emission, by the emission of charged particles such as alpha particles, a principle which is used in $^3$He neutron detectors, or it can decay by fission like uranium in fission reactors. Instead, in the scattering process, the direction or energy of the neutron is changed. The two basic quantities that are measured in neutron scattering experiments are therefore energy and momentum transfer between an initial and final state governed by conservation of energy and momentum, respectively. From momentum conservation, the difference in wavevector between the initial and final state, the momentum transfer, is given by:

$$\begin{aligned} \mathbf{Q} &= \mathbf{k}_0 - \mathbf{k}, \\ Q^2 &= k_0^2 + k^2 - 2kk_0\cos\theta \end{aligned} \tag{4.21}$$

where $\theta$ is the scattering angle. The energy transfer is given by

$$\hbar\omega = E_0 - E = \frac{\hbar^2}{2m}(k_0^2 - k^2), \tag{4.22}$$

where $E_0$, $k_0$ and $E$, $k$ are the energy and wavevector of the initial and final state, respectively. For elastic scattering there is no transfer of energy, and we therefore have $\hbar\omega = 0$, and thus $|\mathbf{k}| = |\mathbf{k}_0|$. However, the direction of the wavevectors is still allowed to change, and also for elastic scattering, $Q$ is a function of the scattering angle as is seen from Eq. 4.21.

Atomic motion undergone by the nuclei is experienced by the neutron and gives rise to inelastic scattering. In inelastic scattering there is transfer of energy, i.e. $|\mathbf{k}| \neq |\mathbf{k}_0|$. Inelastic scattering with a maximum in zero energy transfer is usually referred to as quasi-elastic scattering. Quasi-elastic neutron scattering (QENS) is

typically studied on high-resolution spectrometers and is relevant for studying dynamics, where the broadening around the elastic peak is related to a characteristic time of the process.

The energy of thermal and cold neutrons is too small to create internal excitations of the nuclei or electronic shell in a sample, but the atomic motions with much smaller energies can be felt by the neutrons and will give rise to inelastic scattering. In the limit where the interaction of the neutron beam and the sample is weak, the exchange of energy and momentum is in the linear response regime, and will therefore only depend on properties of the sample. The weak interaction also allows us to treat both the ingoing and outgoing neutrons as plane waves according to the Born approximation as we will use later.

The actual measured property is the cross section, which is a measure of the number of neutrons scattered in a given direction as a function of their energy. The differential cross section gives the probability that a neutron leaves the sample in a solid angle element $\mathrm{d}\mathbf{\Omega}$,

$$\frac{\partial \sigma}{\partial \mathbf{\Omega}}, \tag{4.23}$$

where $\sigma$ is the total number of scattered neutrons. The double differential cross section then gives the probability that a neutron with incident energy, $E_0$, leaves the sample in the solid angle element with an exchange of energy between $\hbar\omega$ and $\hbar(\omega + \mathrm{d}\omega)$:

$$\frac{\partial^2 \sigma}{\partial \mathbf{\Omega} \partial E} = \frac{1}{\hbar} \frac{\partial^2 \sigma}{\partial \mathbf{\Omega} \partial \omega}. \tag{4.24}$$

### Scattering processes

First, we will look at the general case for scattering processes that applies to all kinds of spectroscopic techniques using the quantum mechanics formalism adapted from [16]. If we consider a system in thermal equilibrium at a temperature, $T$, which is composed of $N$ particles and with the total energy of the system characterised by the Hamiltonian, $H_R$ that has eigenvalues $E_{m'}$ and eigenstates $|m'\rangle$, then the probability of being in any state $|m'\rangle$ is given by

$$p_{m'} = \frac{1}{Z_R} \exp(-E_{m'}/k_\mathrm{B}T), \tag{4.25}$$

where

$$Z_R = \sum_m \exp(-E_m/k_\mathrm{B}T). \tag{4.26}$$

Similarly, we define a probe characterised by a Hamiltonian, $H_p$, with eigenvalues and eigenvectors, $E_m$ and $|m\rangle$, respectively. We let the probe and the reservoir couple via a Hamiltonian, $H_c$, which is then used to investigate how the change in molecular properties vary with time. The probe is in an initial state $|m\rangle$ and after the interaction with the system in a final state $|n\rangle$. In the linear response regime, where the coupling Hamiltonian is small compared with that of the system and the probe, the system will go from an initial state $|m'\rangle$ to a final state $|n'\rangle$. The interaction between the probe and the system will, according to Fermi's golden rule,

give the probability per unit time that the total system changes from initial state $|m\rangle|m'\rangle$ to final state $|n\rangle|n'\rangle$:

$$W_{nn'mm'} = \frac{2\pi}{\hbar}|\langle n'|\langle n|H_c|m\rangle|m'\rangle|^2\delta(E_m + E_{m'} - E_n - E_{n'}). \tag{4.27}$$

The principle of scattering spectroscopy is then to measure a response function of the system to the perturbation caused by the probe. In practice, this is done by measuring some quantity proportional to $W_{nm}$ as a function of either the final or the initial state of the probe. Using the fluctuation-dissipation theorem, the above probability can be rewritten as

$$W_{nm} = \frac{2\pi}{\hbar^2}\sum_{n'}\sum_{m'}\frac{1}{Z_R}\exp(-E_{m'}/k_{\mathrm{B}}T)|\langle n'|\bar{H}_c|m'\rangle|^2\delta(\omega_{n'm'} - \omega). \tag{4.28}$$

In practice, what is measured in experiments is a function of the initial and final state of the probe and for simplicity, we therefore use the operator, $\bar{H}_c$ that only works on the system, $\bar{H}_c = \langle n|H_c|m\rangle$. The Dirac-delta function ensures a non-vanishing transition probability when there is no net energy transfer, i.e. for elastic scattering, where $\hbar\omega_{n'm'}$ is the energy gain of the system and $\hbar\omega$ is the energy loss of the probe.

We will now consider a system where the probe is a monochromatic beam of neutrons with incoming energy $E_0$ and wavevector, $\mathbf{k}_0$, reaching a sample, leaving with energy $E = E_0 - \hbar\omega$ and wavevector, $\mathbf{k}$, in the solid angle $\Omega$. If the initial and final state are given by

$$\begin{aligned} |k_0\rangle &= \frac{1}{\sqrt{V}}\exp(i\mathbf{k}_0\cdot\mathbf{r}) \\ |k\rangle &= \frac{1}{\sqrt{V}}\exp(i\mathbf{k}\cdot\mathbf{r}), \end{aligned} \tag{4.29}$$

where $V$ is the sample unit volume, the probability of a transition between the two states is now given by $W_{\mathbf{k}_0\mathbf{k}}$. With an incoming flux of neutrons on a sample, $I_0$, the number of scattered neutrons per second between $\mathbf{k}$ and $\mathbf{k} + \mathrm{d}\mathbf{k}$ is:

$$I = I_0\frac{mV}{\hbar\mathbf{k_0}}W_{\mathbf{k}_0\mathbf{k}}\rho(\mathbf{k})\mathrm{d}\mathbf{k}, \tag{4.30}$$

where $m$ is the neutron mass, and $\rho(\mathbf{k})$ is the density of states of momentum $\mathbf{k}$, given by

$$\rho(\mathbf{k})\mathrm{d}\mathbf{k} = \frac{V}{(2\pi)^3}k^2\mathrm{d}\mathbf{\Omega}\mathrm{d}k. \tag{4.31}$$

The double differential cross section in Eq. 4.24 is then

$$\frac{\partial^2\sigma}{\partial\mathbf{\Omega}\partial\omega} = \frac{1}{\partial\mathbf{\Omega}\partial\omega}\frac{I}{I_0}. \tag{4.32}$$

The neutrons interact with nuclei in the sample either via the nuclear or the magnetic force. Because neutrons are made up of quarks, they possess a magnetic moment, which makes it possible to study magnetic properties in solids by the

interaction between neutrons and unpaired electron spins in atoms. Magnetic interactions are, however, negligible for diamagnetic systems compared to the nuclear interactions, and they are therefore not treated further in this work.

Neutron scattering from a nucleus is considered isotropic because the neutrons are scattered by the strong force in the nucleus, which is in the range of just femtometers. This range is much smaller than that of neutron wavelengths in the range of Ångström, which is also why neutrons cannot probe the internal structure of nuclei. The interaction is therefore considered pointlike. The short-ranged nature of the nucleus-neutron interaction is described by the Fermi pseudo-potential:

$$V(\mathbf{r}) = \frac{2\pi\hbar^2}{m} b_i \delta(\mathbf{r} - \mathbf{R_i}), \tag{4.33}$$

where $\mathbf{R}_i$ is the position of the nucleus while $\mathbf{r}$ is the position of the neutron. The scattering process is characterised by the scattering length parameter, $b$, which is independent of the neutron energy. The scattering length is a complex number where the imaginary part represents absorption and the real part is positive or negative depending on the attractive or repulsive nature of the interaction. The scattering length does not only depend on the atom, but also the spin of the nucleus and is therefore isotope-dependent. For all isotopes and spin states, the average scattering length for atomic species $i$, $\langle b_i \rangle$, is the coherent scattering length, while the incoherent scattering length is defined as the mean-squared deviation of $b_i$ from $\langle b_i \rangle$:

$$b_i^{\text{coh}} = \langle b_i \rangle, \tag{4.34}$$

$$b_i^{\text{inc}} = \left( \langle b_i^2 \rangle - \langle b_i \rangle^2 \right)^{1/2}, \tag{4.35}$$

which refer to collective and self-motion, respectively. We can then define a cross section as

$$\sigma_{\text{coh}} = 4\pi \langle b_i \rangle \tag{4.36}$$

for the coherent cross section, and

$$\sigma_{\text{inc}} = 4\pi \left( \langle b_i^2 \rangle - \langle b_i \rangle^2 \right) \tag{4.37}$$

for the incoherent cross section, that applies in the simple case where it is assumed that the scattering is from a single isotope. The total scattering cross section is the sum of the two,

$$\sigma = \sigma_{\text{coh}} + \sigma_{\text{inc}}. \tag{4.38}$$

A way of experimentally distinguishing between coherent and incoherent scattering is by use of polarised neutrons.

Using Fermi's pseudo-potential for the short-ranged neutron-nucleus interaction potential (Eq. 4.33), the matrix element of the coupling Hamiltonian between the initial and final state can be written as

$$\bar{H}_c = \langle \mathbf{k}_0 | V_r | \mathbf{k} \rangle = \frac{2\pi\hbar^2}{mV} \sum_i b_i \exp(i\mathbf{Q} \cdot \mathbf{R}_i), \tag{4.39}$$

where $\mathbf{R}_i$ is the position operator of an atom $i$. We then end up with a double differential cross section:

$$\frac{\partial^2\sigma}{\partial\mathbf{\Omega}\partial\omega} = \frac{k}{k_0}\frac{1}{2\pi}\sum_i\sum_j\int_{-\infty}^{\infty}\frac{1}{N}\langle b_i b_j \exp(-i\mathbf{Q}\cdot\mathbf{R}_i(t))\times\exp(-i\mathbf{Q}\cdot\mathbf{R}_j(t))\rangle\exp(-i\omega t)\mathrm{d}t, \tag{4.40}$$

where the terms in broken brackets refer to the ensemble average.

It is assumed that there is no coupling between the actual scattering length of a nucleus and its position. The average can then be performed independently of spin state and position of the nucleus. When there is no correlation between the scattering lengths of different isotopes in a sample consisting of $N_\alpha$ and $N_\beta$ number of atoms of type $\alpha$ and $\beta$, then the double differential cross section can be split into two parts, a coherent and an incoherent part. The coherent part is given by:

$$\left(\frac{\partial^2\sigma}{\partial\mathbf{\Omega}\partial\omega}\right)_{\mathrm{coh}} = \frac{1}{N}\frac{k}{k_0}\sum_{\alpha=1}^{n}\sum_{\beta=1}^{n} b_\alpha^{\mathrm{coh}} b_\beta^{\mathrm{coh}}\sqrt{N_\alpha N_\beta}S_{\mathrm{coh}}^{\alpha\beta}(\mathbf{Q},\omega), \tag{4.41}$$

where $S_{\mathrm{coh}}^{\alpha\beta}(\mathbf{Q},\omega)$ is the scattering function, also known as the dynamic structure factor:

$$S_{\mathrm{coh}}^{\alpha\beta}(\mathbf{Q},\omega) = \\ \frac{1}{2\pi\sqrt{N_\alpha N_\beta}}\int_{-\infty}^{\infty}\sum_{i_\alpha=1}^{N_\alpha}\sum_{j_\beta=1}^{N_\beta}\langle\exp(-i\mathbf{Q}\cdot\mathbf{R}_{i_\alpha}(t))\times\exp(-i\mathbf{Q}\cdot\mathbf{R}_{j_\beta}(0))\rangle\exp(-i\omega t)\mathrm{d}t. \tag{4.42}$$

Similarly, we can write up an expression for the incoherent cross section and its dynamic structure factor:

$$\left(\frac{\partial^2\sigma}{\partial\mathbf{\Omega}\partial\omega}\right)_{\mathrm{inc}} = \frac{1}{N}\frac{k}{k_0}\sum_{\alpha=1}^{n} b_\alpha^{\mathrm{inc}} S_{\mathrm{inc}}^{\alpha}(\mathbf{Q},\omega), \\ S_{\mathrm{inc}}^{\alpha}(\mathbf{Q},\omega) = \frac{1}{2\pi N_\alpha}\int_{-\infty}^{\infty}\sum_{i_\alpha=1}^{N_\alpha}\langle\exp(-i\mathbf{Q}\cdot\mathbf{R}_{i_\alpha}(t))\times\exp(-i\mathbf{Q}\cdot\mathbf{R}_{i_\alpha}(0))\rangle\exp(-i\omega t)\mathrm{d}t. \tag{4.43}$$

for a system with atoms of type $\alpha$. We see immediately for both coherent and incoherent cross sections that by selecting the incoming and outgoing value of the wavevector, the change in energy and momentum, only show up in the dynamic structure factor in the cross sections in Eq. 4.41 and 4.43. The dynamic structure factor, $S(\mathbf{Q},\omega)$, which is what we probe in neutron scattering experiments, contain all spatial and dynamic properties, independent on the neutron properties and the type of sample.

The coherent and incoherent scattering functions are quite different in nature, as we saw in the van Hove correlation functions (Eq. 4.10), due to interference effects in the coherent part caused by the sum over the phase shifts of different atoms. For isotopes in general it is true that $b_\alpha^{\mathrm{coh}} \gg b_\alpha^{\mathrm{inc}}$, which will result in neutron spectra that stem mostly from coherent scattering either at the same time, elastic scattering providing information on structure, or at different times, inelastic

scattering reflecting the collective motion of the atoms, the density fluctuations. However, for the special case of hydrogen, $^1$H, it is true that $b_\alpha^{\text{coh}} \ll b_{\text{H}}^{\text{inc}}$, which means that in samples with a relatively high concentration of hydrogen atoms, e.g. molecular liquids, incoherent scattering will be the dominating contribution to the signal, typically $\sim 90\%$ for organic molecular liquids. For this reason, incoherent neutron scattering is a powerful tool for studying self-correlations of hydrogen in all sorts of systems, but in particular in organic systems.

For this work, the relevant scattering functions are those from incoherent scattering, and while the above introduction deals with the general case of a multicomponent system, we will from now on restrict ourselves to a one-component system, assuming that the scattering arise from just one type of system. The double differential cross section is then simplified to

$$\frac{\partial^2\sigma}{\partial\mathbf{\Omega}\partial\omega} = \frac{1}{4\pi N}\frac{k}{k_0}\left(\sigma_{\text{coh}}S_{\text{coh}}(\mathbf{Q},\omega) + \sigma_{\text{inc}}S_{\text{inc}}(\mathbf{Q},\omega)\right), \tag{4.44}$$

where $\sigma_{\text{x}}$ is the isotope specific coherent or incoherent scattering cross section, and the dynamic structure factor is related to the intermediate scattering function through Fourier transform,

$$S(\mathbf{Q},\omega) = \frac{1}{2\pi\hbar}\int_{-\infty}^{\infty} I(\mathbf{Q},t)\exp(-i\omega t)\mathrm{d}t, \tag{4.45}$$

with the coherent and incoherent intermediate scattering functions:

$$\begin{aligned} I_{\text{coh}}(\mathbf{Q},t) &= \frac{1}{N}\sum_i\sum_j\langle\exp(i\mathbf{Q}\cdot\mathbf{R}_i(t))\exp(i\mathbf{Q}\cdot\mathbf{R}_j(0))\rangle \\ I_{\text{inc}}(\mathbf{Q},t) &= \frac{1}{N}\sum_i\langle\exp(i\mathbf{Q}\cdot\mathbf{R}_i(t))\exp(i\mathbf{Q}\cdot\mathbf{R}_i(0))\rangle. \end{aligned} \tag{4.46}$$

By taking the space-Fourier transform of the intermediate scattering function $I(\mathbf{Q},t)$, we can return to real space and obtain the pair-correlation function:

$$G(\mathbf{r},t) = \frac{1}{(2\pi)^3}\int I(\mathbf{Q},t)\exp(-i\mathbf{Q}\cdot\mathbf{r})\mathrm{d}\mathbf{Q}. \tag{4.47}$$

### In the classical limit

In the classical limit, we can neglect any effects from quantum mechanics, i.e. for a particle with mass $m$, both energy and momentum transfer are so small that

$$|\hbar\omega| \ll \frac{1}{2}k_{\text{B}}T \qquad \text{and} \qquad \frac{\hbar^2Q^2}{2m} \ll \frac{1}{2}k_{\text{B}}T, \tag{4.48}$$

and a system can be described by classical mechanics. Here we can neglect kinematic effects of the momentum transfer $\hbar\mathbf{Q}$ from the neutron to the sample, resulting in:

$$S_{\text{cl}}(\mathbf{Q},\omega) = S_{\text{cl}}(-\mathbf{Q},-\omega). \tag{4.49}$$

This is only true for long times and large values of $r$, or equivalently, small $\omega$ and $\mathbf{Q}$. When quantum mechanical effects set in, $S(\mathbf{Q},\omega)$ is not symmetric in $\omega$; there

is a higher probability of a neutron transitioning from a state of higher energy to a state of lower energy than the other way around, i.e. energy loss for a neutron (energy gain for the sample) is preferred in the system to neutron energy gain. The scattering function can be approximated with

$$S(\mathbf{Q},\omega) = \exp\left(\frac{\hbar\omega}{k_{\mathrm{B}}T}\right) S_{\mathrm{cl}}(-\mathbf{Q},-\omega), \tag{4.50}$$

which fulfils the detailed balance condition that gives the relation between the scattering function in the two cases of neutron energy gain, $\hbar\omega < 0$, and neutron energy loss, $\hbar\omega > 0$.

Assuming that our system can be described classically, $\mathbf{r}$ is no longer a non-commuting operator, but instead a position vector. The pair correlation functions can now be written as

$$\begin{aligned} G^{\mathrm{cl}}_{\mathrm{coh}}(\mathbf{r},t) &= \sum_j \left\langle \delta(\mathbf{r} + \mathbf{R}_0(0) - \mathbf{R}_j(t)) \right\rangle, \\ G^{\mathrm{cl}}_{\mathrm{inc}}(\mathbf{r},t) &= \left\langle \delta(\mathbf{r} + \mathbf{R}_0(0) - \mathbf{R}_0(t)) \right\rangle. \end{aligned} \tag{4.51}$$

$G^{\mathrm{cl}}_{\mathrm{coh}}(\mathbf{r},t)$ expresses the probability, given an atom at origin at time $t = 0$, that another atom will be found at position $\mathbf{r}$ at time $t$. $G^{\mathrm{cl}}_{\mathrm{inc}}$ expresses the probability that an atom which was at the origin at time $t = 0$ can be found at position $\mathbf{r}$ at time $t$ under the assumption that all particles are equivalent. This provides the same information as the pair correlation functions in Eq. 4.10.

If we now look at the short-time limit, where we set $t = 0$. We see from Eq. 4.45 that the dynamic structure factor in this limit is the static structure factor, $S(\mathbf{Q}) = I(\mathbf{Q}, t = 0)$ with a coherent part that provides information on the structure of a sample, and an incoherent part that does not provide any information as it will always be equal to 1 as can be seen from Eq. 4.43:

$$S_{\mathrm{inc}}(\mathbf{Q}) = I_{\mathrm{inc}}(\mathbf{Q}, t = 0) = \langle \exp(-i\mathbf{Q}\cdot \mathrm{R}_i(0)) \times \exp(-i\mathbf{Q}\cdot \mathrm{R}_i(0)) \rangle = 1. \tag{4.52}$$

If we instead go to the long-time limit of the incoherent part where we set $t \to \infty$, there is no correlation between the position of the $i$th atom at time $t = 0$ and $\infty$, i.e. between $\mathbf{R}_i(0)$ and $\mathbf{R}_i(\infty)$. The incoherent intermediate scattering function found by space-Fourier transform (Eq. 4.47) will take the form:

$$\begin{aligned} I_{\mathrm{inc}}(\mathbf{Q},\infty) &= \frac{1}{2\pi}\int G_{\mathrm{inc}}(\mathbf{r},\infty)\exp(-i\mathbf{Q}\cdot\mathbf{r})\mathrm{d}\mathbf{r} \\ &= \frac{1}{N}\sum_i |\langle \exp(-i\mathbf{Q}\cdot\mathbf{R}_i)\rangle|^2. \end{aligned} \tag{4.53}$$

We can split the intermediate scattering function into a time-independent and a time-dependent component

$$I_{\mathrm{inc}}(\mathbf{Q},t) = I_{\mathrm{inc}}(\mathbf{Q},\infty) + I_{\mathrm{inc}}(\mathbf{Q},t), \tag{4.54}$$

where the time-dependent component will go to zero when $t \to \infty$. By taking the time-Fourier transform, we arrive at an expression for the dynamic structure factor:

$$S_{\mathrm{inc}}(\mathbf{Q},\omega) = I_{\mathrm{inc}}(\mathbf{Q},\infty)\delta(\omega) + S_{\mathrm{inc}}(\mathbf{Q},\omega). \tag{4.55}$$

We see from the first term that there will be a purely elastic signal in $\omega = 0$ with the intensity of the elastic peak given by the long-time limit of the intermediate scattering function, $I_{\text{inc}}(\mathbf{Q}, \infty)$. This term is often referred to as the elastic incoherent structure factor and has the dimension of a structure factor and is the fraction of the total intensity which originates from the purely elastic signal. The elastic signal thus determines the plateau value of the intermediate scattering function. For $S_{\text{inc}}(\mathbf{Q}, \omega)$, the first term is superimposed onto the quasielastic component, the second term, with a non-vanishing broadening centred in $\omega = 0$. The width of the broadening provides information about characteristic times of the system, which we will use in Ch. 7 and 8.

### Separation of motion

We will in this section look into examples, relevant for this work, of what kind of dynamics we can describe from the information we gain from neutron scattering experiments. We will mainly deal with dynamics from incoherent single-scatterer systems, and we will therefore leave out the subscript $i$ in this section. Most molecular glass-forming liquids contain a large fraction of hydrogen atoms, and because of the dominating incoherent scattering length of hydrogen, to a good approximation, the measured neutron scattering intensity can be considered to arise from just one isotope and to be incoherent, providing information on averaged self-motion dynamics of the molecules.

If we consider the incoherent intermediate scattering function in Eq. 4.46, the position vector $\mathbf{R}$ can be split into two components, a non-local and a local one:

$$\mathbf{R}(t) = \mathbf{R}_{\text{e}}(t) + \mathbf{u}(t). \tag{4.56}$$

$\mathbf{R}_{\text{e}}(t)$ is the time-dependent instantaneous position of equilibrium of the molecule as a whole with respect to some fixed, external coordinate system. In the case of a crystalline material, this would be the crystal lattice, whereas in amorphous systems this position does not show translational symmetry. $\mathbf{R}_{\text{e}}(t)$ represents the time-dependent motion of the molecule as a whole. The local motion is represented by $\mathbf{u}(t)$ and is the displacement of an atom away from its equilibrium position within a molecule, e.g. internal vibrations. The external motion, $\mathbf{R}_{\text{e}}(t)$, is in liquids specific to the system and are often split into terms representing translational and rotational motion. Taking into account all types of motion in the incoherent intermediate scattering function is difficult, but often, different types of motion are assigned different timescales with different spatial dependence and can in this way be distinguished. This can for example be done by the slightly crude assumption that the different types of motion are uncorrelated, and that the internal vibrational states of an atom are not influenced by rotational motion or the lattice vibrations of a molecule, i.e. the energy of the internal vibrational states is higher than the energy related to reorientational motion.

The incoherent intermediate scattering function for a system can be written as a product of the reorientational motion and the local vibrations:

$$I_{\text{inc}}(\mathbf{Q}, t) = I^{\text{R}}_{\text{inc}}(\mathbf{Q}, t) \cdot I^{\text{V}}_{\text{inc}}(\mathbf{Q}, t), \tag{4.57}$$

where

$$\begin{aligned} I^{\mathrm{R}}_{\mathrm{inc}}(\mathbf{Q},t) &= \langle \exp(i\mathbf{Q}\cdot(\mathbf{R}_{\mathrm{e}}(t)-\mathbf{R}_{\mathrm{e}}(0)))\rangle \\ I^{\mathrm{V}}_{\mathrm{inc}}(\mathbf{Q},t) &= \langle \exp(i\mathbf{Q}\cdot(\mathbf{u}(t)-\mathbf{u}(0)))\rangle \end{aligned} \tag{4.58}$$

are the contributions from reorientational motion and intramolecular vibrations, respectively.

From Eq. 4.57, where the total incoherent intermediate scattering function is given as a product, the dynamic structure factor can be written as a convolution product in frequency space:

$$S_{\mathrm{inc}}(\mathbf{Q},\omega) = S^{\mathrm{R}}_{\mathrm{inc}}(\mathbf{Q},\omega) \otimes S^{\mathrm{V}}_{\mathrm{inc}}(\mathbf{Q},\omega), \tag{4.59}$$

where the convolution is given by the integral

$$S^{\mathrm{R}}_{\mathrm{inc}}(\mathbf{Q},\omega) \otimes S^{\mathrm{V}}_{\mathrm{inc}}(\mathbf{Q},\omega) = \int \mathrm{d}\omega' S^{\mathrm{R}}_{\mathrm{inc}}(\mathbf{Q},\omega') S^{\mathrm{V}}_{\mathrm{inc}}(\mathbf{Q},\omega-\omega'). \tag{4.60}$$

If we imagine the reorientational motion is composed of translational and rotational components, each component will be a convolution product, and each of the convolution products will result in a broadening of the spectrum.

If we model the system with a solid, i.e. the external motion is independent of time, a reasonable assumption for highly viscous liquids or glasses, the position vector is now:

$$\mathbf{R}(t) = \mathbf{R}_e + \mathbf{u}(t), \tag{4.61}$$

and we can write the intermediate scattering function as

$$\begin{aligned} I_{\mathrm{inc}}(\mathbf{Q},t) &= \langle \exp(-i\mathbf{Q}\cdot(\mathbf{R}_{\mathrm{e}}+\mathbf{u}(0)))\rangle \langle \exp(i\mathbf{Q}\cdot(\mathbf{R}_{\mathrm{e}}+\mathbf{u}(t)))\rangle \\ &= \langle \exp(-i\mathbf{Q}\cdot\mathbf{u}(0)) \exp(i\mathbf{Q}\cdot\mathbf{u}(t))\rangle \langle \exp(i\mathbf{Q}\cdot(\mathbf{R}_{\mathrm{e}}-\mathbf{R}_{\mathrm{e}}))\rangle \\ &= \langle \exp(-i\mathbf{Q}\cdot\mathbf{u}(0)) \exp(i\mathbf{Q}\cdot\mathbf{u}(t))\rangle , \end{aligned} \tag{4.62}$$

which only gives information on the dynamic part, $\mathbf{u}(t)$, and not on structure. In the long-time limit of Eq. 4.62, we assume that $\mathbf{u}(0)$ and $\mathbf{u}(t)$ are uncorrelated and that time is homogeneous, i.e. the ensemble average $\langle u(t)\rangle$ is constant in time. For $t \to \infty$, we obtain

$$I_{\mathrm{inc}}(\mathbf{Q},t) = \langle \exp(2\mathbf{Q}\cdot\mathbf{u}\rangle, \tag{4.63}$$

which is also called the Debye-Waller factor, $\exp(-2W(\mathbf{Q}))$. In an amorphous solid, we can moreover assume isotropic behaviour, i.e. the average of $\mathbf{Q}\cdot\mathbf{u}$ does not depend on the direction of $\mathbf{Q}$, and we can model the vibrations with a Gaussian distribution, assuming they are harmonic. We thus end up with the expression for the long-time limit:

$$I_{\mathrm{inc}} = \exp\left(-\frac{Q^2\langle u^2\rangle}{3}\right). \tag{4.64}$$

The incoherent intermediate scattering function must start in 1 for $t = 0$ and will then decay to $\exp(-2W(\mathbf{Q}))$ for $t \to \infty$. The long time-limit corresponds to the elastic region in frequency-space. Eq. 4.64 can be used to determine the mean-squared displacement of a system from the elastic intensity, which we will use in Ch. 5.

The inelastic contribution can be approximated by assuming one-phonon scattering, which is valid in the solid state, where only the harmonic forces are considered. The displacement of each atom in a system can then be described as a sum of displacements from a set of normal modes of the system, where each normal mode has an associated frequency and eigenvector, see e.g [153, 87]. The incoherent, inelastic contribution to the dynamic structure factor is

$$S_{\text{inc,inel}}(\mathbf{Q},\omega) = \frac{\exp(-2W)}{2MN}\sum_s \frac{(\mathbf{Q}\cdot\mathbf{e}_s)^2}{\omega_s} \times \left(\langle n_s+1\rangle\delta(\omega-\omega_s) + \langle n_s\rangle\delta(\omega+\omega_s)\right), \tag{4.65}$$

where $\omega_s$ is the frequency of mode $s$ with wavevector $\mathbf{Q}$ and a corresponding polarisation vector, $\mathbf{e}_s$. The first and the second term in brackets are phonon emission and phonon absorption, respectively, where $\langle n_s\rangle$ is the Bose factor, which gives the occupation number of the mode:

$$\langle n_s\rangle = \left(\exp\left(\frac{\hbar\omega}{k_\text{B}T}\right)-1\right)^{-1} \text{ and } \langle n_s+1\rangle = \langle n_s\rangle + 1. \tag{4.66}$$

In the classical limit for $\hbar \to 0$, we have

$$\langle n_s\rangle = \langle n_s+1\rangle = \frac{k_\text{B}T}{\hbar\omega}. \tag{4.67}$$

In this limit, the phonon annihilation and creation process are identical. By substituting the sum with an integral, assuming an isotropic system, we thus average $(\mathbf{Q}\cdot\mathbf{e}_s)^2$ over all modes with frequency $\omega_s$, which we can then replace by $Q^2$. By introducing the vibrational density of states, $g(\omega)$, we end with:

$$S_{\text{inc,inel}}(\mathbf{Q},\omega) = \frac{\exp(-2W)}{2M}Q^2\frac{n(\omega)}{\omega}g(\omega). \tag{4.68}$$

We will use the fact that the inelastic part of the dynamic structure factor is directly coupled to the vibrational density of states in Ch. 8.

### Resolution

So far we have discussed the contributions to the dynamic structure factor from elastic and inelastic scattering and how this can result in a broadening of the neutron signal around the elastic peak, as we also saw in Eq. 4.55

$$S_{\text{inc}}(\mathbf{Q},\omega) = \exp(-2W(Q))[\delta(\omega) + S_{\text{inel}}(\mathbf{Q},\omega)]. \tag{4.69}$$

However, the elastic peak is of course not a delta function in real experiments, and instead of an infinitely sharp signal, the elastic intensity is convoluted with the instrument resolution, resulting in an elastic peak with a finite energy width. The width depends on energy and momentum characteristics of the instrument at use, which means that the resolution of the neutron instrument determines the timescale of the elastic intensity and therefore the timescale of the experiment. The measured

scattering function is a convolution between the resolution function of the instrument and the actual dynamic structure factor:

$$S_{\text{meas}}(\mathbf{Q},\omega) = R(\mathbf{Q},\omega) * S(\mathbf{Q},\omega). \tag{4.70}$$

The measured elastic intensity is thus everything that falls within $0\,\text{eV} \pm \Delta E_{\text{res}}$, i.e. with correlation times longer than that given by the energy resolution, see e.g. [57]. This is illustrated in Fig. 4.3. The resolution function and the elastic intensity therefore determines the plateau value of the intermediate scattering function.

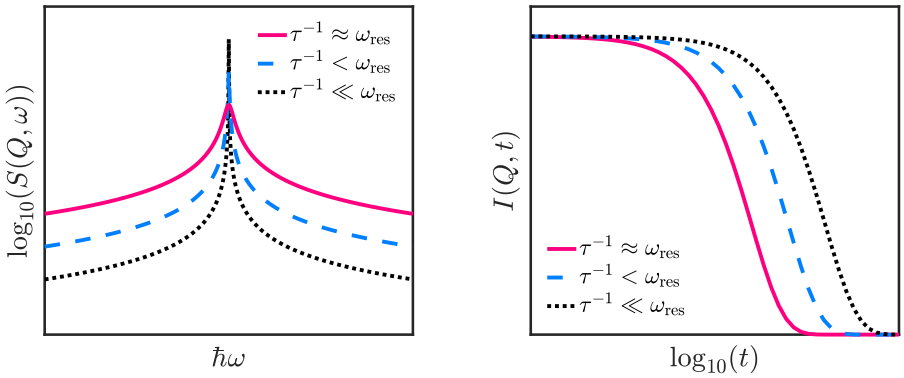


Figure 4.3: Illustration of the consequence of the instrument resolution. The relaxation time that coincides with the instrument resolution will be the lowest resolved relaxation time (full line). Relaxations slower than that the instrument resolution (dashed lines) will go into the elastic intensity and can therefore not be resolved.

The deconvolution of elastic intensity from the energy resolution can be a tricky job when inelastic intensity is also centred around $\omega = 0$ as in quasi-elastic scattering. One approach is to take the inverse Fourier transform of the measured dynamic structure to arrive at the intermediate scattering function, $F(\mathbf{Q},t)$:

$$F(\mathbf{Q},t) = I(\mathbf{Q},t)R(\mathbf{Q},t). \tag{4.71}$$

Instead of a convolution, it is now a product, and the intermediate scattering function is obtained simply by division. However, this method has its drawbacks, for example the loss of information doing numerical Fourier transform and cut-off effects, and is in general a lot harder to do in practice than in theory, and in many cases, it is therefore more convenient to stay in the frequency domain. In Ch. 7.4, we will show an example of the determination of a relaxation time from the intermediate scattering function in the time domain. Below we will introduce the two techniques, time-of-flight and backscattering, which have been used for the work presented in the next four chapters.

### Time-of-flight

The velocity of a neutron and hence its energy can be determined by measuring the time it takes for the neutron to move a certain distance. For thermal neutrons

that move with a velocity of roughly $2\,\mathrm{km\,s^{-1}}$, the velocity and hence the energy can be determined by measuring the time-of-flight over a distance of a few meters. By creating a short starting pulse before the sample and knowing the instrumental flight distance and the starting time, the time-of-flight is measured from the arrival time after the sample. This section will deal with the direct geometry time-of-flight (TOF) instruments IN5 and IN6 at ILL, where the energy resolution is roughly two orders of magnitude coarser than for the backscattering instrument IN16B that is described below. The dynamics accessible with the TOF instruments IN5 and IN6 is in the picosecond range.

IN5 is a multi-chopper TOF spectrometer, where a pulsed beam is created with counter-rotating chopper disks, which is then sent through choppers that prevent frame overlap in the neutron pulses. A system of choppers then selects the incoming wavelength of the beam and the energy resolution by adjusting the speed of the choppers. On this instrument, the choppers are monochromating the neutron beam and provides a nearly Gaussian resolution function. The neutrons are detected in a large array of pixelated position sensitive $^3$He detectors placed around 4 m from the sample in a vacuum chamber.

IN6 at is a TOF chopper spectrometer, where crystal monochromators select the incident energy. The beam is focused vertically by selecting the neutrons with slightly different incident energy from three crystal monochromators. Higher order neutrons reflected from the monochromators are removed using a beryllium filter. The beam then passes a set of Fermi choppers that creates a pulsed beam and prevents an overlap of the pulse into the next measurement frame. The sense of rotation of the Fermi choppers, which are placed close to the sample, is such that the slower neutrons are scattered first and the fastest neutrons last. The energy resolution is determined by the rotation speed of the Fermi choppers. The scattered neutrons are detected in $^3$He tubes in a large detector bank.

An advantage of TOF spectroscopy is the relatively broad range of energy and momentum transfer, $(\mathbf{Q}, \omega)$ space, that can be surveyed. The kinematic range can be calculated by combining Eq. 4.21 and 4.19,

$$\frac{\hbar Q^2}{2m} = E + E_0 - 2(EE_0)^{1/2}\cos\theta \tag{4.72}$$

which expressed as a function of initial energy and energy transfer is

$$\frac{\hbar Q^2}{2m} = 2E_0 - \hbar\omega - 2(E_0(E_0 - \hbar\omega))^{1/2}\cos\theta. \tag{4.73}$$

For direct geometry instrument like IN5 and IN6, the trajectory a detector traces through $(\mathbf{Q}, \omega)$ space will be determined from the energy transfer, $\hbar\omega$, and the intitial energy $E_0$. Because of the large momentum and energy range and the geometry of the instrument, we see from Eq. 4.73 that for studies in energy at constant values of $Q$, one has to interpolate between the different detector angles. TOF instruments are useful for studying picosecond dynamics in glass-forming liquids accessing inelastic excitations and quasielastic broadening as we will see in Ch. 7 and 8.

### Backscattering

Neutron backscattering (BS) spectroscopy is an example of the use of inverse geometry. The neutron energy is determined from Bragg reflection from crystals by using the largest possible Bragg angle, $\theta = 90°$, which results in a very high energy resolution, roughly given by

$$\frac{\Delta\lambda}{\lambda} = \frac{\Delta k}{k} \approx \frac{\Delta d}{d} + \cot\theta\Delta\theta, \tag{4.74}$$

which is the differential of the Bragg equation, where $d$ is the lattice spacing. A backscattering instrument can because of its narrow energy resolution access longer dynamic timescales than for example time-of-flight instruments. In this section we will take a look at the cold BS spectrometer IN16B at the ILL. The inverse geometry settings mean that in this case, the incident energy is varied while the final energy is held fixed.

A polychromatic neutron beam is pulsed by a chopper before it reaches a rotating deflector that sends the neutrons to the monochromator. To minimise the first term in Eq. 4.74, the neutrons are reflected from perfect silicon single-crystal wafers with [111] surface orientation in a 90° Bragg angle to minimise the second term in Eq. 4.74. The monochromator is mounted on a Doppler drive whose speed determines the incoming wavelength. The linear motor Doppler drive has a maximum monochromator speed of $4.7\,\mathrm{m\,s^{-1}}$ for a given velocity profile. For a full spectrum, the moving spherical monochromator will create a sinusoidal velocity profile that continuously selects a narrow band of wavelengths. The neutrons come back and pass through windows in the rotating deflector. The pulsed beam with an energy range determined from the Doppler drive then hits the sample and is scattered in all directions. Only scattered neutrons from the sample with a certain final energy, determined from the backscattering reflection of the analyser crystals, are reflected back to the $^3$He detector tubes and counted. The counting is therefore a function of the speed of the Doppler drive. The experiments carried out in relation to this work were done with the standard settings: incident wavelength $\lambda = 6.27\,\text{Å}$, Si(111) monochromators resulting in an energy resolution of $\Delta E_{\mathrm{res}} = 0.8\,\mu\mathrm{eV}$, energy transfer $\pm 30\,\mu\mathrm{eV}$ and $Q$-range $0.1 - 1.8\,\mu\mathrm{eV}$.

Backscattering instruments moreover provide the option of doing fixed window scans (FWS) with constant incident wavevector, where 'scan' refers to a sample property like temperature or pressure. When the incident and final wavevector are set to the same value, this is called elastic fixed window scans (EFWS) for which $k = k_i$ and $\Delta E = 0$. This is achieved by stopping the Doppler drive in a fixed position. The elastic fixed window scans provide an overview of the dynamics in a sample by measuring $S(Q, 0)$. It is a fast way of obtaining information on a sample, and can for example be used to obtain the mean-squared displacement as a function of temperature from the $Q$-dependence (Eq. 4.64 and Ch. 5).

While the elastic fixed window scans are standard on most backscattering instruments, a reasonably new and refined technique that compliments the elastic fixed window scans are the inelastic fixed window scans (IFWS) available on IN16B [54]. In IFWS, the wavevector is still held constant providing the fixed energy window, but now $k \neq k_0$. In IFWS, the tunable velocity profile of a linear motor Doppler

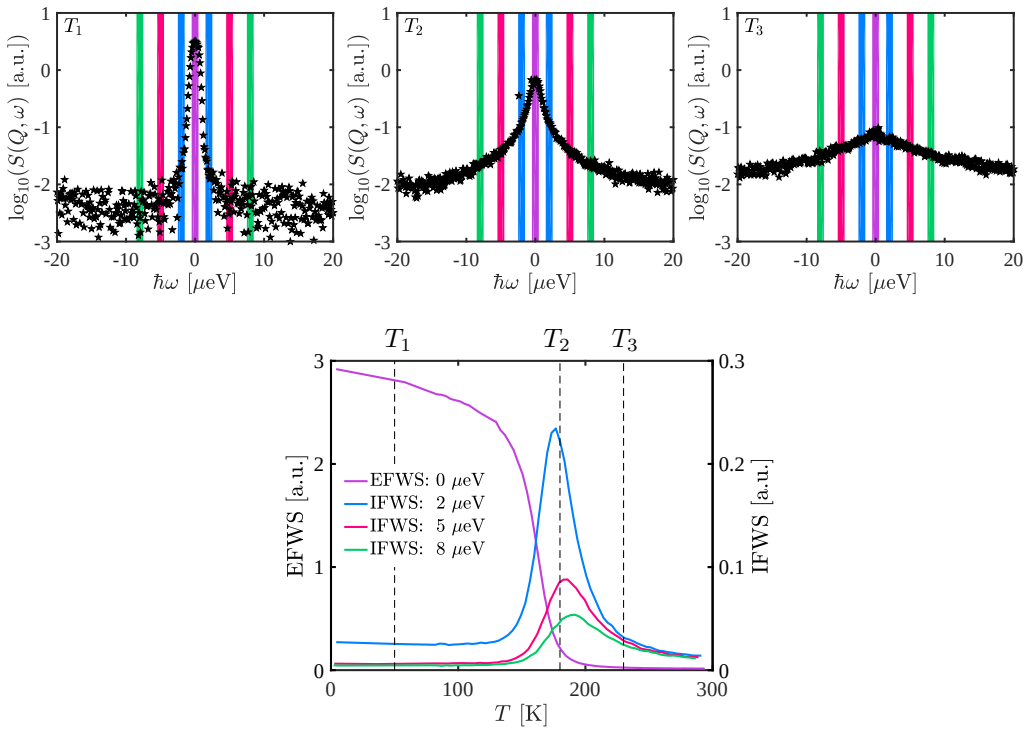


Figure 4.4: Top: Examples of full spectra from IN16B are given for three different temperatures with $T_1 < T_2 < T_3$. The vertical coloured bars refer to the elastic ($\Delta E = 0\,\mu$eV) and inelastic ($\Delta E = 2,\ 5,\ 8\,\mu$eV) window scan intensity that are shown below as a function of temperature. The three temperatures at which the spectra were taken are marked as dashed lines in the temperature scan. At $T_1$, the signal is mainly elastic with only a small wing visible for $\Delta E = 2\,\mu$eV. At $T_2$, broadening of the signal is observed, while the elastic intensity goes down. The inelastic intensities undergo a maximum. At $T_3$, the elastic intensity is basically lost and only broadening is left.

drive is utilised to periodically maintain a constant longitudinal Doppler velocity, $\pm v_D$. The Doppler velocity is kept constant for a long time with only short time used for changing direction, aiming for a rectangular velocity profile. This means that much shorter counting time is needed at a fixed energy in comparison to the time it would take to acquire the same information from the full spectrum where a sinusoidal velocity profile is used.

Doing alternating elastic and inelastic fixed window scan is an easy and fast way of gaining information on not just how the elastic intensity changes upon a temperature or pressure scan as a function of $Q$, but also on how relaxational processes enter the instrument window, causing broadening in the signal. This is illustrated in Fig. 4.4 comparing full spectra for three different temperatures to a FWS scan on temperature for four different settings of $k_i$, resulting in $\Delta E = 0,\ 2,\ 5,\ 8\,\mu\text{eV}$. We will use the IFWS technique for example in the interpretation of the mean-squared displacement found from EFWS in Ch. 5.

### Corrections

All corrections of the measured neutron data presented in this work have been carried out in the data treatment program LAMP developed at the ILL [130, 95]. The data has been normalised to monitor, i.e. neutron count, and the incoherent signal from vanadium. Background from sample cell has been subtracted and corrections have been made for self-shielding, self-absorption and detector efficiency. On IN5 and IN6 with large energy transfer ranges, data has been sliced and interpolated to hold constant values of $Q$.

One thing that we have not discussed so far is the possibility that a neutron can be scattered more than once from the sample. Multiple scattering refers to the fraction of neutron scattering passing the sample twice. It is very difficult to make a good estimate of this fraction. In general, ensuring that the sample thickness as thin as possible will keep multiple scattering at a minimum.

Corrections for multiple scattering can be done in LAMP, where it was found that it changes the relative level of intensity of a quasielastic spectrum but not the shape. For the data presented in this work, we are mainly interested in comparing spectrum to spectrum on the same sample. We will make the somewhat crude assumption that the fraction of multiple scattering is the same for all state points in the same sample and that the effect therefore is negligible.

In Fig. 4.5, we show the same sample and state point measured on different instruments and with different instrumental settings. The measured intensities given by $S(Q,\omega)$ are presented on surface plots as a function of energy transfer and $Q$-dependence for a single state point from IN16B (top) and IN5 (bottom). The $Q$-range spanned by IN16B covers the the $Q$-range spanned by both wavelength settings on IN5. Because of the small energy range on IN16B, we can assume constant value of $Q$ for each detector angle. However, on the TOF instruments, the large energy range require an interpolation between the different detectors to obtain constant values of $Q$. This can be done in the data treatment program LAMP. For the data presented in this work, the energy range was chosen to go to a neutron energy gain of 8 meV. This provides a $Q$-range on IN5 for $\lambda = 5\,\text{Å}$ of $1.2 - 1.9\,\text{Å}^{-1}$, and for $\lambda = 8\,\text{Å}$

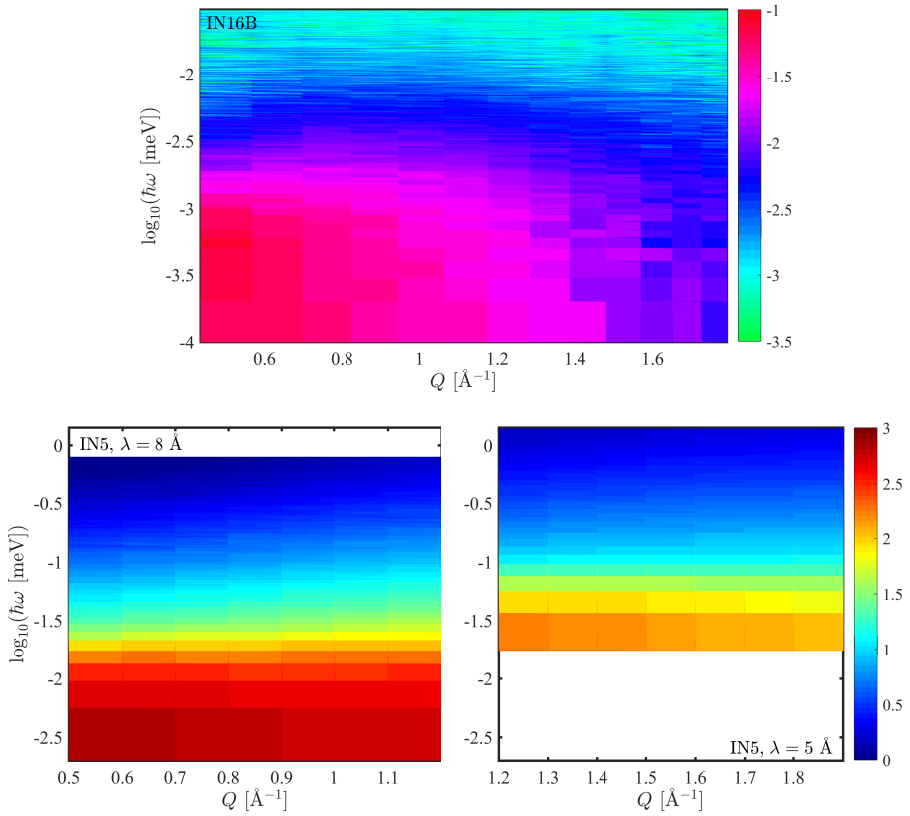


Figure 4.5: $(Q, \omega)$-dependence of spectra at same sample and state point from IN16B (top) and IN5 $\lambda = 8\,$Å and $5\,$Å (bottom). The logarithm of the intensity is shown in the respective colourbars. The two sets of data from IN5 is plotted on the same intensity and energy scale.

of $0.5 - 1.2\,\text{Å}^{-1}$ as shown in Fig. 4.5. There is only little overlap between the $Q$-range spanned by the $\lambda = 8\,\text{Å}$ data and that at $\lambda = 5\,\text{Å}$, in fact, only $Q = 1.2\,\text{Å}^{-1}$ overlaps. The two sets of data from IN5 is plotted on the same intensity and energy scale. We observe the same tendency for the three instrumental settings shown here: high intensity is seen for low $Q$ and low energy transfer, close to the instrumental resolution and the elastic peak, whereas at higher energy transfer and higher $Q$, the intensities become lower. The effects are less pronounced for the faster dynamics measured on IN5 compared to IN16B. The timescale of the instruments given by the HWFM elastic resolution is here calculated from:

$$E_{\text{res}} = \frac{1}{2}mv^2 = \hbar\omega = \frac{\hbar}{\omega} \tag{4.75}$$

and corresponds to $\sim 2\,\text{ns}$ for IN16B with a wavelength of $6.27\,\text{Å}$. For the time-of-flight instruments and settings, we reach faster dynamics in the picosecond range. The corresponding timescales in orders of magnitude which are used throughout this work are provided in Table 4.1.

| | $\lambda$ | $E_{\text{res}}$ | $\sim t_{\text{res}}$ |
|---|---|---|---|
| IN16B | 6.27 Å | 0.75 µeV | $10^{-9}$ s |
| IN13 | 2.23 Å | 8 µeV | $10^{-10}$ s |
| IN5 | 8.0 Å | 0.015 m eV | $10^{-10}$ s |
| IN5 | 5.0 Å | 0.10 m eV | $10^{-11}$ s |
| IN6 | 5.1 Å | 0.070 m eV | $10^{-11}$ s |

Table 4.1: Instrument energy resolution of the elastic intensity and the corresponding time resolution for the different settings and instruments used in this work.

This ends the chapter on the main experimental techniques used in this work. From the framework provided by the introduction to the experimental techniques in this chapter and the research field in Ch. 2 and 3, we will in the rest of the thesis present the experimental work, which has been carried out.

# Chapter 5

# Elastic models

One class of models which was introduced in Ch. 2 that connects fast and slow dynamics and tries to encompass the phenomena of the viscous slowing down as the glass transition is approached is the elastic models. In the view of the potential energy landscape, the elastic models describe a flow event, a molecular rearrangement as barrier transition at short timescales. Because the barrier transition takes place on short timescales, it is governed by the properties of a liquid where it appears as a solid. The transitions themselves are rare in the viscous liquid leading to a slow relaxation. One example of an elastic model is the shoving model.

We test the shoving model for three different van der Waals liquids without pronounced secondary relaxations. If the model is valid, we should find agreement between assumptions and experimental data at least in the simplest case. The aim is not to show if the shoving model is true in all cases, but we want to test if it holds at least in the simplest situation. This is a necessary, but not sufficient test of the model. Most of the work in this chapter is published in [71], here is included one more sample. We use the vibrational mean-squared displacement measured on nanosecond timescale from neutron spectroscopy, the mechanical shear modulus, and the alpha relaxation time in the viscous liquid found from shear mechanics. First will follow an introduction to the shoving model and its predictions. We will then present the experimental data from neutron scattering and shear mechanics used to test an underlying assumption for two versions of the shoving model and our interpretation thereof. Finally, we test the shoving model and end this chapter with a summarising discussion.

## 5.1 The shoving model

Elastic models provide a connection between fast and slow dynamics, a connection that spans more than ten orders of magnitude close to the glass transition where the alpha relaxation slows down dramatically. If we stay in the view of the energy barrier landscape that was introduced in Ch. 2, the basic idea of elastic models is that a molecular rearrangement takes place on very short timescales by barrier transition. The molecular rearrangement can be thought of as a flow event (Fig. 5.1). The relaxation caused by molecular rearrangements is slow because the energy barrier

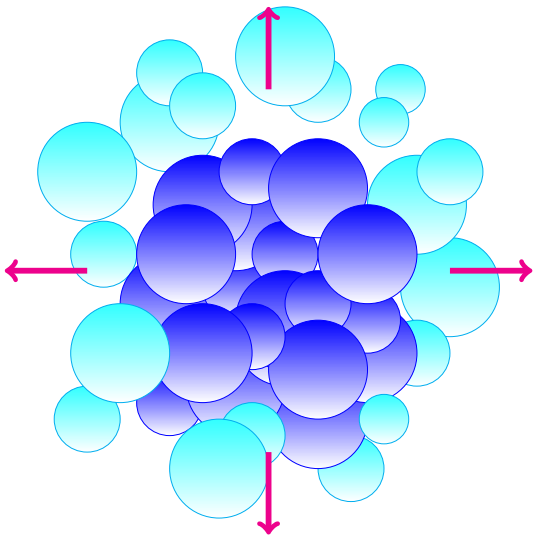

Figure 5.1: In elastic models, the idea is that fast sudden rearrangements of molecules cause the relaxation, which is slow because the energy barrier for making this rearrangement is high, even if the rearrangements themselves are fast.

is high, although the transitions themselves are fast processes. The idea is that the height of the energy barrier can be determined from liquid properties probed on very short timescales thereby connecting fast and slow dynamics.

One particular version of elastic models is the shoving model [50, 74]. In this model, the activation energy for energy barrier transition is identified as the work done shoving aside the surrounding liquid. It is assumed that the activation energy is mainly elastic energy found in the surroundings of the flow event, and that this energy is mainly shear elastic energy, i.e. there is no density change associated with the expansion. Due to the fast rearrangement, which is a basic assumption of elastic models, the surrounding liquid will behave as an isotropic solid during this spherical expansion in some local region. This can be modelled by the two fundamental elastic constants that are present in an isotropic solid, the shear and the bulk moduli, $G$ and $K$, respectively, through the transverse and longitudinal phonons. In an isotropic solid, each wavevector has three degrees of freedom for phonons, two transverse and one longitudinal. The relevant longitudinal modulus $M$ is defined as $M = K + (4/3)G$, while the transverse modulus is simply the shear modulus. Averaging over the two types of phonons, it can be shown that the temperature dependence of the instantaneous shear modulus $G_\infty$, i.e. the plateau value of $G$ probed on short time scales, constitutes more than 92 % of the total temperature dependence of the elastic energy, regardless of how large the bulk modulus is compared with the shear modulus [49]. Under the assumption that the work done is shear energy, the activation energy can be found from the characteristic volume given by $V_c$, which is assumed to be constant in temperature, and from the short-time elastic property, $G_\infty$

$$\Delta E(T) = V_c G_\infty(T). \tag{5.1}$$

Inserting this into the expression for the relaxation time (Eq. 2.1), we arrive at the

new expression for $\tau_\alpha$:

$$\tau_\alpha(T) = \tau_0 \exp\left(\frac{V_c G_\infty(T)}{k_\mathrm{B} T}\right). \tag{5.2}$$

The shoving model predicts that the logarithm of the relaxation time is linearly dependent on $G_\infty(T)/T$. We expect the shoving model to work at least in the range of the dynamics, where we have separation of timescales (Fig. 2.4), i.e. the hopping regime or the viscous liquid.

By normalising to the glass transition, $\tau_g = 100\,\mathrm{s}$, and setting the prefactor to a microscopic time $\tau_0 = 10^{-14}\,\mathrm{s}$, we arrive at the shoving-model prediction

$$\begin{aligned}\log_{10}\tau_\alpha(T) &= (\log_{10}\tau_g - \log_{10}\tau_0)\frac{G_\infty(T)T_g}{G_\infty(T_g)T} + \log_{10}\tau_0 \\ &= 16\frac{G_\infty(T)T_g}{G_\infty(T_g)T} - 14.\end{aligned} \tag{5.3}$$

which gives rise to a shoving plot [74]; a way of testing the shoving model without any free parameters by direct comparison of normalised data to the shoving model prediction.

In the shoving model, the viscosity or the alpha relaxation time is determined by the rate of hopping between local energy minima, where the minima are positions of equilibrium. The relaxation time was determined from the short-time elastic properties under the assumption that a viscous liquid behaves like a solid on short timescales. In the harmonic approximation, the short-time vibrations can also be viewed as vibrational modes taking place around energy minima, resulting in a Gaussian statistical-mechanical probability distribution $\propto \exp(-a^2/\langle u^2\rangle(T))$ , where $\langle u^2\rangle(T)$ is the vibrational mean-squared thermal average around a minimum, where the softness of the potential determines the mean-squared displacement; a softer potential means larger vibrations and a smaller energy barrier. By averaging over the longitudinal and transverse phonons in the harmonically modelled vibrations, the mean-squared displacement is connected to the shear and bulk modulus

$$\langle u^2\rangle(T) \propto T\left(\frac{2}{G_\infty(T)} + \frac{1}{M_\infty(T)}\right). \tag{5.4}$$

Again, we assume that the relevant modulus, in terms of temperature dependence, is the shear modulus, we end with the proportionality,

$$\langle u^2\rangle(T) \propto \frac{T}{G_\infty(T)}. \tag{5.5}$$

Inserting this into the expression for activation energy, one finds

$$\Delta E(T) = k_\mathrm{B} T \frac{a^2}{\langle u^2\rangle(T)}, \tag{5.6}$$

which leads to the following expression for the relaxation time:

$$\tau_\alpha(T) = \tau_0 \exp\left(\frac{a^2}{\langle u^2\rangle(T)}\right). \tag{5.7}$$

Here the temperature dependence of the relaxation time is governed by the temperature dependence of the mean-squared displacement, thus, resulting in a different version of the shoving model, which can also be tested directly in a shoving plot.

The shoving model implies a causality between the fast and the slow dynamics, namely that the slow relaxation is controlled by the fast dynamics probed either from the short-time elastic properties or the mean-squared displacement. The different expressions for activation energy provide following proportionality:

$$\frac{\Delta E(T)}{k_{\mathrm{B}}T} \propto \frac{a^3 G_\infty(T)}{k_{\mathrm{B}}T} \propto \frac{a^2}{\langle u^2 \rangle(T)}, \tag{5.8}$$

Experimentally, we can test the proportionality between the temperature dependence of the short-time elastic modulus scaled with temperature and the mean-squared displacement, an underlying assumption for the shoving model. This is presented in Sec. 5.4.

### 5.1.1 Simple liquids

In the rest of this chapter, the shoving model and the underlying assumption of harmonic approximation will be tested on three different liquids with different fragility. The liquids studied are what we refer to as simple liquids, in this work defined as liquids without directional bonding, with no beta relaxations to complicate the relaxation spectrum, but merely excess wings. The liquids have a high-degree of time-temperature superposition (TTS), i.e. the shape of the spectrum does not change with temperature, only the characteristic time as a function of temperature changes.

The three van der Waals bonded liquids are isopropyl benzene (cumene), 5-polyphenyl ether (PPE) and propylene carbonate (PC) with fragilities $m \approx 70$, 80 and 90, respectively, determined from their relaxation time from the shear mechanics in this work, and in agreement with literature values for cumene and PPE, e.g. [14, 76], respectively. For PC, the fragility has been found to be $m \approx 100$ from dielectric spectroscopy reported in [22], while a fragility of $m \approx 80$ was reported in [32], although this was evaluated at $\tau_\alpha = 10\,\mathrm{s}$, which will give a lower value of the fragility. The high-degree of TTS is shown in Fig. 5.2.

## 5.2 Shear mechanics

The shear moduli for the three samples were determined from a piezo-ceramic shear transducer in the frequency range $10^{-2}$ to $10^4$ Hz, where an electric field probes the mechanical response in a viscous liquid [34]. The response function is complex and the relaxation time of a liquid can be found from the maximum of the loss peak in the imaginary part, similar to dielectric measurements. For some liquids, the glass transition temperature defined as $\tau_\alpha = 100\,\mathrm{s}$ varies a couple of Kelvin between shear mechanics and dielectric spectroscopy. The glass transition temperatures reported in this chapter are from shear mechanics. The shear mechanics data as a function of frequency is presented in Fig. 5.3 for the three samples at different temperatures.

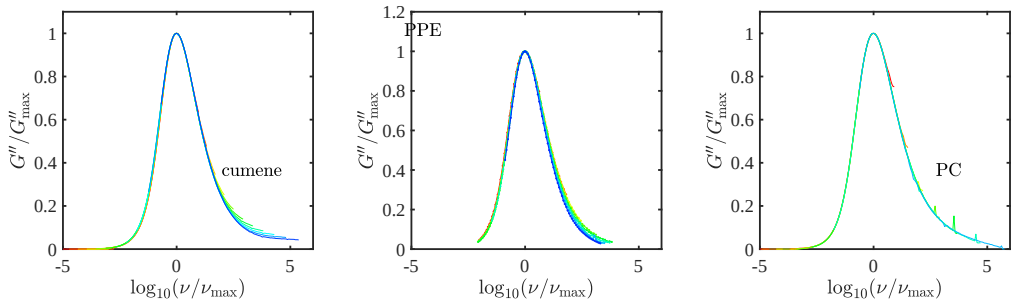


Figure 5.2: Time-temperature superposition for the three samples used in this chapter to illustrate the simple behaviour for cumene ($m \approx 70$), PPE ($m \approx 80$) and PC ($m \approx 90$). The shape of the shear mechanics spectra is practically the same for all temperatures for all three samples. Only a small difference is visible at the excess wing for cumene and PPE.

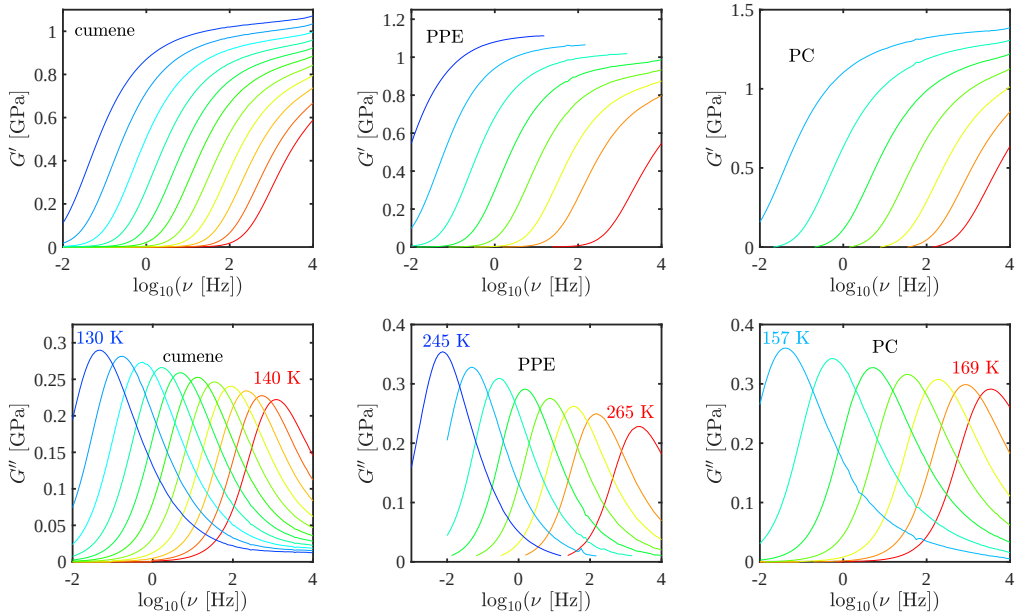


Figure 5.3: Real (top) and imaginary (bottom) part of the shear modulus as a function of frequency plotted for the temperatures measured. Cumene in steps of 1 K from 130 − 140 K. PPE measurements are from [76] in steps of 2.5 K from 245 − 260 K and at 265 K. PC measurements are from [59] in steps of 2 K from 157 − 169 K. Cumene and PC data have not been cut off at high freqencies, and a small tendency is osberved towards a bending in the real part of the shear moduli, most pronounced in the low-temperature cumene data.

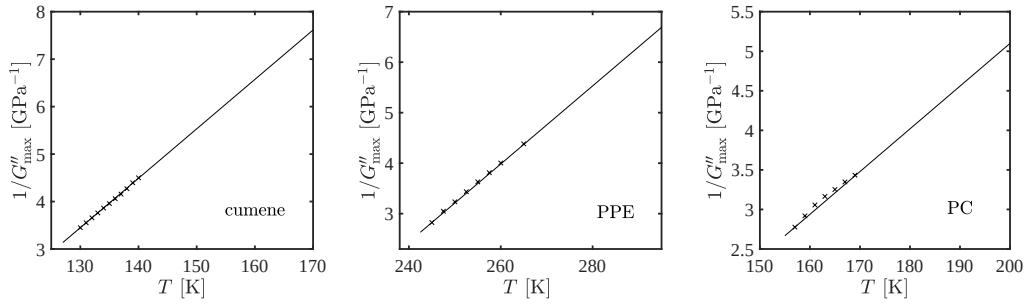


Figure 5.4: Extrapolation in $G''_{\max}$ accroding to Eq. 5.9 from [13] into the entire temperature range in the liquid for which the mean-squared displacement has been measured.

In shear measurements, the real part has a low plateau in the low-frequency range, when the liquid is able to follow the shearing, and reaches a plateau in the high-frequency range which is the elastic modulus, or the instantaneous shear modulus, $G_\infty$. The instantaneous shear modulus is the term needed for testing the shoving model (Eq. 5.2). The exact plateau value is experimentally difficult to determine because of the frequency window of the shear mechanics accessible with the piezoceramic shear transducer. Though it is possible to determine the mechanical moduli in the mega- and gigahertz range from sound waves investigated with Brillouin scattering [88, 77], this is out of the scope for this work. For testing the shoving model, we need the temperature dependence of the instantaneous shear modulus, and we will therefore, instead of the instantaneous shear modulus, use the maximum of the loss peak which is well defined. The real and the imaginary part are related via the Kramer-Kronig's relation, and will therefore have the same temperature dependence. Because we are not interested in the absolute value, but the temperature dependence of the shear modulus, we can therefore substitute $G_\infty(T)$ with $G''_{\max}(T)$.

For testing the underlying assumption of the shoving mode, the relation between the shear modulus and the mean-squared displacement, we use an extrapolation from Barlow et al. [13] to extend the shear temperature range into higher temperatures for comparing with mean-squared displacement data in a larger temperature interval:

$$\frac{1}{G_\infty} = \frac{1}{G_0} + C(T - T_0), \tag{5.9}$$

where $C$ is a constant, and where we again substitute $G''_{\max}(T)$ for $G_\infty(T)$. The extrapolation is shown in Fig. 5.4. We use the value of $G''_{\max}$ and the alpha relaxation found from the peak position in frequency in testing the shoving model, and the extrapolated values of $G''_{\max}$ for testing the connection between the shear modulus and the mean-squared displacement.

## 5.3 Mean-squared displacement

The mean-squared displacement of a sample can be found from the $Q$-dependence of the incoherent elastic neutron scattering intensity as a function of temperature

using the Gaussian approximation (Eq. 4.64). The energy resolution of the neutron scattering instrument determines the timescale of the mean-squared displacement (MSD). The MSD data presented in this chapter are from IN16B, i.e. nanosecond timescale.

The elastic and inelastic fixed window scans (EFWS/IFWS) from IN16B described in Sec. 4.4 can provide information on both relaxation and mean-squared displacement upon a scan in temperature. Since hydrogen makes up $\sim$ 90 % of the signal from the studied glass-formers, the detected neutron is to a good approximation incoherent and therefore provides information on self-motion. From the $Q$-dependence of the incoherent intensity of the elastic scans, we can determine the mean-squared displacement at some timescale. The energy resolution of the instrument determines the timescale of the mean-squared displacement. At IN16B, an energy resolution of $\Delta E \approx 1\,\mu\text{eV}$ gives access to nanosecond dynamic timescale. The coarser the instrumental energy resolution, the faster dynamics one can access (Table 4.1). If the dynamic timescale of the elastic intensity is $t'$, then for elastic scans, $I(Q, t')$ will essentially be time independent and only dependent on the wavevector or scattering vector, $Q$, and the temperature $T$ of the sample. Thus, for this purpose we introduce the incoherent intermediate scattering function $I(Q, T)$. The mean-squared displacement, $\langle u^2 \rangle$, can then be found from the $Q$-dependence of the intensity as a function of temperature using the Gaussian approximation in Eq. 4.64. The Gaussian approximation has been shown to be valid both on short timescales where particles are considered free, and on long timescales when the motion is governed by diffusion [16, 126, 149, 153].

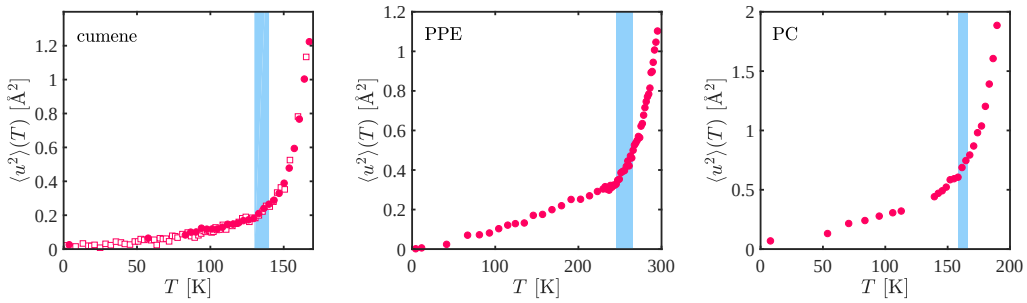


Figure 5.5: Mean-squared displacement as a function of temperature for the three samples. The blue shaded area is the temperature interval in which the shear moduli were measured (Fig. 5.3).

The mean-squared displacement is found by fitting a straight line to the logarithm of the elastic intensity versus $Q^2$ for each temperature according to Eq. 4.64. For each temperature, the data is normalised to the lowest temperature data, thus removing any zero point motion. Normalisation to low-temperature data will also account for any detector deficiency. For the three liquids studied here, the mean-squared displacement as a function of temperature is shown in Fig. 5.5.

The glass transition is observed as a kink in the mean-squared displacement at $T_{g,\text{cumene}} = 127\,\text{K}$, $T_{g,\text{PPE}} = 243\,\text{K}$ and $T_{g,\text{PC}} = 155\,\text{K}$. These glass transition temperatures are obtained from shear modulus data for $\tau_\alpha \approx 100\,\text{s}$. The glass transition

temperature can usually be determined from the mean-square displacement within a couple of Kelvin. The blue shaded area in each MSD plot illustrates the temperature range for which shear mechanics was measured for the three samples (Fig. 5.3). In this narrow range in the MSD, we observed the alpha relaxation move four-five orders of magnitude in the imaginary part of the shear moduli.

## 5.4 Testing the models: $G_\infty$ and MSD

First we will test an underlying assumption for the short-time properties, namely the proportionality defined in Eq. 5.8 between the elastic constants in the kilohertz range and the mean-squared displacement measured on nanosecond timescales. The timescales are separated with five orders of magnitude. In Fig. 5.6, the temperature dependence of the mean-squared displacement is plotted versus the inverse of the maximum of the loss peak scaled with temperature. We use the relation from Eq. 5.9 to extrapolate the shear temperature range in the viscous liquid into the entire temperature range of the mean-squared displacement.

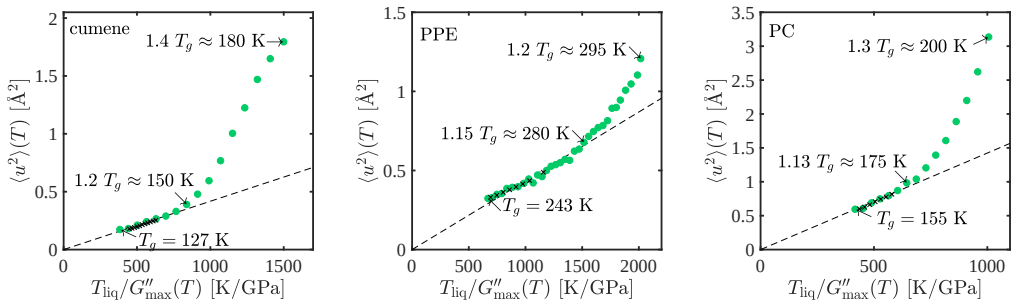


Figure 5.6: Testing the proportionality from Eq. 5.8, which is shown to hold up to some value. The black crosses refer to the shear temperature range. The green circles refer to the MSD temperature range.

We observe the same trend for all three samples: from the glass transition up to $1.13 - 1.2\ T_g$ we observe the proportionality expected from Eq. 5.8. The black dashed line is a one parameter fit through the origin to the data that clearly falls on a straight line. Above the temperature where the data separates from the dashed line, the mean-squared displacement is observed to increase faster with temperature than the corresponding decrease in the shear moduli.

We now take advantage of having acquired both elastic and inelastic fixed window scans on cooling at IN16B, the principle was illustrated in Fig. 4.4. The fixed window scans from IN16B (Fig. 5.7) offer an interpretation of the faster increasing mean-squared displacement, which is observed as the proportionality in Fig. 5.6 breaks down. We observe from the inelastic fixed window scan, the alpha relaxation entering the dynamic window of IN16B. We therefore interpret the stronger temperature dependence of the mean-squared displacement above a threshold temperature as when the alpha relaxation enters the neutron instrument window. In Fig. 5.7, a black dashed line is shown at the temperature where the proportionality in Fig. 5.6 breaks down. In agreement with what was proposed for protein dynamics by Capaccioli et

al. [27], we define a dynamic transition, $T_d$, for when the alpha relaxation time and the instrument dynamic window intersect.

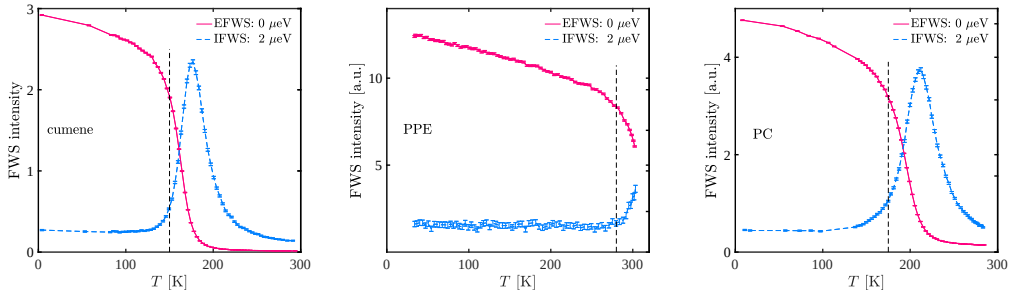


Figure 5.7: Fixed-window scan from IN16B offering an interpretation of the mean-squared displacement.

The glass transition and the dynamic transition are illustrated on a zoom of the mean-squared displacement (Fig. 5.8), where we show dashed line along the three different suggested types of behaviour. The two transitions are seen as changes in the slopes of the mean-squared displacement, where the black lines intersect. In this interpretation of the mean-squared displacement, the first change in slope at the glass transition is due to a stronger temperature dependence of the modulus going from the glass into the liquid state; it is not due to changes in the mechanism of nanosecond dynamics, which is still vibrational. This interpretation of the mean-squared displacement is supported by the IFWS scans. In the temperature range just above the glass transition where the linear relation applies, the temperature dependence of the mean-squared displacement can be predicted from the high-frequency modulus. The second change of slope in the mean-squared displacement comes from the relaxation when it enters the instrument window. The higher the fragility, the closer to $T_g$ we expect the alpha relaxation to enter the instrument window. We can define an index, $T_g/T_d$, which should then be correlated with fragility. For cumene, PPE and PC this index is 0.85, 0.87 and 0.89, respectively. These are quite small changes in the percent range, and their fragilities are also rather close, but the trend is as we would expect.

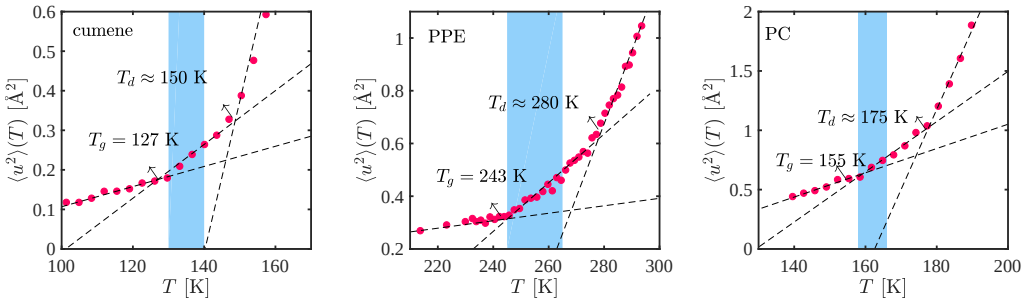


Figure 5.8: Zoom of the mean-squared displacement. Three lines have been fitted to the data in three regions: in the glass, between $T_g$ and $T_d$, and above $T_d$.

## 5.5 Testing the shoving model

To test the shoving model, we construct a shoving plot with the shoving prediction (Eq. 5.3), which under the assumption $G_\infty(T) \propto G''_{\max}(T)$ becomes:

$$\log_{10}\tau(T) = 16\frac{G''_{\max}(T)T_g}{G''_{\max}(T_g)T} - 14 \tag{5.10}$$

and in the mean-squared displacement version:

$$\log_{10}\tau(T) = 16\frac{\langle u^2\rangle_g}{\langle u^2\rangle(T)} - 14. \tag{5.11}$$

A shoving plot for the three samples are shown in Fig. 5.9. The black line is the prediction from the shoving model with a typical prefactor set to a microscopic timescale, $\tau_0 = 10^{-14}$ s. The circles (∘) show a typical Angell fragility plot with $T_g/T$ versus the alpha relaxation time. The squares (□) are the mean-squared displacement scaled to the glass transition value. The mean-sqaured displacement data were interpolated between data points to find the mean-squared displacement at the exact temperatures of the shear mechanics, where the relaxation time was found. The triangles (△) are the normalised shear loss peak maximum scaled with temperature.

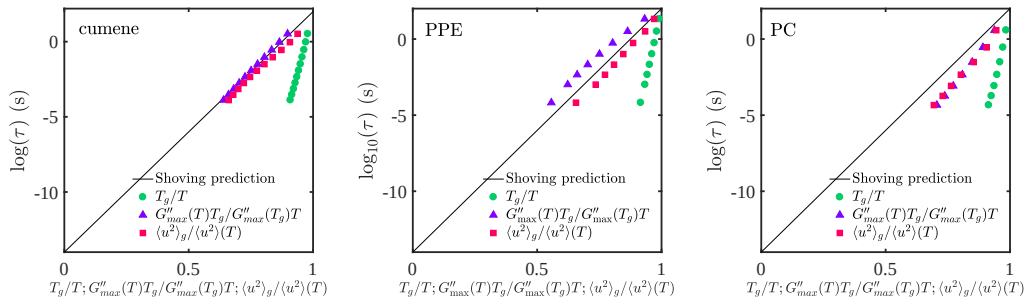


Figure 5.9: Shoving plot for the three samples. Circles (∘) are the typical Angell fragility plot with $T_g/T$ versus alpha relaxation time. Squares (□) are the mean-squared displacement scaled to the glass transition value. Triangles (△) are the normalised shear loss peak maximum.

The three samples follow the same general trend, with the experimental data lying quite close to the shoving prediction, in particular the cumene data, whereas the data from PPE and PC are observed to lie on either side of the prediction, but following the same trend. From Fig. 5.9, we conclude that the shoving model works well for the three simple, van der Waals liquids, and in particular, that the two versions of the shoving model in this dynamic range are in agreement. One version tested the connection between the mean-squared displacement measured on nanosecond timescales and the alpha relaxation, and one connected the short-time elastic modulus measured in the kilohertz range with the alpha relaxation.

## 5.6 Summarising discussion

The elastic models, here represented by the shoving model and the relation between the MSD and the instantaneous shear modulus, work well in describing the three simple systems investigated in this chapter. We use the IFWS as a way of interpreting the mean-squared displacement data and the stronger temperature dependence of the mean-squared displacement above what we refer to as the dynamic transition $T_d$ compared to the corresponding decrease in the shear modulus. The dynamic transition is in this view defined as when the alpha relaxation time intersect with the timescale of the instrument given by the neutron instrument resolution, leaving (at least) three regimes of the mean-squared displacement with different dynamics: the glassy state, the state between the glass transition and the dynamic transition where the elastic modulus becomes more temperature dependent moving out of the glass, and that above $T_d$, where the alpha relaxation is in the neutron window. Just above the glass transition, the temperature dependence of the mean-squared displacement can be predicted from the temperature dependence of the high-frequency modulus.

Mean-squared displacement data could be collected from other neutron instruments with coarser energy resolution; this would allow studying the mean-squared displacement on faster timescales in an attempt to separate contributions to the mean-squared displacement from vibrations and relaxations [57, 25, 113]. We have in this study utilised the IFWS in an attempt to interpret different contributions to the mean-squared displacement on nanosecond timescale. Moving to an instrument with an elastic resolution that corresponds to a shorter timescale, should in principle make the relation between the mean-squared displacement and the modulus hold to higher temperatures.

A natural next step in testing the shoving model is to include more complex systems with for example large beta relaxation or nanoscale structure, and test if and when the model will break down. Buchenau [26] suggested that elastic models cannot account for the full temperature-dependence of the activation energy for all liquids, included in this study are samples with very different fragility and behaviour.

One can imagine systems that have for example a large beta relaxation will show a discrepancy between the elastic modulus on millisecond timescale and the temperature-dependence of the mean-squared displacement on nanosecond timescales or even faster. It is also possible that the relaxational contribution on nanosecond timescales to the mean-squared displacement is larger for liquids with a more complex behaviour. If the temperature-dependence of a fast relaxation has a weaker temperature dependence than the alpha relaxation, this could cause a weaker temperature-dependence of the mean-squared displacement in comparison with that predicted from Eq. 5.8, and will therefore no longer be proportional to the activation energy.

Finally, the shoving model should also be tested under high-pressure. Especially here, one can suspect that the elastic models will only hold for simple liquids; that the relaxational map for more complex liquids will have different temperature and pressure dependencies and that they will no longer follow the predictions of the elastic models.

A lot of theoretical work has proposed that the alpha relaxation time is controlled by a growing length scale. A growing length scale on slowing down of the alpha

relaxation has been shown to exist, e.g. in [20, 4]. However, in recent theoretical work, the shoving model and related elastic models have gained ground, e.g. [165, 167, 169, 91, 111], and suggest that perhaps it is worth looking at local dynamics rather than structure. Based on the experimental work presented in this chapter, we will join those of the opinion that dynamics is the relevant place to look to gain more insight into what governs the viscous slowing down.

# Chapter 6

# High-pressure dielectric and neutron spectroscopy

This chapter will contain details on the design of the sample cell developed for doing simultaneous dielectric and neutron spectroscopy under high pressure. The work has been carried out as a three-year Long-Term Proposal (LTP-6-7) at the Institut Laue-Langevin (ILL) and is a collaboration between Roskilde University, the Service of Advanced Neutron Environment at the ILL, Simone Capaccioli at the University of Pisa and Marian Paluch from the University of Silesia. The sample design was reported in [140]. As we have seen in previous chapters, dynamics in glass-forming liquids covers a large range of timescales from atomic vibrations on picosecond timescales to the alpha relaxation time close the glass transition approaching hundreds of seconds. An understanding of the dynamic behaviour in glass-forming liquids must therefore encompass how the dynamics are related over many orders of magnitude in timescales, and include both temperature and pressure as variables. This leaves an enormous playground for an experimentalist to explore.

The large dynamic range and all the different contributions to the dynamics cannot be covered with just one experimental technique, and we rely on combining and comparing different techniques. The larger the area one wants to (un)cover in terms of temperature, pressure and timescales, the higher is the demand for combining different experimental techniques. In the previous chapter (Ch. 5), the alpha relaxation was shown to change with orders of magnitude within just a few percent of the glass transition temperature. Because of the sensitivity of the dynamics, it is important to know the state of the sample with high accuracy.

In this chapter, we will present the design of the different components of the high-pressure cell for doing combined dielectric and neutron spectroscopy, the two experimental techniques discussed in Ch. 4, and argue why this has significantly improved the way a high-pressure neutron beamtime can be spent and improved the kind of information one can expect to obtain. First, we will try to persuade the reader that combining these two techniques is a good idea in the first place.

## 6.1 Why this is a good idea

Both the neutron and the dielectric community have strong traditions in studying dynamics of glass-forming liquid. Neutron scattering because the self-motion of molecules can be probed directly from the dynamic structure factor, $S(Q, \omega)$, dielectrics because of the fast and easily accessible data that are relatively simple to understand and because a basic dielectric setup can readily and at quite low cost be set up in a lab.

A considerable amount of papers have shown the benefits of comparing dielectric and neutron spectroscopy in the analysis and interpretation of dynamic data, e.g. [7, 9, 41, 113, 141, 150]. A neutron diffraction cell for doing simultaneous dielectric measurements for crystallisation studies where developed by Jiménez-Ruiz et al. [84, 142] to ensure that the measurements were done at exactly the same sample conditions, a critical issue in kinetic studies such as crystallisation.

In the dielectric as well as the neutron community, pressure studies have become more popular in recent years and many things have been learned from pressure experiments from both techniques. In Ch. 3, we discussed how pressure was introduced as an additional variable to temperature to separate thermal and density contributions to the dynamics, and how this has pushed forward experiments and theories to gain further insight into the behaviour of dynamics of glass-forming liquids.

From an experimental design point of view, the two techniques complement each other. The optimal geometry for both dielectric and neutron spectroscopy coincide: in neutron scattering a large sample area will give a strong signal and a small sample thickness is desired in order to avoid multiple scattering, while in dielectric spectroscopy a large area and a small sample thickness will provide the strongest dielectric signal (Ch. 4). Neutron spectroscopy is an excellent technique for studying the fast dynamics from self-correlations on pico- to nanosecond timescales, while dielectrics provides fast (within minutes) and precise measurements in the range from microseconds to hundred of seconds via dipole-dipole correlations. Although, it is different types of dynamics that are probed with the two techniques, as we will see, they supplement each other well.

The two techniques do not overlap in timescales, but they are not as far separated as one might think. This is illustrated in Fig. 6.1 for different dynamic scenarios for the liquid PPE (Ch. 7.1) at $T = 295\,\mathrm{K}$ and at $T_g = 245\,\mathrm{K}$. We sketch the two corresponding states of the intermediate scattering function of simple dynamic behaviour, in the sense that was defined in Sec. 2.2. The hatched areas correspond roughly to the timescales available with the neutron spectroscopy instruments IN5 and IN16B on pico- and nanosecond timescales, respectively. By changing the incoming wavelength on IN5, the gap in timescales between IN5 and IN16B can be closed, although this will also change the $Q$-range (Ch. 4.4). The blue shaded area represents the timescales accessible with dielectrics. The data shown from IN5 and the dielectrics are taken simultaneously in the new combined cell. The nanosecond dynamics data presented in this sketch are older spectra from IN16 with the same energy resolution as IN16B. The IN16 spectra serve only illustrative purposes and are only used in this sketch, otherwise we refer to IN16B.

In the upper part of the illustration, we show spectra in the scenario where

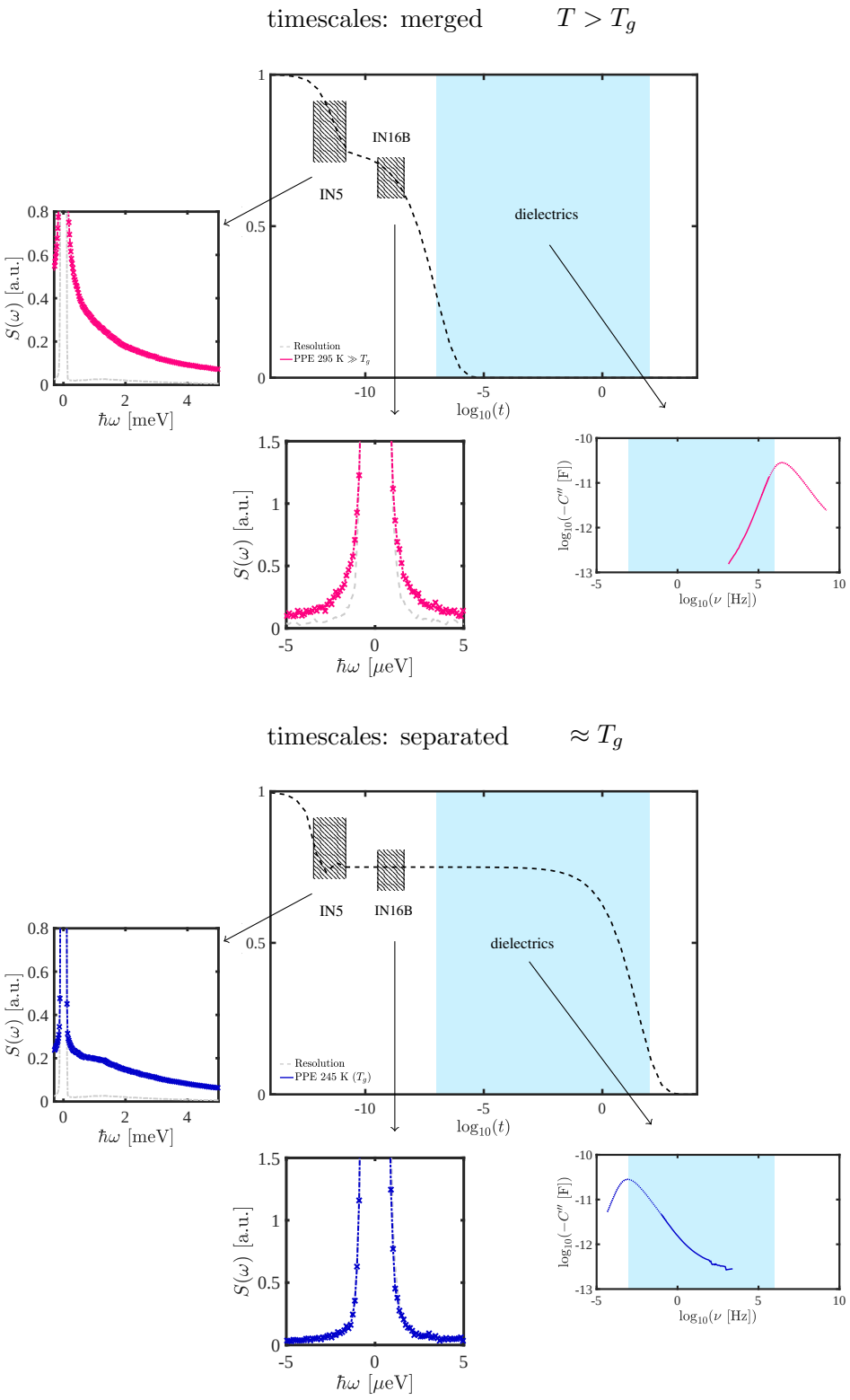


Figure 6.1: Sketch of intermediate scattering function in two different dynamic scenarios illustrated with data on PPE. The hatched areas are the approximate regions in time accessible with IN5/6 and IN16B, picosecond and nanosecond, respectively. The shaded blue region is the time and frequency range accessible with dielectric spectroscopy. Top: relaxation dominates the signal in all three spectrometeres. Bottom: Close to $T_g$, the alpha relaxation is in the dielectric window, there is no broadening observed at IN16, while fast relaxation and vibrations are visible in the spectrum from IN5. Resolution is shown as grey, dashed lines.

relaxation dominates in all three spectrometers. The alpha relaxation stretches out over many orders of magnitude in dynamics. In the dielectrics, we use time-temperature superposition to estimate the maximum in the loss peak and from that find the relaxation time, $\tau_\alpha = 1/(2\pi\nu_{\max})$, which is roughly $\tau_\alpha \approx 10^{-7}$ s. On IN16 and in particular on IN5, we observe a broadening compared to the grey, dashed resolution, indicating relaxation.

In the lower part, we have moved to the glass transition. In the dielectrics, the alpha relaxation is now seen at the side of the frequency window. We estimate the relaxation time from the dielectrics again using time-temperature superposition and find it to be roughly $\tau_\alpha \approx 10^2$ s. Moving to nanosecond timescales on IN16, the sample signal and the resolution overlaps completely, and there is no broadening of the signal. This was also observed at IN16B from the FWS for the same sample at the glass transition (Fig. 5.7). We now proceed to picosecond dynamics on IN5, and we observe a clear signal compared to the resolution. Here, we have contributions from fast relaxations with a broadening around the elastic peak and a vibrational contribution at higher energy transfer.

The dynamic range where it is possible to acquire useful information with dielectrics can be extended further to even less viscous states, in particular for systems with DC-conductivity, or deeper into the glass, for studies of for example secondary relaxations or ageing processes.

## 6.2 The cell and setup

A drawing of the combined cell and the different components are shown in Fig. 6.2. The basic principle is to place a capacitor inside a hollow cylinder neutron high-pressure cell with a plug at one end, which can be used up to a maximum pressure of 500 MPa connecting the capacitor to wires outside the cell for measuring the capacitance inside the neutron beam, and the application of pressure using liquid compression from the other end. Many things need to be taken into consideration to ensure this is possible at all and to optimise the sample signal in both measuring techniques. In this section, we will present the different components of the cell with reasons and choices for the design, starting with the outer body of the cell, then the capacitor inside the cell, before moving on to the plug and its feedthroughs and finally, the sample stick and how everything is assembled.

### Outer body

The outer body serves as the sample chamber, i.e. the actual sample cell. The outer cell should have a reasonably low background and should be able to withstand high pressure. The design of the outer neutron cell is inspired by that developed by Peters et al. [122] for doing high-pressure studies on liquids in solutions. A cell that we have used before the design of the new combined cell, e.g. for taking the cumene data at IN16B presented in Ch. 7.

The signal that we are investigating from glass-forming liquids is mainly located in an energy band centred around the elastic peak. We are therefore looking for a material that has a low elastic signal both on nanosecond and picosecond timescales,

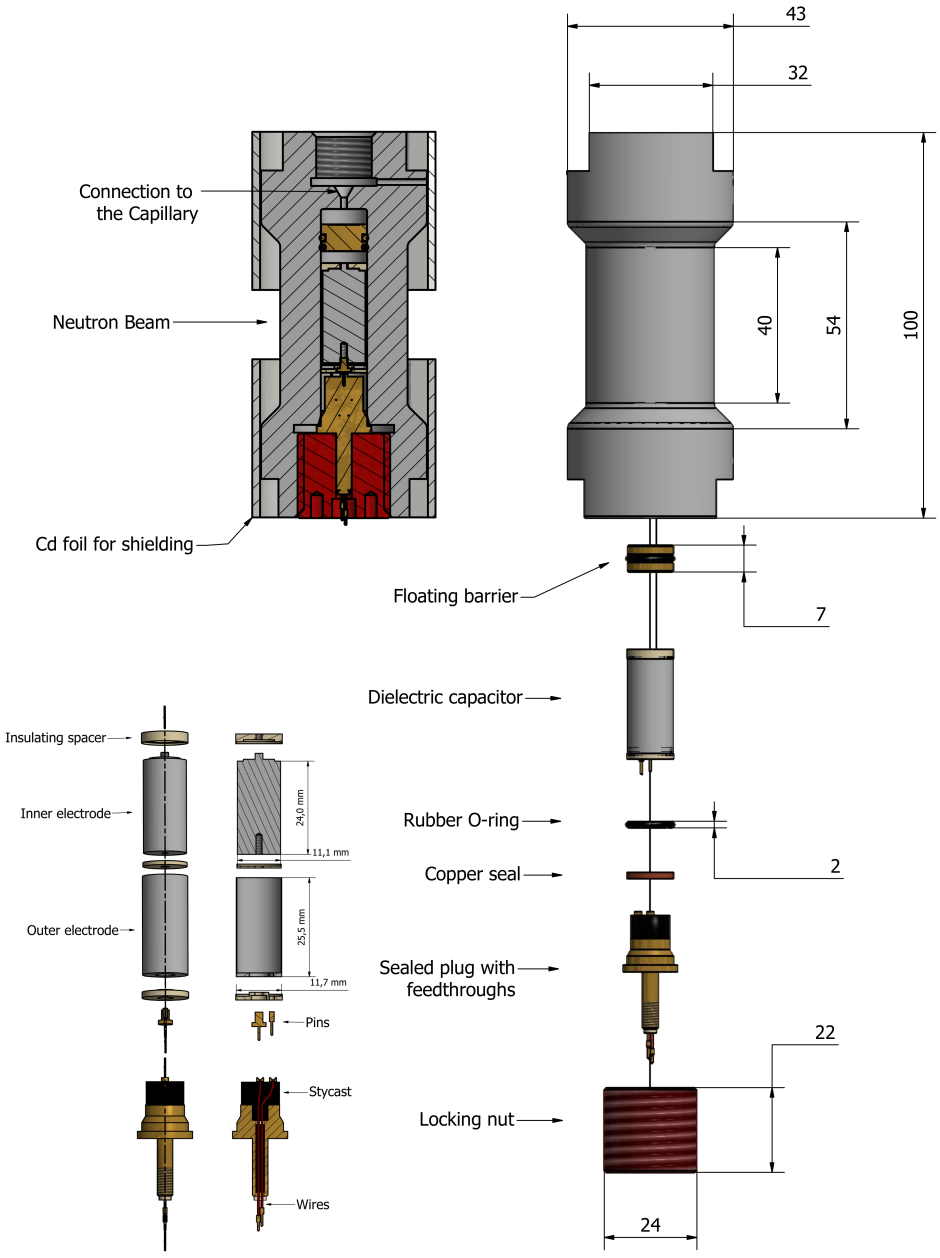


Figure 6.2: Drawing of the high-pressure cell for doing simultaneous dielectric and neutron spectroscopy in exploded and assembled view. See text for details.

and that does not have a large broadening around the elastic peak. This should ensure a large sample-to-noise ratio and easy subtraction of the empty cell. We tested the signal from three different compounds that are well known in high-pressure neutron studies: CuBe commonly used in magnetic studies because it is diamagnetic, TiZr which is often used in diffraction but has a flat incoherent signal, and Al-7049-T6 which is not as strong as the other two materials, but with a large percentage of aluminium which suggests a low neutron attenuation [89]. Data acquired at room temperature from IN6 (picosecond) and IN16B (nanosecond) on the three different materials is presented in Fig. 6.3 and 6.4.

From IN6, we observe distinct phonon signals for CuBe and the aluminium alloy at higher energy transfer, roughly from 10 to 40 meV. If we zoom in on the energy range of particular interest for glass-forming liquids, up to $\sim 10$ meV, we see that the phonons are not pronounced in this energy range and that the elastic peak is well resolved compared to TiZr where a quasi-elastic broadening is observed. The elastic intensity of TiZr is also relatively higher as observed on the log-log scale. The data is also shown relative to the elastic line of vanadium. As we want to resolve the elastic peak and any broadening around the elastic peak, we also studied CuBe and Al-7049-T6 on IN16B where the sample to cell signal in general is weaker and the cell signal more temperature dependent than on the TOF instruments, which increase the importance of the signal from the cell. On IN16B there is no longer phonons in the energy window. We observe a higher neutron transmission for the Al-alloy compared to CuBe, i.e. less signal. Outside the elastic peak at higher energy transfer, we observe less noise from the aluminium alloy. Based on these tests and the fact that the aluminium alloy, Al-7049-T6, has a higher thermal conductivity, Al-7049-T6 was chosen as the material for the outer part of the sample cell. The outer cell body is a hollow cylinder, also referred to as the monobloc. To ensure enough space for the capacitor and a strong sample signal, the inner diameter of the monobloc was set to 12 mm.

The next step is to harden the material for it to withstand elevated pressure. A material has only a finite material strength when exerted to the forces on applied pressure. In a certain pressure range, the material will act as a spring and only deform elastically, this is the area in which we want to be working. Above some threshold pressure called the yield stress, $\sigma_Y$, the deformation of a material will be plastic, i.e. the material will no longer be able to contract back to its initial shape. A way to overcome the pressure limitation of a material is to expose it to 'autofrettage', where pressure above the yield stress limit is applied to the monobloc according to the relation for the maximum pressure:

$$P_{\max} = \frac{2\sigma_Y}{\sqrt{3}} \frac{(K^2 - 1)}{K^2}, \tag{6.1}$$

where $K > 2.2$ and is the ratio between the outer and inner diameter. The yield stress for Al-7049-T6 at 300 K is $\sigma_y = 0.53$ GPa [89] and is strongly dependent on temperature, which also puts an upper limit to the temperature range of the cell, set to 320 K. During the autofrettage process, the material is deliberately overstrained, and the material close to the bore of the monobloc is plastically deformed. The inner plastically deformed part will thus be under compression from the outer part

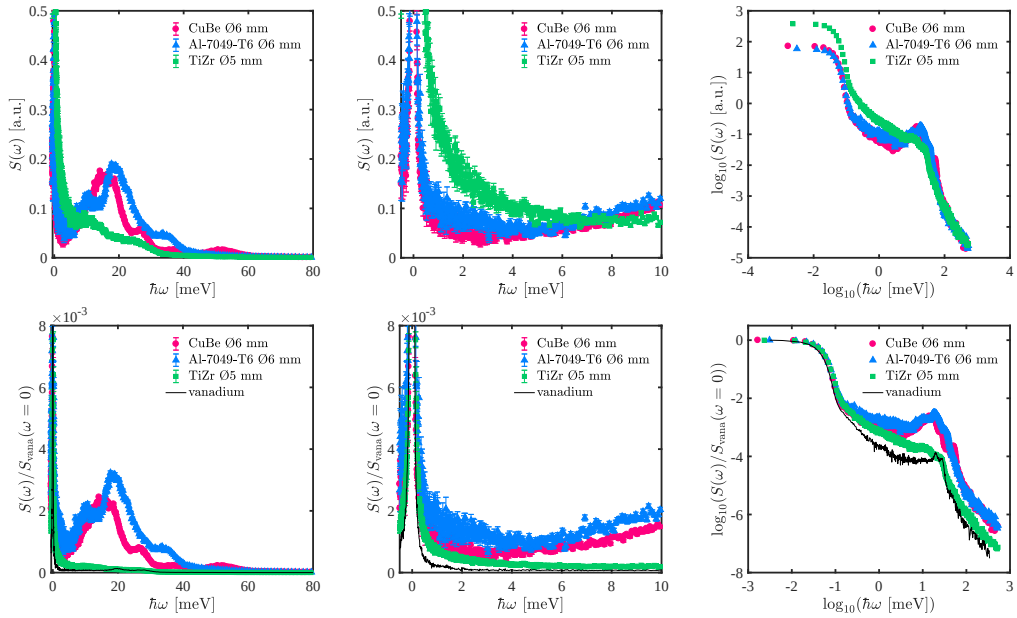


Figure 6.3: Test of the signal of CuBe, Al-7049-T6 and TiZr on IN6 with $\lambda = 5.12\,\text{Å}$ summed over $Q$. Top: data as measured. Bottom: data normalised to vanadium elastic intensity.

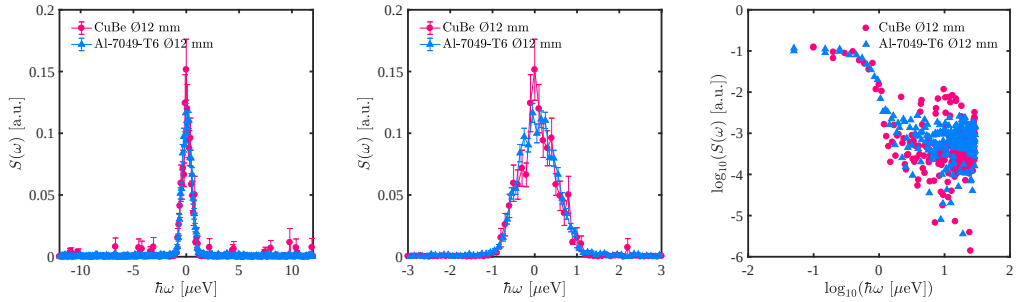


Figure 6.4: Test of the signal of CuBe and Al-7049-T6 on IN16B with $\lambda = 6.27\,\text{Å}$ summed over $Q$.

of the monobloc. The outer diameter of the hollow cell at the beam centre is 33 mm, while the inner diameter is 12 mm, this gives a $P_{\max} \approx 530$ MPa. The cell is first drilled out with an inner diameter of 11.4 mm and then exposed to autofrettage to eliminate effects of plastic deformation of the material, and finally drilled out in the exact, desired 12 mm diameter. This should ensure that the pressure used in the autofrettage process is the new pressure limit with only elastic deformation up to that pressure value.

Given that the yield stress for CuBe is about twice the size of that of Al-7049-T6 and that it has a not so different background signal, it would be interesting to also make a cell in CuBe, to push the pressure limit to higher pressure and see if this would affect the signal, hoping that temperature changes will not be significantly slower. It should be noted, however, that the rest of the pressure equipment at the ILL has an upper limit of 7 MPa so this is really the maximum.

### Capacitor

Now, with the outer body in place, we need an inner capacitor which will serve two purposes, first of all, of course, to measure the capacitance of the sample, but it will also serve as an inset to the monobloc that ensures a sufficiently low sample thickness, in the sub-millimetre range, to have a strong neutron scattering signal with lower risk of multiple scattering. The strength of the measured capacitance is given as a function of the ratio between the area, $A$ and the distance between the two electrodes, $d$:

$$C = \varepsilon\varepsilon_0 \frac{A}{d}, \tag{6.2}$$

where $\varepsilon$ is the permittivity of the sample, and $\varepsilon_0$ is the permittivity of vacuum. This means that a small sample thickness also gives a strong signal in the dielectrics. We use an annular, cylindrical capacitor with an empty capacitance of approximately 50 pF made from aluminium. The cylindrical capacitor is kept electrically isolated with thin PEEK (polyether ether ketone) plates in the top and bottom, separating the outer and inner electrode, and keeping the capacitor electrically isolated from the outer neutron cell. The annular capacitor is 27 mm in height, with a diameter of the inner electrode of 11.1 mm, while the outer electrode has an inner diameter of 11.4 mm and an outer diameter of 11.7 mm. This gives two compartments of sample environment, one between the inner and outer electrode and one between the outer electrode and the outer cell, each with a sample thickness of 0.15 mm.

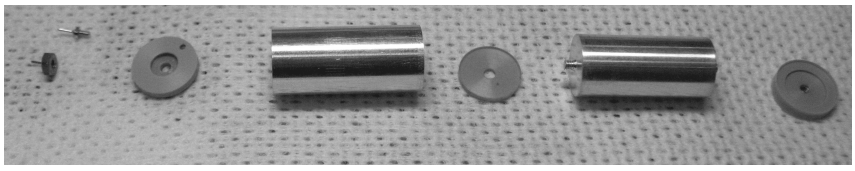

Figure 6.5: Inner and outer aluminium electrodes and insulating PEEK spacers with holes to ensure that the capacitor can be connected to the plug via small brass screws.

A great challenge in the design of the capacitor was how to connect the outer and inner electrode to the plug, while ensuring that they were electrically isolated, but also that it is sufficiently robust for high pressure and easy to work with. The final design, depicted in Fig. 6.2 and 6.5, is a solution where the outer electrode with the PEEK bottom acts as a cup with the inner electrode placed inside, held in place by the PEEK spacers. Holes in the PEEK spacers (Fig. 6.5) allow electric contact to the electrode through small brass screws to the plug. This design is easy to work with and has proven to be able to withstand many, many pressure cycles, in fact all data presented in this work using the new sample cell has been taken using the same capacitor. The exact value of the empty capacitor needed to find the relative permittivity of a sample varies with the exact experimental conditions, but it can easily be determined with great precision before each experiment.

### Plug and feedthrougs

This has been one of the greatest challenges of this cell, to design and make a plug that can withstand pressure up to 500 MPa with electric feedthroughs so that the capacitance of the sample can be measured across the inner and outer electrode from outside the outer cell. This means that it has to offer electric as well as mechanical shielding to the sample environment.

The design of the plug was partially inspired by [106], who developed a high-pressure plug using dental cement for dielectric spectroscopy. The plug designed for this cell is made of brass and filled with the epoxy encapsulant STYCAST ® 2850 FT. A drawing of the plug and a cross-sectional view are shown in Fig. 6.2 and photographs are shown in Fig. 6.6. The wires are fed through a cylinder of brass, and the empty space is filled with stycast, which is a dense paste that is cured into a hard and electrically resistant material.

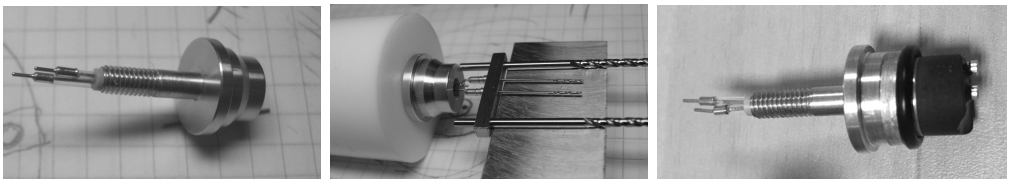

Figure 6.6: Plug before and after casting the stycast.

A rubber o-ring and a copper sealing ring ensure that upon applied pressure, the cell is tight also around the plug. At low pressure, the o-ring will deform thus keeping the sealing tight, and as pressure is increased the sealing ring will take over, deform and prevent the plug from leaking.

The plug is the weak point of the cell, as they have a limited lifetime before they will start leaking. In particular, because there is really no telling whether a plug is approaching the end of its lifetime, or even if its a plug with a short or a long lifetime. In general though, with the current status of the plug production, one plug has been able to withstand numerous pressure cycles on a four-day beamtime in at IN5 without leaking.

### Cell assembly and sample control

Putting everything together, the combined cell is assembled by first filling the capacitor using the capillary force. By placing the capacitor in a few millimetres of sample, the small holes in the insulating PEEK in the bottom of the capacitor will fill the cell. For samples that are relatively viscous at room temperature, heating the sample liquid can speed up the process of filling the cell. A floating barrier or a separator is placed in the outer body, the monobloc, to keep the pressure liquid separated from the sample. The monobloc with the floating barrier inside is then filled with sample, and the capacitor attached to the plug is carefully placed inside and closed with the copper sealing, o-ring and closing nut. There is a sample reservoir between the capacitor and the floating barrier, which ensures that a) pressure is not applied on closing the cell, i.e. the floating barrier can adjust upon closing, and b) that when up to 5000 times atmospheric pressure is applied during the experiment there is as a sample buffer between the floating barrier and the capacitor. When the closing nut is closed, the rubber o-ring will start to give in, while just a little bit of pressure is added to the sample, which is enough to avoid any air bubbles trapped inside the sample volume.

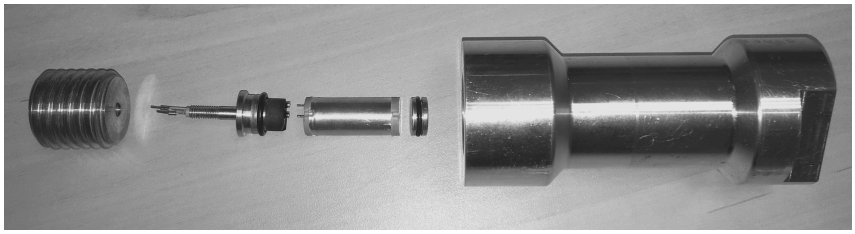

Figure 6.7: The different components of the combined high-pressure dielectric and neutron cell before assembling. The cell is attached to the sample stick from the right, where pressure is applied through the capillary running through the sample stick. The wires from the dielectric setup are attached to the plug at the bottom of the cryostat, this would be on the left here.

Once the cell is filled and closed, it is attached to the sample stick and connected to the dielectric setup. Wires from the sample stick are carefully connected to the plug at the bottom of the sample cell, which goes to the bottom of the cryostat. The connection from the capacitor to the dielectric setup is done via coaxial cables, which are led up through the sample stick and can be connected outside the cryostat with BNC-connectors to the dielectric setup.

For transmitting pressure we use a compression liquid, Fluorinert$^{TM}$, a fluorocarbon with high stability and small neutron signal. The compression liquid is led down to the sample cell from the compressor via a heated capillary inside the sample stick next to the cables for the dielectrics. The thermally isolated and heated capillary makes sure that the pressure liquid does not freeze as it passes the cold point in the orange cryostats, thus preventing blocking of the pressure transmission. The pressure is transmitted onto the sample using the floating barrier that separates the sample from the pressure liquid. The floating barrier is made of brass, and the two liquids are kept isolated using a rubber o-ring. Pressure is controlled via a pressure

multiplicator inside the pressure controller *Louise* [122]. The pressure tolerance of *Louise* is set to $\pm 3$ MPa throughout this work, which decides the accuracy of which we can determine pressure.

The position of the capacitor is held fixed by the plug, i.e. at the bottom of the cell, and will therefore not move upon applied pressure. The cell can thus be carefully covered in cadmium, a neutron absorber, except for the central part of the capacitor to prevent neutron signal from any other part of the neutron cell than the sample and aluminium to reach the detectors. The wires are led up along the cell to the sample stick from the bottom of the cell, and are likewise covered in Cd, and placed at a 90° angle to the neutron beam. The sample stick is then placed inside the cryostat and adjusted to have the centre of the capacitor in the centre of the neutron beam.

The dielectric signal is measured with an LCR-meter in the high-frequency range from $10^2$ to $10^6$ Hz. A homebuilt setup with a multimeter is used in the frequency range from $10^{-3}$ to $10^2$ Hz, where a current-to-voltage converter is used to avoid any leak currents. The dielectric setup is run with an input voltage of 1 V. The multimeter-range is sensitive to the output voltage, and for samples for example with high DC-conductivity, the input voltage can be lowered. This dielectric setup is run and controlled through MatLab using code developed at Roskilde University.

The plug on the sample cell has two connectors, while the LCR-meter has four. The wires are either collected two and two in T-connectors for BNC caples at the top of the sample stick outside the cryostat for the two-wire sample stick, or collected two and two just outside the sample cell at the bottom of the cryostat for the four-wire sample stick. Regardless of which sample stick is used, to avoid any grounding problems, the LCR-meter must be grounded to the sample stick or the cryostat. This is done easiest be letting one of the masses from the BNC-connectors at the sample stick be in electrical contact with the sample stick itself.

Both the control of the pressure controller and the dielectric setup is implemented in NOMAD, the instrument control software at the ILL, for easy use and data storage.

## 6.3 What we measure

In this section, we will outline what kind of information that can be obtained from the dielectrics and have this has improved and optimised the use of time during beamtimes of high-pressure studies.

An important point to stress is that this combined cell does not compromise the neutron data, it is an additional probe providing extra information as a supplement to the neutron data. The simultaneous dielectric spectra can be thought of as a 'timestamp' for the neutron spectra of the dynamics of the investigated system, when it gives information on the alpha relaxation time of the sample in a broad temperature-pressure range. Even if the alpha relaxation is merely seen as a tail in the dielectrics either in the low frequency-part close to the glass transition or in the high-frequency part well into the liquid, time-temperature superposition often can be used to extrapolate into the frequency-ranges that are not covered by the setup.

For samples with DC-conductivity, the signal will prevail in the dielectrics even after the alpha relaxation has completely left the frequency window. Just as important, as we will discuss below, the dielectrics provides information about the stability of the sample. First, we will show an example of data from IN16B upon a pressure scan, using the fixed window scan (FWS) technique and the dielectrics.

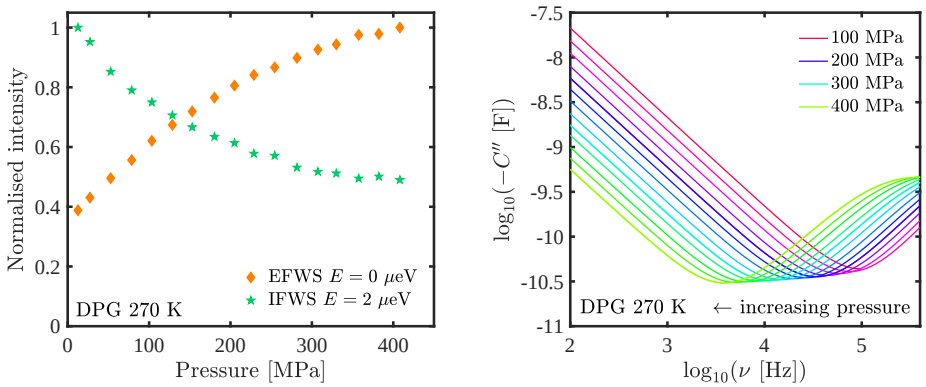


Figure 6.8: An example of a pressure scan on dipropylene glycol (DPG) at $T = 270\,\mathrm{K}$. Left: fixed window scan from IN16B summed over $Q$. Right: dielectric spectra.

In Fig. 6.8, we show an example of data from the backscattering instrument IN16B with the combined cell on dipropylene glycol (DPG, Sec. 7.1). This shows a pressure scan at 270 K alternating between elastic and inelastic fixed window scan (Sec. 4.4) in neutrons combined with dielectric spectra. We observe the alpha relaxation in the inelastic fixed window is pushed out of the time window of IN16B and enters the frequency window of the dielectrics upon compression. This data was acquired in two hours and provides a lot of information on the dynamics along an isotherm.

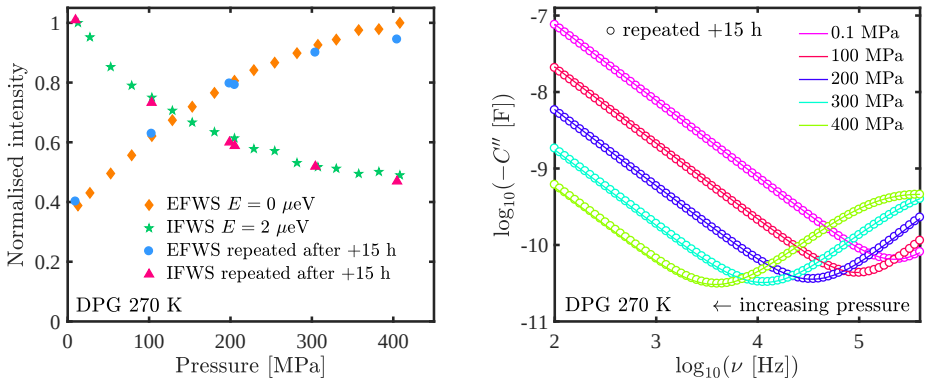


Figure 6.9: Same data as in Fig. 6.8 including data obtained 15 h later at some of the same state points: 0.1, 100, 200, 300 and 400 MPa.

The ability of the combined cell to reproduce data is shown in Fig. 6.9 for pres-

sures 0.1, 100, 200, 300 and 400 MPa at 270 K. The second set of data was recorded after more than 15 h, during which full spectra had been done and a few cycles up and down in pressure. We observe a small discrepancy at 400 MPa where data from the second set is a bit lower in intensity – this can be due to a technicality of the high-pressure limit settings and ±3 MPa tolerance on *Louise*. But otherwise, the data reproduces nicely in both the neutron and dielectric signal.

### Experimental gain

Studying liquids under pressure in general, regardless of the dielectrics, the sample cell and the sample stick are rather large in terms of the amount of material compared to an ambient pressure setup, which makes temperature changes and waiting for the sample to reach equilibrium a relatively slow process. In fact, during a beamtime, a lot of the time is spent changing temperature and waiting for the sample to reach thermal equilibrium, processes which can be monitored carefully in the dielectrics due to the sensitivity of the probe.

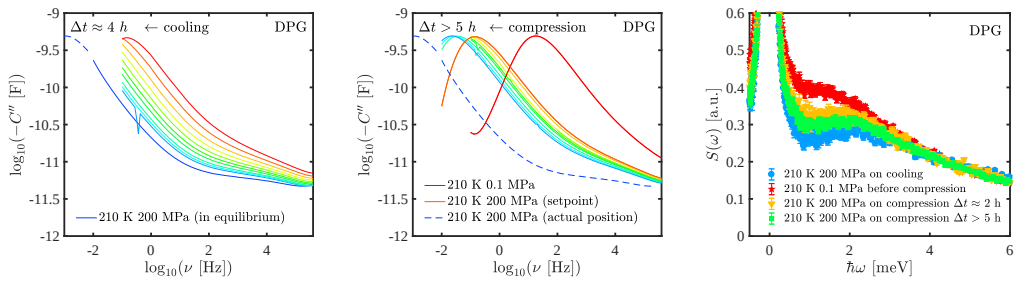


Figure 6.10: Data on dipropylene glycol from IN6 showing the dynamics coming into equilibrium at $T = 210\,\mathrm{K}$ and $P = 200\,\mathrm{MPa}$ upon cooling and an attempt to reach the same state point on compression. See text for details.

In Fig. 6.10, we show data from IN6 on DPG, summed over $Q$, as it approaches the glass transition state point at $T = 210\,\mathrm{K}$ and $P = 200\,\mathrm{MPa}$. All of the data shown here has the same temperature and pressure reading from the instrument, namely $T = 210\,\mathrm{K}$ and $P = 200\,\mathrm{MPa}$. The difference between reaching the state point upon cooling and compression is illustrated in the dielectrics. Upon cooling (left), pressure is applied far above $T_g$ and then cooled. It is seen from the dashed line obtained with time-temperature superposition that the peak position after $\sim 4\,\mathrm{h}$ reaches the glass transition with $\nu \approx 10^{-3}\,\mathrm{Hz}$.

On compression (centre) from $T = 210\,\mathrm{K}$ and $P = 0.1\,\mathrm{MPa}$ to $T = 210\,\mathrm{K}$ and $P = 200\,\mathrm{MPa}$ (centre), we observe that the dielectric peak stops moving after having waited more than 5 h. The dashed curve illustrates the dielectric spectra at the state point we want to reach. We interpret this as a sign that pressure is not properly transmitted to the sample. Normally, the sample reaches a new equilibrium on increased pressure within seconds, unlike the changes in temperature. A likely scenario is that the sample simply becomes too viscous to properly transmit pressure. From the neutron data (right), the blue data is the spectra at the glass transition at $T = 210\,\mathrm{K}$ and $P = 200\,\mathrm{MPa}$ that we have reached upon cooling. The other three

spectra are taken upon compression. We also observe in the neutron data that we never reach the same spectral shape when we try to compress to $T_g$ as we did on cooling. Based on this observation, in this work, pressure has always been applied in the liquid, far above $T_g$, monitored by the dielectrics, and then cooled.

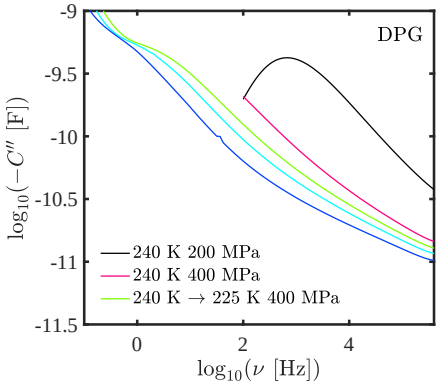


Figure 6.11: A spurious conductivity signal showed up in the dielectric signal as pressure was increased and the cooling started, interpreted as pressure liquid mixing with the sample.

In Fig. 6.11, we show how the dielectrics was used to, as we interpret the data, detect that pressure liquid had mixed with the sample. The black line shows the signal before compression, the red line shows the signal before cooling started, but the peak is not yet visible here. Upon cooling with longer frequency scans to lower frequencies, the peak is no longer visible in the dielectrics and instead a strange conductivity signal shows up, which is most likely due to plasticising effect from mixing.

These are examples of how the dielectrics can be used to monitor the sample. Both are examples that would take forever to detect from the neutron signal along, if at all. In summer 2015 before this new cell, we lost three days of beamtime on IN16B measuring on DPG not understanding the data that we acquired, which was supposedly due to problems with pressure transmission. Something that we would have been able to detect with the dielectrics.

### Example of kinetic study

The combined cell can also be used for doing real-time studies of kinetics, e.g. crystallisation. Although this type of study will not play a role for the rest of this work, this is an interesting topic for future projects and serves as an example of the versatility of the cell.

In Fig. 6.12, we show crystallisation of the van der Waals bonded liquid, propylene carbonate under pressure from IN16B. The real part of the capacitance at a fixed frequency, $\nu = 10\,\text{kHz}$, and the normalised intensity of the fixed window scans is shown as a function of time during the crystallisation process. In the dielectric signal, we observe the crystallisation process starting just before 1 ks and decays to a constant value just before 10 ks, where the crystallisation process seems to have

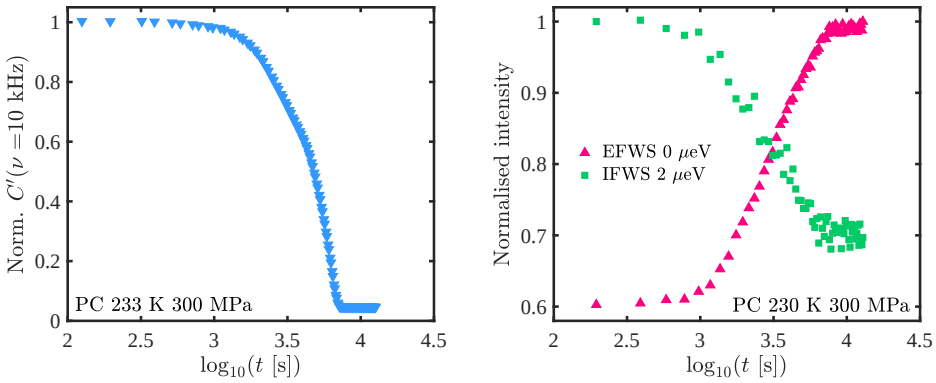


Figure 6.12: Real part of capacitance at a fixed frequency, $\nu = 10$ kHz (left) and normalised intensity of elastic and inelastic FWS summed over $Q$ (right) as a function of time during crystallisation process on propylene carbonate (PC) measured at IN16B.

come to an end. We observe the same kinetic behaviour in the FWS, that the crystallisation process starts just before 1 ks, causing an increased intensity in the elastic intensity and a decrease in the inelastic intensity because of reduced mobility. The process is also seen in the FWS to come to an end approaching 10 ks.

A drawback of the design for kinetic studies that are also sensitive to the exact sample environment, is the fact that we have two sample compartments making up the sample environment in the neutron beam, whereas the dielectrics only measures in the inner one, and although the two compartments are in principle identical, this could be an issue for crystallisation. With respect to studying dynamics as we do throughout the rest of this work, the two sample compartments are considered identical and this should not give an effect.

## 6.4 Summarising discussion

The newly developed sample cell for doing simultaneous dielectric and neutron spectroscopy under high pressure has proven extremely useful during high-pressure beamtimes. The new cell also means that experimental protocols can be repeated offline after an experiment to check the measured data, and that an experimental protocol can be tested before a beamtime, for example to locate particular state points in temperature and pressure, which can then be relocated online.

In this high-pressure design, where we also have the dielectrics, we have a plug in the bottom of the cell, which makes the setup somewhat more fragile as it does leak from time to time. Different measures have been made by the workshop in Roskilde to improve the quality of the plugs, and the quality has gone up so that it was able to last a four-day beamtime on IN5, cycling up and down in pressure repeatedly on one plug.

There is a problem in the very high frequency end of the dielectric spectrum that we have not discussed so far. In approximately the last decade in the high-frequency

end, induction effects show up as a small increase in the sample signal. The four-wire sample stick was thought to solve this problem, but instead this small increase in the capacitance has turned into a small decrease. Either way, this has not been observed to change signal dramatically, in particular, not the position of the alpha relaxation.

Despite the imperfections, to sum up, the combined measurements provides certainty on state points and allow for repetition of measurements offline either beforehand for preparation of beamtime or afterwards for checking reproducibility. Because of the sensitivity of the dynamics in glass-forming liquids to relatively small changes in temperature and pressure, the fast and precise spectra from the dielectrics, the additional probe to the neutrons serve not only as an extension of the accessible timescales, but also as a probe for checking experimental conditions. This includes the monitoring of pressure transmission of the sample coming into and reaching thermal equilibrium, that pressure liquid has not reached and mixed with the sample environment, that there is no leak, and so on. The new combined high-pressure sample cell has meant that we have been able to do more accurate measurements in temperature and pressure, but also to a large extent because of its role as sample environment monitor, that we can optimise how we spend the valuable beamtime.

# Chapter 7

# Searching for isomorphs in real glass formers Part I

In this and the next chapter we will present experimental tests of isomorph theory through density scaling and isochronal superposition of dynamic spectra. In this chapter, we will focus on the dynamics where the alpha relaxation is in the window of the neutron scattering instruments, i.e. mainly from micro- to nanosecond timescales. This corresponds to the 'merged' scenario sketched in Fig. 6.1, where the alpha relaxation is merged with faster dynamics such as vibrations and fast relaxations. In the next chapter (Ch. 8), we will test isomorph theory close to the glass transition when we have separation of timescales. All studies presented in this and the next chapter, except for cumene on IN16B, which was measured summer 2015 before the development of the new cell, have been performed with the combined high-pressure sample cell for doing simultaneous dielectric and neutron spectroscopy that was presented in Ch. 6. The combined cell has been a crucial part of this work, for identifying isochrones on different timescales and ensuring that measurements were indeed done along isochrones.

In isomorph theory (Sec. 3.5), we have assumed the existence of isomorphs, where two points in the phase diagram are isomorphic when the probability of the two configurations in reduced units are identical. The relevant scale according to isomorph theory is in reduced units that per definition are dimensionless and identified with a tilde (Eq. 3.9). From neutron scattering, the dynamic structure factor is measured as a function of wavevector and frequency, where the frequency becomes the energy transfer when multiplied by the constant, $\hbar$, that relates wave properties to the sample.

The frequency expressed in reduced units is

$$\tilde{\omega} = \omega t_0 = \omega \rho^{-1/3} \sqrt{m/(k_{\mathrm{B}} T)} \tag{7.1}$$

where $\omega$ corresponds to the energy transfer if we set $\hbar = 1$. Here, $\rho$ is the number density and $m$ is the average particle mass, the latter assumed to be constant. We set $m = k_B = 1$. Effectively, the reduced energy unit thus becomes

$$\tilde{\omega} = \omega \rho^{-1/3} T^{-1/2}, \tag{7.2}$$

where $\rho$ is now the volumetric mass density. This is the energy scale in reduced units, which a lot of the neutron spectra will be shown on. We will use equations of state from literature presented below (Sec. 7.1) to calculate the density at the studied state points for the different samples. The change in density is in the percent range, thus, the inverse of the cubic root of the density will only have a small effect on the scaling. Plotting data in reduced energy units will mainly be affected by temperature changes. As we shall see in Sec. 7.3, the scaling has little effect only visible for higher energy transfer, and we will therefore ignore the reduced units for the inelastic window scan.

Just like reduced energy units, the wavevector or momentum transfer, $Q$, should also be presented in reduced units:

$$\tilde{Q} = Q\rho^{-1/3} \tag{7.3}$$

The density changes are in the percent range in this study and scaling of $Q$ will be around 1%, which will be within the uncertainty of the data and is therefore neglected throughout this study.

It is common in the neutron scattering community to correct the dynamic structure factor by the temperature-dependent Bose factor to account for the occupation number and arrive at the susceptibility via the fluctuation-dissipation theorem (Sec. 4.2 and Eq. 4.50):

$$\chi''(Q,\omega) = \frac{S(Q,\omega)}{1-n(\omega)}, \tag{7.4}$$

where the Bose factor is

$$n(\omega) = \left(\exp\left(\frac{-\hbar\omega}{k_B T}\right) - 1\right)^{-1}, \tag{7.5}$$

defining $\hbar\omega < 0$ as the neutron gain side. However, this only corrects the data for the number of phonons in temperature and not in pressure, and we would then have a pressure dependent susceptibility.

Before we present the data, will follow an introduction to the three samples used for the experiments presented in this and the next chapter. Then we will show density scaling and isochronal superposition for the samples on dynamics from picosecond to millisecond dynamics focusing mainly on alpha relaxation dynamics, before analysing the Fourier transformed spectra for one of the samples, cumene, in the time domain.

## 7.1 Samples and data reduction

These experimental isomorph tests have been performed on the two van der Waals liquid isopropyl benzene (cumene) and PPE (5-polyphenyl ether) and the hydrogen bonding liquid dipropylene glycol (DPG) which will be presented below. The criteria for choosing these liquids have been that they should have little or no beta-relaxation, a strong incoherent signal, a relatively low glass transition temperature at ambient pressure and a reasonable pressure response. The samples should preferably not be

prone to crystallisation. The samples were chosen where $PVT$-data already existed that could provide equations of state for converting the measured $(T, P)$ state points into functions of temperature and density.

All experiments were carried out at the Institut Laue-Langevin (ILL) on the backscattering instrument, IN16B and the time-of-flight instruments IN5 and IN6 (Sec. 4.4). All neutron data has been corrected in the standard way by normalising to monitor and vanadium, subtracting background, and correcting for self-shielding, self-absorption and detector efficiency in LAMP, a data treatment program developed at the ILL. The reader is referred to Ch. 4.4 for details on data correction and instrument settings. Cumene and DPG were both measured at IN16B with an elastic energy resolution of $\Delta E_{\text{res}} = 0.75\,\mu\text{eV}$ accessing timescales up to roughly $\sim 1\,\text{ns}$. The data is presented in the $Q$-range from $0.4\,\text{Å}^{-1}$ to $1.8\,\text{Å}^{-1}$, roughly in steps of $0.1\,\text{Å}^{-1}$ and has been binned in steps of $0.1\,\mu\text{eV}$. To improve statistics, the data are presented as a sum of $Q$ unless otherwise stated.

Cumene and PPE were both measured at IN5 at a wavelength of $5\,\text{Å}$ with an elastic energy resolution $\Delta E_{\text{res}} \approx 0.1\,\text{meV}$, roughly corresponding to $\sim 10\,\text{ps}$ accessing a $Q$-range from $1.2 - 1.9\,\text{Å}^{-1}$. The data was grouped for constant $Q$-values in steps of $0.1\,\text{Å}^{-1}$. Cumene has furthermore been measured on IN5 with $\lambda = 8\,\text{Å}$, corresponding to an elastic energy resolution $\Delta E_{\text{res}} \approx 0.015\,\text{meV}$, which is roughly $\sim 100\,\text{ps}$ in the $Q$-range $0.5 - 1.2\,\text{Å}^{-1}$, grouped for constant $Q$ in steps of $0.1\,\text{Å}^{-1}$. DPG was measured on IN6 with $\lambda = 5.1\,\text{Å}$ corresponding to $\Delta E_{\text{res}} \approx 0.07\,\text{meV}$, roughly accessing $\sim 10\,\text{ps}$ in the $Q$-range from $1.2 - 1.7\,\text{Å}^{-1}$, grouped for constant $Q$ in steps of $0.1\,\text{Å}^{-1}$.

To study density scaling and isochronal superposition (Ch. 7.2 and 7.3), we will mostly focus on the summed $Q$ spectra for better statistics. According to isomorph theory, the scaling behaviour should not depend on the length scale of which it is studied, and the value of $Q$ should therefore in principle not have any influence on the results. For $Q$, because the scaling will only have a tiny effect, we ignore the reduced units that in principle is required from isomorph theory. For cumene, we take a closer look into the $Q$-dependence of the dynamics in the Fourier transformed data (Ch. 7.4).

The dynamic structure factor, $S(Q, \omega)$, will in most cases be presented as a function of the reduced energy units, $S(Q, \tilde{\omega})$. The intensity of the dynamic structure factor is always presented on an axis of arbitrary units. The scale of the intensities of the dynamic structure factor is different from experiment to experiment or instrument to instrument and will therefore be different in magnitude. Data from the same instrument and sample are always shown on the same scale, i.e. there has not been done any scaling on the $y$-axis within an experiment.

The uncertainty with which we can determine the temperature and pressure of state points are given by limitations of the instruments and the pressure equipment. The pressure can be determined with high precision, but has a $\pm 3\,\text{MPa}$ pressure tolerance, which determines how precise it can be set according to a given set point. The temperature stability of the neutron instruments is typically $\pm 0.1\,\text{K}$, but the exact temperature may vary a couple of Kelvin across different instruments according to temperature calibrations and offsets. A couple of Kelvin and a few MPa, can

change the alpha relaxation time with orders of magnitude. Because we rely on locating isochrones very precisely in this study, we have benefited from the dielectric measurements which allow us to make sure that we are actually on isochronal state points, and that the same state points can be found on another instrument.

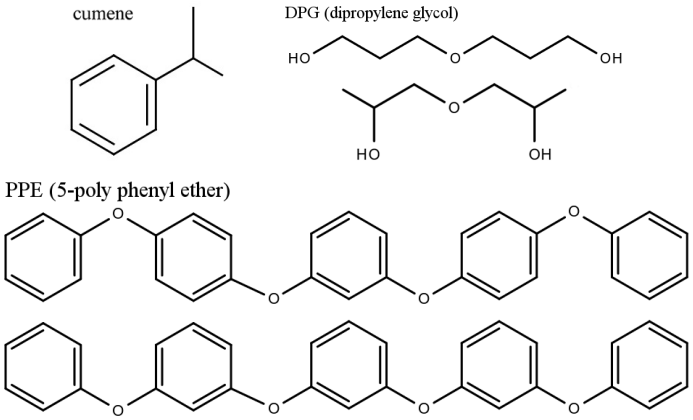


Figure 7.1: Sketches of the molecular structure of the three samples studied in this chapter. DPG and PPE are mixtures of isomers.

## Cumene

Cumene (isopropyl benzene) is a rather small molecule (Fig. 7.1) with a melting temperature of $T_m = 177\,\mathrm{K}$ and a glass transition temperature found from dielectric spectroscopy of $T_g \approx 126\,\mathrm{K}$, both at ambient pressure. Cumene is a van der Waals bonded liquid with the molecular formula $C_9H_{12}$. The density at atmospheric pressure and room temperature is $0.860\,\mathrm{g\,cm^{-3}}$. The estimated incoherent neutron signal from cumene is $\sim 95$ %. The ambient pressure fragility of cumene is $m \approx 70$ ([127], Sec. 5 from shear mechanics). Barlow et al. [14] measured the viscosity as a function of temperature, extended to the low temperature region by Ling & Willard [99]. The viscosity as a function of pressure was measured by Li et al. [97], who also presented the light scattering data used for comparison in Sec. 7.4.

Ransom & Oliver [127] presented a modified equation of state to calculate the density along the glass transition in a large pressure range up to more than 4 GPa. The original equation of state from Cibulka and Takagi [37] was based on compression measurements by Bridgman [24] and their own measurements and only valid for temperatures around room temperature, far above the melting temperature:

$$\rho(T,P) = \frac{\rho_0(T)}{1 - C(T)\ln\left(\frac{B(T)+P}{B(T)+0.0001\,\mathrm{GPa}}\right)} \tag{7.6}$$

where $\rho_0(T)$ is the ambient pressure density, and $C(T)$ and $B(T)$ are temperature-dependent parameters. Ransom and Oliver modified the equation of state to include low temperatures by using the temperature dependence of toluene, a molecule similar in structure to cumene, which has been measured in a much larger temperature

interval, to better estimate the two parameters $B(T)$ and $C(T)$ [127]:

$$B(T) = \sum_{i=0}^{4} b_i \left( \frac{T - T_0}{100} \right)^i \tag{7.7}$$

with $T_0 = 298.15\,\mathrm{K}$ and

$$\bar{b} = \begin{bmatrix} 0.111\,102\,\mathrm{GPa} \\ -0.080\,954\,\mathrm{GPa\,K^{-1}} \\ 0.0226\,\mathrm{GPa\,K^{-2}} \\ -0.0034\,\mathrm{GPa\,K^{-3}} \\ 0.000\,28\,\mathrm{GPa\,K^{-4}} \end{bmatrix}$$

and

$$C(T) = 0.093736 - 0.8 \left( (0.005\,004\,\mathrm{K^{-1}}) \frac{(T - T_0)}{100} \right).$$

Ransom et al. made the viscosity data as a function of pressure and temperature from Li et al. collapse using the density scaling exponent $\gamma = 4.77$ found by a power law fit to $T_g(P)$ all the way up to 4.5 GPa. This equation of state and the exponent $\gamma = 4.77$ from [127] have been used throughout this chapter. The large number of significant figures on the fitting parameters for the equation of state and on $\gamma$ has been included in the data analysis in this work, although they by no means reflect the uncertainty on the calculated density.

The glass transition line for cumene in the pressure interval of this study has a slope of $\mathrm{d}T_g/\mathrm{d}P = 0.085\,\mathrm{K\,MPa^{-1}}$. The low glass transition temperature, the high incoherent signal and the relatively high pressure-response of cumene makes it a sample well suited for neutron scattering. However, working in the supercooled state of cumene is tricky because of its ability to crystallise. There is a region between the glass transition and the melting point where crystallisation takes place quite easily, although at different rates. At ambient pressure, the region around $160\,\mathrm{K} \pm 10\,\mathrm{K}$ is experimentally difficult to access in the supercooled regime. For this reason, the first data measured on cumene from IN16B, without the dielectric cell to monitor the sample, were taken around or above the melting temperature. In this area of temperature and pressure, the alpha relaxation is completely out of the dielectric frequency window, but coincides with where the relaxation is in the IN16B instrumental window, nanosecond timescale, as was shown from the fixed window scan in Fig. 5.7.

The dielectric relaxation strength for cumene is rather weak with $\Delta\epsilon \approx 0.3$ with a high-frequency plateau value of the permittivity $\epsilon_\infty \approx 2.3$, exhibiting only a small excess wing in the imaginary part. We use time-temperature superposition of the spectrum to find relaxation times from the dielectrics for low temperatures close to the glass transition where we do not have the entire loss peak in the frequency window.

The data from IN16B on cumene was measured before the development of the combined cell for doing simultaneous dielectric and neutron spectroscopy. This means that when we studied cumene on IN5 in the new combined cell, we could

not use the dielectric signal to accurately locate the same state points as the one we had studied at IN16B, ensuring that the data were taken under the same conditions. Because of the relatively high temperature and pressure region studied on IN16B, there was no relaxational signal left in the dielectrics, thus we cannot use the dielectrics to estimate the relaxation time for the high-temperature data on cumene from IN5.

The sample was purchased from Sigma Aldrich with a purity of $> 99$ % and used as acquired. Data from cumene will be presented in pink-purple colours.

## PPE

PPE (5-polyphenyl ether) is a van der Waals bonded liquid and is a mixture of isomers as sketched in Fig. 7.1. The molecular formula is $C_{30}H_{22}O_4$ and the density at atmospheric pressure and room temperature is $1.25\,\mathrm{g\,cm^{-3}}$. The estimated incoherent neutron signal from PPE is $\sim 90$ %. The ambient pressure fragility of PPE is $m \approx 80$ ([76], Sec. 5 from shear mechanics). PPE is a diffusion pump oil that has been well studied within the Glass & Time group with dielectrics and shear mechanics in e.g. [76, 133, 168, 71]. The pressure response of PPE is relatively large with $\mathrm{d}T_g/\mathrm{d}P = 0.18\,\mathrm{K\,MPa^{-1}}$ in the pressure range used in this study. However, as was shown from the fixed window scan in Fig. 5.7, the relatively high $T_g(P_{\mathrm{amb}})$ means that we only just see the alpha relaxation entering the instrument window of IN16B, nanosecond timescales, at ambient pressure at the maximum temperature of the setup. Applying pressure will only move the relaxation further away from the instrumental window on IN16B, which means that basically there is nothing to see. Data on PPE in this chapter will therefore only be on picosecond timescales from IN5 where there is still plenty of signal.

The dielectric relaxation strength for PPE is $\Delta\epsilon \approx 1.5$ with a high-frequency plateau value of $\epsilon_\infty \approx 2.95$. PPE exhibits only a small excess wing in the imaginary part. We use time-temperature superposition of the spectrum to find relaxation times from the dielectrics when the loss peak itself is not in the frequency window.

The equation of state for PPE was found by Gundermann [69] from a fit of the Tait equation to PVT data:

$$\rho(T,P) = \left( V_0 \exp(\alpha_0 T) \left\{ 1 - C \ln \left[ 1 + \frac{P}{b_0 \exp(-b_1 T)} \right] \right\} \right)^{-1}, \qquad (7.8)$$

where $\rho$ is in g/cm$^3$ and equal to $1/V_{sp}$, the specific volume, $P$ is pressure in MPa and $T$ is temperature in °C. The fitting parameters are $V_0 = 0.82$, $\alpha_0 = 6.5 \times 10^{-4}$, $C = 9.4 \times 10^{-2}$, $b_0 = 286$ and $b_1 = 4.4 \times 10^{-3}$.

The density scaling exponent has been determined from previous experiments [70] and found to be $\gamma = 5.5$ from $PVT$ data. The equation of state and the density scaling exponent were used by Xiao et al. [168] to predict the pressure dependence of the alpha relaxation measured with dielectrics for PPE from isochronal superposition.

The sample was purchased from Santolubes and used as acquired. Data from PPE will be presented in yellow-red colours.

The two van der Waals liquids, cumene and PPE, compliment each other quite well. For PPE, there is absolutely no risk of crystallisation and the intermediate range where the alpha relaxation is in the dielectric window that was not accessible with cumene, halfway between the glass transition and nanosecond dynamics, is easily accessible with PPE. For cumene, on the other hand, because of its low glass transition temperature, we are actually able to see the relaxation move through the neutron instrument window. With the two liquids combined, we can cover quite a large dynamic area in the temperature-pressure phase diagram.

### DPG

To test the robustness of isomorph theory, we also test a hydrogen bonding sample. A challenge for hydrogen bonding samples is that they typically do not respond as well to pressure many van der Waals liquids. To compare the dynamics say along an isotherm or an isochrone, we are interested in a sample where there is an actual change in the dynamics with pressure. We chose to study DPG (dipropylene glycol), which is a hydrogen bonding liquid and a mixture of isomers as sketched in Fig. 7.1. The molecular formula is $C_6H_{14}O_3$ and the density at atmospheric pressure and room temperature is $1.02\,\mathrm{g\,cm^{-3}}$. The estimated incoherent neutron signal from DPG is $\sim 95$ %. The ambient pressure fragility of DPG is $m \approx 65$ [96, 66]. The glass transition line of DPG changes with a slope of $\mathrm{d}T_g/\mathrm{d}P \approx 0.075\,\mathrm{K\,MPa^{-1}}$ in the pressure range of this study. This is not too far from the slope of the cumene glass transition, however, the glass transition temperature of cumene is only 2/3 of that of DPG, which makes the relative change in the glass transition temperature with pressure for cumene much larger than that of DPG.

DPG has a strong dipole moment, resulting in a strong dielectric relaxation strength $\Delta\epsilon \approx 20$ with a high-frequency plateau value of $\epsilon_\infty \approx 3$ in agreement with [15], who also show the change in dielectric relaxation strength with temperature. For DPG, a DC conductivity power-law tail is visible in the imaginary part in frequencies slower than the alpha relaxation. Moreover, a faster dynamic contribution is visible as a pronounced excess wing in the dielectric spectrum, see e.g. [30, 66]. Grzybowski et al. [68] found that density scaling did not apply for DPG using a best fit value of the density scaling exponent $\gamma = 1.5$. However, five years later they revised the equation of state, and found density scaling to apply for $PVT$ data of DPG with the same gamma exponent [67]. The revised equation of state is used in this work:

$$V(T,P) = \frac{A_0 + A_1(T-T_0) + A_2(T-T_0)^2}{\left(1 + (P-P_0)b_1 \exp(b_2(T-T_0))\right)^{1/\gamma_{\mathrm{eos}}}} \tag{7.9}$$

with the fitting parameters $A_0 = 0.85907$, $A_1 = 4.25 \times 10^{-4}$, $A_2 = 1.45 \times 10^{-6}$, $B_{T_0} = 3436$, $b_2 = 6.18 \times 10^{-3}$, $\gamma_{\mathrm{eos}} = 9.52$, $b1 = \gamma_{\mathrm{eos}}/B_{T_0}$ and $T_0 = T_{g,\mathrm{amb}} = 195\,\mathrm{K}$ and $P_0 = 0.1\,\mathrm{MPa}$. Alpha relaxation times were measured with broadband dielectrics all the way down to nanoseconds at ambient pressure for DPG in [15, 66, 90]. The alpha relaxation time as a function of temperature was fitted using the VFT function

in [90]:

$$\tau_\alpha(T) = \tau_0 \exp\left(\frac{DT_{\mathrm{VF}}}{T - T_{\mathrm{VF}}}\right), \tag{7.10}$$

where the fitting parameters are $\tau_0 = 25\,\mathrm{fs}$, $D = 10$, and $T_{\mathrm{VF}} = 150$. For dielectrics, secondary relaxations were shown to have a much weaker temperature dependence compared to the alpha relaxation [66], while a beta relaxation was found to show practically no pressure dependence in dielectrics at $T = 217$ and $226\,\mathrm{K}$ [30].

DPG is relatively easy to work with, and as for PPE, there is no risk of crystallisation. The relatively low glass transition temperature at room temperature means, just like for cumene, that we are able to observe the alpha relaxation in the neutron instrument window. Moreover, the strong conductivity signal means that we can monitor DPG with the dielectrics in a much larger dynamic range than the two van der Waals liquids.

The sample was purchased from Sigma Aldrich with a purity of 99 % and used as acquired. Data from DPG will be presented in green-blue colours.

## 7.2 Density scaling

We will now move on to experimental tests, starting with density scaling that refers to the observation of constant relaxation time as a function of $\Gamma = \rho^\gamma/T$ as was introduced in Ch. 3.3. We test density scaling for elastic and inelastic fixed window scans (EFWS/IFWS) from IN16B ([54] and Sec. 4.4) and for the dielectric measurements, all in all, spanning dynamic timescales from nanosecond to second timescales on the van der Waals liquid, cumene and the hydrogen bonding liquid, DPG.

To do density scaling, the dynamics must be plotted as a function of $\Gamma = \rho^\gamma/T$, which cannot be done directly from experimental data where temperature and pressure are our variables. Instead, we use the equations of state presented in the previous section (Sec. 7.1) to find $\rho(T, P)$ for the given state points.

As was explained in Sec. 4.4, the fixed window scan technique available on IN16B, and in particular the inelastic fixed window option, is an excellent tool for mapping out relaxations as a function of temperature and pressure on nanosecond timescales. By alternating between different instrumental settings, it is possible to do fast scans as a function of temperature and pressure and in this way construct a sample-specific relaxation map from which one can construct for example isochrones. Isochrones are defined as lines with constant alpha relaxation time (Sec. 3.1), and can on any timescale, for example is it possible to find isochrones based on nanosecond dynamics from the IFWS when the alpha relaxation is in the instrument window of IN16B. The data is presented in subsection according to the sample.

### Cumene

Data from EFWS and IFWS is shown for cumene for three isotherms as a function of pressure shown in Fig. 7.2 as a sum over $Q$. In the elastic intensity, the intensity is observed to increase with increased pressure, as the liquid is moving closer to the glassy state. In the inelastic intensity, we observe how the alpha relaxation is pushed

through the experimental time window of the neutron instrument upon increased pressure. In the lower part of Fig. 7.2, the data are plotted as a function of $\Gamma = \rho^\gamma/T$ using $\gamma = 4.77$ from Ransom et al. [127]. The data in the density scaled plot is made to collapse to a good degree in agreement with what we would expect from density scaling. The scaling is not perfect as can be seen from the IWFS. An explanation of this, other than it being due to experimental uncertainties on the pressure transmission, can be that this is caused by detector efficiency in summing over $Q$ as seen in Fig. 7.4. Another possible explanation is that intra-molecular dynamics could contribute to the dynamics on this timescale, although the full spectra in Fig. 7.16 does not support this. Cumene contains methyl groups and dynamics from methyl group rotations are often observed on the timescale of backscattering instruments. Methyl group rotation often prevails into the glass and can in this way be separated from the alpha relaxation on nanosecond timescales. However, for cumene, only one relaxation process is observed from the IFWS on temperature (Fig. 5.7). Intramolecular dynamics is in general not pressure dependent and is therefore not expected to scale with density scaling, which is a scaling in temperature as well as density. One way of assigning the neutron signal to specific parts of a molecule is by using partly deuterated samples. By deuterating the phenyl ring in cumene, it would be possible to assign the part of the signal that stems from the motion of the methyl groups to account for its dynamic contribution. This was unfortunately not possible within the frame of this work. However, if the dynamics from the methyl group rotation behaved significantly different from that of the alpha relaxation, it would show up in the data; half of the hydrogen atoms on cumene are located on the methyl groups.

From NMR studies it is suggested that the methyl group rotation on millisecond timescale follows the overall dynamics of the molecule down to around 140 K [10], in agreement with *ab initio* molecular calculations supporting a staggered molecular arrangement [143]. From a solid-state spin relaxation study on partly deuterated samples [124], it was shown that in the solid state between 100 and 150 K, methyl group reorientation took place on microsecond timescales. This supports the fact that we do not observe a distinct signal from methyl group rotation on IN16B.

In Fig. 7.3, we show the elastic intensity measured on the backscattering instrument IN13 also at the ILL, which has a coarser energy resolution than IN16B. The energy resolution on IN13 with an incident wavelength of $\lambda = 2.23$ Å is $E_{\text{res}} = 8\,\mu\text{eV}$, corresponding to a timescale of approximately 0.5 ns, i.e. an order of magnitude faster than on IN16B. The data is shown summed over $Q$ in the quite large range from 0.1 to 4.9 Å. The pressure scans presented in Fig. 7.3 are done at the same temperatures as those from IN16B. We observe that elastic intensity data is brought to collapse on density scaling.

We now proceed to explore the $Q$-dependence of the alpha relaxation from the IFWS, and we plot the three isotherms from Fig. 7.2 in a surface plot in Fig. 7.4, where the colour code refers to the intensity. The data is shown as a function of $Q$, and pressure and $\Gamma = \rho^\gamma/T$, respectively. The data has been normalised to the elastic intensity at lowest temperature and highest pressure, i.e. highest intensity, to account for detector efficiency. For the two lowest values of $Q$, we observe a relatively high intensity in the normalised data compared with the other $Q$-values

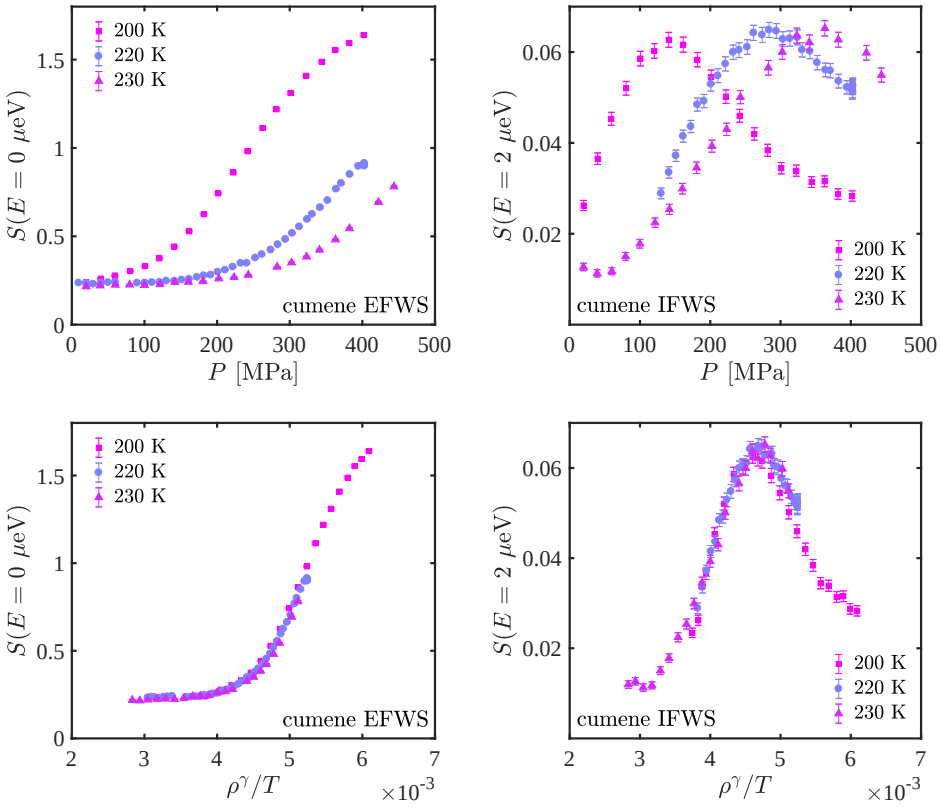


Figure 7.2: EFWS (left) and IFWS (right) from IN16B on cumene summed over $Q$ from IN16B. Intensity of EFWS and IFWS plotted for three isotherms (200 K, 220 K, 230 K) as a function of pressure (bottom) and as a function of $\Gamma = \rho^\gamma/T$.

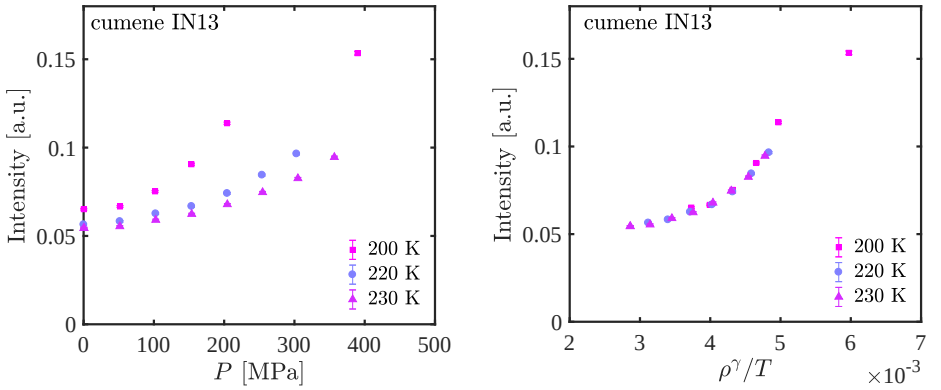


Figure 7.3: Elastic intensity from IN13 summed over $Q$. Left: three isotherms (200 K, 220 K, 230 K) as a function of pressure. Right: Density scaling of left plotted as a function of $\Gamma = \rho^\gamma/T$.

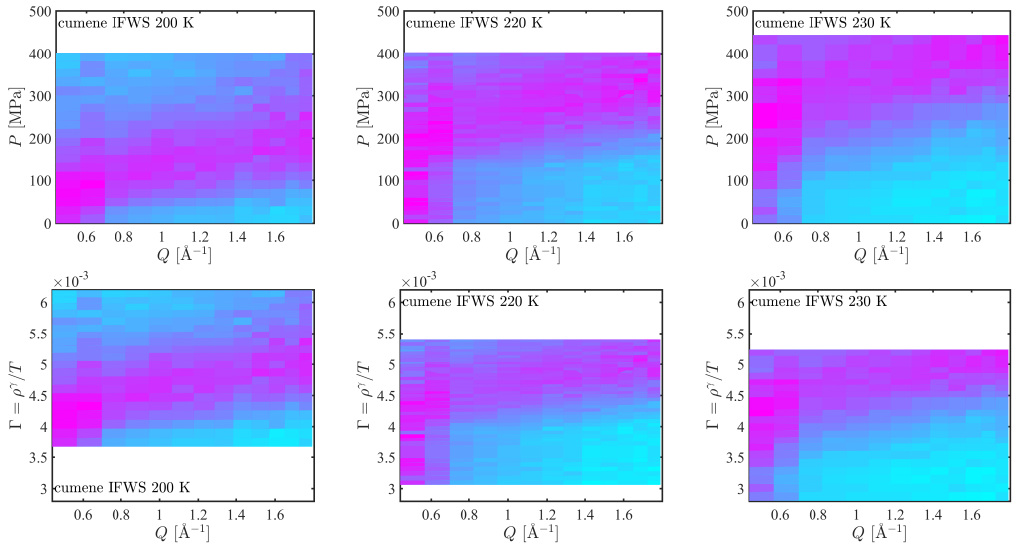


Figure 7.4: $Q$-dependence of the three IFWS from IN16B on cumene (Fig. 7.2). Pink colours are high intensities, while light blue is low intensity. Top: $Q$-dependence of the alpha relaxation for the three isotherms 200 K, 220 K, 230 K as a function of pressure. Bottom: Density scaling of top panels.

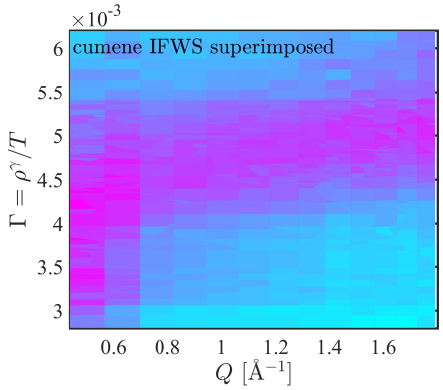


Figure 7.5: Superposition of the density scaled pressure scans shown in Fig. 7.4. A relaxation is observed to move through the instrumental window. The $Q$-dependence suggest this is of translational character.

in the temperature scans at $T = 220$ and 230 K, which suggest some offset in the detectors.

The relaxation process is observed to move through the instrumental window on increased pressure, and also regarding length scale. The $Q$-dependence of the IFWS provides information on the length scale dependence of the broadening. Because there is a $Q$-dependence, this implies translational motion. On increasing pressure, we observe the maximum in intensity of the broadening moving towards higher values of $Q$, i.e. shorter distances, for each of the three isotherms.

The broadening can be moved into the same position for all values of $Q$ by plotting the data as a function of $\Gamma = \rho^\gamma/T$. A superposition of the three density-scaled pressure scans is shown in Fig. 7.5. The parameter $\Gamma = \rho^\gamma/T$ is believed to control the timescale of the experiment, which is in agreement with the superposition of data from the three isotherms in Fig. 7.5, where the same relaxation process is not expressed in terms of temperature and pressure, independently, but in terms of $\Gamma = \rho^\gamma/T$. For cumene, the broadening is identified as the alpha relaxation.

The interpretation of the IFWS is only possible under the assumption that the spectral behaviour is the same for all three pressure scans; that we have only one relaxational process entering the instrument window and that it is the same for all three temperatures. In this sense, isochronal superposition is assumed in order to interpret the IFWS data.

For the study of isochronal superposition in the next section (Sec. 7.3), where we use the full spectra, we use the fixed window scans to determine state points in temperature and pressure of constant alpha relaxation time on nanosecond timescale. From Fig. 7.2, where the data is summed over $Q$, we use from the EFWS $S(E = 0\,\mu\text{eV}) \approx 0.6$ and from IFWS $S(E = 2\,\mu\text{eV}) \approx 0.06$ on the right side of the alpha relaxation maximum to identify the isochrone used for the isochronal study of the alpha relaxation. The same state points are studied on IN16B and IN5.

### DPG

The hydrogen bonding sample, DPG, was not treated in Ch. 5 in relation to elastic models. To obtain an overview of the dynamic map on IN16B of DPG, we therefore first present two temperature scans using the fixed window scan at two different pressures (Fig. 7.6). The glitch in data observed around 150 K is related to a change in temperature protocol on cooling. If we compare this data to the IFWS from cumene and PPE in Fig. 5.7, we observe that the data from the temperature scan is slightly more complex in the case of DPG. Around 300 K, we observe what we interpret as the pressure-dependent alpha relaxation similar to what was observed for cumene and PPE. But around 200 K, we see another much broader bump in the IFWS which is more or less independent on pressure. The lack of pressure dependence and $Q$-dependence (Fig. 7.13) suggest that the extra bump is from intramolecular methyl-group rotation. This could suggest that the beta relaxation observed in [30] that was assigned a relaxation time of $10^{-5}$ s at slightly lower temperatures, but also independent of pressure, is related to intramolecular motion.

From a density scaling point of view, we will first present the pressure dependence of the FWS along isotherms, similar to what we did for cumene, summed over $Q$.

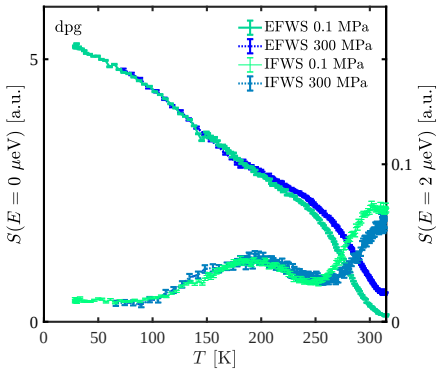


Figure 7.6: FWS from IN16B on DPG as a function of temperature at ambient pressure and 300 MPa. The pressure-dependent alpha relaxation is observed to enter the instrument window at around 300 K, while the pressure-independent methyl-group rotation is visible over a broad temperature range with a maximum at roughly 200 K.

Fixed window scans on DPG were taken using the combined cell, which means that not only do we have information from the EFWS and IFWS, but also from the dielectrics. In Fig. 7.7, we present the EFWS and the IFWS along five isotherms presented as a function of pressure and $\Gamma = \rho^\gamma/T$. Using a gamma exponent from literature [68, 67], $\gamma = 1.5$, we observe a collapse of data for the fixed window pressure scans upon density scaling.

Combining the temperature and pressure scan, we can plot the density scaled fixed window scans in a large temperature and pressure range. This is shown in Fig. 7.8. We see that although the alpha relaxation dynamics that we assign to be visible in the pressure scans at temperatures $T \geq 270$ K collapse nicely, the two temperature scans bifurcate at $\rho^\gamma/T \approx 5 \times 10^{-3}$, corresponding to where the pressure-independent motion assigned to methyl-group rotation sets in. Data on temperature scans are only included down to the glass transition temperatures due to the density estimations from the equation of state. We observe that the temperature scans are a bit off compared to the pressure scans in the interval where they overlap. The exact temperature is difficult to assign on a 'moving' temperature scan with a quite massive cell, even if tried to keep the cooling rate slow, $1\,\mathrm{K\,min^{-1}}$, there will be a lack between the reading and the actual sample temperature, compared to the pressure scans done in thermal equilibrium.

We can construct a plot similar to that from the fixed window scan technique on IN16B from the dielectric signal to test density scaling on the dielectric data on longer timescales. In Fig. 7.9, we show an example of the imaginary part of the dielectric data for a pressure scan at 270 K on DPG. The logarithmic of the imaginary part of the capacitance is plotted against frequency. DC conductivity is observed as a straight line in the lower frequency part of the spectrum, while at higher frequencies the alpha relaxation is pushed into the frequency window on increased pressure. The frequencies marked by the vertical dotted lines are used for doing a fixed frequency plot from the dielectric data similar to that from the

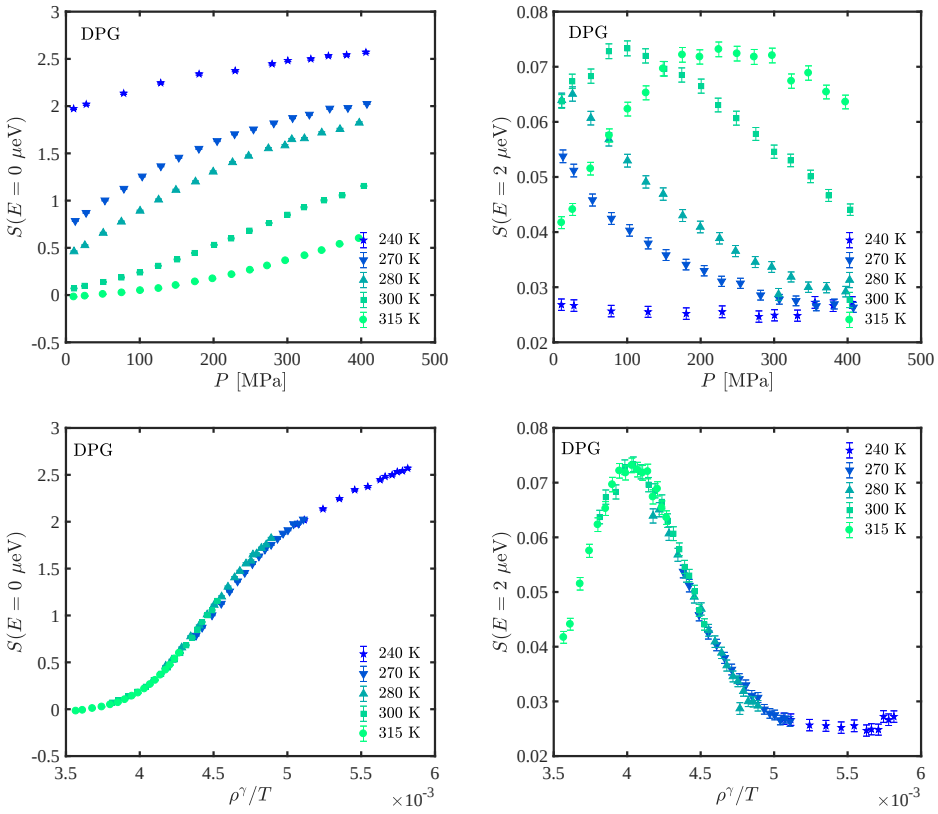


Figure 7.7: FWS from IN16B on DPG. Top: Intensity of EFWS and IFWS plotted for five isotherms (240 K, 270 K, 280 K, 300 K, 315 K) as a function of pressure. Bottom: Density scaling of top panels.

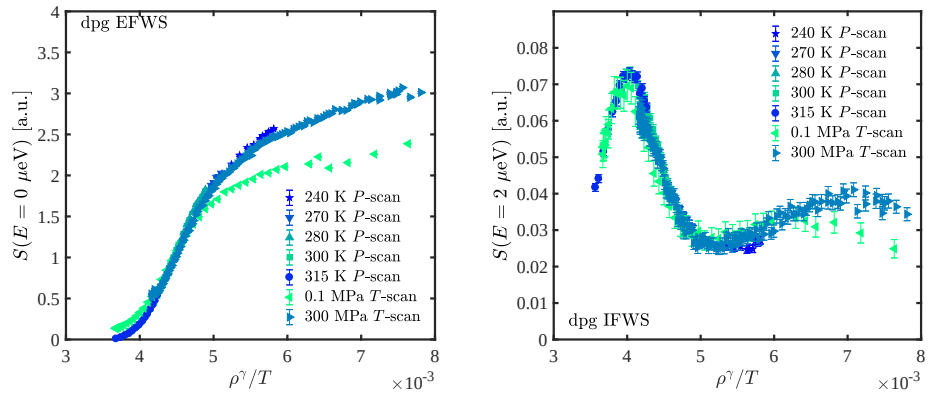


Figure 7.8: Density scaling of the combined temperature and pressure EFWS (left) and IFWS (right) from IN16B on DPG that were shown in Fig. 7.6 and 7.7.

FWS in Fig. 7.7. But first a few general comments on the dielectric data from the pressure scan. We observe a slight increase in the minimum observed between the DC conductivity and the alpha relaxation upon increased pressure. For the published dielectric data on DPG where this minimum is included [66], this minimum is observed to increase in permittivity as a function of both temperature and pressure up to frequencies of the order of $10^4$ Hz, above which the minimum is not included in the data set. From our data set, it is clear that some of the increase in the signal comes from the inductance problem mentioned in Sec. 6.4 in the combined cell. However, repeated measurements offline in another cell and setup at Roskilde University show similar behaviour for a pressure scan at $T = 270$ K. In any case, a change in the minimum suggests that there is a decoupling between the conductivity and the alpha relaxation, which means that estimating the relaxation time by time-temperature superposition using both conductivity and alpha relaxation is perhaps on the border of what is reasonable. However, we will do it in this study, assuming the effect of decoupling is within the uncertainty that can be obtained from neutron scattering.

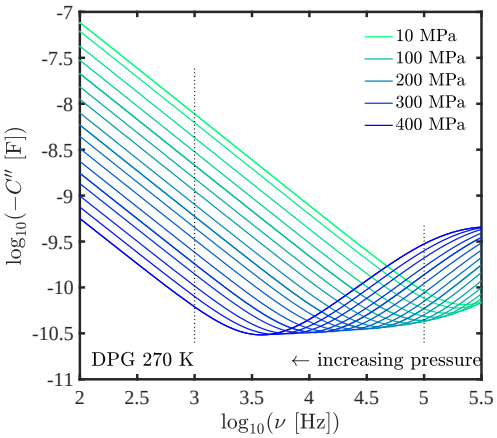


Figure 7.9: Imaginary part of dielectrics from pressure scan on DPG at 270 K on IN16B. Black dotted lines at 1 kHz and 100 kHz.

In Fig. 7.10, the fixed frequency data from the dielectric spectra is shown for the five isotherms as a function of pressure and $\Gamma = \rho^\gamma/T$ for two frequencies, $\nu = 1$ kHz and 100 kHz. For the data at 1 kHz, it is mostly the DC conductivity that is in the frequency window, although for the 240 K isotherm we clearly see the alpha relaxation passing through the window on applied pressure. For the 100 kHz data, we see parts of the alpha relaxation for the three lowest temperatures. The DC conductivity of the 270 K data seems to be somewhat high compared to the other isotherms, especially visible in the 1 kHz data, both when plotted against pressure and $\Gamma$. The dielectrics are extremely sensitive to tiny changes in sample environment and it does not seem very likely that there is something happening at 270 K that would cause density scaling to break down at this specific temperature, but not for those higher or lower, especially considering the collapse observed in the neutron FWS at the same temperature. As with the neutron fixed window scans,

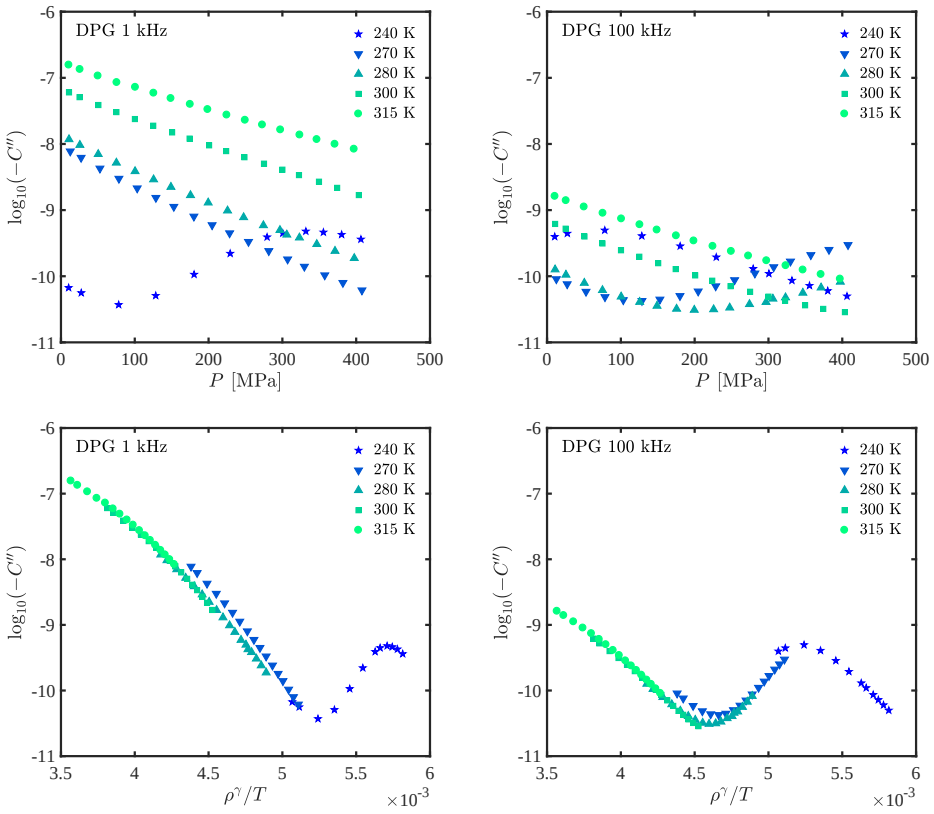


Figure 7.10: Fixed frequency plots from imaginary part of the capacitance measured at IN16B on DPG simultaneously with FWS data in Fig. 7.7. Top: Intensity plotted for five isotherms (240 K, 270 K, 280 K, 300 K, 315 K) as a function of pressure. Bottom: Density scaling of top panels plotted as a function of $\Gamma = \rho^\gamma/T$.

the data seems to collapse nicely, even if there is only little overlap between the different parts of the curve close to the alpha relaxation. This also supports that using the conductivity to estimate that alpha relaxation time from time-temperature superposition is probably okay.

Comparing the two constructed fixed frequency curves from the dielectrics at 1 and 100 kHz, roughly timescales of $10^{-4}$ and $10^{-6}$ s, respectively, to the $10^{-9}$ s timescale of the dynamics from the FWS on IN16B (Fig. 7.7), we observe the alpha relaxation moving towards lower values of $\rho^{\gamma}/T$ on faster timescales.

In Fig. 7.11, we show the pressure and $Q$-dependence of the IFWS for the four isotherms shown in Fig. 7.7 at $T = 270$, 280, 300 and 315 K. As we did for cumene, the fixed window intensities have been normalised to the elastic intensity at a low-temperature and high-pressure state point to account for detector efficiency. The top panel shows the data as a function of pressure, while the bottom panel is the density scaled data. From the density scaled data, it is clear that the overlap in $\Gamma$ is smaller between the different isotherms in comparison to the cumene data (Fig. 7.4). But we observe the same kind of translational behaviour, suggesting that this signal is indeed the alpha relaxation.

A superposition of the four isotherms is shown in Fig. 7.12 for the density scaled data. As we observed for cumene, the relaxation is seen to pass through the instrument window of IN16B in terms of $\gamma^{\rho}/T$ and $Q$.

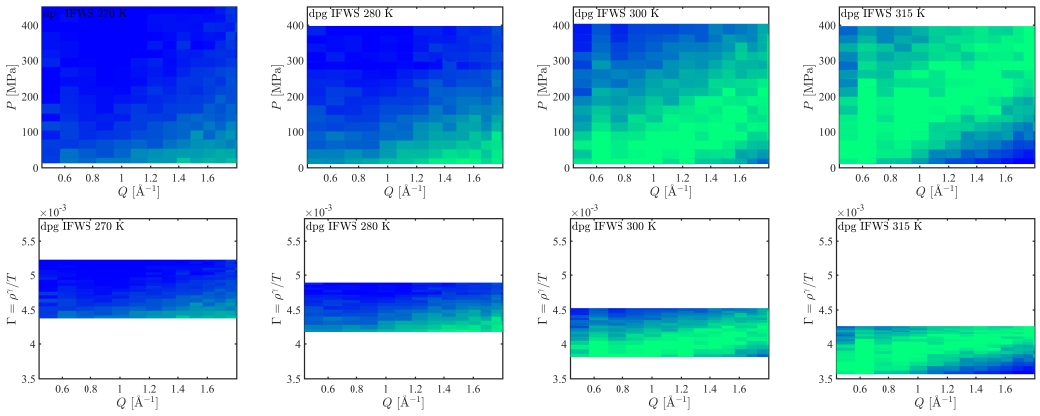


Figure 7.11: $Q$-dependence of four IFWS isotherms from IN16B on DPG (Fig. 7.7). Light green colours are high intensities, while dark blue is low intensity. Top: $Q$-dependence of the alpha relaxation for the four isotherms at $T = 270$, 280, 300 and 315 K as a function of pressure. Bottom: Density scaling of top panels.

The intensity of the 240 K-isotherm presented in Fig. 7.13 is very low compared to the other isotherms and is therefore plotted on a different intensity scale than the other pressure scans in Fig. 7.11. We observe hardly any pressure effect on the intensity on increased pressure. From the $Q$-dependence, we observe a stronger signal at high $Q$, corresponding to shorter length scales. This suggests a local motion, which we interpret as methyl-group rotation, often observed on nanosecond timescale [55, 54].

Similar to what we did for cumene, we use the FWS data to define an isochrone

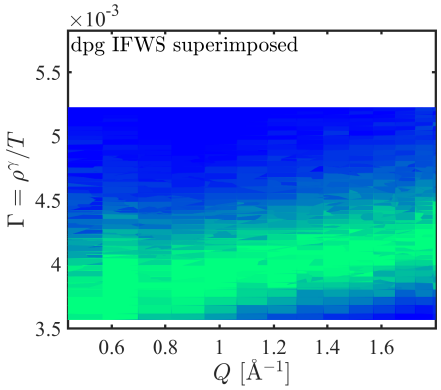


Figure 7.12: Superposition of the density scaled pressure scans shown in Fig. 7.11. A relaxation is observed to move through the instrumental window. The $Q$-dependence suggest this process is of translational character.

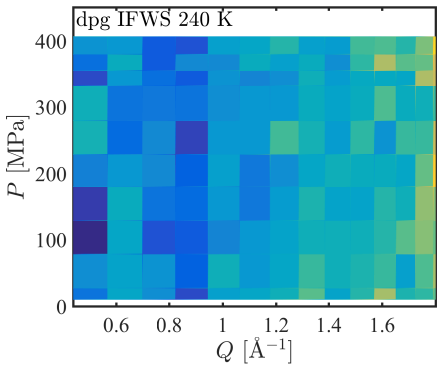


Figure 7.13: $Q$-dependence of the IFWS at $T = 240\,\mathrm{K}$ as a function of pressure from IN16B on DPG (Fig. 7.7).

on nanosecond timescale for the study of isochronal superposition in the next section (Sec. 7.3). We use $S(E = 0\,\mu\text{eV}) \approx 0.5$ and $S(E = 2\,\mu\text{eV}) \approx 0.065$ from the data summed over $Q$, located on the right side of the alpha relaxation maximum as seen in Fig. 7.7 to identify the isochrones. Only this time, we can use the dielectrics to check that the state points are isochronal on different timescales at the same time. We also use the dielectrics to make sure that we find the same state points on another spectrometer, IN6, for comparison (Sec. 7.3).

### Subconclusion

We have shown density scaling to work for two samples with different interaction, a van der Waals liquid and a hydrogen bonding liquid, for the dynamics related to the alpha relaxation in a fairly large range of temperature and pressure on the dynamic timescale of IN16B, i.e. nanoseconds. For the alpha relaxation, density scaling of the FWS for DPG seems to work better than for cumene, even if the overlap between the different pressure scans in $\rho^\gamma/T$ is somewhat smaller. The dynamics of DPG was extended up to milliseconds by using the combined cell for doing simultaneous dielectric and neutron spectroscopy. The values of $\gamma$ used for scaling with $\Gamma = \rho^\gamma/T$ are quite different in nature for the two samples. For cumene, we have used $\gamma = 4.77$ found from $T_g(P)$ measurements from [127], which was found to also apply for viscosity data from [97]. While for DPG, we have used $\gamma = 1.5$ from [68] based on dielectric data. The two sample-specific gamma values were found on dynamic timescales with experimental techniques very different from neutron spectroscopy, but both work well on the data from the two samples within this work.

The low value of $\gamma$ for DPG is quite typical for hydrogen bonding samples (e.g. [29]) compared to for example cumene with a $\gamma$-value which is more than thrice the size of that of DPG. On an absolute temperature scale, the two samples have a similar pressure response of the alpha relaxation. For DPG, we observe that density scaling breaks down for the intramolecular motion similar to what was observed for faster relaxations for the hydrogen bonding glass-former ternidazole in [138].

Density scaling is predicted from isomorph theory, as was described in Sec. 3.5. Isomorph theory turns the temperature-pressure phase diagram into one of one dimension where the governing parameter is $\Gamma = \rho^\gamma/T$, where the timescale of an experiment is determined from $\Gamma$. This is illustrated in Fig. 7.4 for cumene where the alpha relaxation at nanosecond timescales is seen at the same $\Gamma$-values for the three isotherms using a relatively high value of the scaling exponent, $\gamma$. This was also shown to work well for the alpha relaxation of DPG. By expanding the accessible timescales with the combined cell, for DPG, we did also fixed frequency plots. From the IFWS and the fixed frequency plots, we observed the alpha relaxation moving towards lower values of $\Gamma = \rho^\gamma/T$ on faster timescales.

We will now move on to study the dynamic behaviour along the isochrones determined from the fixed window scans on IN16B.

## 7.3 Isochronal superposition

We introduced isochronal superposition in Ch. 3.2, which is the invariance of dynamics along isochrones, i.e. for constant relaxation time, and implies that the relaxation time determines the shape of the spectrum. Isochronal superposition is another example of an experimentally observed phenomenon that can be explained in the view of isomorph theory. In this section, we will study the alpha relaxation dynamics on different timescales along isochrones and for comparison, along isobars and isotherms. In the temperature-pressure phase diagrams, the errorbars in pressure correspond to the pressure tolerance of the compressor and the uncertainty in temperature is given by the symbol size. The data in this section will be presented by sample: first the cumene data from IN16B and for the two different wavelength settings on IN5, next PPE data from IN5 with dielectrics, and then the DPG data from IN16B and IN6 with dielectrics.

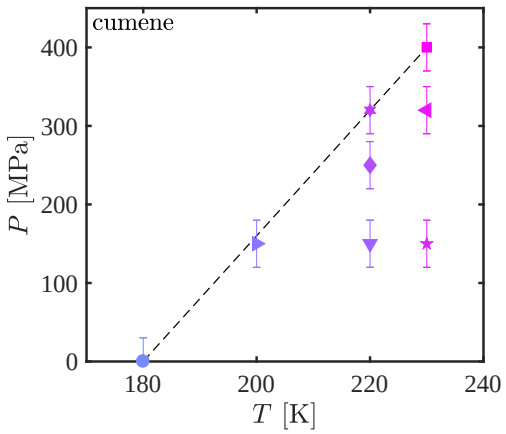


Figure 7.14: Phase diagram for cumene showing the state points as a function of temperature and pressure used on all spectrometers. Spectra were taken at IN16B and at IN5 for $\lambda = 8\,\text{Å}$ and $5\,\text{Å}$. The dashed line corresponsd to the isochrone determined from FWS on IN1B.

### Cumene

We will begin with the cumene data from IN16B. State points where spectra were measured are shown in the phase diagram in Fig. 7.14 as a function of temperature and pressure. The dashed line is a guide to the eye to illustrate the isochrone determined from the FWS also at IN16B (Sec. 7.2) with a gradient of $\mathrm{d}T_\alpha(P)/\mathrm{d}P = 0.125\,\mathrm{K\,MPa^{-1}}$. Spectra from IN5 on cumene that we will discuss below were acquired on the same state points.

First, to illustrate the effect of plotting in reduced units, we show the dynamic structure factor as a function of energy transfer for an isobar and an isochrone on an absolute energy scale and in the reduced energy units in Fig. 7.15. The effect of plotting the data in reduced units is barely visible at low energy transfer, but a

small effect is observed for higher energy transfer from the isochronal state points. Even if the effect is small, the spectra show slightly better superposition at higher energy transfer when they are plotted in reduced units. In consistency with isomorph theory, the data presented in this section will henceforth be shown in reduced energy units.

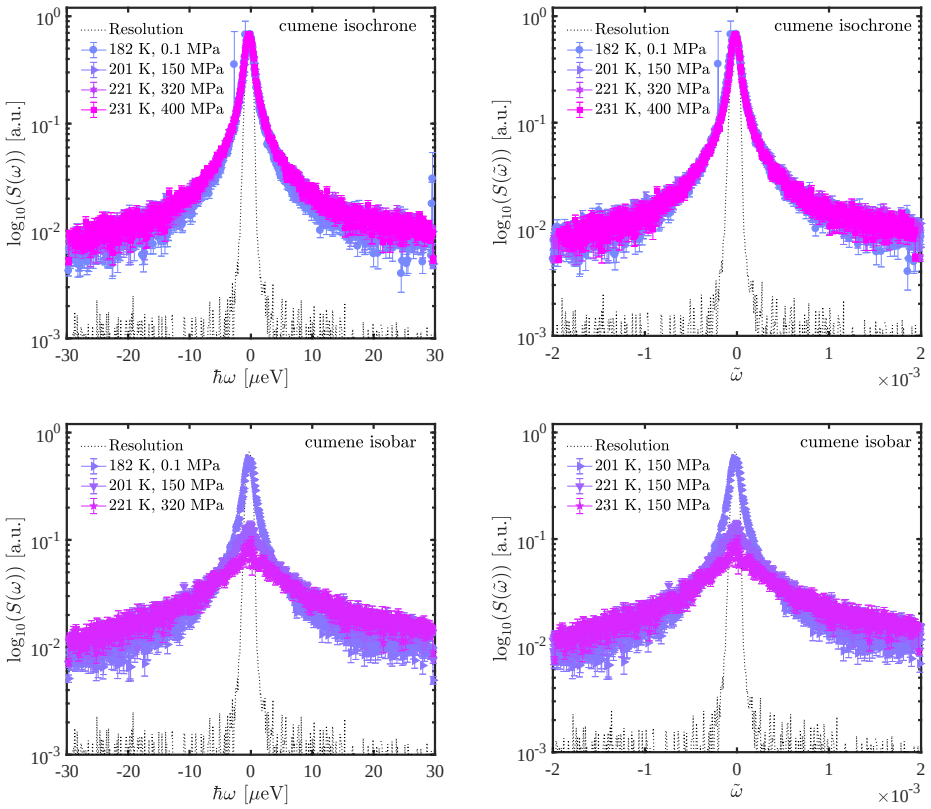


Figure 7.15: Spectra on cumene from IN16B summed over $Q$. Isochrone (top) determined from FWS intensity and an isobar (bottom) as a function of energy transfer on absolute energy scale (left) and in reduced units (right).

The data in Fig. 7.15 are shown on a semilog scale with the intensity on a logarithmic scale. This is a typical way of plotting neutron quasi-elastic spectra to enhance the effect of broadening to the eye, but the data can of course be presented in different ways, conveying different information, and we will therefore present data on both a linear scale, a lin-log scale and a log-log scale. In Fig. 7.16, we present spectra from IN16B from an isochrone, an isobar and an isotherm. From the data in Fig. 7.16, we observe an invariance of the nanosecond dynamics along the isochrone in all three data presentations. As the isochrone was determined from the fixed window scan that we assume gives an idea of the changes in the spectral shape from the intensities around the elastic line $E = 0\,\mu\text{eV}$ and in an inelastic energy window around $E = 2\,\mu\text{eV}$ from the same spectrometer, we would also expect the spectra along this isochrone to have the same shape.

The resolution function is scaled to the elastic intensity and therefore only shown

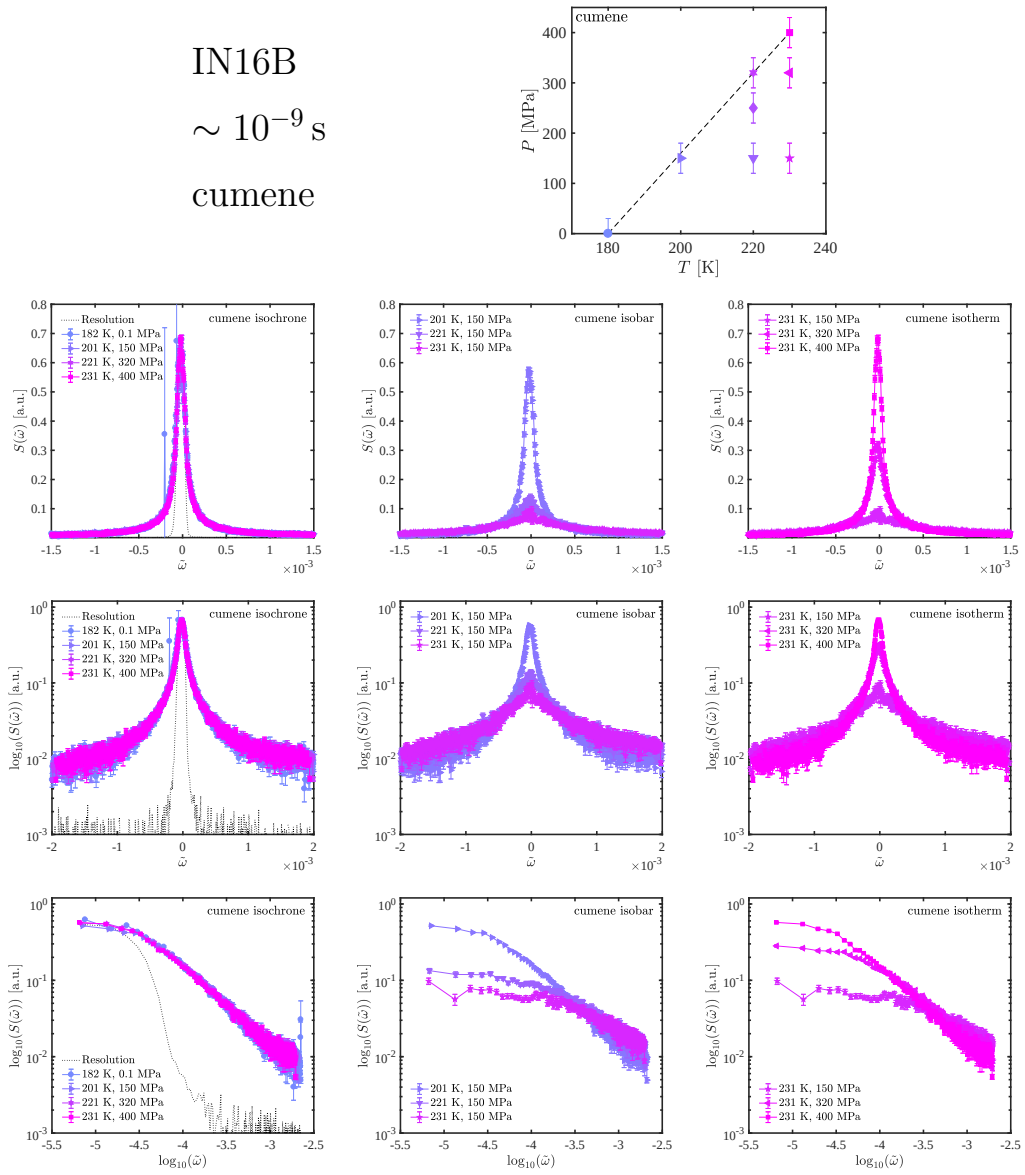


Figure 7.16: Spectra on cumene from IN16B. An isochrone determined from fixed window scan, an isobar at 150 MPa and an isotherm at 220 K are plotted on a linear scale (top panel), a lin-log scale (middle) and a log-log scale (bottom panel).

in the isochronal spectra. From the spectra along the isobar, we observe a clear change in dynamics on heating; more relaxation enters the instrumental window, until the elastic peak has practically disappeared and only broadening or relaxation is left. We observe a similar behaviour for the isotherm on releasing pressure; the elastic peak disappears and mainly relaxation is left in the instrument window. In the lin-lin representation, we have zoomed slightly in on the energy axis as there is not much information conveyed at high energy transfer here compared to the two log-representations.

We measured spectra at the same state points on IN5 at two different wavelengths, $\lambda = 8$ and 5 Å, corresponding to timescales of roughly $\sim 100$ ps and $\sim 10$ ps, respectively. The dynamics are shown in Fig. 7.17 and 7.18 for $\lambda = 8$ and 5 Å, respectively. The data from IN5 were done in the new combined pressure cell. But as we discussed above (Sec. 7.1), this is in the part of the phase diagram where there is only a constant signal left in the dielectrics, and we have therefore not been able to check from the dielectrics that the state points were indeed isochronal across the different instruments.

First, we present the 8 Å data in Fig. 7.17, where we have moved one order of magnitude in timescale compared to IN16B, visible from the energy transfer which is approximately a factor ten higher. The resolution is shown with the isochronal spectra. We observe the same overall trend at this spectrometer and timescale as we did on IN16B. The effects of changing pressure and temperature in the same intervals are less pronounces compared to the nanosecond dynamics (Fig. 7.16). We observe a decrease in the relaxational contribution and an increase of the elastic intensity upon increased pressure or cooling. The dynamics along the isochrone based on nanosecond dynamics from IN16B is to a good degree invariant, although the data from the two lowest temperature state points do not fall exactly on top of the two spectra at higher temperatures. We do not have dielectrics for these state points so we cannot check that we are in fact at exactly the same state points as IN16B. The changes in dynamics are, however, much larger for the data along the isotherm and isobar than the isochrone. We ascribe the small variance in the spectral shape for the isochronal state points to be from the difficulty in finding exact isochronal state points without the dielectrics.

In Fig. 7.18, the data from IN5 at $\lambda = 5$ Å is presented. This corresponds to an even shorter timescale with an energy resolution corresponding to $\sim 10$ ps. We notice that the invariance of dynamics along the isochrone found from FWS at IN16B is less convincing at this timescale, again the data from the two lowest temperature state points are not falling on top of the data from the two highest temperature state points along the isochrone. As we have again jumped an order of magnitude in timescale, the effects in changing temperature and pressure in this region of the dynamics are smaller. The alpha relaxation was observed in the middle of the instrument window on IN16B, which is two orders of magnitude slower, and we have thus moved further away in the phase diagram from the alpha relaxation. The isochronal overlap of spectra is not as convincing for the picosecond data as it was for the slower dynamics.

The general behaviour is the same as for the dynamics on the other two timescales; upon decreased pressure or heating more relaxation enters into the instrument win-

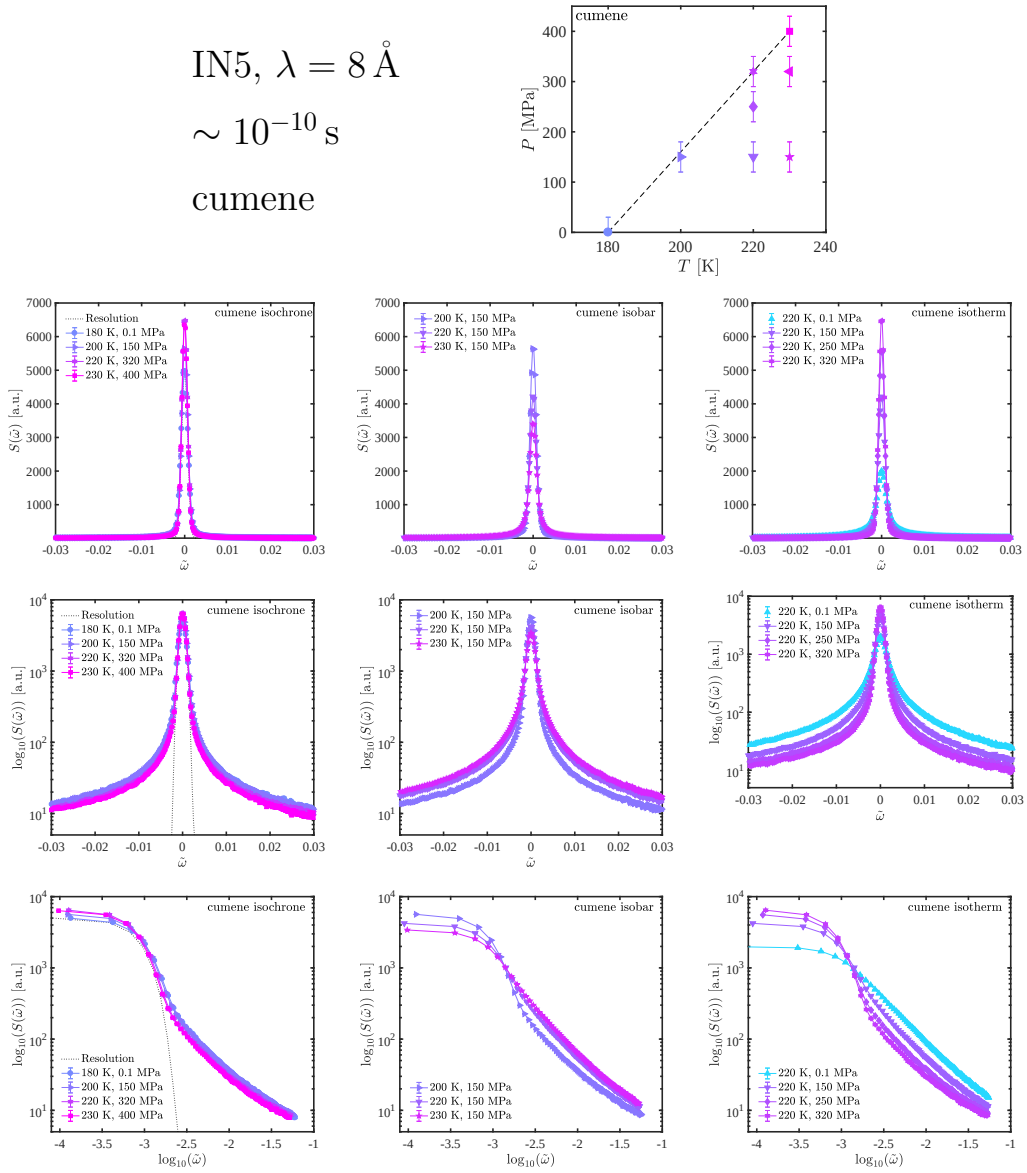


Figure 7.17: Spectra on cumene from IN5 at $\lambda = 8$ Å. Isochrone determined from fixed window scan on IN16B, isobar at 150 MPa and an isotherm at 220 K are plotted on a linear scale (top panel), a lin-log scale (middle) and a log-log scale (bottom panel).

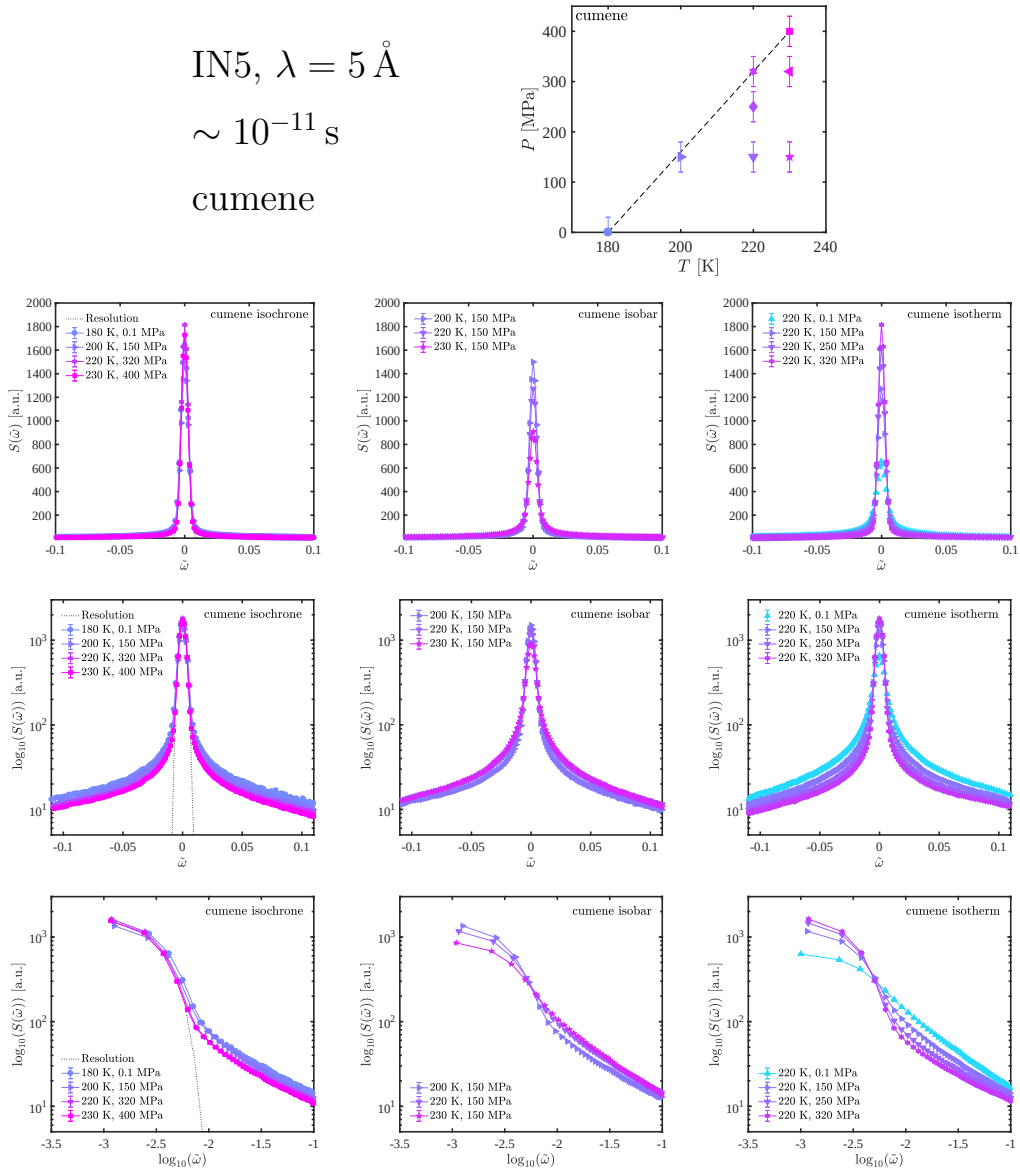


Figure 7.18: Spectra on cumene from IN5 at $\lambda = 5\,\text{Å}$. Isochrone as determined from fixed window scan on IN16B, isobar at 150 MPa and an isotherm at 220 K are plotted on a linear scale (top panel), a lin-log scale (middle) and a log-log scale (bottom panel).

dow. The change in accessible timescale on IN5 is in particular seen for the low pressure, high temperature state points in the isobars, where there is only little effect in changing pressure compared to IN16B. At IN16B, the elastic intensity was more or less gone, but from both IN5 datasets, the elastic intensity is still quite strong. The incomplete superposition could originate from short-range correlations from coherent elastic contributions in the Debye-Waller factor that would move towards lower $Q$ on increased pressure. But it is more likely related to why the combined high-pressure cell was build in the first place. The dynamics are very sensitive to the exact temperature and pressure conditions and comparing measurements for the same state points across different sample cells and instruments is challenging and requires high precision.

As mentioned above and in Sec. 7.1, the state points for cumene discussed here (Fig. 7.14) are close to the melting point and all out of reach for any relaxational process in the dielectrics. The dielectric signal is constant in this region and does therefore not provide much information. The dielectrics on IN5 for cumene at these high temperatures were therefore used merely to monitor the sample: to make sure pressure was properly transmitted and that crystallisation was avoided. The region of the phase diagram where there would be signal from the alpha relaxation in both techniques is kind of a no-man's land for cumene because of its tendency to crystallise. We will show below for PPE how precise we can find isochrones with the combined cell when the dielectrics can be utilised properly with signal from relaxation in dielectrics and in the picosecond dynamics from IN5.

We will analyse the $Q$-dependence of the Fourier transformed cumene spectra in the next section (Sec. 7.4) to find relaxation times for the state points presented above.

### PPE

PPE was measured in the combined cell at IN5 with $\lambda = 5\,\text{Å}$ in a temperature and pressure region, where we have signal in both techniques. The timescale of the neutron spectrometer is here again roughly 10 ps. The studied state points are shown in Fig. 7.19 as a function of temperature and pressure. We studied the dynamics along two isotherms at $T = 293\,\text{K}$ and 315 K. From the dielectric signal, we were able to identify two pairs of isochronal state points from the pressure scans along the two isotherms. The dielectric data of the two pairs, labelled A and B, is shown in Fig. 7.20. The two pairs of isochronal state points are connected by dashed lines in the phase diagram.

The alpha relaxation time of the isochronal state points is found from the maximum in the dielectric loss peak and gives roughly $\tau_\alpha \approx 10^{-2}\,\text{s}$ and $10^{-6}\,\text{s}$ for isochrone A and B, respectively. With isomorph theory in mind, we should in principle locate isochrones from the dielectrics represented as a function of frequency in reduced dimensionless units. However, in Fig. 7.20, we show that it does not change the relative position nor the shape of the dielectric spectra to plot the loss peaks as a function of the dimensionless reduced frequency. We, therefore, conclude that we can determine meaningful isochrones with respect to isomorph theory from the alpha relaxation loss peak from dielectrics as a function of frequency on an absolute

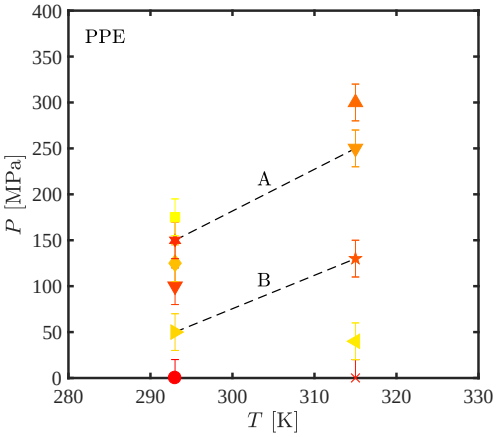


Figure 7.19: Phase diagram in temperature and pressure for PPE dielectics and spectra from IN5 $\lambda = 5\,\text{Å}$. The dashed lines are isochrones determined from dielectrics.

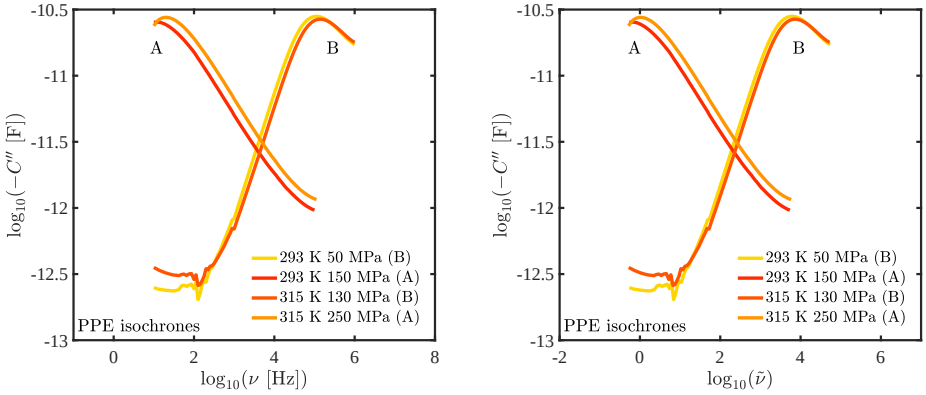


Figure 7.20: Two pairs of isochronal state points determined from the dielectric loss peak on PPE measured on IN5, $\lambda = 5\,\text{Å}$. Relaxation time for isochrone A is $\tau_\alpha \approx 10^{-2}\,\text{s}$ and for B $\tau_\alpha \approx 10^{-6}\,\text{s}$. Right: dielectric data plotted as a function of frequency in reduced units.

energy scale as measured in Hertz.

The pressure gradients for the two isochrones, A and B, are $\mathrm{d}T_\alpha(P)/\mathrm{d}P = 0.22\,\mathrm{K\,MPa^{-1}}$ and $0.275\,\mathrm{K\,MPa^{-1}}$, respectively. Please note that the slope of the isochrones as they are depicted in the phase diagram of Fig. 7.19 is the inverse of the stated pressure gradients $\mathrm{d}T_\alpha(P)/\mathrm{d}P$. We note that the slower the alpha relaxation time, the steeper (flatter) the isochrone in the temperature-pressure (pressure-temperature) phase diagram will be, also comparing to the pressure dependence of the glass transition isochrone, $\mathrm{d}T_g(P)/\mathrm{d}P = 0.18\,\mathrm{K\,MPa^{-1}}$. This means that the slower the alpha relaxation, the more pressure dependent it is. Out of the three samples studied here, PPE is the one with the highest fragility, the highest pressure dependence of the dynamics and highest value of $\gamma$.

The neutron spectra from IN5 on PPE are presented in Fig. 7.21. Spectra along the two isochrones A and B are shown in the left column, while the two isotherms at 293 K and 315 K are shown in the centre and right column, respectively. The spectra are again shown in three different representations. The resolution function is shown in the isochrone plots.

We observe the same dynamic behaviour along the two isotherms as we did for cumene: on increased pressure, the dynamics becomes slower and less relaxation is in the instrument window. The behaviour of the two isochronal state points follows the relaxation time found from the dielectrics. The isochrone with the slowest relaxation time, A, has a higher elastic intensity and less broadening, compared to B which has a shorter alpha relaxation time. We observe a complete invariance in the spectra from the two sets of isochronal state points in the left column in all three data representations. This serves as an example of how precise we can do experiments in temperature and pressure when we have the dielectric data as a complement to the neutron data.

An interesting observation from the isochronal state points, which is clear from the logarithmic plots, is that while we have the dielectric loss peak in the frequency window of the dielectrics, we also observe a clear broadening around the elastic resolution in the neutron spectra at picosecond timescale. We can imagine extending the loss peak tails of the alpha relaxation in the dielectrics in Fig. 7.20 out to frequencies of around $10^{10}$ Hz and that the tail of the alpha relaxation is what is visible as a broadening in the time window of IN5.

The PPE spectra show isochronal superposition on a large range of timescales. From alpha relaxation determined to be $10^{-2}$ s and $10^{-6}$ s from dielectric spectroscopy, we observe that spectra on picosecond dynamics superimpose completely. The broadening we observe on picosecond timescale at IN5 for PPE could suggest that a tail of the alpha relaxation is stretched out in time and can be observed across many orders of magnitude, or at least that the dynamics observed on picosecond timescale is somehow related to the much slower alpha relaxation.

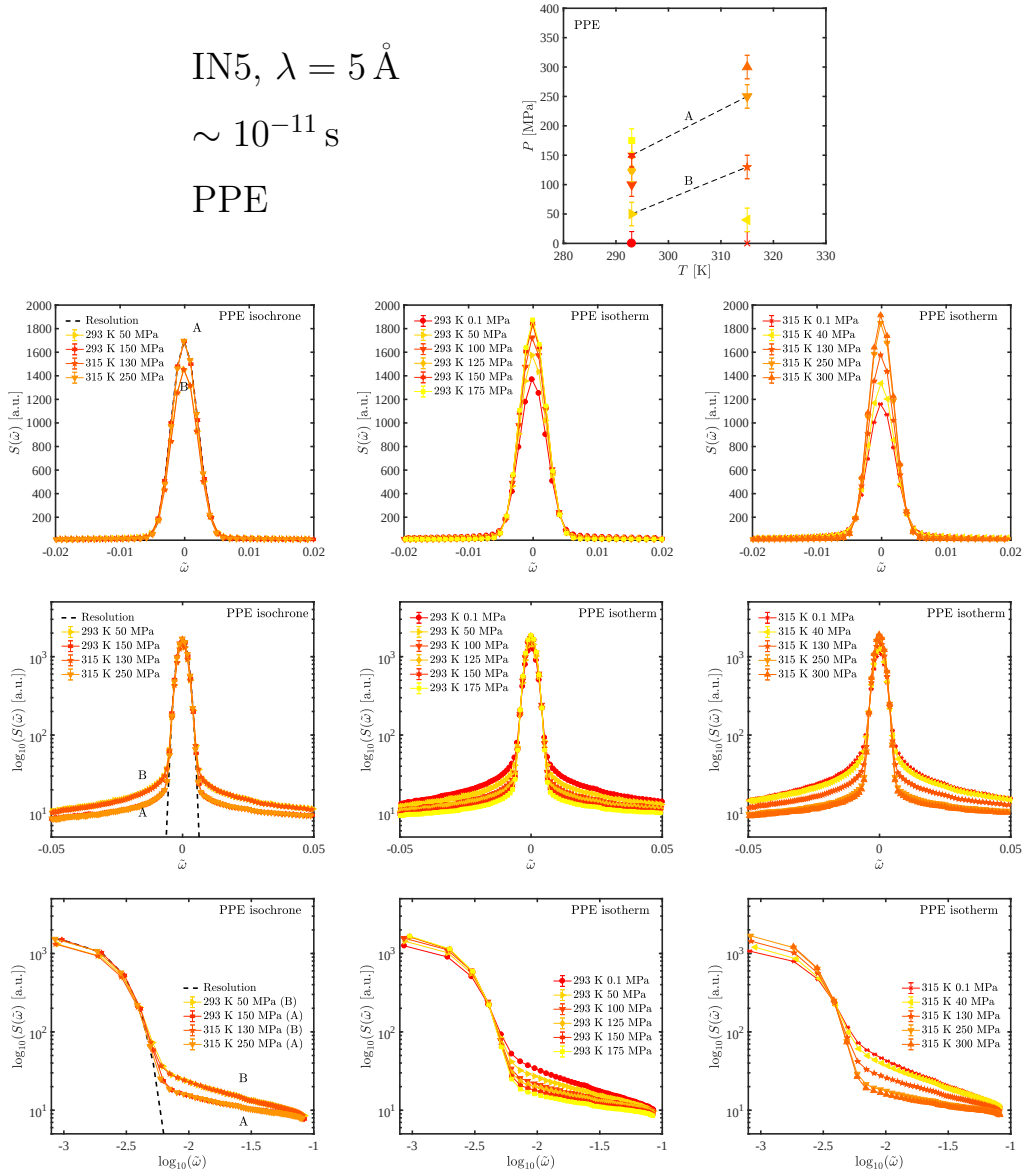


Figure 7.21: Spectra on PPE from IN5 at $\lambda = 5$ Å. Left: Two isochrones found from dielectrics. Centre and right: isotherms at 293 K and 315 K, respectively, plotted on linear (top panel), lin-log (middle) and log-log (bottom panel) scales.

## DPG

DPG was measured in the combined high-pressure cell for doing simultaneous dielectric and neutron spectroscopy. The temperature-pressure phase diagram in Fig. 7.22 contains the state points for which full spectra have been taken on IN16B and IN6 for DPG. The dashed line corresponds to the isochrone as determined from the fixed window scans on IN16B (Fig. 7.7) and from the simultaneous dielectric measurement. Dielectric data are as shown in Fig. 7.23 for the three isochronal state points and for the neighbouring state points where spectra were also taken at IN16B for comparison. The pressure gradient of the isochrone is $\mathrm{d}T_\alpha(P)/\mathrm{d}P = 0.0875\,\mathrm{K\,MPa^{-1}}$. In the dielectrics, the DC conductivity is visible for all state points and for almost all of them, the tail of the alpha relaxation is just visible. We use the tail of the alpha relaxation time and the conductivity to estimate the alpha relaxation time using time-temperature superposition. As discussed previously in Sec. 7.2 for the fixed window pressure scans on DPG, the change in minimum with temperature and pressure between the conductivity and the alpha relaxation suggest that the two processes are decoupled, however, we will use the time-temperature superposition for a somewhat crude estimate of the relaxation time here.

The estimated loss peak in the dielectrics for the isochronal state points is located roughly at $\log_{10}(\nu_{\max}) \approx 7.5$, which corresponds to a relaxation time of a few nanoseconds and coincides with the timescale of IN16B, in agreement with our interpretation of the IFWS in Fig. 7.7. The estimated relaxation time for the state point at ambient pressure along the isochrone, $T = 280\,\mathrm{K}$, is also in agreement with literature data [15].

We observe from the dielectric spectra that the three isochronal state points determined from the FWS on IN16B have the same minimum between the DC conductivity and the alpha relaxation. It seems that even if the two processes are decoupled, they have the same isochrone. This is in agreement with what we would expect from isomorph theory for isomorphs.

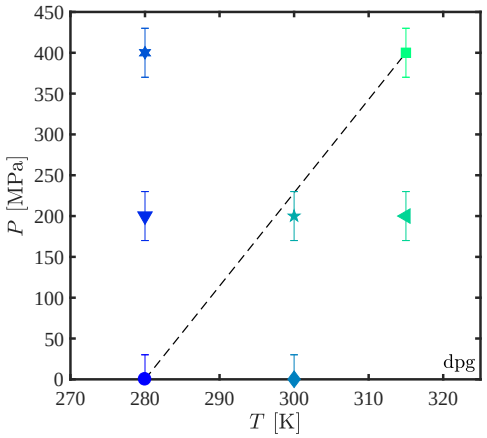


Figure 7.22: Phase diagram in temperature and pressure for DPG spectra from IN16B and IN6. The dashed line correspond to the isochrone determined from the FWS on IN16B and dielectric data.

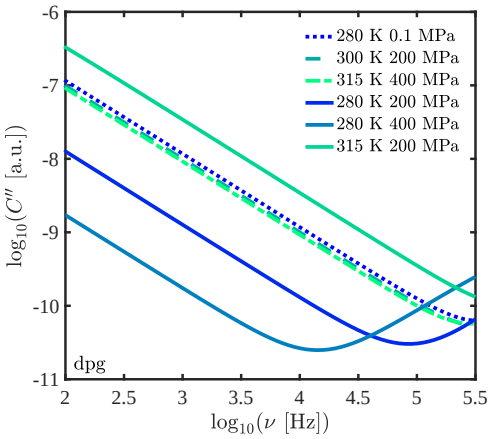


Figure 7.23: Imaginary part of dielectric signal from the different state points on IN16B. The state points represented by the dashed and dotted lines are isochronal state points determined from FWS (Fig. 7.7). Full lines are neighbouring state points for comparison.

In Fig. 7.24, we present the full spectra from IN16B. In the first column, we show the isochrone determined from the FWS, also in IN16B (Fig. 7.7), and the dielectrics (Fig. 7.23), in the second and third column are shown for comparison an isobar and an isotherm, respectively.

We present the data in three different representations again, and we observe the same kind of behaviour as was seen for the nanosecond dynamics for cumene: the dynamics are to a good degree invariant along the isochrone, while the dynamics change for the isobar and the isotherm in the same way as we observed for the two other samples, where the alpha relaxation was observed to dominate for higher temperature and lower pressure, while the elastic intensity goes down. This is in particular visible from the data on the isotherm. There is a small offset in the elastic intensity between the isochronal state points, best seen in the log-log representation, although these changes are small compared to the changes observed along the isobar and the isotherm.

Most of the state points that were studied at IN16B were also studied at IN6 at $\lambda = 5.12\,\text{Å}$ with an elastic energy resolution corresponding to a timescale of $\sim 60\,\text{ps}$. The spectra are shown in Fig. 7.25. The dielectrics were used to make sure that we were found the same state points as on IN16B, which is especially important along the isochrone. For the IN6 data on DPG, we see a trend similar to that observed for the IN16B spectra, the two isochronal state points do not overlap completely, but they vary less than the spectra taken along the isobar and isotherm. Just as was observed for cumene, where the alpha relaxation dynamics was also in the IN16B instrument window for the studied state points, changes in temperature and pressure on faster timescales have a less pronounced effect, suggesting that a smaller fraction of the alpha relaxation is visible on the IN6 picosecond timescale in this part of the temperature-pressure phase diagram compared to IN16B.

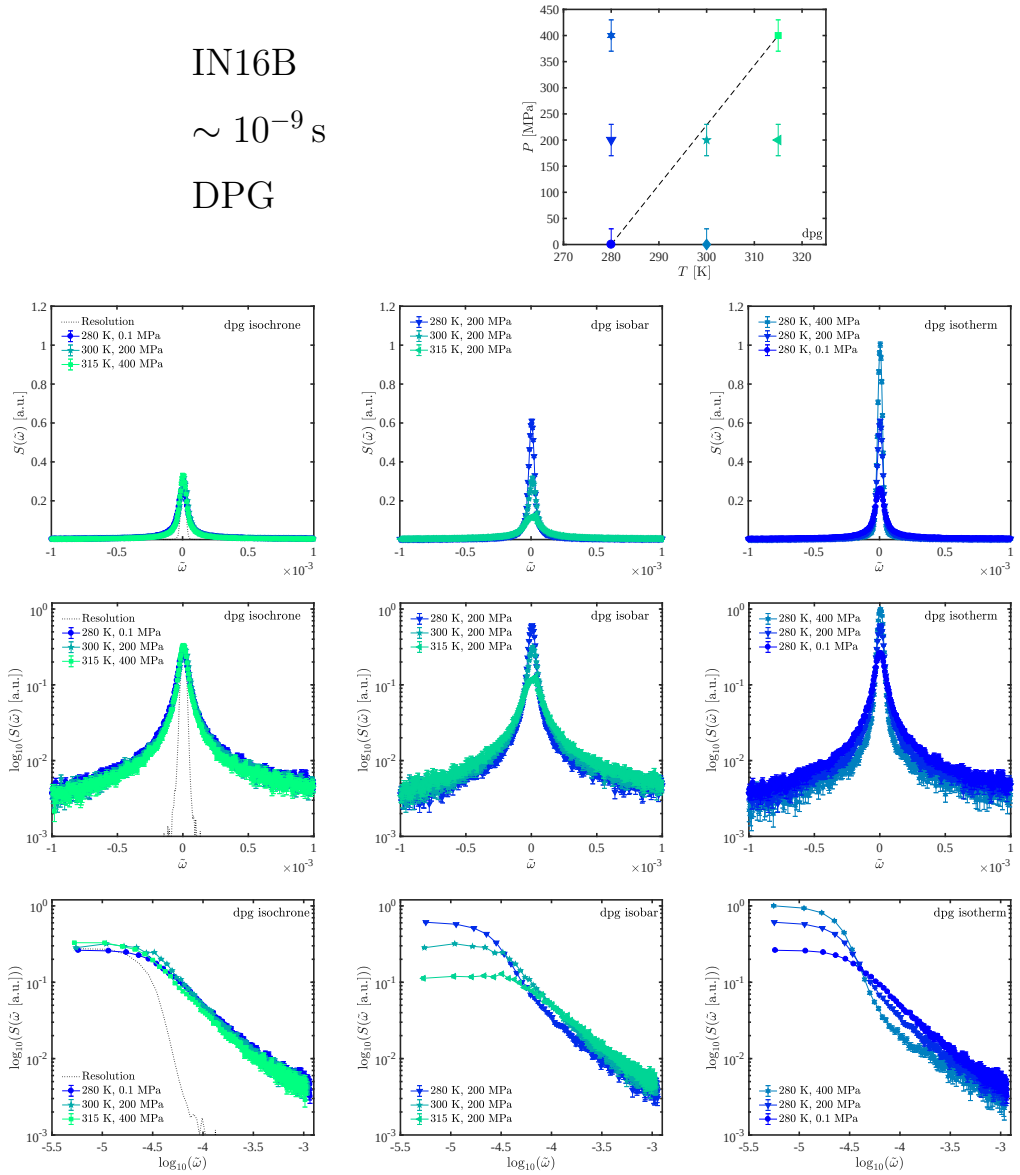


Figure 7.24: Spectra on DPG from IN16B from an isochrone determined from FWS and dielectrics (left column), an isobar (centre column) and an isotherm (right column) shown on linear (top row), lin-log (middle row) and log-log scales (bottom row).

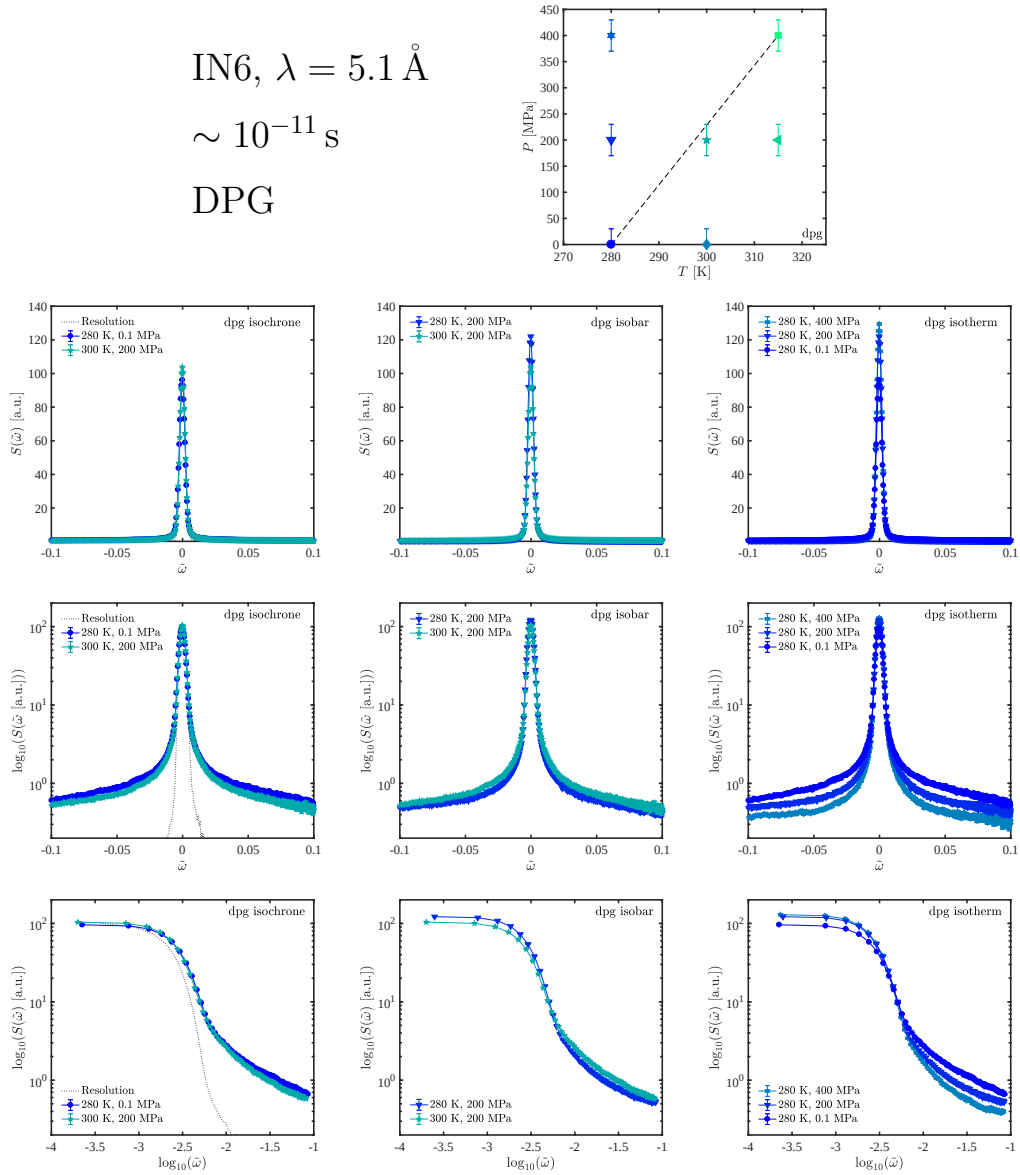


Figure 7.25: Spectra on DPG from IN6 from an isochrone (left column) determined from FWS on IN16B and dielectrics, an isobar (centre column) and an isotherm (right column) shown on linear (top row), lin-log (middle row) and log-log scales (bottom row).

### Subconlusion

In this section, we looked into isochronal superposition and found for all three samples to a good approximation of isochronal superposition. PPE was the most convincing example, a van der Waals liquid, for which isochronal superposition was shown to hold for picosecond dynamics and the dielectric data for alpha relaxation time up to roughly $10^{-2}$ s, i.e. isochronal superposition on the same state points separated by roughly ten orders of magnitude on dynamic timescales. For cumene, which is also a van der Waals liquid, this was shown to apply on timescales on nano- and picosecond from the three different neutron instrumental settings, unfortunately we could not use the dielectrics to find the exact isochronal state points. For the hydrogen bonding system DPG, we observed the same tendency as was seen for cumene, that isochronal superposition works quite well in this region of the phase diagram where the alpha relaxation is in the instrument window of IN16B. Like for cumene, it does not work perfectly, but quite well. Isochronal superposition for DPG was also observed on the timescales of the dielectrics, spanning ten orders of magnitude in dynamics.

In the region of the temperature-pressure phase diagram treated in this and the previous section on density scaling, the alpha relaxation is the dominating contributor to the dynamics. For the purpose of testing isomorph theory, we have shown that isochronal superposition applies to the dynamics related to the alpha relaxation spanning timescales from milli- to picoseconds both for the two van der Waals liquids and the hydrogen bonding sample that we have tested. This suggests that isomorph theory is perhaps more robust than we expected or that there exists a more fundamental explanation of isochronal superposition. From isomorph theory, we expected isochronal superposition to work for the van der Waals systems that are regarded $R$-simple (Sec. 3.5), i.e. they have no directional bonding and show no large secondary relaxations. The hydrogen bonding system is on the other hand not expected to be $R$-simple, and thus to follow the predictions from isomorph theory. In this study, the hydrogen bonding system represents a class of liquids with strong directional bonding, which from an isomorph theory point of view is predicted to break down, for example by not showing isochronal superposition. Experimentally, it is difficult to make a measure of how well isochronal superposition works, and how well it works will depend on the lens of the looking glass in hand. This is quite clear from for example the DPG spectra from IN6, where there are only few state points to compare, and the pressure and temperature induced effects in the spectra are rather small.

Roed et al. [133] compared the degree of isochronal superposition from several systems, including both van der Waals liquids and hydrogen bonding liquids, in a very detailed study of the shape of the dielectric loss peak where they were able to define a measure of how well the isochronal spectra superimposed. They found that isochronal superposition worked better for the van der Waals liquids than the hydrogen bonding liquids. Unfortunately, the neutron scattering spectra do not allow for the same kind of detailed study because of the more scattered data with less statistics and therefore noisier. We will therefore based on the data presented in this section, join a recent group of papers that agree that isochronal superposition

works quite well also for hydrogen bonding samples, in particular on the alpha relaxation dynamics [2, 138]. We will in Sec. 7.3 revisit isochronal superposition on picosecond timescales close to the glass transition where the alpha relaxation is completely out of the neutron instrument window. But we will first determine the timescale of the alpha relaxation on cumene from the Fourier transformed spectra.

## 7.4 Fourier transform to time domain

The cumene data that was presented in the previous section was taken in a region of the phase diagram where the relaxation time is outside the dielectric frequency window. We will instead find the relaxation time of the spectra from the Fourier transformed data and compare the obtained values to light scattering data analysed in the mode-coupling view [97]. In Ch. 4.4, we described how it is possible to go from the frequency-dependent dynamic structure factor, $S(Q,\omega)$, to the time-dependent intermediate scattering function $I(Q,t)$. The convolution of the dynamic structure factor and the energy resolution provides the measured dynamic structure factor

$$S_{\text{meas}}(Q,\omega) = S(Q,\omega) \otimes R(Q,\omega). \tag{7.11}$$

Taking the measured dynamic structure factor into the time domain, the convolution of the resolution and the actual dynamic factor turns into a product:

$$F(Q,t) = I(Q,t)R(Q,t). \tag{7.12}$$

The intermediate scattering function can then be found by dividing the Fourier transformed signal with the resolution function. The data can then in principle be fitted with an appropriate model, where the resolution has been eliminated from data and the fitting procedure. In theory, this is a cleaner way of analysing the data, e.g. [40, 81]. However, in practice, information is lost on doing numerical Fourier transformation, and the transformed data is prone to artefacts for example due to cut-off effects in energy. We will, however, make an attempt in this section.

As we saw from the FWS previously in this chapter (Fig. 7.4), the alpha relaxation dynamics probed with neutron scattering is $Q$-dependent. The relaxation time found from neutron scattering will therefore, of course, also be $Q$-dependent as we shall see below. The length scale dependence of the relaxation time is an example of how different the nature of the information accessible from dielectric and neutron spectroscopy is. In the previous section, we were not concerned with the $Q$-dependence for investigating isochronal superposition. The dynamics on an isomorph should be invariant on all length scales according to isomorph theory, and we therefore expect in invariance of the dynamics also as a function of $Q$ on an isochrone. Given the relatively small range that we cover and that scaling is only with density (Eq. 7.3), we ignore that the length scale, according to isomorph theory, should be presented in reduced units.

The intermediate scattering function from the energy gain side obtained by Fourier transform of the cumene data is shown for a state point in Fig. 7.26 for the entire available $Q$-range for the settings used in this work. The IN5 data taken with $\lambda = 5\,\text{Å}$ span timescales from $\log_{10}(t) \approx -13.2$ to $-11.5$ in the $Q$-range from 1.2 to

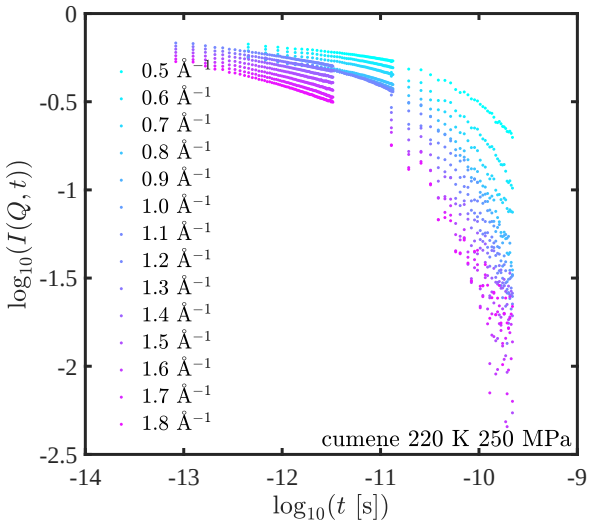


Figure 7.26: $Q$-dependence of Fourier transformed cumene spectra at 220 K 250 MPa from IN16B and IN5, $\lambda = 8$ Å and 5 Å. See text for details.

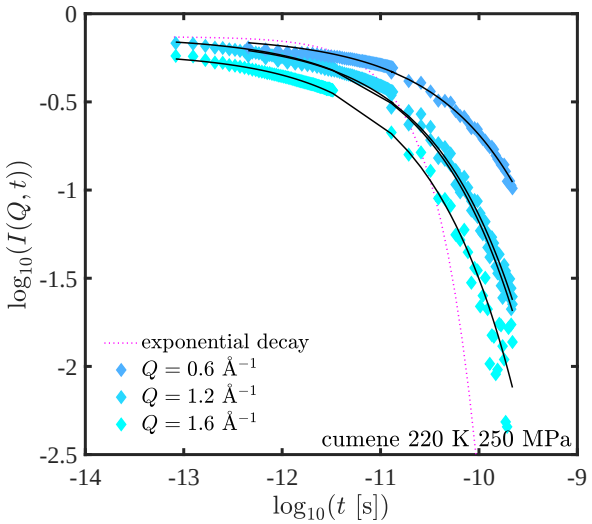


Figure 7.27: Example of fits of a strectched exponential to the Fourier transformed cumene data at three different $Q$-values at 220 K 250 MPa. Two curves are fitted to the two 1.2 Å$^{-1}$ data set. The dotted pink line is an exponential for comparison.

.

$1.8\,\text{Å}^{-1}$, the $\lambda = 8\,\text{Å}$ data spans timescales $\log_{10}(t) \approx -12.4$ to $-10.8$ in the $Q$-range from 0.5 to $1.2\,\text{Å}^{-1}$, while the IN16B data spans timescales from $\log_{10}(t) \approx -9.5$ to $-10.9$ in the entire $Q$-range, in the interval from 0.5 to $1.8\,\text{Å}^{-1}$, which coincides with the two sets of IN5 data. The data on longer timescales from IN16B is more scattered in intensity than the IN5 data; a combination of the fact that more relaxation is in the IN16B window, causing a lower intensity, and that we in general have worse statistics for the IN16B data. The IN5 data at $\lambda = 5\,\text{Å}$ and the IN16B data have been normalised to their respective low-temperature sample resolution. The levels in intensity agree well for those data. We did not measure the sample resolution at low temperature for the IN5 data at $\lambda = 8\,\text{Å}$, and we therefore only have the resolution measured with vanadium, which does not give the right level in intensity compared to the other data. The Fourier transformed $\lambda = 8\,\text{Å}$ data from IN5 has therefore been shifted in the log-log plot, corresponding to multiplying by a scaling factor, to fit the data from IN5 at $\lambda = 5\,\text{Å}$ and IN16B. The same $Q$-dependent scaling factor have been used for all the IN5 data taken with $\lambda = 8\,\text{Å}$. We show an example of the $Q$-dependence of the relaxation in Fig. 7.26, where the intermediate scattering function is observed to decay faster for higher values of $Q$, corresponding to shorter timescales.

In Fig. 7.27, we show an example of fits to the data with a stretched exponential, the phenomenological Kohlrausch-Williams-Watts (KWW) function for three values of $Q$:

$$I_w(Q,t) = A_w e^{-(t/\tau_w)^\beta}, \tag{7.13}$$

with an amplitude $A_w$, a characteristic relaxation time $t_w$, and the stretching parameter $\beta$ that determines the shape of the function, i.e. the deviation from exponential behaviour. In Fig. 7.27, the dotted pink line illustrates an exponential function, which clearly does not mimic the shape of the relaxation. For all of the state points and $Q$ values, the stretching parameter was first left as a free fitting parameter, returning values around $0.5 \pm 0.1$. The stretching parameter $\beta$ was therefore fixed at 0.5 to eliminate one free parameter, leaving only two fitting parameters, the amplitude $A_w$ and the relaxation time $\tau_w$. A constant stretching parameter is a stronger statement than isochronal superposition because it implies that the shape of the relaxation for all state points and values of $Q$ is constant. We will return to the value of the stretching parameter in the comparison below to light scattering data [97]. The data at $Q = 1.2\,\text{Å}$ is at the only $Q$-value where there is overlap between the IN5 data at $\lambda = 5\,\text{Å}$ and $8\,\text{Å}$ in this energy range. For consistency, to make sure there is agreement between the two data sets constructed from IN5 data at $\lambda = 5\,\text{Å}$ and IN16B data at low $Q$ and IN5 data at $\lambda = 8\,\text{Å}$ and IN16B data at high $Q$, respectively, we check in Fig. 7.27 that the two fits match at $Q = 1.2\,\text{Å}$ where there is an overlap.

All spectra from the state points shown in the phase diagram in Fig. 7.28 have been Fourier transformed and are presented in Fig. 7.27. These were the same state points that were presented in the isochronal study (Sec. 7.3) summed over $Q$. In Fig. 7.29, for $Q = 1.2\,\text{Å}$ where there is overlap in $Q$, we present the Fourier transformed data from IN5 at $\lambda = 5$ and $8\,\text{Å}$ and IN16B, along an isochrone, an isobar and two isotherms. These are data from the same state points as the spectra

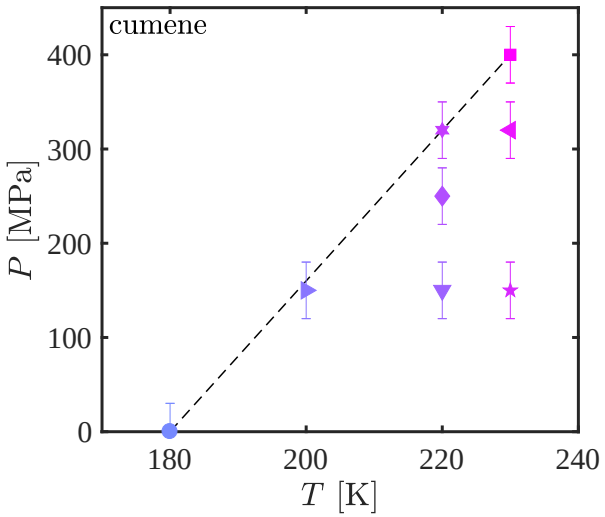


Figure 7.28: Phase diagram in temperature and pressure of cumene for the Fourier transformed spectra from IN16B and IN5 with $\lambda = 8\,\text{Å}$ and $5\,\text{Å}$.

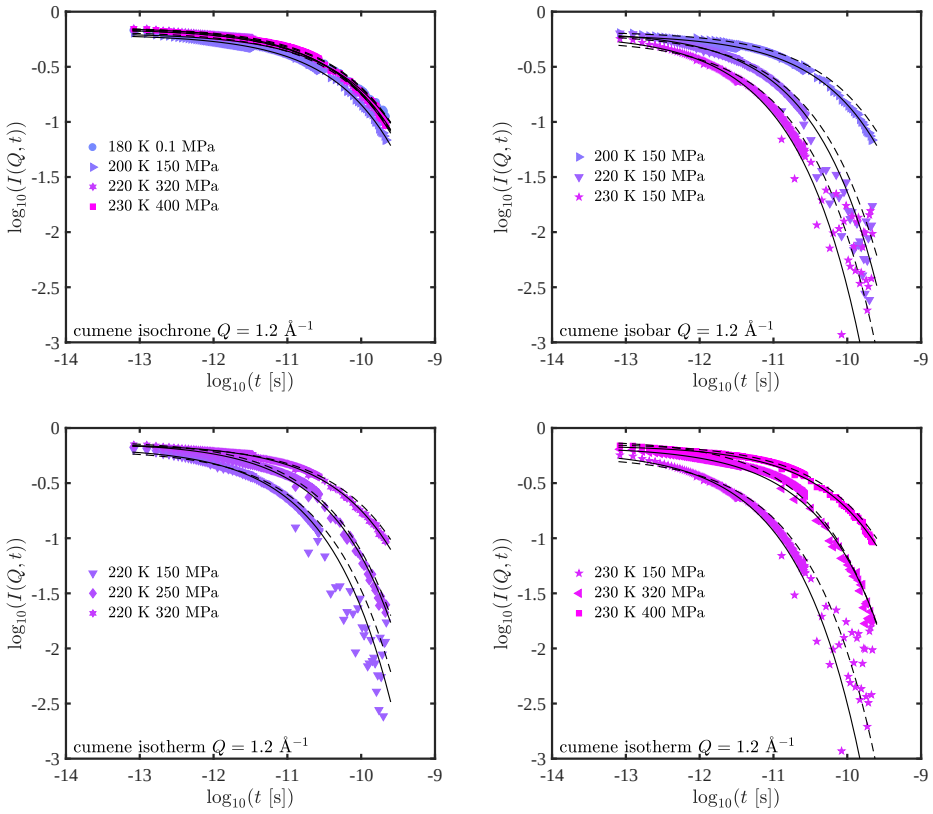


Figure 7.29: Fourier transform of cumene spectra from IN16B and IN5 with $\lambda = 5\,\text{Å}$ and $8\,\text{Å}$ for $Q = 1.2\,\text{Å}^{-1}$. Full line is fit to data from IN16B and IN5 with $\lambda = 5\,\text{Å}$, and dashed line is fit to data from IN16B and IN5 at $8\,\text{Å}$.

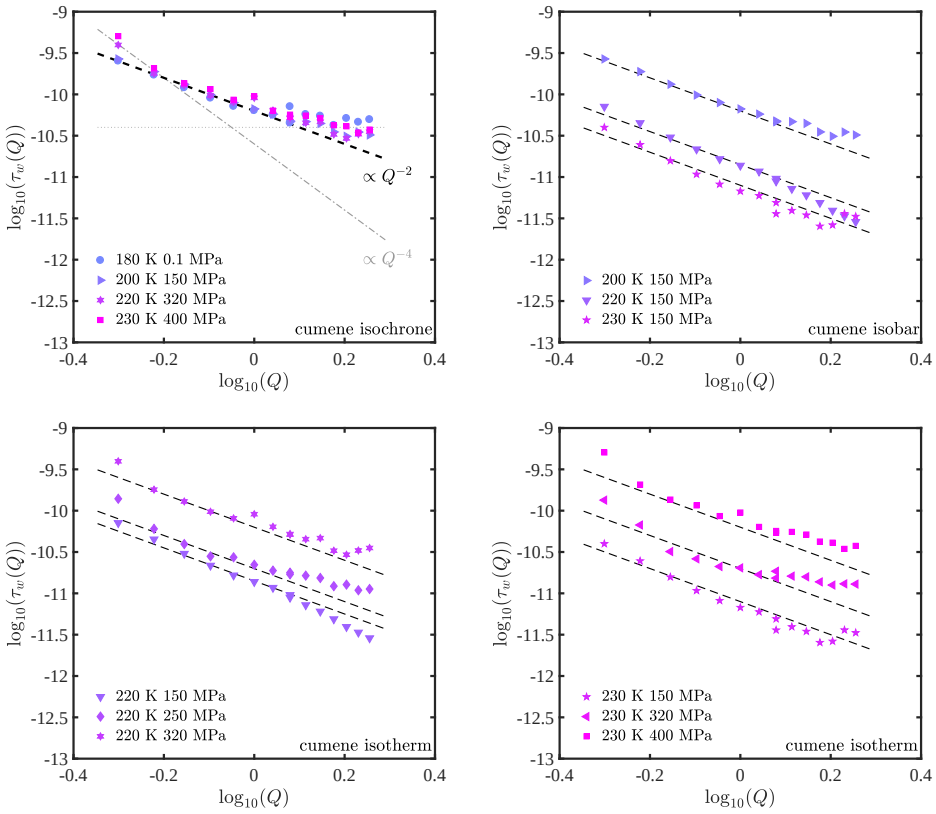


Figure 7.30: The relaxation time $\tau_w$ as a function of $Q$ for cumene obtained from a stretched exponential fit to the Fourier transformed spectra from IN5 and IN16B along an isochrone, an isobar and two isotherms. The dashed lines corresponds to a $Q^{-2}$ dependence of the relaxation time.

in Fig. 7.16, 7.17 and 7.18.

As in the frequency domain in the previous section, we observe a high degree of invariance in dynamics along the isochrone. The superposition is not perfect, but the intermediate scattering function is more or less constant along the isochrone. The same dynamic behaviour is observed as in the spectra in Fig. 7.16, 7.17 and 7.18, the alpha relaxation becomes faster and more relaxation is visible in the instrument windows on increased temperature or decreased pressure.

The relaxation time is found from fits of Eq. 7.13 to the cumene data as a function of $Q$. Examples of fit to the data are shown in Fig. 7.29 for $Q = 1.2\,\text{Å}$, the only value of $Q$ where there is overlap in $Q$ for these spectra. We observe that while the two fits done to the two data sets, one from IN16B and IN5 with $\lambda = 5\,\text{Å}$, and one from IN16B and IN5 with $8\,\text{Å}$, in most cases agree well with each other and the data, there is some scatter in the IN16B data at 220 K 150 MPa and 230 K 150 MPa. Going back to the IN16B spectra in Fig. 7.16, the elastic peak is almost out of the energy window. It seems like there could be a small problem with the subtraction of the empty cell along the elastic line which would then transfer into the time-domain. We have used the empty cell measured at the highest temperature, i.e. lowest background signal, for these state points. The fitting of the data at these two state points is done to the IN5 data.

The relaxation time as a function of $Q$ obtained from the fits are presented in Fig. 7.30. We observe to a good approximation the same behaviour along the four isochronal state points. We observe a clear change in relaxation time with $Q$ at all the state points, which is close to linear in a large range of $Q$ with a slope close to $-2$. For the highest $Q$-values, the relaxation time seems to bend off from a $Q^{-2}$-dependence to nearly constant values of $\tau_w$. The $Q^{-2}$-dependence suggests Gaussian behaviour and the bending suggest that this does not hold for large values of $Q$. Colmenero and Arbe [41] observed for both molecular liquids and polymers at low $Q$-values a $Q^{-2/\beta}$ dependence that at high $Q$-values becomes a $Q^{-2}$ dependence in the same overall $Q$-range. This would in this case correspond to a $Q^{-4}$ dependence. They ascribe the difference in slope to heterogeneous and homogeneous nature of the diffusion. For some of the state points, there could perhaps be a small tendency to a change in slope at low $Q$ that would suggest another $Q$-dependence. But it is not clear if this change of slope is true for the dynamics in cumene in this region.

We compare the relaxation times found in Fig. 7.30 to those found from other techniques. In Fig. 7.31, we compare relaxation times found from high-pressure light scattering data from Li et al. [97] and own ambient pressure dielectric data. The relaxation time is shown for the lowest value of $Q = 0.5\,\text{Å}^{-1}$, as this is the $Q$-value closest to that used in the light scattering data. The relaxation times found from the neutron data fits well into the general trend of the relaxation times. Fig. 7.31 illustrates density scaling of the alpha relaxation on timescales separated by more than 12 orders of magnitude from three different techniques using the same value of $\gamma = 4.77$ that was found from viscosity data [127] and used also on the glass transition isochrone up to very high pressure, above 4 GPa.

Li et al. [97] also assumed an invariant shape of their spectra in their mode-coupling analysis of the light-scattering data. The found values for the mode-coupling parameter, $\gamma_{\text{mct}} = 1/(2a) + 1/(2b)$, where $a$ and $b$ are fitting parameters

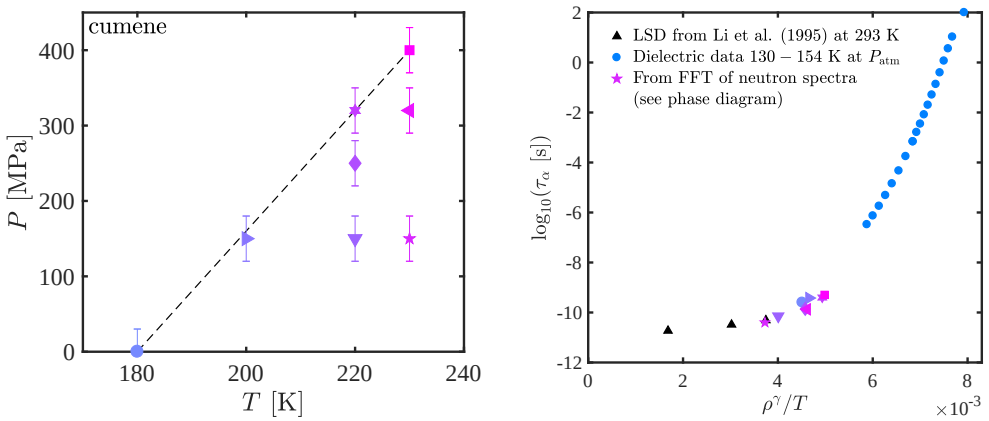


Figure 7.31: Density of the alpha relaxation time for cumene spanning more than 12 orders of magnitude in relaxation time and including data from three different techniques. Blue circles are form ambient pressure dielectric data. Black triangles are obtained from high-pressure light scattering data [97]. The relaxation time found from the Fourier transformed spectra from IN16B and IN5 are shown from the different $(T, P)$ state points. Consult phase diagram for symbol, colour and corresponding temperature and pressure.

and related to a critical point in the susceptibility. The found the same fitting parameters for isobaric and isothermal data. They reported the values $a = 0.28$ and $b = 0.48$. They reported a value for the parameter $\lambda$ that according to Götze et al. [64] is directly related to stretching parameter $\beta$ from the stretched exponential (Eq. 7.13) through the relation

$$\beta = \frac{-\log 2}{\log(1-\lambda)}. \tag{7.14}$$

From the reported value of $\lambda = 0.8$ by Li et al., one obtains $\beta = 0.43$. This is not exactly $\beta = 0.5$ as was chosen for this study, but also not very far away, and it supports the idea of fixing the stretching parameter in temperature and pressure.

Götze et al. [64] also suggest a fit to viscosity or relaxation time data using the value of $\gamma_{\mathrm{mct}}$

$$\tau_{\mathrm{mct}} = \frac{\tau_0}{((T-T_c)/T_c)^{\gamma_{\mathrm{mct}}}}. \tag{7.15}$$

Mode-coupling theory is not valid below a critical temperature and is therefore not useful for viscous liquids. However, it has shown effective in analysing dynamics on shorter timescales, e.g. in neutron scattering [160]. Both a critical density and a critical temperature are reported for cumene by Li et al., $T_c = 150\,\mathrm{K}$ and $\rho_c = 0.982\,\mathrm{g\,cm^{-3}}$. If we substitute the temperatures in Eq. 7.15 with $(\rho^\gamma/T)^{-1}$, and replace the critical temperature with $(\rho_c^\gamma/T_c)^{-1}$, we find an expression to fit the relaxation times in Fig. 7.31 with only $\tau_0$ as a fitting parameter, found to be $\tau_0 = 10^{11}\,\mathrm{s}$.

We will use this expression to make a simplistic model of the FWS on cumene from IN16B (Fig. 7.2). If we assume a simplistic model of the cumene dynamics

on IN16B, where the intensity is given as a sum of an elastic contribution and one relaxational process modelled by a Lorentzian, which corresponds to setting $\beta = 1$, i.e. neglecting any stretching, we have

$$I \propto (1 - A(Q)) \frac{\tau}{1 + \omega^2 \tau^2}, \tag{7.16}$$

where $A$ is the elastic incoherent scattering factor. Here we have, also rather crudely, ignored effects from the convolution of measured intensity with the energy resolution. We furthermore ignore the $Q$-dependence of the elastic incoherent scattering factor and assume it is constant in this temperature and pressure range.

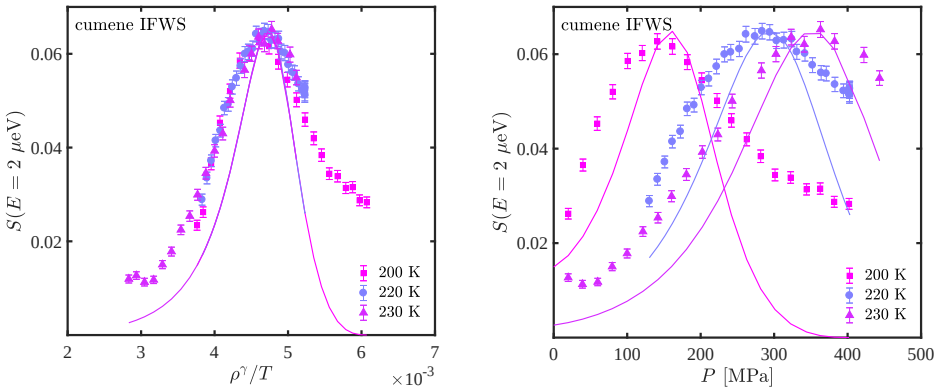


Figure 7.32: Comparison of simplified model in Eq. 7.17 (full lines), based on relaxation times obtained from the full spectra, and data on three isotherms from IFWS on IN16B. The density scaled data is shown to the left and as a function of pressure to the right.

By inserting the modified expression for $\tau_{\mathrm{mct}}$ as a function of $(\rho^\gamma/T)$ from Eq. 7.15 into the simple model in Eq. 7.16 and selecting an energy corresponding to the IFWS with $\Delta E = 2\,\mu\mathrm{eV}$, we compare in Fig. 7.32 the measured data and result of the simplistic model:

$$I_{\mathrm{IFWS}} \propto \frac{\tau_{\mathrm{mct}}(\rho^\gamma/T)}{1 + \omega_{\mathrm{IFWS}}^2 \tau_{\mathrm{mct}}(\rho^\gamma/T)^2}. \tag{7.17}$$

This oversimplified model is not able to take into account the total inelastic form factor. However, by using the density scaled alpha relaxation times and the mode-coupling parameters from [97] as input into the model, we are able to construct our own fixed window scan, where we extract the relative intensity at $\Delta E = 2\,\mu\mathrm{eV}$. We compare the modelled data to the IFWS from IN16B on the three isotherms, and we find that from the model we can recreate the position of the maxima as a function of pressure.

In this section, we have found the alpha relaxation time for cumene, which seems to be in agreement with previously obtained data from other techniques. When the Fourier transformed data where fitted to obtain the relaxation time, we fixed the stretching parameter $\beta$ to 0.5. The stretching parameter is what controls the shape of the relaxation. As we fixed this value for all the state points we have measured,

we assume that the spectral shape is the same everywhere in the studied phase diagram, which makes isochronal superpositioning trivial if the relaxation looks the same everywhere. If the alpha relaxation indeed has the same shape everywhere, perhaps we need to look for something more fundamental or universal than isomorph theory.

## 7.5 Summarising discussion

In this chapter, we studied density scaling and isochronal superposition for two van der Waals liquids and a hydrogen bonding liquids. The alpha relaxation dynamics were shown to density scale and superpose along isochrones for all three samples. For DPG, the hydrogen bonding system, we observed that density scaling broke down for the intramolecular motion of the methyl-group rotation.

From the observation that density scaling and isochronal superposition of the alpha relaxation also work on the hydrogen bonding sample, and that the shape of the alpha relaxation on the Fourier transformed spectra is invariant, suggest that perhaps there exists a more fundamental and universal description of the alpha relaxation that the one provided by isomorph theory.

The test of isochronal superposition which was presented in this chapter was done along isochrones found from the alpha relaxation, while also probing dynamics related to the alpha relaxation dynamics. Even if the probed dynamics was far away in timescales from the actual alpha relaxation time, we saw, in particular for PPE, that the alpha relaxation was stretching out across the timescales and visible in both the dielectrics and the neutron spectra at the same time.

With the purpose of testing isomorph theory and the assumption that isomorphs exist, the best we can do experimentally is to use the isochrones to identify possible isomorphs. To do a more direct test of the existence of isomorphs, we will therefore in the next chapter use neutrons to explore the region of the phase diagram close to the glass transition where there is separation of timescales.

# Chapter 8

# Searching for isomorphs in real glass formers Part II

In this last chapter presenting experimental data, we will present a more direct test of the existence of isomorphs according to isomorph theory (Ch. 3.5) by studying the fast picosecond dynamics along the glass transition line, where the fast dynamics is completely separated from the alpha relaxation. In the previous chapter (Ch. 7), the search for isomorphs took us into nanosecond and picosecond dynamics in a part of the temperature-pressure phase diagram where the alpha relaxation was also either at the same timescale or stretching into that timescale. In this chapter, we will study picosecond dynamics along the glass transition line and in the glass on the same samples as in the previous chapter (Sec. 7.1). Referring to the simple dynamic view sketched in Fig. 2.4 and 6.1, at the glass transition, we will have complete separation of timescales. Using the combined high-pressure cell for simultaneous dielectric and neutron spectroscopy (Ch. 6), we can follow and monitor the alpha relaxation on timescales of hundreds of seconds at the glass transition with the dielectrics, while measuring the picosecond dynamics with time-of-flight instruments like IN5 and IN6 (Sec. 4.4). The first section in this chapter concerns a test of isomorph theory and is published in [72]. The second part of this chapter will be an analysis of the main contributions to the dynamics on picosecond timescales at the glass transition and in the glass, namely those from fast relaxation and vibrations.

## 8.1 Isomorphs

We tested density scaling and isochronal superposition in Ch. 7 for the alpha relaxation dynamics for a large range of timescales and showed that it works reasonably well for all three studied samples, the two van der Waals liquids and the hydrogen bonding system, cumene, PPE and DPG, respectively (see Sec. 7.1 for sample details). We will in this section present what we consider a more direct test of isomorph theory. As we discussed in Sec. 3.5, an assumption in isomorph theory is the existence of isomorphs, where dynamics on all timescales are invariant along an isomorph. Experimentally, we can identify possible isomorphs, where isochrones are defined as a line in the temperature-pressure phase diagram of constant alpha

relaxation time. For state points with the same relaxation time, i.e. isochrones, e.g. the glass transition, one way of testing an invariance in dynamics is by isochronal superpositioning, which is the invariance in spectral shape (Sec. 3.2). We therefore expect isochronal superposition to apply for isochrones if the system has isomorphs.

As we sketched in Fig. 6.1 close to the glass transition, the picosecond dynamics will be completely separated from the alpha relaxation. This idea is supported by the inelastic fixed window scans from IN16B (Sec. 4.4), which provides information on the nanosecond dynamics, presented in Fig. 5.7 and 7.6 for the three samples. We observed that at the glass transition, the alpha relaxation is too slow and therefore completely out of the instrument window on nanosecond timescales. For the two van der Waals liquids, there are no relaxational processes on nanosecond timescales in the proximity of the glass transition or in the glass. For DPG, we observed a low intensity methyl-group rotation on nanosecond timescale close to the glass-transition. However, moving to faster dynamics on picosecond timescales, we observe dynamic contributions for all three systems all the way into the glass (Sec. 2.5).

As mentioned, if a real liquid has isomorphs, the dynamics must be invariant on all timescales along an isomorph. We therefore expect that the fast relaxational and vibrational contributions to the dynamics on picosecond timescales are invariant along the glass transition isochrone, $T_g(P)$. We do not expect this to apply to intramolecular dynamics or systems with strong directional bonding, such as hydrogen bonding. We will test the idea of isomorphs in this section and present data from IN5 and IN6 along the glass transition isochrone, mapped out by the dielectrics, for the two van der Waals liquids, PPE and cumene, and for the hydrogen bonding liquid, DPG. The data will be presented in subsections by sample as in the previous chapter. We will end this section by discussing and showing the consequences of a real liquid that has isomorphs.

Sample and instrument-specific details are given in Sec. 7.1. All data was measured with the combined high-pressure cell for dielectric and neutron spectroscopy presented in Ch. 6. Pressure has for all state points been applied in the liquid, monitored by the dielectrics, and then cooled down to the desired state point. Glass transition state points were found from dielectrics defined as when $\tau_\alpha \approx 100\,\mathrm{s}$ using $\tau_\alpha = 1/(2\pi\nu''_{\max})$. This corresponds to a frequency value of $\nu''_{\max} \approx 1.6 \times 10^{-3}\,\mathrm{Hz}$. We have used time-temperature superposition of the spectra to extrapolate to the decades below $10^{-1}\,\mathrm{Hz}$ for cumene and PPE. Due to the relatively low flux on IN6 compared to IN5, which meant that the acquiring time for the spectra measured on IN5 where about one fifth of that on IN5, we could measure longer dielectric spectra to lower frequencies for DPG, and it is therefore only the last decade from $10^{-2}\,\mathrm{Hz}$ and down, which is missing for DPG.

The neutron data has been corrected in the standard way as discussed in Ch. 4.4. The dynamic structure factor from IN5 and IN6 will be presented as a function of energy transfer in the reduced dimensionless energy units, $\tilde{\omega}$, that was discussed at the beginning of Ch. 7, which are the relevant units for isomorph theory. We will again assume $\tilde{Q} \approx Q$. The data has not been corrected or shifted on the $y$-axis in any way. The data in this section are mostly shown summed over $Q$, the $Q$-dependence will be studied in more detail in the next section. The errorbars are left out in the spectra summed over $Q$ in this chapter, the size of the symbols correspond to the

errorbars.

### Cumene

The state points on cumene from IN5 with $\lambda = 5\,\text{Å}$ that we will treat in this section are shown in Fig. 8.1, where the focus is on the dynamic behaviour along the glass transition isochrone marked with a full black line. Data along an isotherm in the liquid and in the glass are shown for comparison.

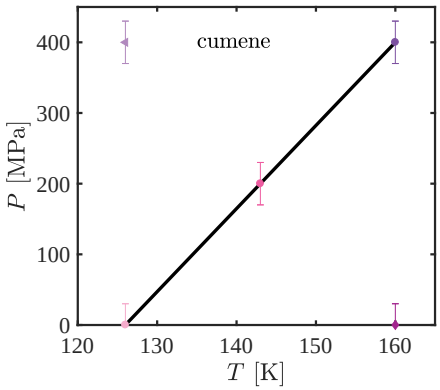


Figure 8.1: Phase diagram of state points in temperature and pressure that are studied in this section. The black line is the glass transition isochrone found from dielectrics.

In Fig. 8.2, we show the spectra as a function of energy transfer in the reduced dimensionless energy units (Eq. 7.2) presented on a linear scale, lin-log and log-log scale along the glass transition isochrone, an isotherm in the liquid and an isotherm in the glass.

We observe isochronal superposition of the spectra from the glass transition isochrone, i.e. an invariance in the dynamics. Along the isotherm in the liquid, we observe a decrease in elastic intensity and an increase in inelastic intensity seen as a large broadening of the spectrum when pressure is released from the glass transition state point, i.e. we move to faster dynamics. In the glass, we observe along the isotherm that the fast relaxational contribution, observed as a broadening around the elastic intensity at the glass transition, disappears as we move deeper into the glass. The black line in the plot of the glass, is a state point at 70 K and ambient pressure, where we observe that there is no fast relaxation left, but only vibrational contribution. The vibrational contribution shows up as a peak in the signal around $\tilde{\omega} \approx 0.1$, which we identify as the excess vibrational density of state, the Boson peak. Along the glass transition the Boson peak and the fast relaxation are merged, and the Boson peak merely shows up as a shoulder. In the log-log representation, where we can compare the elastic peak intensity, we observe a very small discrepancy in the intensity of the elastic peak, but the spectra overlap to great extent, in particular comparing to the data from the two isotherms. From the data presented in Fig. 8.2 on cumene, we observe actual changes in the spectral shape very different in nature

than what we observed for cumene in the previous chapter (Sec. 7.4). The alpha relaxation is for completely out of the instrument window at the glass transition, but we still observe isochronal superposition. Because of the observed invariance in spectra shape along $T_g(P)$, we interpret this as a signature of an invariance in the vibrational contribution and the fast relaxations along the glass transition isochrone.

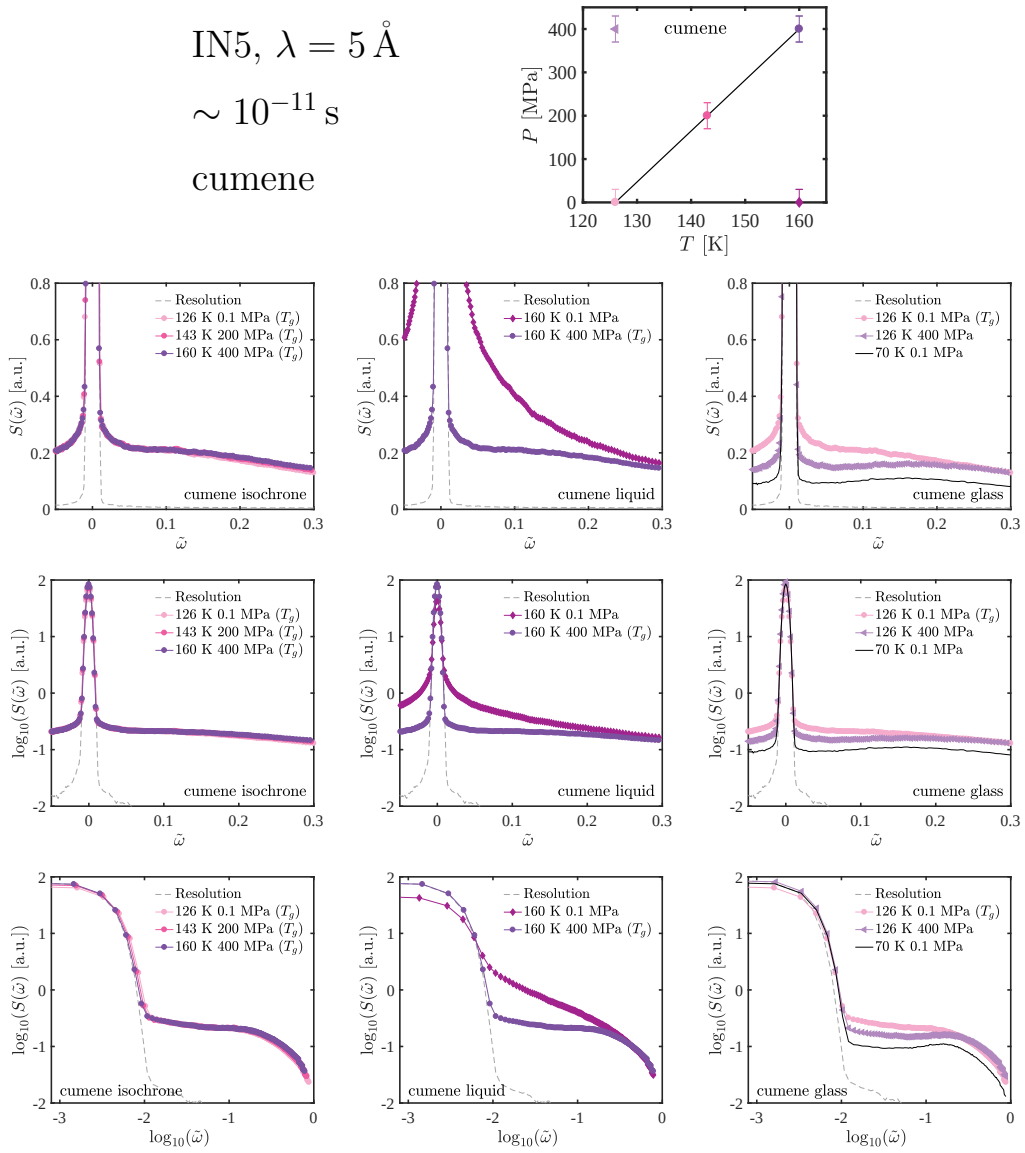


Figure 8.2: Spectra from IN5, $\lambda = 5\,\text{Å}$, on cumene is represented on a linear scale (top row), lin-log scale (middle row) and log-log scale (bottom row) along the glass transition isochrone (left column), an isotherm in the liquid (centre column) and an isotherm in the glass (right column) as a function of energy transfer in the reduced energy units. Errorbars correspond to the symbol size.

In Fig. 8.3, we plot the same spectra as a function of energy transfer in absolute

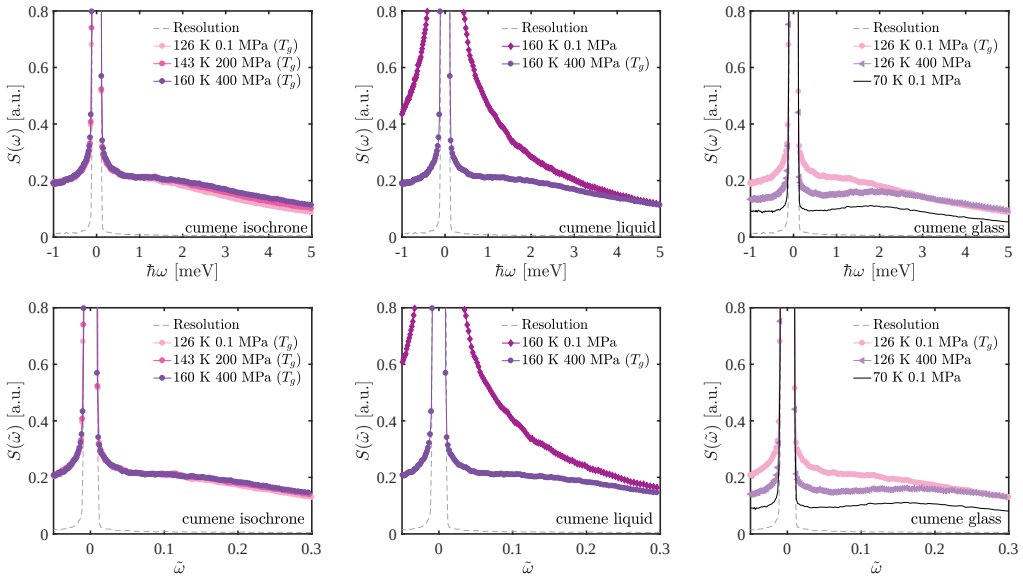


Figure 8.3: Comparison of the cumene spectra as a function of energy transfer plotted as a function of energy on absolute scale and in reduced units.

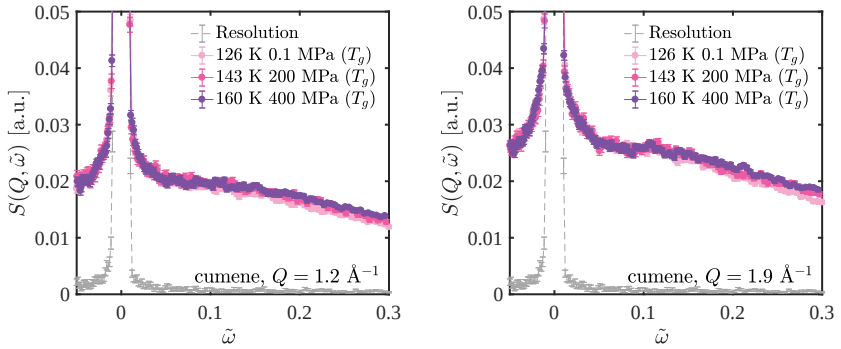


Figure 8.4: Comparison of the minimum and maximum $Q$-values along the glass transition isochrone on cumene from IN5. Errorbars are included in this plot.

energy units (m eV) next to the spectra shown as a function of the dimensionless reduced energy units for comparison. We observe that plotting the spectra in reduced energy units has an effect at larger energy transfer where it causes the signal to collapse for the glass transition isochrone.

The data shown in this section are all plotted as a sum over $Q$ to improve statistics, but we show the glass transition isochrone for two values of $Q$ in Fig. 8.4 to convince the reader that we observe isochronal superposition in the entire $Q$-range that we have studied. The data are shown for the minimum and maximum value of $Q$, 1.2 and 1.9 $\text{Å}^{-1}$, respectively, used in this study. We observe the same trend for both values of $Q$, and we observe that on increased value of $Q$, i.e. shorter length scale, more inelastic signal enters the instrument window.

## PPE

In Fig. 8.5, the state points of PPE spectra from IN5 that will be presented in this section are shown in the phase diagram. We will for this system also look at the spectra along an isotherm in the liquid and in the glass for comparison of the picosecond dynamics. In Fig. 8.5, we also show the dielectric signal from those state points. The black line in the phase diagram represents the glass transition isochrone found from the dielectrics by time-temperature-superposition. As discussed in the previous chapter, the alpha relaxation time of PPE has a large response to compression and it does not crystallise in the region above the glass transition. Therefore, as we will see, it has been possible to explore the liquid phase diagram to a larger extent with PPE than it was with cumene.

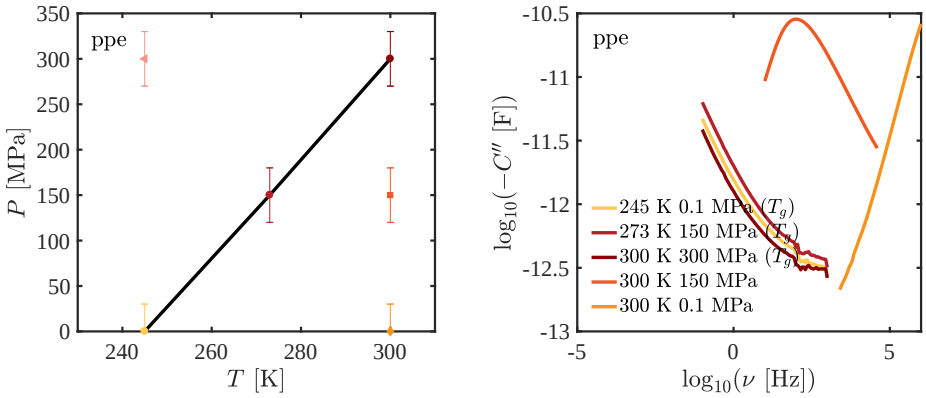


Figure 8.5: Left: Phase diagram of state points in temperature and pressure that are studied in this section on PPE from IN5. The black line is the glass transition isochrone found from dielectrics. Right: Imaginary part of capacitance from state points shown to the left.

In Fig. 8.6, we show the spectra on PPE as a function of energy transfer in reduced energy units represented on a linear scale, lin-log scale and log-log scale along the glass transition isochrone, an isotherm in the liquid and an isotherm in the glass. We observe again an overlap of the spectra along the glass transition

isochrone, implying an invariance in dynamics. Along the isotherm in the liquid, we observe that when pressure is released from the glass transition state point, we move to faster dynamics with a decrease in elastic intensity and an increase in relaxation. We note that releasing pressure at 300 K from 300 to 0.1 MPa changes the alpha relaxation time observed as the maximum in the loss peak in the dielectrics (Fig. 8.5), more than eight orders of magnitude. In the glass, we observe along the isotherm that the fast relaxational contribution, observed as a small broadening around the elastic intensity at the glass transition, disappears as we move deeper into the glass. The black line in the plot of state points in the glass is a state point at 100 K and ambient pressure, where we observe that there is practically no fast relaxation left, but mostly vibrational contribution. The vibrational contribution shows up as a peak in the signal around $\tilde{\omega} \approx 0.1$ that we again identify as the excess vibrational density of state, the Boson peak. We identify the Boson peak, the vibrational contribution, as a shoulder in the spectra from the glass transition isochrone, where it is merged with a fast relaxation process. We thus conclude that for PPE both the vibrational contribution and the fast relaxation on picosecond timescales invariant along the glass transition isochrone found from the dielectrics, similar to what we observed for cumene.

In Fig. 8.7, we compare the effect of plotting the spectra as a function of energy transfer on an absolute energy scale and in reduced energy units. We observe again that the effect of plotting in reduced units is only seen at larger energy transfer. The effect is hardly visible, but a small effect is observed along the glass transition isochrone, where the tales are made to collapse on the reduced energy scale.

In Fig. 8.4, we show that the superposition of spectra also holds in the full range of the studied $Q$-values. We observe the same kind of spectral overlap for the minimum and maximum value of $Q$, 1.2 and 1.9 $\text{Å}^{-1}$. The data in this section is therefore summed over $Q$ to improve statistics. The $Q$-dependence will be studied in the next section.

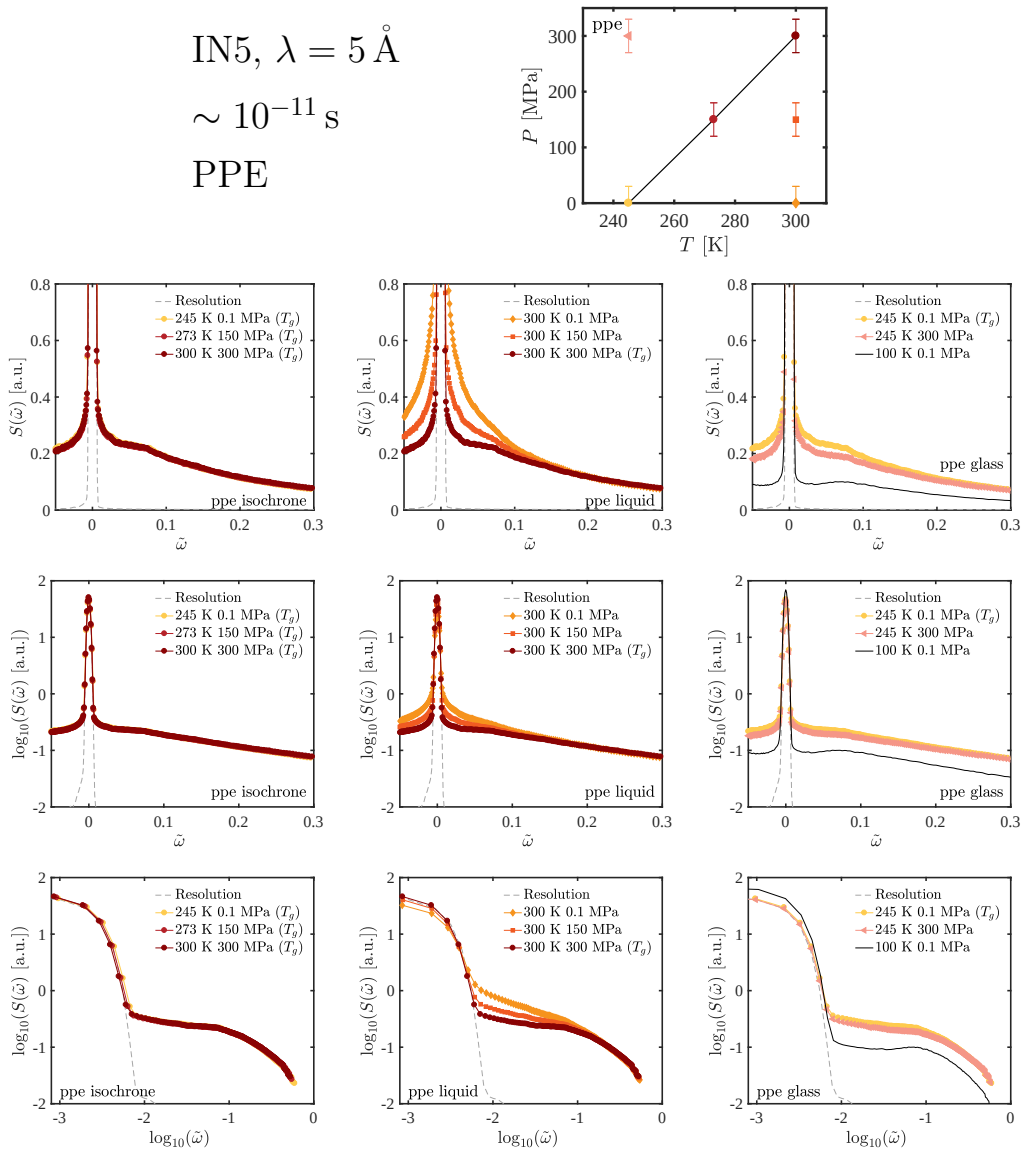


Figure 8.6: Spectra from IN5 on PPE as a function of energy transfer plotted in reduced units represented on a linear scale (top row), lin-log scale (middle row) and log-log scale (bottom row) along the glass transition isochrone (left column), an isotherm in the liquid (centre column) and an isotherm in the glass (right column). Errorbars correspond to the symbol size.

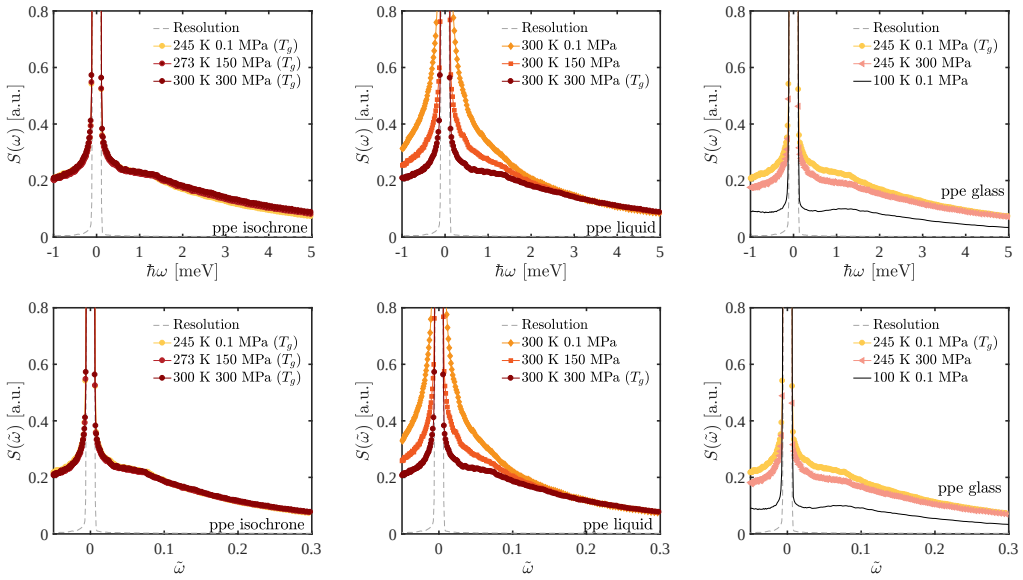


Figure 8.7: Comparison of spectra as a function of energy transfer plotted on absolute scale and in reduced units for the PPE spectra from IN5.

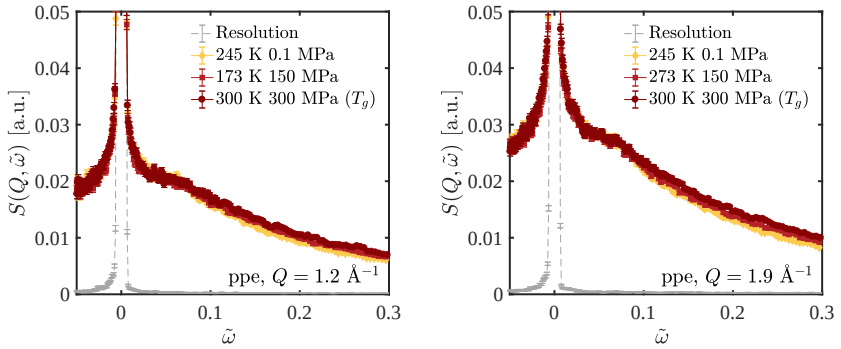


Figure 8.8: Comparison of the minimum and maximum $Q$-values along the glass transition isochrone on PPE from IN5. Errorbars are included in this plot.

## DPG

The picosecond dynamics on DPG were, like the ones presented in Ch. 7, studied on IN6. The state points at which spectra were collected are shown in Fig. 8.9 with the isochrone found from dielectrics marked as a black line. DPG was the first sample that we measured on picosecond timescales and the distribution of state points in temperature and pressure is therefore slightly different from the two van der Waals liquids studied on IN5. The dielectric spectra are also shown in Fig. 8.9. The ambient pressure dielectric signal along the isochrone is missing here because the connection to the dielectrics went. However, the peak position obtained with time-temperature superposition for the two high-pressure state points match with ambient pressure literature data [66] and high-pressure data [30].

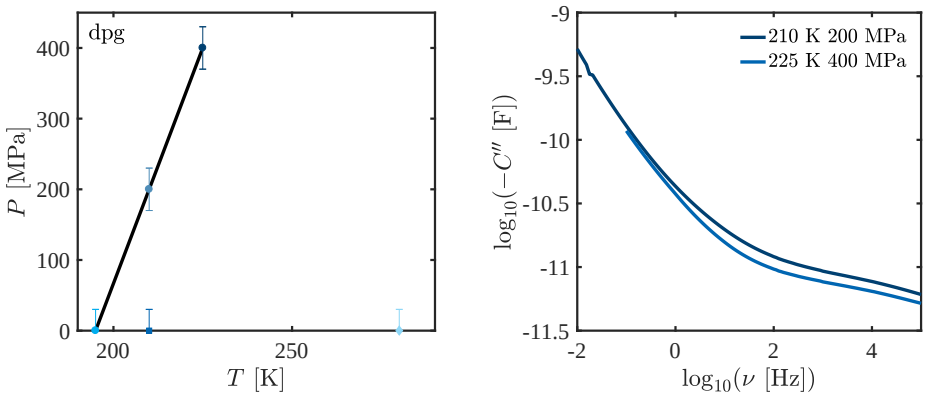


Figure 8.9: Phase diagram (left) of state points in temperature and pressure that are studied in this section on DPG from IN6. The black line is the glass transition isochrone found from dielectrics that are shown to the right.

The data are presented summed over $Q$ as a function of energy transfer in reduced energy units in three different representations along the glass transition isochrone, compared to state points in the liquid and state points in the glass. At the glass transition isochrone, we observe a clear shift in the Boson peak position. We identify the Boson peak from the spectrum of the state point in the glass (black line) as we did for the two previous samples. Along the glass transition, we observe the peak position to move towards higher energy transfer and lower intensity on increased pressure. For the state points in the liquid, we observe the alpha relaxation dominating the signal for the state points at the highest temperature. In the glass, we observe for the full black line at 100 K and ambient pressure that the fast relaxation is much less intense and that mainly the Boson peak remains in the signal.

For completeness, we also show in Fig. 8.11, the data as a function of energy transfer plotted on an absolute energy scale and in reduced energy units. Again, we observe only a small effect of plotting the data in reduced units, which is mainly visible at higher energy transfer. In Fig. 8.12, we show the data at $Q = 1.2$ and 1.7 Å, the minimum and maximum values of $Q$ used in this study from IN6, respectively. This is a slightly smaller $Q$-range than at IN5. We observe same dynamic behaviour for all values of $Q$. Thus to improve statistics, the data is shown as a sum over $Q$.

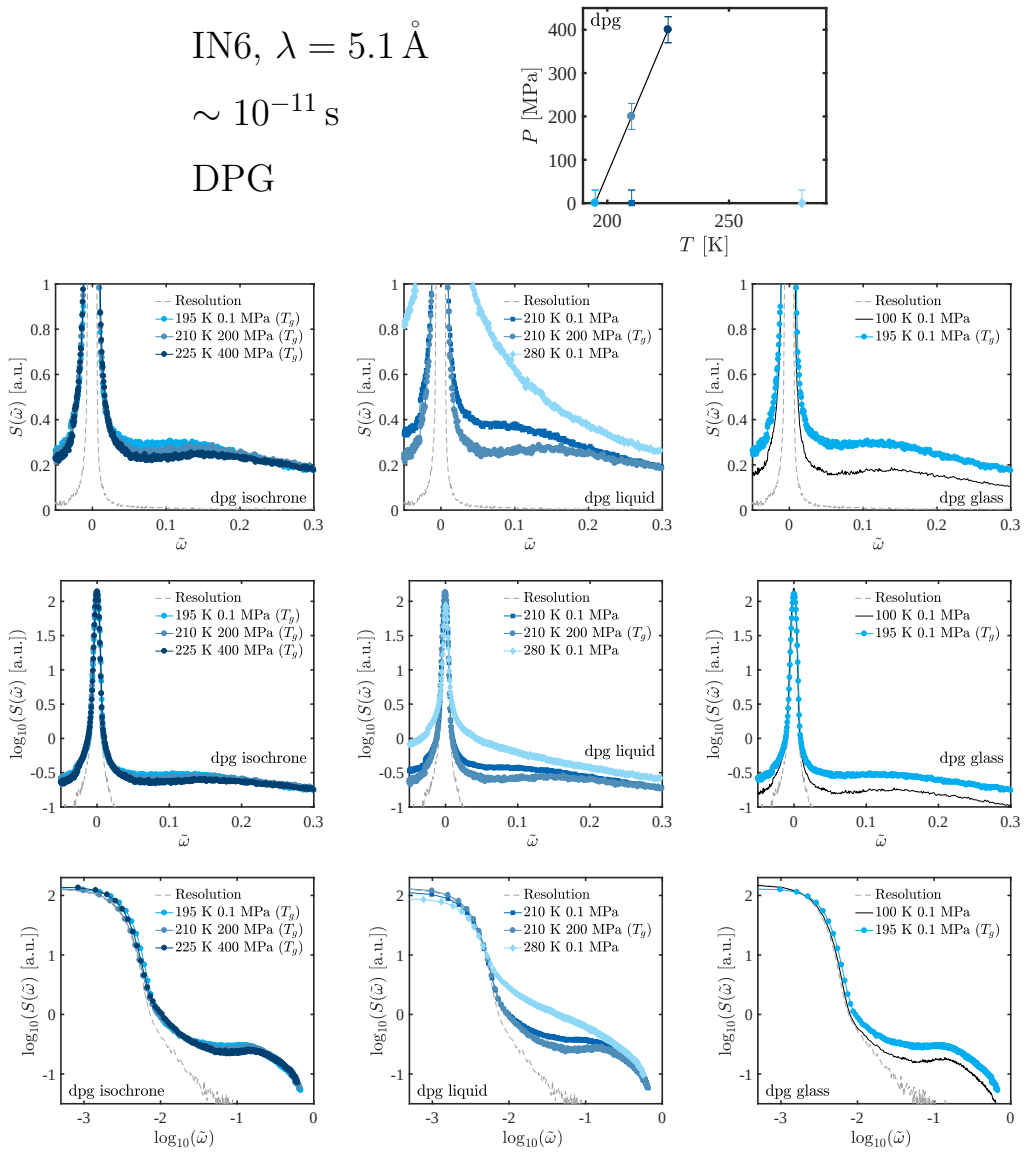


Figure 8.10: The spectra on DPG from IN6 as a function of energy transfer in reduced energy units represented on a linear scale (top row), lin-log scale (middle row) and log-log scale (bottom row) along the glass transition isochrone (left column), state points in the liquid (centre column) and in the glass (right column). Errorbars correspond to the symbol size.

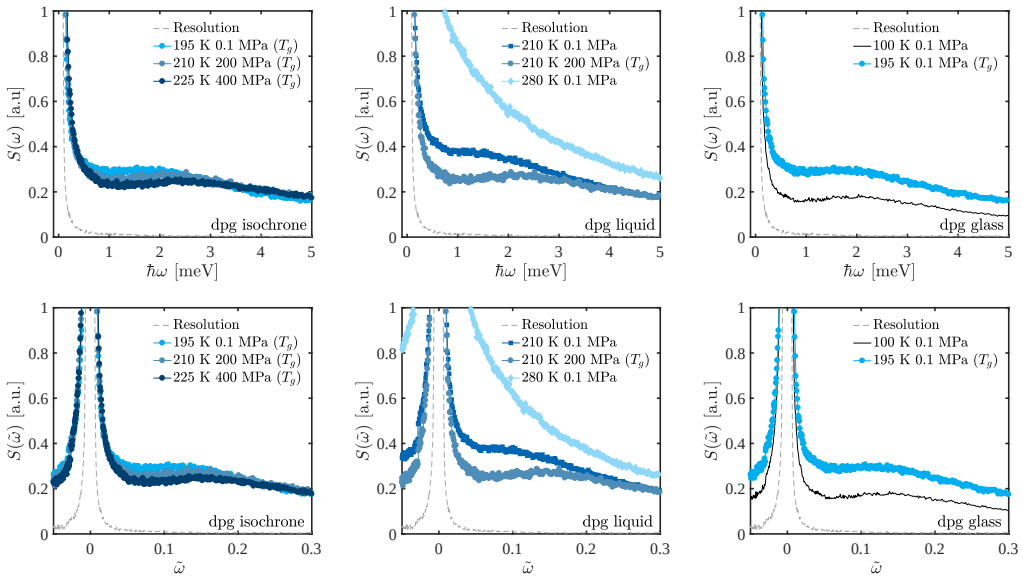


Figure 8.11: Comparison of the DPG spectra from IN6 as a function of energy plotted on absolute scale and in reduced units.

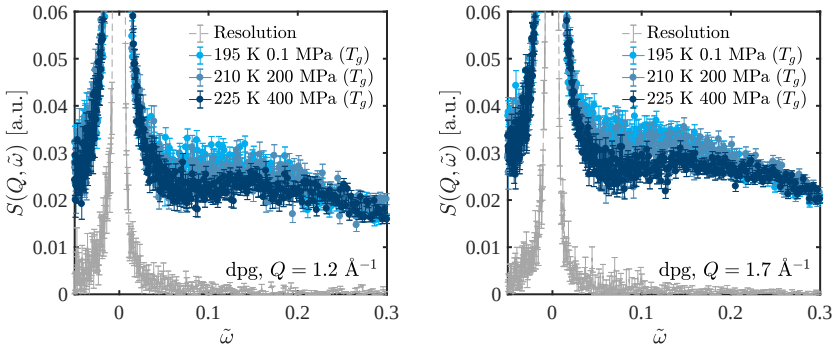


Figure 8.12: Comparison of the DPG spectra from IN6 along the glass transition isochrone for two $Q$-values.

### Glass transition dynamics

We now zoom in on the picosecond dynamics along the three isochronal state points along the glass transition isochrone for each of the three samples. The difference in behaviour is clear: We observe an invariance of the dynamics for the two van der Waals liquids, PPE and cumene, while we observe a change in dynamics for the hydrogen bonding liquid, DPG. For DPG, upon increased pressure the peak position of the Boson peak shifts towards higher energy transfer and lower intensity. For the two van der Waals liquids, the invariance in dynamics is observed on timescales separated by 14 orders of magnitude. We observed the fast relaxational and vibrational contributions to have different temperature and pressure dependencies in Fig. 8.6 and 8.2. Yet, the contributions are invariant along the glass transition isochrone. For the two van der Waals liquids, these are dynamical contributions on picosecond timescales that are completely separated from the alpha relaxation. We interpret this as a signature that the two van der Waals liquids have real isomorphs.

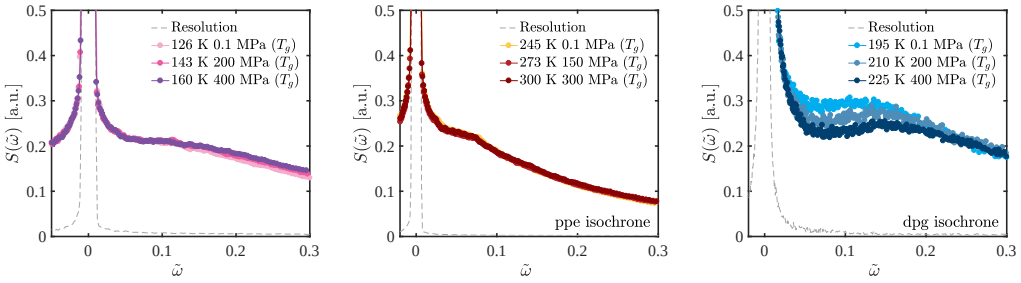


Figure 8.13: Zoom on picosecond dynamics along the glass transition isochrone for the three studied samples.

An energy transfer of $\tilde{\omega} = 0.06$ is approximately $\hbar\omega = 1\,\text{meV}$, which corresponds to a timescale of $\sim 1\,\text{ps}$, while the glass transition state points were found from dielectrics with $\tau_\alpha \approx 100\,\text{s}$. For the two van der Waals liquids that are very different in molecular structure and size (Sec. 7.1), this an invariance in dynamics observed on timescales separated by 14 orders of magnitude. In Fig. 8.14, we attempt to illustrate the degree of invariance for the different state points presented above. We plot the intensity of all the spectra from the three samples in a fixed reduced energy window for comparison along isochrones, isobars and isotherms, at $\tilde{\omega} = 0.06$ corresponding to a timescale of roughly a picosecond. The intensities at $\tilde{\omega} = 0.06$ along isochrones, isobars and isotherms are shown as a function of temperature and pressure in Fig. 8.14, normalised to the value at the lowest temperature and ambient pressure, respectively. In this plot, we have added the high-temperature isochrones presented in Sec. 7.3 in the previous chapter for PPE and DPG, the two samples where we have dielectric spectra to ensure that we are at isochronal state points. We observe that the intensities from isochrones of the two van der Waals liquids fall within the dashed grey lines that are guides to the eye at $1 \pm 0.05$, whereas the dynamics of the hydrogen bonding liquid on picosecond timescale is observed to change. This is in agreement with the observation of isochronal superposition for the van der Waals liquids of the fast relaxations, the vibrational contribution and for

the alpha relaxation dynamics. This represents both the dynamic scenarios sketched in Fig. 6.1, when there is separation of timescales and when the alpha relaxation is in the neutron energy window and the processes therefore are merged.

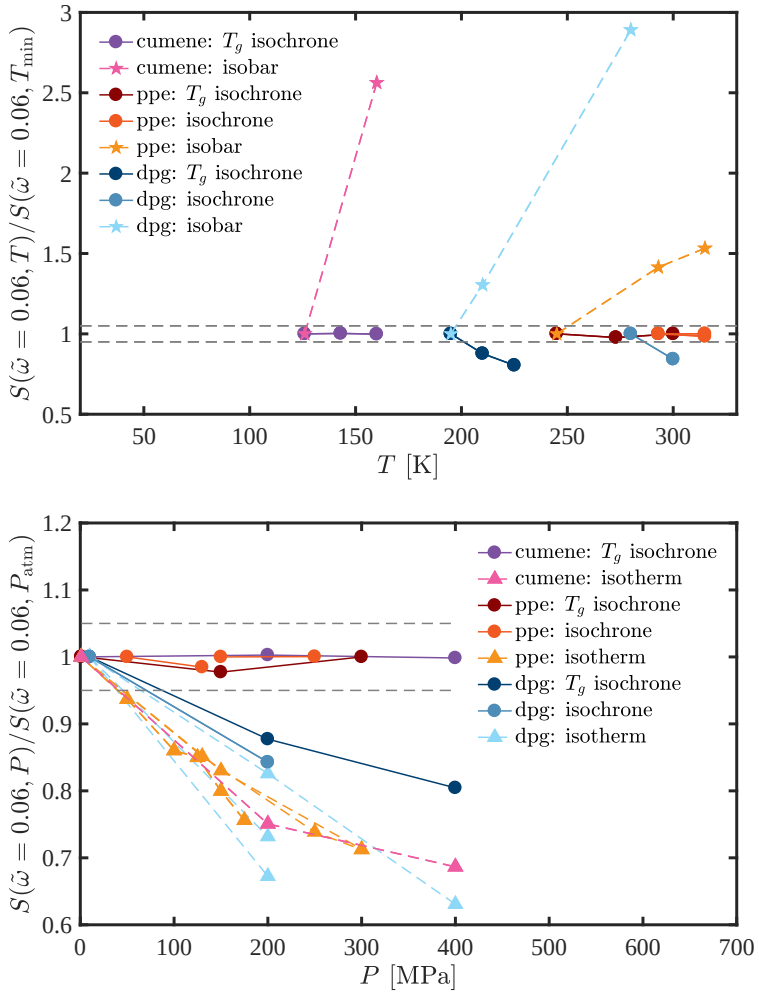


Figure 8.14: Comparison between state points from Fig. 8.6, 8.2 and 8.10 from the inelastic intensity in a fixed reduced energy window at $\tilde{\omega} = 0.06$ along isochrones, isotherms and isobars. Top: as a function of temperature normalised to value at lowest temperature. Bottom: as a function of pressure normalised to the value at ambient pressure. Dashed lines are guides to the eye at $1 \pm 0.05$. Errorbars would be smaller than the symbol size.

### One-dimensional phase diagram

A system that obeys isomorph theory must have isomorphs, and the prediction from isomorph theory is the one-dimensional phase diagram with just one governing parameter, $\Gamma = \rho^\gamma/T$ (Sec. 3.5). In real liquids, this means that the usual two-dimensional phase diagram in temperature and pressure, should collapse into one of just one dimension where the controlling parameter is $\Gamma$. What will determine the dynamics is therefore not where on an isomorph you are, but on what isomorph you are located. Experimentally, we have estimated isomorphs from the isochrones for the two van der Waals liquids. Thus, the dynamics should be invariant for constant alpha relaxation time.

The picosecond dynamics studied on IN5 for PPE presented in this section combined with the data presented in the previous chapter (Fig. 7.20 and 7.21) span around ten orders of magnitude in terms of the alpha relaxation time found from the dielectrics. In Fig. 8.15, we therefore plot the inelastic structure factor for PPE integrated over $Q$ within different fixed energy windows in reduced energy units against the alpha relaxation time found from dielectrics for three isotherms and an isobar. We observe that the picosecond dynamics for all five values of fixed energy window, $\tilde{\omega} = 0.02,\ 0.04,\ 0.06,\ 0.08,\ 0.1$, fall along the same lines. We observe that close to the elastic line, for low energy transfer, the spectral change with $\tau_\alpha$ is much more pronounced than in the higher energy transfer region, which is also clear from the full spectra shown in Fig. 7.21.

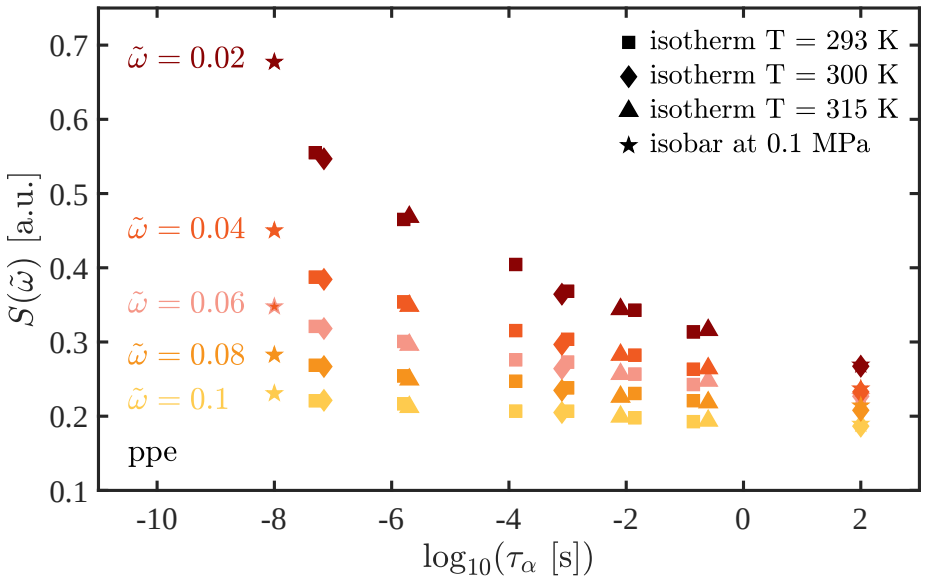


Figure 8.15: Inelastic intensity at fixed reduced energy for PPE as a function of $\tau_\alpha(T, P)$ for three isotherms, $T = 293\,\mathrm{K}$ (□), $300\,\mathrm{K}$ (◇), $315\,\mathrm{K}$ (△), and an isobar (×) for the reduced energies $\tilde{\omega} = 0.02,\ 0.04,\ 0.06,\ 0.08,\ 0.1$ covering more than ten orders of magnitude in alpha relaxation time.

The collapse of the two-dimensional $(T, P)$ phase diagram into one of just one

dimension, here shown as a function of $\tau_\alpha$, illustrates the power of isomorph theory. The dynamics are not determined explicitly from its temperature, pressure or density, i.e. from its state point, but instead from what isomorph the state point is located on. From an experimental point of view, this is approximated by what isochrone the state point is on. We observe from Fig. 8.15 that the picosecond dynamics, the spectral shape can be expressed as a function of $\tau_\alpha$, which is in agreement with the concept of a one-dimensional phase diagram.

In experiments, this one dimension will correspond to lines moving perpendicular to the isochrones in the usual temperature-pressure phase diagram. A practical example of the consequence of the one-dimensional phase diagram for a liquid with isomorphs, such as what we believe is the case for PPE for example, is that the picosecond dynamics in a very large region of the $(T, P)$ phase diagram can be mapped out easily. In principle, it would be enough to do one scan in temperature with the combined dielectric and neutron cell, and by combining this with a pressure scan in the dielectrics to map out the isochrones, all information about the dynamic behaviour on picosecond timescales from the neutron temperature scan can then be mapped onto the rest of the $(T, P)$ phase diagram.

Isomorph theory does not predict the behaviour of the dynamics on different timescales, i.e. we cannot predict the shape of the curves in Fig. 8.15, and an assumption like the one we did for the shape of the alpha relaxation of cumene in Sec. 7.4 would not be able to cover all the different contributions to the dynamics on picosecond timescales for such a large range of the alpha relaxation time as we have here.

In the previous chapter, we showed that isochronal superposition worked quite well for all three studied samples, the two van der Waals liquids and the hydrogen bonding liquid, when we are just looking at the alpha relaxation. In this section, where we just look at fast relaxation and vibrational contribution to the picosecond dynamics, we find a high degree of isochronal superposition for the two van der Waals liquid over a dynamic range of 14 orders of magnitude. This observation implies that the dynamics in some liquids show simple dynamic behaviour. However, from Fig. 8.13, where we zoomed in on the inelastic broadening along the glass transition, we saw a clear change in the spectral shape along the glass transition isochrone for the hydrogen bonding system, DPG. This means that isomorph theory does not work equally well for all systems. As we expected, isomorph theory is not in that sense not universal.

But what we also notice is that even if the scaling is not perfect along the glass transition isochrone for the hydrogen bonding system, the spectral shape is still not completely off. If we compare the different spectra in Ch. 8.10, the dynamics is seen to change much less along the glass transition compared to the isobar or isotherm. The alpha relaxation is therefore still a quite good indicator of the picosecond dynamics and probably the best tool we have for predicting the spectral shape.

## 8.2 Glassy dynamics

In this section, we will take a step back from isomorph theory and reduced energy units to compare our data to other pressure experiments from the glassy state [78, 112]. The time-of-flight spectra from IN5 and IN6 are therefore shown in this section as a function of energy transfer on an absolute energy scale. We will study the shape and the $Q$-dependence of the spectra on compression along the glass transition isochrone and on an isotherm in the glass for all three samples, cumene, PPE and DPG. For cumene, the isotherm was chosen at 70 K, well below $T_g(P)$, while for PPE and DPG that has much higher $T_g(P)$, the isotherm was studied at 100 K.

We have fitted the data using the same function as Hong et al. [78]. The data are fitted outside the elastic peak to a sum of two terms, a Lorentzian to the fast relaxational process and a log-normal to the Boson peak [102]:

$$I(\omega) = A\left(\frac{\omega_0}{\omega_0^2+\omega^2}\right) + I_{\mathrm{BP}}\exp\left(-\frac{\left(\ln(\omega/\omega_{\mathrm{BP}})\right)^2}{2W_0^2}\right). \tag{8.1}$$

The width (HWHM) of the Lorentzian is given by $\omega_0$ and its amplitude by $A$, the intensity and the position of the Boson peak are given by the parameters $I_{\mathrm{BP}}$ and $\omega_{\mathrm{BP}}$, respectively. $W_0$ is a shape parameter of the log-normal function. Fast relaxations are often observed to have exponential decay, and a Lorentzian should therefore in this case be valid for this kind of relaxation. Examples of fit to data for one state point for each of the three sample are shown in Fig. 8.16.

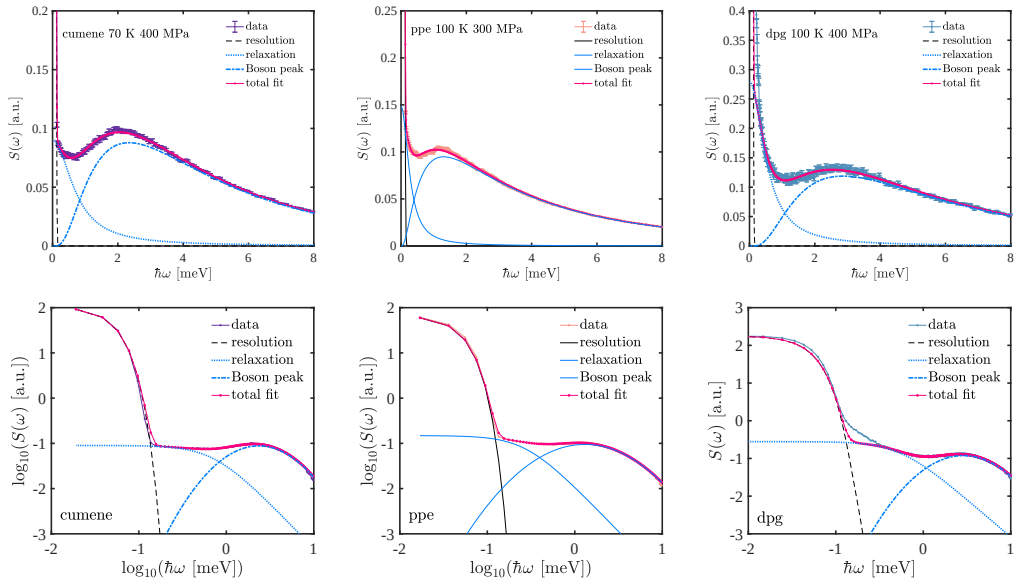


Figure 8.16: Top panel: Examples of fit to data summed over $Q$ using Eq. 8.1 under the assumption that the instrument resolution is a Gaussian. The total fit is a sum of a gaussian fit to the energy resolution, a Lorentzian to fit the fast relaxation and a log-normal to fit the Boson peak. Bottom panel: double logarithmic representation of top panel.

The energy resolution from IN5, where cumene and PPE were measured, is assumed to be a Gaussian, and the total fit as illustrated in Fig. 8.16. Here, we have not done a convolution between the energy resolution and the data, but the sum of the fitting function and the Gaussian follows the data quite well for cumene and PPE. However, for DPG, we observe a clear difference between fit and data in the log-log comparison of fit and data close to the elastic energy resolution at $\hbar\omega \approx 0.1\,\mathrm{m\,eV}$. DPG was measured on IN6, which is known to have an energy resolution with a tail at low energy transfer. This is for example visible in the log-log representation in Fig. 7.25. Unfortunately, the energy resolution that we measured is either vanadium at room temperature or the sample at 50 K ambient pressure, and which seems to give an overestimation of the energy resolution tail, which is not well described by adding an extra Lorentzian or Gaussian term. The tail in the energy resolution at IN6 could be what causes the discrepancy between the total fit and the data, which is observed close to the elastic line. It is therefore difficult to say how much of the part of the fit that is fitted with Lorentzian is actually fast relaxation and how much would be the tail from the instrument resolution, or if the Lorentzian describes the fast relaxation properly. There could also be other dynamic contributions centred around zero which are not contained in this model, for example from methyl groups. But for the comparisons in this section, we will assume that the dynamics can be described by Eq. 7.25 and a Gaussian energy resolution, and use the extracted parameters for comparison to other studies.

First, in Fig. 8.17, we show the spectra summed over $Q$ along with the fit to the data for the three samples along the glass transition isochrone and the isotherm in a linear and a log-log representation. Compared to the previous section, the energy range of the spectra is extended from 5 to 8 m eV in this section. For cumene, along the glass transition isochrone, we observe a clear shift on increased pressure in the intensity at large energy transfer, which more or less disappeared when the energy transfer was plotted in the reduced energy units (Fig. 8.3). At large energy range, the dynamics in the glass is often observed to be merely temperature-dependent and a matter of occupation number that can be corrected for with the Bose factor. But we can see from Fig. 8.17 that this is not always true, as we observe a decrease in intensity on increased pressure along an isotherm at high energy transfer for example for the PPE isotherm. For PPE, in the glass, we observe a very small pressure response for PPE on the isotherm. We will remind the reader that for each of the glassy state points, pressure was applied in the liquid and cooling was then done along an isobar. For DPG and cumene in the glass, we observe a shift in intensity on increased pressure towards higher energy transfer and lower intensity of the Boson peak at higher energy transfer similar to what was observed in [53, 112].

In Fig. 8.18, we show the same data as in Fig. 8.17, but now scaled to the intensity and the energy of the Boson peak obtained from the fits to compare the spectral shapes. For PPE, we observe a complete superposition of spectra along the glass transition and on the isotherm. The same seems to be true for the DPG data; that when normalised to the Boson peak, the spectral shape does not change. However, for cumene, along the isotherm in the glass there is a clear change on applied pressure in the low energy transfer region. Cumene was also measured at 100 K 0.1, 200 and 400 MPa, where we observe the same trend. The fit results to the

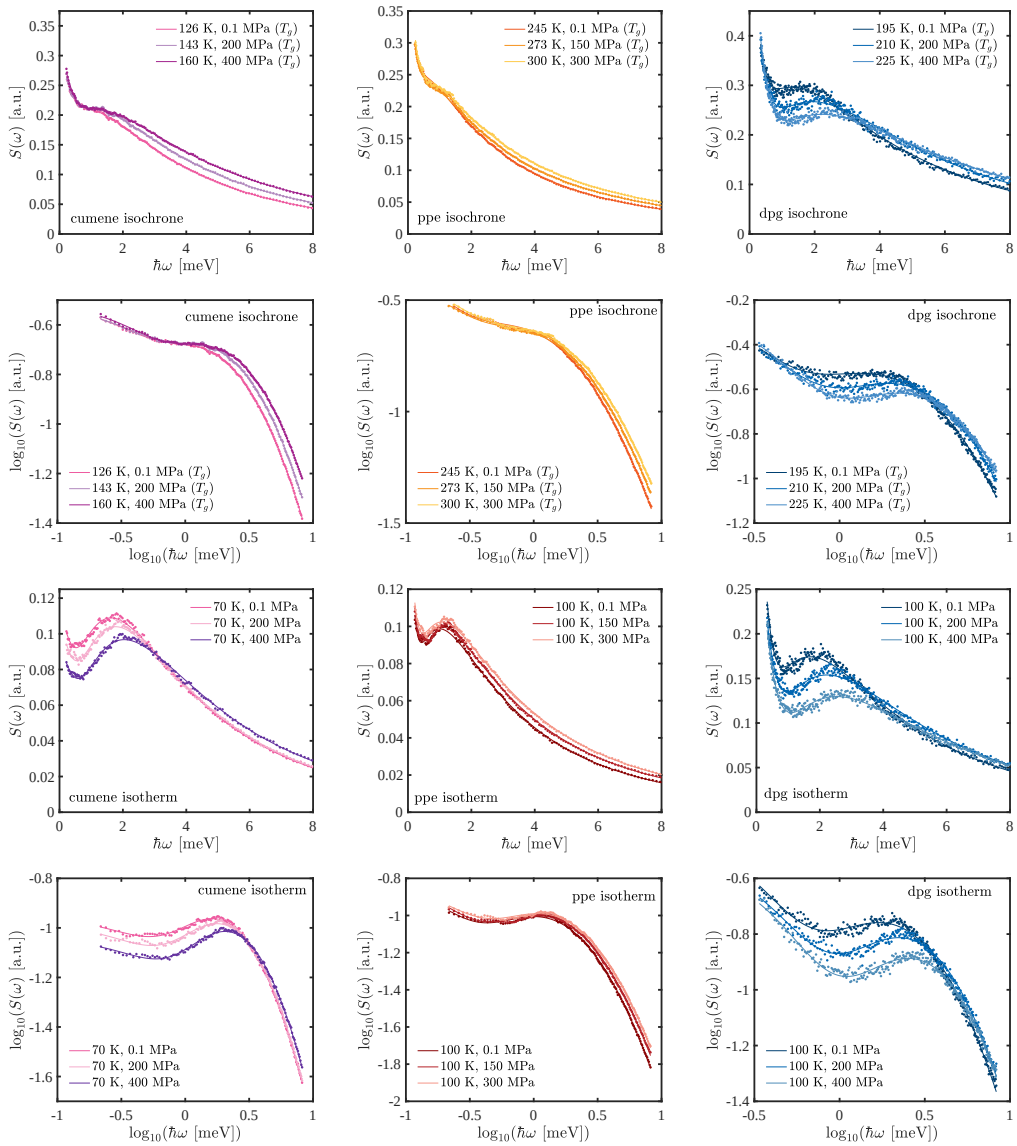


Figure 8.17: Time-of-flight spectra and fits to the data for cumene (left column), PPE (centre column) and DPG (column) along the glass transition isochrone (upper half) and an isotherm in the glass (lower half) in a linear representation (first and third row) and log-log representation (second and fourth row).

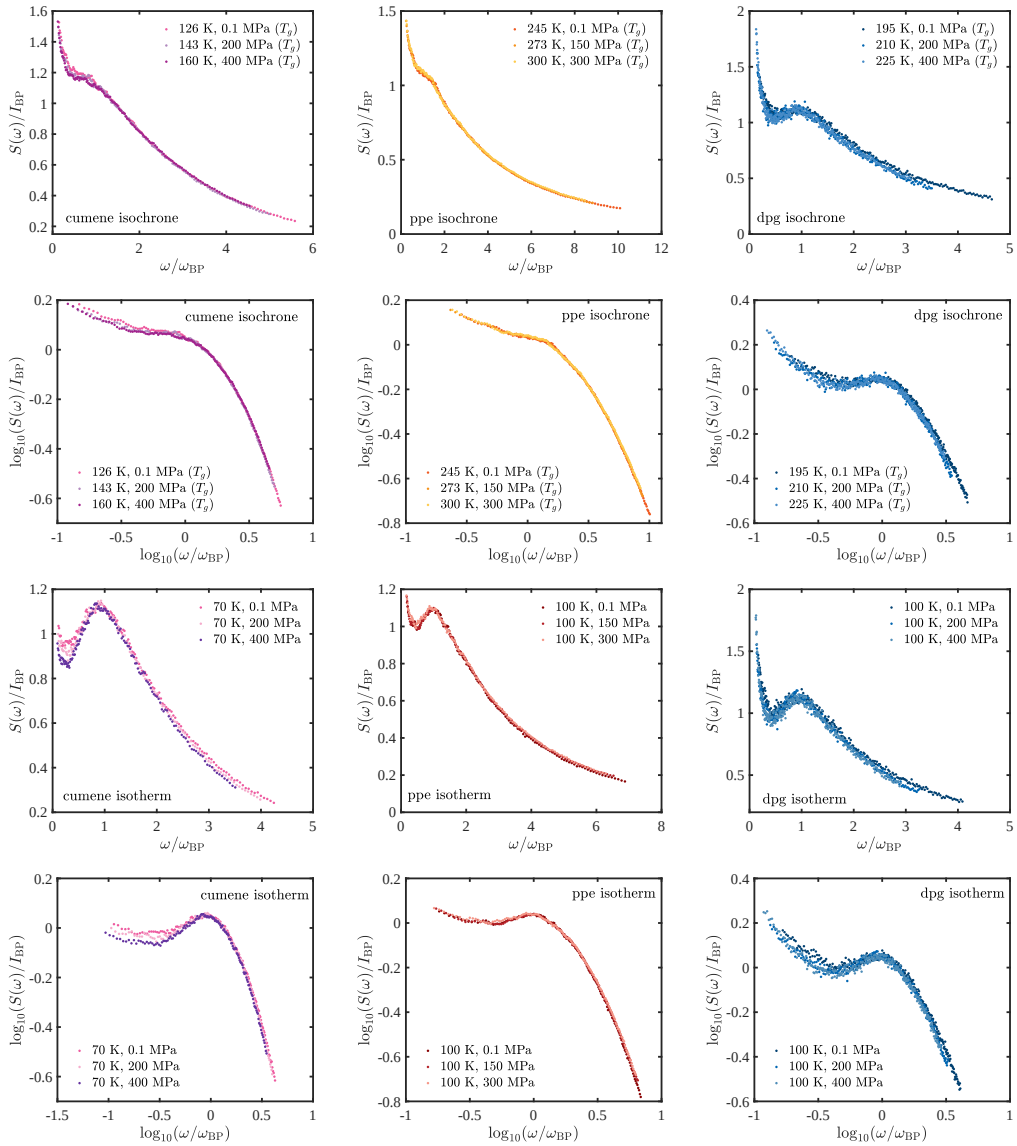


Figure 8.18: Same spectra as in Fig. 8.17, but $y$- and $x$-axis normalised to the intensity and the energy, respectively, of the Boson peak found from the fitting funtion in Eq. 8.1.

100 K data on cumene are included in Fig. 8.19, and the data is shown in Fig. 8.20.

The shape of the Boson peak after rescaling with position and energy has previously been shown to be invariant on quenching [107], which implies that the relative excess vibrational density of states compared to the Debye level remains constant, and on compression [112], suggesting that the observed shift on compression is related to a hardening of the structure. We show a similar invariance for the spectral shape of the scaled data for all three samples. For the low temperature data in the glass on cumene, we observe clearly at lower energy transfer for the rescales Boson peak, what seems like a suppression of the fast relaxational contribution closest to the elastic line.

The fitting function used in this section was also used in Hong et al. [79, 78] on high-pressure light scattering data. We plot some the fitting parameters against each other and as a function of pressure in Fig. 8.19 for direct comparison with [78]. Hong et al. [79, 78] studied seven different systems, including cumene, using light scattering and found for most of their systems, including a 100 K isotherm for cumene, a clear decrease in amplitude on increased pressure. Their pressure range is three times than what we can access, but includes several data points in our pressure range for cumene.

In Fig. 8.19, we therefore plot in the left column fitting parameters as a function of pressure, the boson peak energy and intensity and the amplitude of the fast relaxation. In the right column, we plot first the boson peak position in energy versus its inverse amplitude, then the same plot normalised to the ambient pressure values, and finally, the intensity of the fast relaxation versus the intensity of the boson peak. In the normalised plots, dashed lines are shown at $1 \pm 5$ % as a guide to the eye. On applied pressure, we observe a clear trend for the boson peak position moving towards higher energy transfer. This is true also for the isochronal state points for the van der Waals liquids; the spectra along the isochrone plotted as a function of energy transfer on an absolute energy scale, and not in reduced energy units, are observed to deviate at high energy transfer (Fig. 8.17). While the position of the Boson peak moves away from the elastic line on compression, the intensity decreases for isotherms, tendencies also shown to be true for many systems, e.g. [53, 112, 78]. However, the intensity of the Boson peak seems to be almost constant with the $\pm 5$ % along the glass transition isochrone for cumene, and constant in general for PPE. When we plot the intensity of the Boson peak versus its inverse energy, we see that it is more or less constant for PPE and for the cumene isochrone. For the isotherm in cumene and the DPG data, there seems to be a connection between the intensity and the inverse of its energy. We also show the pressure dependence of the amplitude of the fast relaxation, and we observe that it hardly changes with pressure. A small change can be observed for DPG, but this suggests that signal from fast relaxation should increase on applied pressure, which seems somewhat unphysical, and we therefore ascribe this to the tail in the instrument resolution or other kinds of relaxation as discussed above.

Hong et al. [78] observed for all of their seven systems, including cumene at 100 K, a correlation between the amplitude of the fast relaxation and the intensity of the Boson peak. As can be seen from the bottom row in Fig. 8.19, we do not observe such a correlation from our cumene data or any of our data, using the same

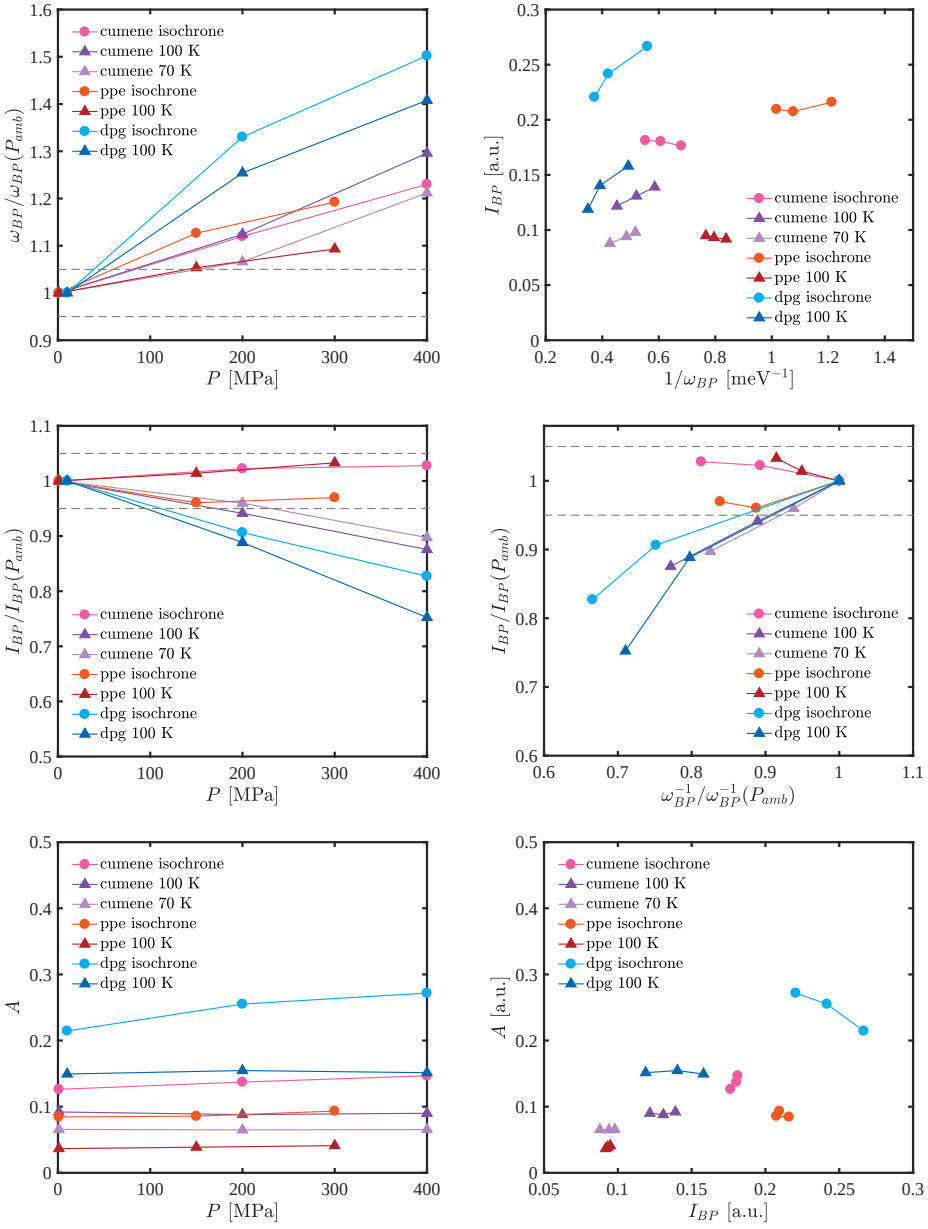


Figure 8.19: Fitting parameters from Eq. 8.1 to data shown in Fig. 8.17 plotted as a function of pressure (left column). Right: boson peak versus inverse intensity (top), same as top normalised to the ambient pressure values (middle), intensity of the fast relaxation versus the intensity of the boson peak (bottom).

fitting function as they did to our data. In Fig. 8.20, we show the fit to lowest and highest pressure state points along the 100 K isotherm and the two dynamic contributions that we have assumed when fitting the data. Here, we observe that while the Boson peak clearly changes with pressure, there is only a very small change in the fast relaxation. This suggests that the two processes have different pressure dependencies, and that they are therefore not correlated as what was observed in [78].

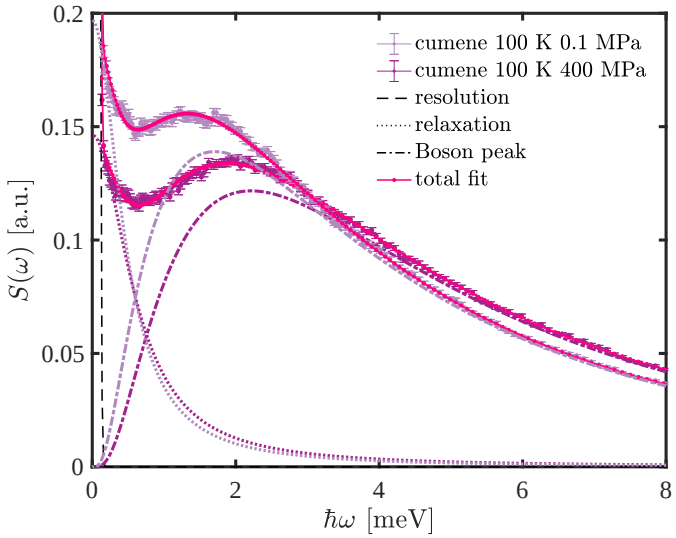


Figure 8.20: Fit to cumene spectra at 100 K, 0.1 MPa and 400 MPa: a sum of a Lorentzian relaxation and a log-normal function to fit the Boson peak. The amplitude of the fast relaxation from the fit is three orders of magnitude smaller than the elastic peak intensity.

Until now, we have studied the data summed over $Q$, and we will look at the $Q$-dependence of our data. In Fig. 8.21, we show the fitting parameters from Eq. 8.1 as a function of $Q^2$. We observe a weak $Q$-dependence in the intensity of the Boson peak and of the fast relaxation, which seems to be a bit steeper for the glass transition isochrones compared with the isotherms in the glass for all three samples. The fast relaxation is often assumed to be a local process, which agrees with the small change in $Q$ we observe. The $Q$- and pressure dependence of the Boson peak suggest that this is not (strictly) a local process.

From the spectral shape in the cumene data scaled to the Boson peak intensity and energy, it seemed that the shape of the Boson peak was invariant on compression while the fast relaxation on compression. However, the fits seem to suggest that it is in fact the fast relaxation which is invariant on compression. Also, we did not find any correlation between the fast relaxation and the Boson peak as was observed in [79, 78]. This supports observation from [118] that the two processes have different temperature and pressure dependencies, which makes the isochronal superposition along the glass transition in the previous section all the more striking.

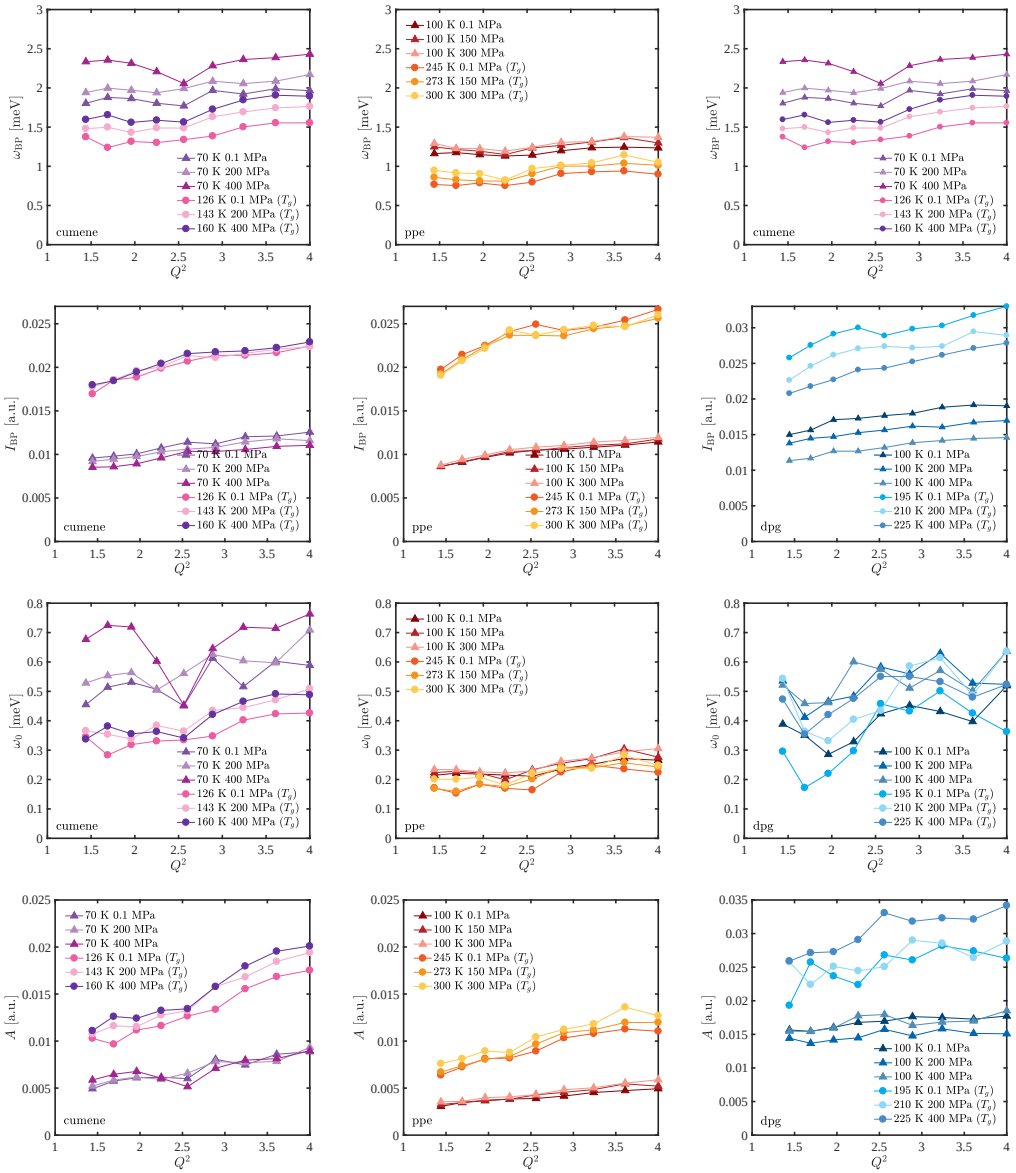


Figure 8.21: $Q$-dependence of the fitting parameters from Eq. 8.1 to the same state points as in Fig. 8.17 plotted as a function of $Q^2$.

## 8.3 Summarising dicussion

We have shown isochronal superposition for the picosecond dynamics for two van der Waals liquids studied with neutron time-of-flight along the glass transition isochrone, where dielectrics was used to find the isochrone. We interpret this as a signature of real isomorphs in these two liquids and that they therefore obey isomorph theory. This is a connection between dynamics separated by 14 orders of magnitude. For systems that obey isomorph theory the dynamics is believed to be controlled by properties of the liquid that obey isomorph invariance.

We saw from Fig. 8.15, where the picosecond dynamics was shown as a function of just one parameter, the alpha relaxation, spanning ten orders of magnitude in relaxation time. This is in agreement with the existence of a one-dimensional phase diagram from isomorph theory. Isomorph theory is approximate in nature, but it seems that for some systems, where the dynamics are what we consider simple, including the two van der Waals systems, we can identify actual isomorphs. We also observed for the hydrogen bonding liquid with a more complex dynamic map that the dynamics is not invariant and therefore cannot be mapped down into one dimension as a function of the relaxation time. At least not as precise as for the two van der Waals liquids.

An interesting observation from isochronal superposition of the picosecond dynamics in the scenario where there is timescale separation, i.e. where we assume only fast relaxational and vibrational contributions, is that these two contributions to the dynamics each have different temperature and pressure dependencies. From Fig. 8.19, we saw the relative intensities of the Boson peak and the fast relaxation vary independently along isotherms. We also note that this dynamic scenario is very different in nature from the dynamic scenario where the alpha relaxation dominates the spectral shape as we saw in the previous chapter (Ch. 7.3), where isochronal superposition was shown to work to a good degree for all three systems.

Whether it is the hydrogen bonds or intra-molecular dynamics, such as the methyl-group rotation (Sec. 7.2), that causes the break-down of isomorph theory for DPG, we do not know. It would be interesting to either study DPG partly deuterated to mask the methyl groups or another hydrogen bonding liquid without methyl groups, to see whether such a system would show isochronal superposition on picosecond dynamics along the glass transition isochrone.

Normally, the alpha relaxation is understood as being cooperative in nature, and the fast relaxations are understood as some kind of local cage rattling, while the nature of the Boson peak is still up for debate. But the findings of isomorphs presented in this chapter for the simple liquids suggest that the distinct dynamic features are all controlled by a single governing parameter, $\Gamma$, as suggested by isomorph theory. From this perspective, we conclude that a universal theory of the glass-transition, should such one exist, must be consistent with the one-dimensional phase diagram.

# Chapter 9

# Concluding discussion

When a liquid is cooled and avoids the crystalline state, it enters a supercooled regime before it reaches the glass transition and ends up in the glass. In the supercooled regime, a viscous slowing down is observed with a stronger than Arrhenius behaviour. Changes in dynamics of glass-forming liquids can be induced either by changing temperature or pressure. In this work, we have taken an experimental approach to test first the shoving model, which is proposed to work in the viscous regime, where we have separation of timescales, and then isomorph theory that has been proposed as a more general explanation of the dynamic behaviour of glass-forming liquids. These are primarily tested on liquids with simple dynamic behaviour, which we consider a prerequisite for the proposed predictions to work.

In Ch. 2, we discussed previous work suggesting connections between fast and slow dynamics in relation to the understanding of the slowing down through the temperature-dependence of different properties. In Ch. 5, we tested the shoving model belonging to the class of models referred to as elastic models. In the shoving model, the relaxation is caused by molecular rearrangements that can be thought of as a flow event. The molecular rearrangements are proposed to take place by energy barrier transition that in itself is a fast process, but takes place more rarely as the liquid is cooled, and the idea is that the height of the energy barrier can be determined from a liquid's short-time properties.

The shoving model was tested on three liquids with simple dynamic behaviour in two different versions, one which is expressed in terms of the instantaneous shear modulus and one as a function of the mean-squared displacement. We showed how the temperature dependence of the short-time properties of local dynamics, the mean-squared displacement found from neutron scattering on nanosecond timescale and the elastic modulus from shear mechanics on second to kilosecond timescales, correlates with the alpha relaxation time and the fragility in agreement with predictions from the shoving model. This suggests that the slowing down of the alpha relaxation time is governed by these short-time properties. The underlying assumption that connects the two versions of the shoving model was also tested, which is directly connecting the shear modulus and the mean-squared displacement. We observe the relationship to hold in the viscous liquid, but observe that once the alpha relaxation enters the neutron instrument window, observed from inelastic neutron scattering, the temperature dependence of the mean-squared displacement is stronger than the

corresponding decrease in the shear modulus. The shoving model may break down for systems with a more complex dynamic behaviour. The experimental observations reported in this work support the notion that the slow dynamics are controlled by the fast dynamics, i.e. the viscous slowing down is governed by the short-time properties.

The dynamics in glass-forming liquids can be altered by compression in a similar fashion as on cooling, thus, the alpha relaxation can also be slowed down on applied pressure. From pressure experiments (Ch. 3.3), where thermal and density contributions to the dynamics can be separated, we learned from previous experimental observations that an understanding of the viscous slowing down must encompass the isochronal lines, i.e. constant relaxation time in the temperature-pressure phase diagram, and density scaling, i.e. constant relaxation time for $\Gamma = \rho^\gamma/T$. Isomorph theory has been proposed as a possible explanation of these observations by assuming the existence of isomorphs that are curves in the phase diagram along which structure and dynamics on all timescales is invariant in reduced dimensionless units. Their potential energy landscape of two isomorphic state points can therefore be mapped onto each other. To a good approximation, possible isomorphs can be experimentally identified by isochrones.

We developed a new sample cell for doing simultaneous dielectric and neutron spectroscopy at elevated pressure (Ch. 6). The new high-pressure sample cell allowed us to do accurate measurements of dipole-dipole correlations in the range from microseconds to hundreds of seconds, while at the same time studying self-correlations on nano- and picosecond timescales with neutron spectroscopy. This new sample cell has improved how we can spend a high-pressure beamtime.

In Ch. 7 and 8, we presented an experimental test using the new high-pressure sample cell of isomorph theory by checking isochronal superpositioning, i.e. an invariance in spectral shape for isochronal state points, which is interpreted as an invariance in dynamics along isochrones. From the dielectric signal, we could determine the alpha relaxation time in a large area of the temperature-pressure phase diagram, which we used to identify isochronal lines in temperature and pressure, while we studied the dynamics from neutron spectroscopy on nano- and picosecond for testing isomorph theory. This was done on a range of different timescales spanning from hundreds of seconds at the glass transition to the fast picosecond dynamics for two simple van der Waals bonded liquids and a hydrogen bonding liquid with a more complex relaxation map. We found the concept of isomorphs to hold for the two simple van der Waals liquids. We consider this finding as a signature of real isomorphs. The hydrogen bonding system was observed to break down in two cases: for density scaling of the intramolecular methyl-group rotation and in isochronal superpositioning of the picosecond dynamics at the glass transition, where the alpha relaxation is completely separated vibrations and fast relaxations on picosecond timescales. This observation is in agreement with predictions from isomorph theory. Whether it is the hydrogen bonds or intramolecular motion that causes the isomorphic behaviour to break down we do not know. With this in mind, it would be interesting to pursue the search for real isomorphs on other hydrogen-bonding liquids without methyl-group rotation or van der Waals liquids with known methyl-group rotation.

Recent work on molecular dynamics computer simulations that incorporated spring-like bonds [163, 117], suggested that isomorphs can only be found when intramolecular dynamics are separated from intermolecular motion, which means that if the intra- and intermolecular contributions are merged, the isomorphs are lost. They found that isomorphs could be relocated, so-called pseudo-isomorphs, by separation of the dynamical processes where they only considered intermolecular vibrations. They showed that the alpha relaxation was constant along the same lines in the phase diagram. With this in mind, they rationalised the observation of density scaling and isochronal superposition also in some systems with internal degrees of freedom.

The aim of this work has been to try to build bridges between modelling of theoretical character and experimental observations. It has not been the purpose to claim that the models are of universal character, but rather to test them in the simplest case. It is a minimum requirement that they should apply here if they are to work at all. This has among other considerations been done by careful sample selection. We found both the shoving model and isomorph theory to work well for the two van der Waals liquids, cumene and 5-polyphenyl ether, molecules that are quite different in size and nature. Cumene is a small molecule and it has been shown from experiments presented in this and other work that the scaling properties work well in a rather large area of the temperature-pressure phase diagram, including several experimental techniques spanning many orders of magnitude in dynamics. Cumene is an interesting molecule in many aspects, in particular because of its size and chemical structure, which is close to what can be modelled in the kind of molecular dynamics computer simulations that have been used for testing isomorph theory so far. The experimental data reported in this work from neutron scattering on nano- and picosecond timescales are within reach of the computer simulations, and it shall therefore be interesting to see what we can learn from new computer simulations on a more realistic system, or what the computer simulations can learn from experimental observations.

From isomorph theory, we do not know whether the fast dynamics control the slow relaxation as in the shoving model, or if the alpha relaxation controls the picosecond vibrations, but for liquids with isomorphs, but there is undeniable a connection. For the two van der Waals liquids, the observed connection span 14 orders of magnitude in dynamic timescale. Isomorph theory, however, seems to suggest that the dynamics are governed by the same underlying mechanism rather than there being causality between the fast and slow dynamics. In the light of isomorph theory, we would expect the shoving model to work also at elevated pressure for simple liquids as the relative changes in temperature should be the same for simple systems. For one of the van der Waals liquids, we show how the picosecond dynamics can be expressed as a function of the alpha relaxation time rather than independently of temperature and pressure. This is in agreement with the prediction from isomorph theory on the existence of a one-dimensional thermodynamic phase diagram controlling the dynamics. We conclude from the observations that whatever is governing the dynamics for $R$-simple liquids, in simulations as well as in real glass-formers, it must be isomorph invariant.

It is tempting to ask, a bit provocative perhaps, if we, the glass science community, became any wiser on the nature of the glass transition. Although isomorph theory has predictive character in the sense that we can for example reduce the dimensions of the experimental two-dimensional phase diagram in temperature and pressure to one of just one dimension, it certainly has its limitations. It does not provide predictions as to *how* the different dynamic contributions behave in the phase diagram on different timescales, only that they should be the same on isomorphs. It provides correlations, but we need information on dynamic behaviour of the system as input. Neither does it provide any explanation of the viscous slowing down, the super-Arrhenius behaviour of the alpha relaxation observed in most glass-formers. In that sense, a model like the shoving model is more useful as it provides a simple, physical explanation of the viscous slowing down, although this is limited to the dynamics in the viscous regime.

Another limitation of the shoving model and isomorph theory is that they are only expected to work on simple systems. We know that the ability to form a glass is a universal property, it is therefore intriguing to think that a universal explanation exists. However, there is not much pointing in that direction. Some systems have been observed to be particularly simple in terms of dynamics. This is seen from the invariance in the shape of the alpha relaxation observed for some systems across different experimental techniques on a broad range of timescales, not just on isochrones, but everywhere in the phase diagram. The observation of invariance of the spectral shape of the alpha relaxation suggests that there is something more fundamental in play. The simplicity of the alpha relaxation is perhaps a key to a more fundamental understanding of the glass transition. This is another argument for studying simple systems as a first approach rather than more complex systems, in this way to be able to study a 'cleaner' system, the physicist's approach.

A problem with experiments is often the interpretation of what we measure. We need to make assumptions on the systems, include modelling, interpolate, extrapolate, and interpret the data with this in mind. The signal we measure will very often consist of a combination of different contributions, so when the simulation people ask us, 'what is it exactly you are measuring? Relaxation or vibrations?', we have to answer that we do not know. We can assume a number of things and then make a qualified guess, but the answer is that we do not know exactly.

The experiments presented in this work were designed to test theoretical predictions. They were not done to characterise systems, i.e. the systems as such are, putting it a bit harsh, uninteresting and act as a tool, where we can tune the complexity of a problem. On the other hand, to use a system to test a theory we also need characterisation to interpret what we observe, and we may, of course, also learn something about the system from understanding the theory better. Therefore we cannot do one without the other. The experiments can support the theory or show something different than what was proposed, but we can never show that a theory is for example universal.

The glass transition is sometimes considered the simplest complex problem. And we would like to think that understanding this problem, will help us in understanding other complex problems. The stretched exponential is an example of an experimental

observation that can be found across many disciplines, and we wonder what kind of physics is hidden in that? Returning to the quote by Philip W. Anderson (Ch. 1), we have no doubt that studies of glass-forming liquids will have intellectual spin-off, but whether we have moved closer to an understanding of the nature of the glass transition is questionable. In this research field of glass science on the border between physicists and chemists, simplicity and complexity, there is still plenty of work to do.

# Bibliography


[1] Adam, G., and Gibbs, J. H. On the temperature dependence of cooperative relaxation properties in glass-forming liquids. *Journal of Chemical Physics 43*, 1 (1965), 139–146.

[2] Adrjanowicz, K., Pionteck, J., and Paluch, M. Isochronal superposition and density scaling of the intermolecular dynamics in glass-forming liquids with varying hydrogen bonding propensity. *Royal Society of Chemistry Advances 6* (2016), 49370–49375.

[3] Alba-Simionesco, C., Cailliaux, A., Alegría, A., and Tarjus, G. Scaling out the denisty dependence of the $\alpha$ relaxation in glass-forming polymers. *Europhysics Letters 68* (2004), 58–64.

[4] Albert, S., Bauer, T., Michl, M., Biroli, G., Bouchaud, J.-P., Loidl, A., Lunkenheimer, P., Tourbot, R., Wiertel-Gasquet, C., and Ladieu, F. Fifth-order susceptibility unveils growth of thermodynamic amorphous order in glass-formers. *Science 352*, 6291 (2016), 1308–1311.

[5] Anderson, P. W. Through the glass lightly. *Science 267*, 5204 (1995), 1615–1616.

[6] Angell, C. Relaxation in liquids, polymers and plastic crystals – strong/fragile patterns and problems. *Journal of Non-Crystalline Solids 131* (1991), 13 – 31.

[7] Arbe, A., Alegría, A., Colmenero, J., Hoffmann, S., Willner, L., and Richter, D. Segmental dynamics in poly(vinylethylene)/polyisoprene miscible blends revisited. A neutron scattering and broad-band dielectric spectroscopy investigation. *Macromolecules 32*, 22 (1999), 7572–7581.

[8] Arbe, A., Alvarez, F., and Colmenero, J. Neutron scattering and molecular dynamics simulations: synergetic tools to unravel structure and dynamics in polymers. *Soft Matter 8* (2012), 8257–8270.

[9] Arbe, A., Malo de Molina, P., Alvarez, F., Frick, B., and Colmenero, J. Dielectric susceptibility of liquid water: Microscopic insights from coherent and incoherent neutron scattering. *Physical Review Letters 117* (2016), 185501.

[10] Artaki, I., and Jonas, J. N.M.R. study of the dynamics structure of isopropylbenzene. *Molecular Physics 55* (1985), 867–885.

[11] Bailey, N. P., Pedersen, U. R., Gnan, N., Schrøder, T. B., and Dyre, J. C. Pressure-energy correlations in liquids. I. Results from computer simulations. *Journal of Chemical Physics 129*, 18 (2008), 184507.

[12] Bailey, N. P., Pedersen, U. R., Gnan, N., Schrøder, T. B., and Dyre, J. C. Pressure-energy correlations in liquids. ii. analysis and consequences. *Journal of chemical physics 129*, 18 (2008), 184508.

[13] Barlow, A. J., Erginsav, A., and Lamb, J. Viscoelastic relaxation of supercooled liquids. II. *Proceedings of the Royal Society A 298* (1967), 481–494.

[14] Barlow, A. J., Lamb, J., and Matheson, A. J. Viscous behaviour of supercooled liquids. *Proceedings of the Royal Society of London. Series A, Mathematical and Physical Sciences 292* (1966), 322–342.

[15] Bartoš, J., Šauša, O., Köhler, M., Švajdlenková, H., Krištiak, P. L., and Loidl, A. Positron annihilation and broadband dielectric spectroscopy: A series of porpylene glycols. *Journal of Non-Crystalline Solids 357* (2011), 376–384.

[16] Bée, M. *Quasielastic Neutron Scattering – Principles and Applications in Solid State Chemistry, Biology and Materials Science.* Adam Hilger, 1988.

[17] Bengtzelius, U. Theoretical calculations on liquid-glass transitions in Lennard-Jones systems. *Physical Review A 33* (1986), 3433–3439.

[18] Bengtzelius, U., Götze, W., and Sjølander, A. Dynamics of supercooled liquids and the glass transition. *Journal of Physics C: Solid State Physics 17*, 33 (1984), 5915.

[19] Bernini, S., Puosi, F., and Leporini, D. Weak links between fast mobility and local structure in molecular and atomic liquids. *Journal of Chemical Physics 142* (2015), 124504.

[20] Berthier, L., Charbonneau, P., Jin, Y., Parisi, G., Seoane, B., and Zamponi, F. Growing timescales and lengthscales characterizing vibrations of amorphous solids. *Proceedings of the National Academy of Sciences* (2016), 201607730.

[21] Bøhling, L., Ingebrigtsen, T. S., Grzybowski, A., Paluch, M., Dyre, J. C., and Schrøder, T. B. Scaling of viscous dynamics in simple liquids: theory, simulation and experiment. *New Journal of Physics 14* (2012), 113035.

[22] Böhmer, R., Ngai, K., Angell, C., and Plazek, D. Nonexponential relaxations in strong and fragile glass formers. *Journal of Chemical Physics 99*, 5 (1993), 4201–4209.

[23] Bridgman, P. W. Volume-tempeature-pressure relations for several non-volatile liquids. *Proceedings of the American Academy of Arts and Sciences 67* (1932), 1–27.

[24] Bridgman, P. W. Further rough compressions to 40,000 kg/cm$^3$, especially certain liquids. *Proceedings of the American Academy of Arts and Sciences 77* (1949), 129–146.

[25] Buchenau, U., and Zorn, R. A relation between fast and slow motion in glassy and liquid selenium. *Europhysics Letters 18* (1992), 523–528.

[26] Buchenau, U., Zorn, R., and Ramos, M. A. Probing cooperative liquid dynamics with the mean square displacement. *Physical Review E 90* (2014), 042312.

[27] Capaccioli, S., Ngai, K. L., Ancherbak, S., and Paciaroni, A. Evidence of coexistence of change of cage dynamics at $T_g$ and the dynamic transition at $T_d$ in solvated proteins. *Journal of Chemical Physics 116* (2012), 1745–1757.

[28] Casalini, R., Capaccioli, S., Lucchesi, M., Rolla, P. A., and Corezzi, S. Pressure dependence of structural relaxation time in terms of the Adam-Gibbs model. *Physical Review E 63* (Feb 2001), 031207.

[29] Casalini, R., and Roland, C. Determination of the thermodynamic scaling exponent for relaxation in liquids from static ambient-pressure quantities. *Physical Review Letters 113* (2014), 085701.

[30] Casalini, R., and Roland, C. M. Excess wing in the dielectric loss spectra of propylene glycol oligomers at elevated pressure. *Physical Review B: Condensed Matter and Materials Physics 69* (2004), 094202.

[31] Casalini, R., and Roland, C. M. Thermodynamical scaling of the glass transition dynamics. *Physical Review E 69* (2004), 062501.

[32] Casalini, R., and Roland, C. M. Scaling of the supercooled dynamics and its relation to the pressure dependences of the dynamic crossover and the fragility of glass formers. *Physical Review B 71* (2005), 014210.

[33] Chang, K. The nature of glass remains anything but clear. *NY Times* (2008).

[34] Christensen, T., and Olsen, N. A rheometer for the measurement of a high shear modulus covering more than seven decades of frequency below 50 kHz. *Review of Scientific Instruments 66* (1995), 5019–5031.

[35] Chumakov, A. I., Monaco, G., Monaco, A., Crichton, W. A., Bosak, A., Rüffer, R., Meyer, A., Kargl, F., Comez, L., Fioretto, D., Giefers, H., Roitsch, S., Wortmann, G., Manghnani, M. H., Hushur, A., Williams, Q., Balogh, J., Parliński, K., Jochym, P., and Piekarz, P. Equivalence of the boson peak in glasses to the transverse

acoustic van hove singularity in crystals. *Physical Review Letters 106* (2011), 225501.

[36] Chumakov, A. I., Sergueev, I., van Bürck, U., Schirmacher, W., Asthalter, T., Rüffer, R., Leupold, O., and Petry, W. Collective nature of the boson peak and universal transboson dynamics of glasses. *Physical Review Letters 92* (2004), 245508.

[37] Cibulka, I., and Takagi, T. $P-\rho-T$ data of liquids: Summarization and evaluation. 5. aromatic hydrocarbons. *Journal of Chemical & Engineering Data 44*, 3 (1999), 411–429.

[38] Cohen, M. H., and Grest, G. S. Liquid-glass transition, a free-volume approach. *Physical Review B 20* (1979), 1077–1098.

[39] Cohen, M. H., and Turnbull, D. Molecular transport in liquids and glasses. *Journal of Chemical Physics 31*, 5 (1959), 1164–1169.

[40] Colmenero, J., Arbe, A., and Alegria, A. Crossover from Debye to non-Debye dynamical behavior of the $\alpha$ relaxation observed by quasielastic neutron scattering in a glass-forming polymer. *Physical Review Letters 71*, 16 (1993), 2603.

[41] Colmenero, J., Arbe, A., Alegria, A., Monkenbusch, M., and Richter, D. On the origin of the non-exponential behaviour of the-relaxation in glass-forming polymers: Incoherent neutron scattering and dielectric relaxation results. *Journal of Physics: Condensed Matter 11*, 10A (1999), A363.

[42] Costigliola, L., Schrøder, T. B., and Dyre, J. C. Communication: Studies of the Lennard-Jones fluid in 2, 3, and 4 dimensions highlight the need for a liquid-state 1/d expansion. *Journal of Chemical Physics* (2016).

[43] Doolittle, A. K., and Doolittle, D. B. Studies in newtonian flow. v. further verification of the free-space viscosity equation. *Journal of Applied Physics 28*, 8 (1957), 901–905.

[44] Dreyfus, C., Aouadi, A., Gapinski, J., Matos-Lopes, M., Steffen, W., Patkowski, A., and Pick, R. M. Temperature and pressure study of brillouin transverse modes in the organic glass-forming liquid orthoterphenyl. *Physical Review E 68* (2003), 011204.

[45] Dyre, J. C. Colloquium: The glass transition and elastic models of glass-forming liquids. *Reviews of Modern Physics 78* (2006), 953–972.

[46] Dyre, J. C. Hidden scale invariance in condensed matter. *Journal of Physical Chemistry B 118* (2014), 10007–10024.

[47] Dyre, J. C. Simple liquids' quasiuniversality and the hard-sphere paradigm. *Journal of Physics: Condensed Matter 28*, 32 (2016), 323001.

[48] Dyre, J. C., Hechsher, T., and Niss, K. A brief critique of the Adam-Gibbs entropy model. *Journal of Non-Crystalline Solids 355*, 10 (2009), 624–627.

[49] Dyre, J. C., and Olsen, N. B. Landscape equivalent of the shoving model. *Physical Review E: Statistical, Nonlinear, and Soft Matter Physics 69* (2004), 042501.

[50] Dyre, J. C., Olsen, N. B., and Christensen, T. Local elastic expansion model for viscous-flow activation energies of glass-forming molecular liquids. *Physical Review B 53* (1996), 2171–2174.

[51] Fragiadakis, D., and Roland, C. M. On the density scaling of liquid dynamics. *Journal of Chemical Physics 134*, 4 (2011), 044504.

[52] Fragiadakis, D., and Roland, C. M. Are polar liquids less simple? *Journal of Chemical Physics 138*, 12 (2013), 12A502.

[53] Frick, B., and Alba-Simionesco, C. Pressure dependence of the Boson peak in poly(butadiene). *Applied Physics A 74*, 1 (2002), s549–s551.

[54] Frick, B., Combet, J., and van Eijck, L. New possibilities with inelastic fixed window scans and linear motor Doppler drives on high resolution neutron backscattering sprectrometers. *Nuclear Instruments and Methods in Physics Research A 669* (2012), 7–13.

[55] Frick, B., and Fetters, L. Methyl group dynamics in glassy polyisoprene: a neutron backscattering investigation. *Macromolecules 27*, 4 (1994), 974–980.

[56] Frick, B., and Richter, D. The microscopic basis of the glass transition in polymers from neutron scattering studies. *Science 267*, 5206 (1995), 1939–1945.

[57] Frick, B., Richter, D., Petry, W., and Buchenau, U. Study of the glass transition order parameter in amorphous polybutadiene by incoherent neutron scattering. *Zeitschrift für Physik B Condensed Matter 70*, 1 (1988), 73–79.

[58] Fulcher, G. S. Analysis of recent measurements of the viscosity of glasses. *Journal of the American Ceramic Society 8*, 6 (1925), 339–355.

[59] Gainaru, C., Hecksher, T., Olsen, N. B., Böhmer, R., and Dyre, J. C. Shear and dielectric responses of propylene carbonate, tripropylene glycol, and a mixture of two secondary amides. *Journal of Chemical Physics 137*, 6 (2012), 064508.

[60] Gibbs, J. H., and DiMarzio, E. A. Nature of the glass transition and the glassy state. *Journal of Chemical Physics 28*, 3 (1958), 373–383.

[61] Gnan, N., Schrøder, T. B., Pedersen, U. R., Bailey, N. P., and Dyre, J. C. Pressure-energy correlation in liquids. IV. "Isomorphs" in liquid phase diagrams. *Journal of Chemical Physics 131* (2009), 234504.

[62] Goldstein, M. Viscous liquids and the glass transition: A potential energy barrier picture. *Journal of Chemical Physics 51*, 9 (1969), 3728–3739.

[63] Götze, W. *Complex Dynamics of Glass-Forming Liquids – A Mode-Coupling Theory*. Oxford University Press, Oxford, 2009.

[64] Götze, W., and Sjögren, L. $\alpha$-relaxation near the liquid-glass transition. *Journal of Physics C: Solid State Physics 20*, 7 (1987), 879.

[65] Grigera, T., Martín-Mayor, V., Parisi, G., and Verrocchio, P. Phonon interpretation of the 'boson peak' in supercooled liquids. *Nature 422*, 6929 (2003), 289.

[66] Grzybowska, K., Pawlus, S., Mierzwa, M., Paluch, M., and Ngai, K. L. Changes of relaxation dynamics of a hydrogen-bonded glass former after removal of the hydrogen bonds. *Journal of Chemical Physics 125* (2006), 144507.

[67] Grzybowski, A., Grzybowska, K., Paluch, M., Swiety, A., and Koperwas, K. Density scaling in viscous systems near the glass transition. *Physical Review E 83* (2011), 041505.

[68] Grzybowski, A., Grzybowska, K., Zioło, J., and Paluch, M. Correlations between isobaric and isochoric fragilities and thermodynamical scaling exponent for glass-forming liquids. *Physical Review E 74* (2006), 041503.

[69] Gundermann, D. Testing predictions of the isomorph theory by experiment. PhD thesis, Roskilde University, DNRF centre "Glass & Time", 2013.

[70] Gundermann, D., Pedersen, U. R., Hecksher, T., Bailey, N. P., Jakobsen, B., Christensen, T., Olsen, N. B., Schrøder, T. B., Fragiadakis, D., Casalini, R., Michael Roland, C., Dyre, J. C., and Niss, K. Predicting the density-scaling exponent of a glass-forming liquid from Prigogine-Defay ratio measurements. *Nature Physics 7* (2011), 816–821.

[71] Hansen, H. W., Frick, B., Hecksher, T., Dyre, J. C., and Niss, K. Connection between fragility, mean-squared displacement, and shear modulus in two van der waals bonded glass-forming liquids. *Physical Review B 95* (2017), 104202.

[72] Hansen, H. W., Sanz, A., Adrjanowicz, K., Frick, B., and Niss, K. Evidence of a one-dimensional thermodynamic phase diagram for simple glass-formers. *Nature Communication: http://go.nature.com/2ytIvl5* (2017).

[73] Hansen, J.-P., and McDonald, I. R. *Theory of Simple Liquids*, 3rd ed. Academic Press, 2006.

[74] Hecksher, T., and Dyre, J. C. A review of experiments testing the shoving model. *Journal of Non-Crystalline Solids 407* (2015), 14–22.

[75] Hecksher, T., Nielsen, A. I., Olsen, N. B., and Dyre, J. C. Little evidence for dynamic divergences in ultraviscous molecular liquids. *Nature Physics 4* (2008), 737–741.

[76] Hecksher, T., Olsen, N. B., Nelson, K. A., and Dyre, J. C. Mechanical spectra of glass-forming liquids. I. low-frequency bulk and shear moduli of DC704 and 5-PPE measured by piezoceramic transducers. *Journal of Physical Chemistry 138* (2013), 12A543.

[77] Hecksher, T., Torchinsky, D. H., Klieber, C., Johnson, J. A., Dyre, J. C., and Nelson, K. A. Toward broadband mechanical spectroscopy. *Proceedings of the National Academy of Sciences* (2017), 201707251.

[78] Hong, L., Begen, B., Kisliuk, A., Novikov, V. N., and Sokolov, A. P. Influence of pressure on fast picosecond relaxation in glass-forming materials. *Physical Review B 81* (2010), 104207.

[79] Hong, L., Begen, B., Kisliuk, A., Pawlus, S., Paluch, M., and Sokolov, A. P. Influence of pressure on quasielastic scattering in glasses: Relationship to the boson peak. *Physical Review Letters 102* (2009), 145502.

[80] Hoover, W. G., Ross, M., Johnson, K. W., Hendersson, D., Barker, J. A., and Brown, B. C. Soft-sphere equation of state. *Journal of Chemical Physics 52* (1970), 4931–4941.

[81] Howells, W. The use of fourier transforms in the analysis of qens data. *Physica B: Condensed Matter 226*, 1 (1996), 78 – 81.

[82] Ingebrigtsen, T. S., Schrøder, T. B., and Dyre, J. C. Isomorphs in model molecular liquids. *Journal of Physical Chemistry B 116* (2012), 1018–1034.

[83] Jakobsen, B., Niss, K., Maggi, C., Olsen, N. B., Christensen, T., and Dyre, J. C. Beta relaxation in the shear mechanics of viscous liquids: Phenomenology and network modeling of the alpha-beta merging region. *Journal of Non-Crystalline Solids 357* (2011), 267.

[84] Jiménez-Ruiz, M., Sanz, A., Nogales, A., and Ezquerra, T. Experimental setup for simultaneous measurements of neutron diffraction and dielectric spectroscopy during crystallization of liquids. *Review of Scientific Instruments 76*, 4 (2005), 043901.

[85] Kauzmann, W. The nature of the glassy state and the behaviour of liquids at low temperatures. *Chemical Reviews 43* (1948), 219–256.

[86] Khodadadi, S., and Sokolov, A. P. Protein dynamics: from rattling in a cage to structural relaxation. *Soft Matter 11* (2015), 4984–4998.

[87] Kittel, C. *Introduction to Solid State Physics*, 8th ed. John Wiley & Sons, Inc., 2005.

[88] Klieber, C., Hecksher, T., Pezeril, T., Torchinsky, D. H., Dyre, J., and Nelson, K. A. Mechanical spectra of glass-forming liquids. II. Gigahertz-frequency longitudinal and shear acoustic dynamics in glycerol and DC704 studied by time-domain billouin scattering. *Journal of Chemical Physics 138* (2013), 12A544.

[89] Klotz, S. *Techniques in high pressure neutron scattering.* CRC press, Taylor & Francis Group, 2013.

[90] Köhler, M., Lunkenheimer, P., Goncharov, Y., Wehn, R., and Loidl, A. Glassy dynamics in mono-, di- and tri-propylene glycol: From the $\alpha$- to the fast $\beta$-relaxation. *Journal of Non-Crystalline Solids 356* (2010), 529–534.

[91] Krausser, J., Samwer, K. H., and Zaccone, A. Interatomic repulsion softness didirect controls the fragility of supercooled metallic melts. *Proceedings of the National Academy of Sciences 112* (2015), 13762–13767.

[92] Kremer, F., and Schönhals, A. *Broadband Dielectric Spectroscopy.* Springer-Verlag, 2003.

[93] Langer, J. S. Theories of glass formation and the glass transition. *Reports on Progress in Physics 77* (2014), 042501.

[94] Larini, L., Ottochian, A., de Michele, C., and Leporini, D. Universal scaling between structural relaxation and vibrational dynamics in glass-forming liquids and polymers. *Nature Physics 4* (2008), 42–45.

[95] Laue-Langevin, I. LAMP, the Large Array Manipulation Program. `http://www.ill.eu/data_treat/lamp/the-lamp-book/`.

[96] León, C., Ngai, K. L., and Roland, C. M. Relationship between the primary and secondary dielectric relaxation processes in propylene glycol and its oligomers. *Journal of Chemical Physics 110*, 23 (1999), 11585–11591.

[97] Li, G., H. E. King, J., Oliver, W. F., Herbst, C. A., and Cummins, H. Z. Pressure and temperature dependence of glass-transition dynamics in a "fragile" glass former. *Physical Review Letters 74* (1995), 2280–2283.

[98] Lin, X. H., and Johnson, W. L. Formation of Ti-Zr-Cu-Ni bulk metallic glasses. *Journal of Applied Physics 78*, 11 (1995), 6514–6519.

[99] Ling, A. C., and Willard, J. E. Viscosities of some organic glasses used as trapping matrixes. *Journal of Physical Chemistry 72*, 6 (1968), 1918–1923.

[100] López, E. R., Pensado, A. S., Comuñas, M. J., Pádua, A. A., Fernández, J., and Harris, K. R. Density scaling of the transport properties of molecular and ionic liquids. *Journal of Chemical Physics 134*, 14 (2011), 144507.

[101] Lovesey, S. W. *Theory of Neutron Scattering from Condensed Matter*. Oxford Science Publications, 1984.

[102] Malinovsky, V., Novikov, V., and Sokolov, A. Log-normal spectrum of low-energy vibrational excitations in glasses. *Physics Letters A 153*, 1 (1991), 63–66.

[103] Martinez, L.-M., and Angell, C. A. A thermodynamic connection to the fragility of glass-forming liquids. *Nature 410* (2001), 663.

[104] Mattsson, J., Bergman, R., Jacobsson, P., and Börjesson, L. Chain-length-dependent relaxation scenarios in an oligomeric glass-forming system: from merged to well-separated $\alpha$ and $\beta$ loss peaks. *Physical Review Letters 90*, 7 (2003), 075702.

[105] Maxwell, J. C. On the dynamical theory of gases. *Philosophical Transactions of the Royal Society of London 157* (1867), 49–88.

[106] Mierzwa, M., Pawlus, S., Paluch, M., Zioło, J., and Szulc, A. Note: New feedthrough insulation method for the dielectric spectroscopy under ultrahigh pressure conditions. *Review of Scientific Instruments 81*, 6 (2010), 066101.

[107] Monaco, A., Chumakov, A., Yue, Y.-Z., Monaco, G., Comez, L., Fioretto, D., Crichton, W., and Rüffer, R. Density of vibrational states of a hyperquenched glass. *Physical Review Letters 96*, 20 (2006), 205502.

[108] Ngai, K. L. Why the fast relaxation in the picosecond to nanosecond time range can sense the glass transition. *Philosophical Magazine 84*, 13-16 (2004), 1341–1353.

[109] Ngai, K. L., Casalini, R., Capaccioli, S., Paluch, M., and Roland, C. M. Do theories of the glass transition, in which the structural relaxation time does not define the dispersion of the structured relaxation, need revision? *Journal of Physical Chemistry B 109* (2005), 17356–17360.

[110] Ngai, K. L., Habasaki, J., Prevosto, D., Capaccioli, S., and Paluch, M. Thermodynamic scaling of $\alpha$-relaxation time and viscosity stems from the Johari-Goldstein $\beta$-relaxation or the primitive relaxation of the coupling model. *Journal of Chemical Physics 137*, 3 (2012), 034511.

[111] Ninarello, A., Berthier, L., and Coslovich, D. Models and algorithms for the next generation of glass transition studies. *Physical Review X 7*, 2 (2017), 021039.

[112] Niss, K., Begen, B., Frick, B., Ollivier, J., Beraud, A., Sokolov, A., Novikov, V., and Alba-Simionesco, C. Influence of pressure on the Boson peak: stronger than elastic medium transformation. *Physical Review Letters 99*, 5 (2007), 055502.

[113] Niss, K., Dalle-Ferrier, C., Frick, B., Russo, D., Dyre., J., and Alba-Simionesco, C. Connection between slow and fast dynamics of molecular liquids around the glass transition. *Physical Review E: Statistical, Nonlinear, and Soft Matter Physics 82* (2010), 021508.

[114] Niss, K., Dalle-Ferrier, C., Giordano, V. M., Monaco, G., Frick, B., and Alba-Simionesco, C. Glassy properties and viscous slowing down: An analysis of the correlation between nonergodicity factor and fragility. *Journal of Chemical Physics 129*, 19 (2008), 194513.

[115] Novikov, V. N., Ding, Y., and Sokolov, A. P. Correlation of fragility of supercooled liquids with elastic properties of glasses. *Physical Review E 71* (2005), 061501.

[116] Novikov, V. N., and Sokolov, A. P. Poisson's ratio and the fragility of glass-forming liquids. *Nature 431* (2004), 961–963.

[117] Olsen, A. E., Dyre, J. C., and Schrøder, T. B. Communication: Pseudoisomorphs in liquids with intramolecular degrees of freedom. *Journal of Chemical Physics 145*, 24 (2016), 241103.

[118] Patkowski, A., Lopes, M. M., and Fischer, E. W. Pressure dependence of the high-frequency light scattering susceptibility of ortho-terphenyl: A mode coupling analysis. *Journal of Chemical Physics 119*, 3 (2003), 1579–1585.

[119] Pedersen, U. R., Bailey, N. P., Schrøder, T. B., and Dyre, J. C. Strong pressure-energy correlations in van der waals liquids. *Physical Review Letters 100*, 1 (2008), 015701.

[120] Pedersen, U. R., Costigliola, L., Bailey, N. P., Schrøder, T. B., and Dyre, J. C. Thermodynamics of freezing and melting. *Nature Communications 7* (2016), 12386.

[121] Pedersen, U. R., Peters, G. H., Schrøder, T. B., and Dyre, J. C. Correlated volume- energy fluctuations of phospholipid membranes: A simulation study. *Journal of Physical Chemistry B 114*, 6 (2010), 2124–2130.

[122] Peters, J., Trapp, M., Hughes, D., Rowe, S., Demé, B., Laborier, J.-L., Payre, C., Gonzales, J.-P., Baudoin, S., Belkhier, N., and Lelièvre-Berna, E. High hydrostatic pressure equipment for neutron scattering studies of samples in solutions. *High Pressure Research 32*, 1 (2012), 97–102.

[123] Phillips, W., Ed. *Amorphous Solids: Low Temperature Properties*. Springer-Verlag, Berlin, 1981.

[124] Plofker, A. L., and Beckmann, P. A. Solid-state proton spin relaxation and methyl reorientation in isopropylbenzene. *Journal of Physical Chemistry 99*, 1 (1995), 391–394.

[125] Puosi, F., Chulkin, O., Bernini, S., Capaccioli, S., and Leporini, D. Thermodynamic scaling of vibrational dynamics and relaxation. *Journal of Chemical Physics 145*, 23 (2016), 234904.

[126] Rahman, A., Singwi, K., and Sjölander, A. Theory of slow neurton scattering by liquids. I. *Physical Review 126* (1962), 986–996.

[127] Ransom, T. C., and Oliver, W. F. Glass transition temperature and density scaling in cumene at very high pressure. *Physical Review Letters 119* (2017), 025702.

[128] Reiser, A., Kasper, G., Gainaru, C., and Böhmer, R. Communications: High-pressure dielectric scaling study of a monohydroxy alcohol. *Journal of Chemical Physics 132*, 18 (2010), 181101.

[129] Ribeiro, M. C. C., Scopigno, T., and Ruocco, G. Computer simulation study of thermodynamic scaling of dynamics of $2\,Ca(NO_3)_2{\cdot}3\,KNO_3$. *Journal of Chemical Physics 135*, 16 (2011), 164510.

[130] Richard, D., Ferrand, M., and Kearley, G. J. Analysis and visualisation of neutron-scattering data. *Journal of Neutron Research 4*, 1-4 (1996), 33–39.

[131] Richert, R., Duvvuri, K., and Duong, L.-T. Dynamics of glass-forming liquids. VII. dielectric relaxation of supercooled tris-naphthylbenzene, squalane, and decahydroisoquinoline. *Journal of Chemical Physics 118*, 4 (2003), 1828–1836.

[132] Richert, R., and Weinstein, S. Nonlinear dielectric response and thermodynamic heterogeneity in liquids. *Physical Review Letters 97* (2006), 095703.

[133] Roed, L., Gundermann, D., Dyre, J. C., and Niss, K. Communication: Two measures of isochronal superposition. *Journal of Chemical Physics 139* (2013), 101101.

[134] Roland, C. M., Bair, S., and Casalini, R. Thermodynamic scaling of the viscosity of van der waals, H-bonded, and ionic liquids. *Journal of Chemical Physics 125*, 12 (2006), 124508.

[135] Roland, C. M., Casalini, R., Bergman, R., and Mattson, J. Role of hydrogen bonds in the supercooled dynamics of glass-forming liquids at high pressures. *Physical Review B 77* (2008), 012201.

[136] Roland, C. M., Casalini, R., and Paluch, M. Isochronal temperature-pressure superpositioning of the $\alpha$-relaxation in type-A glass formers. *Chemical Physics Letters 367* (2003), 259–264.

[137] Roland, C. M., Hensel-Bielowka, S., Paluch, M., and Casalini, R. Supercooled dynamics of glass-forming liquids and polymers under hydrostatic pressure. *Reports on Progress in Physics 68* (2005), 1405–1478.

[138] Romanini, M., Barrio, M., Macovez, R., Ruiz-Martin, M. D., Capaccioli, S., and Tamarit, J. L. Thermodynamic scaling of the dynamics of a strongly hydrogen-bonded glass-former. *Scientific Reports 7* (2017), 1346.

[139] Sanz, A. Private communication. Unpublished data, 2017.

[140] Sanz, A., Hansen, H. W., Jakobsen, B., Pedersen, I. H., Capaccioli, S., Adrjanowicz, K., Paluch, M., Gonthier, J., Frick, B., Lelièvre-Berna, E., Peters, J., and Niss, K. High-pressure cell for simultaneous dielectric and neutron spectroscopy. *arXiv:1709.09859* (2017).

[141] Sanz, A., Nogales, A., Ezquerra, T. A., Häussler, W., Soccio, M., Lotti, N., and Munari, A. Homogeneous dynamics within inhomogeneous environment in semicrystalline polymers. *Macromolecules 44*, 20 (2011), 8124–8128.

[142] Sanz, A., Nogales, A., Puente-Orench, I., Jiménez-Ruiz, M., and Ezquerra, T. A. Detection of early stage precursor during formation of plastic crystal ethanol from the supercooled liquid state: A simultaneous dielectric spectroscopy with neutron diffraction study. *Physical Review Letters 107* (2011), 025502.

[143] Schaefer, T., Sebastian, R., and Penner, G. H. Theoretical and experimental data on the internal rotational potential in isopropylbenzene. *Canadian Journal of Chemistry 66*, 6 (1988), 1495–1499.

[144] Schneider, U., Lunkenheimer, P., Brand, R., and Loidl, A. Dielectric and far-infrared spectroscopy of glycerol. *Journal of Non-Crystalline Solids 235* (1998), 173–179.

[145] Schrøder, T. B., Bailey, N. P., Pedersen, U. R., Gnan, N., and Dyre, J. C. Pressure-energy correlations in liquids. III. Statistical mechanics and thermodynamics of liquids with hidden scale invariance. *Journal of Chemical Physics 131*, 23 (2009), 234503.

[146] Schrøder, T. B., and Dyre, J. C. Simplicity of condensed matter at its core: Generic definition of a Roskilde-simple system. *Journal of Chemical Physics 141*, 20 (2014), 204502.

[147] Schrøder, T. B., Sastry, S., Dyre, J. C., and Glotzer, S. C. Crossover to potential energy landscape dominated dynamics in a model glass-forming liquid. *Journal of Chemical Physics 112* (2000), 9834–9840.

[148] Scopigno, T., Ruocco, G., and Sette, F. Is the fragility of a liquid embedded in the properties of its glass? *Science 302* (2003), 849–852.

[149] Sidebottom, D. L. *Fundamentals of Condensed Matter and Crystalline Physics*. Cambridge University Press, 2012.

[150] Sillrén, P., Matic, A., Karlsson, M., Koza, M., Maccarini, M., Fouquet, P., Götz, M., Bauer, T., Gulich, R., and Lunkenheimer, P. Liquid 1-propanol studied by neutron scattering, near-infrared, and dielectric spectroscopy. *Journal of Chemical Physics 140*, 12 (2014), 124501.

[151] Sokolov, A., Calemczuk, R., Salce, B., Kisliuk, A., Quitmann, D., and Duval, E. Low-temperature anomalies in strong and fragile glass formers. *Physical Review Letters 78*, 12 (1997), 2405.

[152] Sokolov, A. P., Rössler, E., Kisliuk, A., and Quitmann, D. Dynamics of strong and fragile glass formers: Differences and correlation with low-temperature properties. *Physical Review Letters 71* (1993), 2062.

[153] Squires, G. *Introduction to the Theory of Thermal Neutron Scattering*. Cambridge University Press, 1978.

[154] Stillinger, F. H., and Debenedetti, P. G. Glass transition thermodynamics and kinetics. *Annual Review of Condensed Matter Physics 4* (2013), 263.

[155] Tammann, V., and Hesse, W. Die Abhängigkeit der Viskosität von der Temperatur bei unterkühlten Flüssigkeiten. *Zeitschrift für anorganische und allgemeine Chemie 8* (1926), 339.

[156] Tanaka, H. Relation between thermodynamics and kinetics of glass-forming liquids. *Physical Review Letters 90* (2003), 055701.

[157] Tarjus, G., Kivelson, D., Mossa, S., and Alba-Simionesco, C. Disentangling density and temperature effects in the viscous slowing down of glassforming liquids. *Journal of Chemical Physics 120*, 13 (2004), 6135–6141.

[158] Tölle, A. Neutron scattering studies of the model glass former *ortho*-terphenyl. *Reports on Progress in Physics 64* (2001), 1473–1532.

[159] Tölle, A., Schober, H., Wuttke, J., Fujara, F., and Randl, O. Incoherent dynamical structure factor of the compressed fragile liquid orthoterphenyl. *Physica B: Condensed Matter 234* (1997), 428 – 430. Proceedings of the First European Conference on Neutron Scattering.

[160] Tölle, A., Schober, H., Wuttke, J., Randl, O. G., and Fujara, F. Fast relaxation in a fragile liquid under pressure. *Physical Review Letters 80* (1998), 2374–2377.

[161] Tölle, A., Zimmermann, H., Fujara, F., Petry, W., Schmidt, W., Schober, H., and Wuttke, J. Vibrational states of glassy and crystalline orthoterphenyl. *European Physical Journal B 16*, 1 (2000), 73–80.

[162] Trachenko, K., and Brazhkin, V. V. Collective modes and thermodynamics of the liquid state. *Reports on Progress in Physics 79*, 1 (2016), 016502.

[163] Veldhorst, A. A., Dyre, J. C., and Schrøder, T. B. Scaling of the dynamics of flexible Lennard-Jones chains: Effects of harmonic bonds. *Journal of Chemical Physics 143*, 19 (2015), 194503.

[164] Vogel, H. Das Temperaturabhängigkeitsgesestz der Viskosität von Flüssigkeiten. *Physikalische Zeitschrift 22* (1921), 645–646.

[165] Widmer-Cooper, A., and Harrowell, P. Predicting the long-time dynamic heterogeneity in a supercooled liquid on the basis of short-time heterogeneities. *Physical review letters 96*, 18 (2006), 185701.

[166] Williams, E., and Angell, C. Pressure dependence of the glass transition temperature in ionic liquids and solutions. evidence against free volume theories. *Journal of Physical Chemistry 81*, 3 (1977), 232–237.

[167] Wyart, M. Correlations between vibrational entropy and dynamics in liquids. *Physical Review Letters 104* (2010), 095901.

[168] Xiao, W., Tofteskov, J., Christensen, T. V., Dyre, J. C., and Niss, K. Isomorph theory prediction for the dielectric loss variation along an isochrone. *Journal of Non-Crystalline Solids 407* (2015), 190.

[169] Yan, L., Düring, G., and Wyart, M. Why glass elasticity affects the thermodynamics and fragility of supercooled liquids. *Proceedings of the National Academy of Sciences 110*, 16 (2013), 6307–6312.

[170] Yannopoulos, S. N., and Johari, G. P. Poisson's ratio and liquid's fragility. *Nature 442* (2006), E7–E8.

[171] Zheng, Q., and Mauro, J. C. Viscosity of glass-forming systems. *Journal of the American Ceramic Society 100*, 1 (2017), 6–25.


I’m supercool,
but I don’t freeze